

Université
de Toulouse

THÈSE

En vue de l'obtention du

DOCTORAT DE L'UNIVERSITÉ DE TOULOUSE

Délivré par l' Université Paul Sabatier

Discipline ou spécialité : Mécanique des fluides

Présentée et soutenue par
Houssam SOUEID

Le 16 avril 2008 à Gênes, Italie

Titre : Optimisation of the kinematics of flapping airfoils
for micro air vehicle applications

Optimisation de la cinématique d'un profil battant
pour des applications aux micro-drônes

JURY

Prof Angelo Iollo (président du jury)

Dr Christophe Airiau

Prof Alessandro Bottaro

Prof Elisabetta Arato

Dr Ardeshir Hanifi

Prof Jean-Marc Moschetta

Prof Enrico Foti

Ecole doctorale : Mécanique, Energétique, Génie civil, Procédés
Unité de recherche : Institut de Mécanique des Fluides de Toulouse, UMR5502

Directeur(s) de Thèse : Prof A. Bottaro (Univ. Gênes) et Dr C. Airiau (UPS)

Rapporteurs : Dr Ardeshir Hanifi et Prof Angelo Iollo



Università di Genova & Université Paul Sabatier, Toulouse III

Optimisation of the kinematics of flapping airfoils for micro air vehicle applications



Houssam SOUEID

January 2008

Università degli Studi di Genova

Université Paul Sabatier, Toulouse III

Dipartimento di Ingegneria delle Costruzione, dell'Ambiente e del Territorio

&

Institut de Mécanique des Fluides de Toulouse

Dottorato di ricerca in fluidodinamica e processi dell'ingegneria
ambientale - XX CICLO

Docteur de recherche de l'université Paul Sabatier en dynamique des
fluides

Optimisation of the kinematics of flapping airfoils for micro air vehicle applications

Houssam SOUEID

January 2008

Supervisors:

Prof. Alessandro Bottaro - Università degli Studi di Genova

Dr. Christophe Airiau - Université Paul Sabatier, Toulouse III

Università degli Studi di Genova
Dottorato di ricerca in fluidodinamica e processi dell'ingegneria ambientale
XX ciclo

Université de Toulouse
Doctorat de recherche de l'école doctorale de mécanique, énergétique, génie civil et
procédés

Jury:

Dr. Christophe Airiau - University of Toulouse III - France
Prof. Elisabetta Arato - University of Genoa - Italy
Prof. Alessandro Bottaro - University of Genoa - Italy
Prof. Enrico Foti - University of Catania - Italy
Dr. Ardeshir Hanifi - Royal institute of technology - Sweden, referee
Prof. Angelo Iollo - University of Bordeaux I - France, referee
Prof. Jean-Marc Moschetta - Aeronautics and space institute - Toulouse - France

Final presentation:

16 April 2008

Houssam SOUEID

Dipartimento di Ingegneria delle Costruzioni, dell'Ambiente e del Territorio
Università di Genova, Via Montallegro 1
16145 Genova - Italia

phone: +39 010 3532479

fax: +39 010 3532546

e-mail: houssam.soueid@unige.it

Institut de Mécanique des Fluides de Toulouse
1, Avenue du Pr. Camille Soula
31400 Toulouse - France

phone: +33 5 61 28 59 02

fax: +33 5 61 28 58 99

e-mail: soueid@imft.fr

Optimisation de la cinématique d'un profil battant pour applications aux micro-drones

Mots-clès:

Mirco-drones, vol battu, optimisation numérique, sensibilités, pas complexe

L'optimisation du battement d'un profil d'aile est réalisée par simulations numériques. L'objectif principal est d'identifier les paramètres de battement capables d'assurer à un micro-drone de bonnes performances aérodynamiques en termes de forces de poussée, de portance et de rendement propulsif. Les variables de contrôle sont les amplitudes des oscillations verticales et de tangage, leur déphasage, leur fréquence, et l'angle d'incidence moyen. Une fois déterminées, les cinématiques optimales sont confrontées aux valeurs observées dans la nature.

La méthodologie est basée sur la résolution de l'écoulement autour d'un profil NACA0012 battant. Diverses fonctionnelles coût sont minimisées en fonction de la mission du véhicule. Leur gradients par rapports aux paramètres cinématiques sont calculés par la technique des sensibilités et la méthode du pas complexe. Un algorithme de quasi-Newton permet d'actualiser avec les gradients le mouvement du profil vers un optimum de la fonctionnelle.

Les résultats montrent la capacité d'un profil optimisé d'aile battante à produire de grandes forces de poussée et de portance avec un rendement propulsif acceptable. Pour ce faire, il faut que les oscillations de tangage précèdent celles de translation verticale par un déphasage de l'ordre de 90° et que le nombre de Strouhal soit dans l'intervalle $[0.2, 0.4]$. Augmenter le nombre de Reynolds a pour effet de réduire les pertes d'énergie liées à la viscosité et d'augmenter le rendement propulsif. Ce rendement a aussi été accru pour les cas de grandes forces de poussée en incluant des harmoniques d'ordre supérieur dans les oscillations verticales.

Reduced abstract

Keywords:

bio-inspired robots, flapping foils, numerical optimisation, sensitivity, complex step derivative

The optimisation of the kinematics of a two-dimensional flapping airfoil is carried out by numerical simulation to identify flapping parameters capable to ensure high aerodynamic performances for a micro air vehicle application. Attention is focused on the lift and thrust and on the propulsive efficiency. The control variables are the amplitudes of the combined motions of heaving and pitching and the phase angle between them. Additionally, the flapping frequency and the mean angle of attack are considered. The optimal kinematics are compared to observations in nature on birds, insects and fish.

The methodology is based on the solution of the flow field around a NACA0012 airfoil submitted to translational and angular oscillations. Then, the gradients of the cost functional with respect to the control parameters are evaluated thanks to the sensitivity technique and the complex step derivative method. The gradients are subsequently used in a quasi-Newton update algorithm to direct the solution towards its optimal value.

Results show the ability of optimised flapping airfoils to produce large thrust and lift, with an acceptable efficiency. This is ensured when the pitching oscillations lead the heaving ones by a phase angle close to 90° and when the Strouhal number of oscillations is in the range $[0.2,0.4]$. It is expected that the optimal efficiency would increase for higher Reynolds number, without much variation in the optimal kinematics. Furthermore, the drop in efficiency at high thrust forces may be limited by including higher order terms in the expression of heaving.

Acknowledgments

Before addressing the topic of flapping airfoils, investigated during a part of my PhD thesis, I should thank all those who made my research work possible and in pleasant and enriching environment. A very special acknowledgment goes to Professor Alessandro Bottaro who was a perfect supervisor during three years. His enthusiasm, motivation and engagement triggered the will to discover the academic research world back during the period in which I was an undergraduate student. His wide knowledge, consistent availability and efficient methodology helped in driving this work towards its objectives. A special thanks goes also to Dr Christophe Airiau, who was a very good supervisor during the stay period in France for this PhD thesis in collaboration between the universities of Genoa in Italy and Toulouse in France. His passion for airplanes and wide knowledge of the aeronautical sector brought to this work a panoramic point of view. His interesting ideas and suggestions were crucial for some of the choices adopted in the present work. And like Prof. Bottaro, despite their numerous responsibilities and duties, he was always available and ready for help.

A special acknowledgment is reserved for Dr Laura Guglielmini, who developed the flow solver during her thesis and was an example of kindness, availability and hard worker with a wonderful team spirit. She never hesitated to share her knowledge and to offer her time to make this contribution progress. She was very patient accepting to spend long hours for the reading of the different papers and internal reports written during this thesis. A hard task, shared also by Profs. Bottaro and Airiau who read passionately and corrected patiently all what has been written during three years. I should also thank Professor Paolo Blondeaux who followed a large number of my seminars on the topic and offered by his questions, discussions and suggestions very interesting points of view. In the same manner, Mr Joel Guerrero who is preparing his PhD on a close topic helped with his experience of the commercial computational fluid dynamics softwares and by launching some validation runs.

Finally, I cannot forget to thank all the other PhD students, professors and staff in the Institut de Mécaniques des Fluides de Toulouse and Dipartimento di ingegneria delle Costruzione, dell'Ambiente e del Territorio in Genoa who made this three-years

period so lovely. A special thanks to my office mates, so kind that they faked understanding my Italian during my whole stay in Italy, to the Flubio project fellows in Genoa and the Aerotranet project fellows in Toulouse. Thanks to my family and friends who always supported me during my long studies.

Contents

Abstract	1
Introduction	7
1 Flapping airfoils and applications to MAVs	13
1.1 Micro air vehicles	13
1.1.1 MAVs' definition and applications	14
1.1.2 MAVs advantages and avionics	15
1.1.3 Mobile- versus fixed-wing MAVs	17
1.2 Low Reynolds number aerodynamics	18
1.3 Flapping airfoils	20
1.3.1 Heaving airfoils	22
1.3.2 Pitching airfoils	23
1.3.3 Combination of heaving and pitching	24
1.4 Birds, insects and fish	27
1.4.1 Birds	27
1.4.2 Insects	30
1.4.3 Aquatic animals	32
2 Problem formulation	35
2.1 The geometry	36
2.2 The scaling	39
2.3 The flow equations	42
2.4 Direct variables	45
2.5 The optimisation approach	47
2.5.1 Cost functional	47
2.5.2 Control parameters	49
2.5.3 Evaluating the gradient	51
3 Gradient evaluation	53
3.1 Sensitivity technique	54

3.1.1	Sensitivity equations	54
3.1.2	Sensitivity gradient	57
3.2	Complex step derivative method	58
3.2.1	The principle of the method	59
3.2.2	Coding tricks	61
3.2.3	Application to flapping airfoil	62
3.2.4	Complex-step gradient	63
3.3	From CSDM to sensitivity	63
3.3.1	Burgers' equation	63
3.3.2	Flapping airfoil	65
4	Numerical aspects	71
4.1	On the grid adequacy	72
4.2	Boundary conditions validity	78
4.3	Solver validation	81
4.4	Optimisation update	85
5	Kinematics optimisation	89
5.1	Thrust and lift generation	90
5.2	Sensitivity fields	93
5.3	Critical Strouhal number	94
5.4	Effect of heaving and pitching amplitudes	98
5.4.1	Optimal amplitudes	98
5.4.2	Effective angle of attack	101
5.5	Effect of the phase angle	104
5.6	Lift analysis	107
5.6.1	Lift of a flapping airfoil	107
5.6.2	Comparison of still and flapping airfoils	109
5.7	Optimal configurations	113
5.7.1	Basic configuration	113
5.7.2	Thrust configuration	114
5.7.3	Practical configuration	117
5.8	High order harmonics	118
5.8.1	Optimised high order harmonics configurations	119
5.8.2	Non-optimised configurations	124
5.9	Frequency and Reynolds number effects	125
5.9.1	Reynolds number effect	126
5.9.2	Reduced frequency effect	129
5.10	Gliding	131
	Conclusions	137

A	Comparison of fixed- and mobile-wing powers	145
B	Reference systems and transformations	148
C	Details of the flow and sensitivity equations	150
C.1	Flow equations	150
C.2	Sensitivity equations	152
C.2.1	The gradient terms	152
C.2.2	The kinematics	153
C.3	CSDM equations	154
D	Discretization	157
D.1	The flow equations	157
D.1.1	The vorticity equation	157
D.1.2	The stream function equation	161
D.2	The sensitivity equations	162
D.2.1	The vorticity sensitivity	162
D.2.2	The stream function sensitivity	165
E	The boundary conditions	167
E.1	Flow boundary conditions	167
E.1.1	The vorticity equation	168
E.1.2	The stream function equation	169
E.2	Sensitivity boundary conditions	171
E.2.1	The sensitivity of the vorticity	171
E.2.2	The sensitivity of the stream function	172
	Bibliography	173

List of Figures

1	The Strouhal number for some swimming and flying species.	8
2	Ranges of the frequency and the velocity of motions of species.	9
3	Universal law for the force developed by some species and for the wing span of flying animals.	10
1.1	A fixed-wing MAV prototype versus a similar sized bird.	14
1.2	Comparison of mass breakdown between a micro air vehicle and a classical full-scale civil aircraft.	16
1.3	A flapping-wing MAV prototype and a sketch of Da Vinci's flying machine.	17
1.4	Mass versus Reynolds number ranges of some flying animals and vehicles.	19
1.5	Evolution of lift and drag coefficients with the Reynolds number for smooth still airfoils	19
1.6	General definition of flapping and reduced frequency range versus Reynolds number for flying animals and vehicles.	21
1.7	Classic and reversed von Karman streets.	21
1.8	Wake structure of a purely heaving airfoil dominantly producing thrust force.	23
1.9	Wake vortex structure in the two gaits typical of birds.	28
1.10	Effect of the presence of a bird's tail on separation and on the nature of the wake.	29
1.11	An insect-like MAV compared to a dragonfly insect.	31
1.12	A micro scale flying device using helicopter principle.	32
1.13	An autonomous underwater vehicle compared to a fish.	33
2.1	Definition of flapping and of the different frame references used.	37
2.2	Comparison between the airfoil used in the present study and a NACA0012 airfoil.	38
2.3	Plot of a coarse grid showing the circular form of the computational domain and the effect of the stretching law in the radial direction.	39
2.4	Location of the imposed boundary conditions.	45

2.5	Different position of an airfoil at uniform intervals over a period of oscillation for a classical flapping motion.	50
3.1	Comparison of the relative error versus the step size between finite difference and complex step derivative methods	60
3.2	Comparison of finite difference and complex step methods for a simple function.	60
4.1	Plot of the mesh topology at the airfoil surface near the leading and trailing edges.	73
4.2	Plot of a coarse grid showing the position of R_{int} and R_{max} (red circles) and the associated distribution of points.	75
4.3	Effect of the grid choice on the error for thrust and its gradient with respect to the heave amplitude.	76
4.4	Distribution of points in the radial direction for various grids.	77
4.5	Evolution of the instantaneous lift force and its gradient with respect to the heave amplitude for long-term simulation.	78
4.6	Propagation of the shed vorticity in the wake towards the limit of the computational domain.	79
4.7	The horizontal velocity field for a small and average computational domain.	80
4.8	Validity of the boundary conditions for a small grid.	80
4.9	Validity of the boundary conditions for an average grid.	81
4.10	Validation of the solver of the gradient with respect to the heave amplitude.	82
4.11	Validation of the solver of the gradient with respect to the phase angle τ_1 and the pitching amplitude.	83
4.12	Validation of the solver of the gradient with respect to the phase angle ϕ_1	84
4.13	Comparison between the steepest descent and quasi-Newton algorithms for control parameter update.	86
5.1	Temporal evolution of the heave distance and the pitch angle and the associated forces and torque acting on the airfoil.	91
5.2	Pressure coefficient for a non-lifting configuration and lift total force and pressure component versus the pitching angle.	92
5.3	Stream function and vorticity fields for a flapping airfoil.	92
5.4	Comparison of the vorticity field to its sensitivity fields with respect to the amplitudes and the phase angle.	93
5.5	Sensitivity fields of the Stream function.	95

5.6	Vorticity fields for a deflected wake behind an airfoil flapping at large value of the Strouhal number.	95
5.7	Vorticity fields for a neutral wake behind an airfoil flapping at the critical value of the Strouhal number.	96
5.8	Values of the critical Strouhal for various pitching amplitudes and various phase angles.	97
5.9	Linear dependency between the optimal heaving and pitching amplitudes.	99
5.10	Values of the cost functional for optimal heaving and pitching amplitudes.	99
5.11	Comparison of vorticity fields between a bad propulsive efficiency configuration and an optimised one.	101
5.12	Comparison of the horizontal velocity fields between a bad propulsive efficiency configuration and an optimised one.	103
5.13	Evolution over one period of the effective angle of attack.	104
5.14	Values of the maximal effective angle of attack for optimal amplitudes.	104
5.15	Values of the optimal phase angles and the associated values of the cost functional for various heaving and pitching amplitudes.	105
5.16	Vorticity and velocity fields for an optimised phase angle configuration.	106
5.17	Lift and thrust/drag coefficients versus mean angle of attack for flapping airfoils.	108
5.18	Efficiency and cost functional variation with the mean angle of attack.	109
5.19	Lift coefficients for flapping and fixed airfoils over wide range of angle of attack.	110
5.20	Evolution of the lift coefficient in time for flapping and still NACA0012 airfoils.	111
5.21	Relative horizontal velocity fields for a fixed NACA0012 airfoil at 30° angle of attack and $Re_c = 1100$	112
5.22	Stream function fields for a fixed NACA0012 airfoil at 30° angle of attack and $Re_c = 1100$	112
5.23	Vorticity velocity fields for an optimised thrust coefficient.	116
5.24	Relative velocity fields for an optimised thrust coefficient.	116
5.25	Temporal evolution of the lift force for high order harmonic oscillations.	119
5.26	Variation of the propulsive efficiency and the thrust force with the Strouhal number for monochromatic oscillations and various pitching amplitudes.	120
5.27	Variation of the propulsive efficiency with the thrust force for monochromatic oscillations and various pitching amplitudes.	121
5.28	Influence of the high order terms on the efficiency versus thrust coefficient variations.	122

5.29	Influence of the high order terms on the heaving motion and the effective angle of attack.	123
5.30	Heave motion and effective angle of attack for various high-order configurations.	125
5.31	Variation of the propulsive efficiency and the thrust force with the Reynolds number.	127
5.32	Vorticity and relative horizontal velocity fields for $Re_c = 3500$	128
5.33	Comparison of the pressure coefficient on the airfoil for $Re_c = 1100$ and $Re_c = 3500$	128
5.34	Effect of the reduced frequency on the thrust coefficient and the propulsive efficiency.	130
5.35	Effect of the Strouhal number on the propulsive efficiency by modifying the flapping frequency.	130
5.36	Temporal evolution of the propulsive efficiency and the thrust force during the gliding phase.	133
5.37	Temporal evolution of lift and thrust forces during the gliding phase.	134

List of Tables

2.1	Scaling quantities based on the frequency of flapping	40
2.2	Scaling quantities based on velocity at infinity	40
4.1	The grid parameters for a selection of the tested meshes.	75
5.1	Optimal kinematics when controlling the heaving and pitching amplitudes for $N = 1, f_r = 0.3665$ and $Re_c = 1100$	103
5.2	Optimal kinematics when controlling the phase angle for $N = 1, f_r = 0.3665$ and $Re_c = 1100$	106
5.3	Optimal kinematics yielding good efficiency with limitation on the cost of the control for $N = 1, f_r = 0.3665$ and $Re_c = 1100$	114
5.4	Optimal kinematics yielding good efficiency without limitation on the cost of the control for $N = 1, f_r = 0.3665$ and $Re_c = 1100$	114
5.5	Optimal kinematics yielding imposed thrust coefficients for $N = 1, f_r = 0.3665$ and $Re_c = 1100$	115
5.6	Optimal kinematics yielding good thrust, lift and efficiency with limited oscillations for $N = 1, f_r = 0.3665$ and $Re_c = 1100$	117
5.7	Optimal kinematics yielding good thrust, lift and efficiency without limitation on oscillation amplitudes for $N = 1, f_r = 0.3665$ and $Re_c = 1100$	118
5.8	Optimal kinematics yielding imposed thrust for $N = 5$ acting on odd harmonics together with $\alpha_0 = 0^\circ, f_r = 0.3665$ and $Re_c = 1100$	121
5.9	Optimal kinematics yielding imposed thrust for $N = 5$ acting on odd harmonics together with $\alpha_0 = 0^\circ, f_r = 0.3665$ and $Re_c = 1100$	123
5.10	Non-optimised kinematics for high order harmonics together with $\alpha_0 = 0^\circ, \alpha_1 = -35^\circ, \phi_1 = 90^\circ, f_r = 0.3665$ and $Re_c = 1100$	124
5.11	List of the gliding configuration simulated for $N = 1, h_1 = 3, \tau_1 = 90^\circ, \alpha_1 = -35^\circ, f_r = 0.3665$ and $Re_c = 1100$	133

Abstract

The optimisation of the kinematics of a two-dimensional flapping airfoil is carried out numerically for a small value of the Reynolds number. The main goal is to identify flapping parameters capable to ensure high aerodynamic performances for a micro air vehicle application. Attention is focused on the lift and thrust forces and on the propulsive efficiency developed from the flapping motion. The control variables are the amplitudes of the combined motions of heaving and pitching and the phase angle between them. Additionally, the flapping frequency and the mean angle of attack are considered. The goals are, first, to find the optimal kinematics of the wing, and, second, to link these optimal configurations to observations in nature of animals using flapping motion for their locomotion, such as birds, insects and fish. Once achieved, the numerical optimisation may be seen as a proof that animals' motion is naturally optimised for their environments and the various conditions they encounter.

The methodology is based on the solution of the flow field around a NACA0012 airfoil submitted to translational and angular oscillations. Then, the gradients of the cost functional with respect to the control parameters are evaluated thanks to the sensitivity technique and the complex step derivative method. These two approaches of optimisation can be linked to one another by simple examination of the equations corresponding to real and complex variables. The gradients are subsequently used in a quasi-Newton update algorithm to direct the solution towards its optimal value.

Once the solver is validated, it is applied for the optimisation of each parameter separately and then to multi-parameters cases. Results show the ability of optimised flapping airfoils to produce large thrust and lift forces, with an acceptable efficiency. This is ensured when the pitching oscillations lead the heaving ones by a phase angle close to 90° and when the frequency of oscillations is such that the Strouhal number is in the range $[0.2, 0.4]$. Attempts to improve the relatively low efficiency were made by applying more complex motions, by varying the Reynolds number and by simulating gliding phases. It is expected that the optimal efficiency would increase for higher Reynolds number, without much variation in the kinematics compared to the

optimal solution for the small Reynolds number. Furthermore, the drop in efficiency at high thrust forces may be limited, for average amplitudes of pitching, with the presence of higher order terms in the expression of heaving. The simple gliding approach adopted here has not led to a better global efficiency, but has allowed to show the possibility of animals or vehicles to adopt this type of flight for long stretches of time.

French abstract

L'optimisation de la cinématique d'une aile bidimensionnelle battante est réalisée numériquement pour un nombre de Reynolds relativement bas. L'objectif principal est d'identifier les paramètres de battement capables d'assurer des bonnes performances aérodynamiques pour les appliquer au cas d'un micro drone à ailes mobiles. L'attention est focalisée sur les forces de poussée et de portance et sur l'efficacité propulsive développées au cours du battement de l'aile. Cette efficacité est définie comme le rapport des puissances utile à l'avancement de l'aile et celle nécessaire à son battement. Le mouvement de l'aile est décomposable en oscillations de translation verticale et angulaires de tangage. Les variables de contrôle sont les amplitudes des oscillations, leur fréquence, le déphasage entre elles et l'angle moyen d'attaque. Une fois bien définies pour plusieurs types de missions, les cinématiques optimales sont confrontées aux valeurs observées dans la nature pour des animaux ayant un mode de propulsion similaire, notamment certaines espèces d'oiseaux, d'insectes et de poissons. Cette comparaison pourrait être considérée comme une preuve que les animaux ont naturellement évolué vers des configurations optimales et adaptées à leur environnement.

La méthodologie est basée sur la résolution de l'écoulement autour d'un profil NACA0012 soumis à une combinaison de mouvements de translation et de rotation. Ensuite, les gradients d'une fonctionnelle coût, par rapport aux paramètres de contrôle, sont calculés avec la technique des sensibilités et la méthode du pas complexe. Le choix de la fonctionnelle est étroitement lié à la mission du véhicule, favorisant l'efficacité, et donc l'autonomie, pour les missions de longues durées et les forces, et donc les manoeuvres, pour les phases à risque. Les gradients sont ultérieurement utilisés dans un algorithme de quasi-Newton pour actualiser les paramètres dirigeant la solution vers son optimum.

Une fois validé, le code est appliqué à l'optimisation et l'étude de l'effet de chaque paramètre séparément et puis des cas d'optimisation multi-paramètres sont réalisés. Les résultats montrent la capacité d'une aile battante optimisée à produire des larges forces de poussée et de portance avec une efficacité acceptable. Pour ce faire, il

faut que les oscillations de tangage précèdent celles de translation verticale par un déphasage de l'ordre de 90° et que le nombre de Strouhal, défini comme le rapport de la vitesse de battement à celle d'avancement, soit dans l'intervalle $[0.2,0.4]$. Des tentatives d'améliorer l'efficacité ont été faites en variant le nombre de Reynolds, en complexifiant le mouvement de l'aile et en simulant des périodes de vol plané. L'effet d'un plus grand nombre de Reynolds résulte par des pertes visqueuses moins importantes et, par conséquence, une meilleure efficacité. Ceci étant, une cinématique optimale pour une telle configuration l'est aussi pour un faible nombre de Reynolds avec l'avantage de la réduction du coût des calculs. La chute de l'efficacité a été aussi limitée pour les cas de grandes forces de poussée et d'amplitude de tangage modérée en incluant des harmoniques d'ordre supérieur dans les oscillations verticales. L'approche simpliste du vol plané n'a pas apporté une amélioration de l'efficacité propulsive globale mais a permis de démontrer l'aptitude des animaux ou des véhicules à utiliser ce mode de vol pour des longues durées.

Italian abstract

L'ottimizzazione della cinematica di un'ala bidimensionale che batte è studiata numericamente per un numero di Reynolds relativamente basso. L'obiettivo principale è quello di identificare i parametri relativi al battito capaci di assicurare alte caratteristiche aerodinamiche, eventualmente per applicarli al caso di un micro aereo senza pilota con ale mobili. L'attenzione è focalizzata sulle forze di spinta e di portanza e sull'efficienza propulsiva sviluppata durante il battito dell'ala. Questa efficienza è definita come il rapporto della potenza utile al movimento dell'ala rispetto a quella necessaria al suo battito. Il moto dell'ala è scomponibile in oscillazioni di traslazione verticale e angolare. Le variabili di controllo sono le ampiezze delle oscillazioni, la loro frequenza, lo sfasamento e l'angolo di attacco medio. Una volta ben definite per ogni tipo di missione del veicolo, le cinematiche ottimali, esse vengono confrontate ai valori osservati in natura per animali con simile modo di propulsione, specialmente per certe specie di uccelli, insetti e pesci. Questo legame può essere considerato come una prova che gli animali hanno naturalmente evoluto verso delle configurazioni ottimali, adattandosi all'ambiente.

La metodologia è basata sulla risoluzione del flusso intorno ad un profilo NACA0012 sottomesso ad una combinazione di moti di traslazione e di rotazione. I gradienti di un funzionale costo sono calcolati rispetto ai parametri di controllo con la tecnica delle equazioni di sensibilità e il metodo del passo complesso. La scelta del funzionale è legata alle missioni del veicolo, privilegiando l'efficienza, e dunque l'autonomia, per il caso delle missioni a durate lunghe e le forze, e dunque le manovre, per i periodi a rischio. I gradienti sono poi usati in un algoritmo quasi-Newton per dirigere i parametri verso la soluzione ottimale.

Una volta validato, il codice è applicato allo studio dell'effetto di ogni parametro, preso singolarmente e poi dei casi di ottimizzazione multi-parametrica sono realizzati. I risultati mostrano la capacità di un battito ottimizzato a produrre grandi forze di spinta e un'alta portanza, mantenendo un' accettabile efficienza. Nel caso ottimo, le oscillazioni angolari precedono quelle di traslazione verticale con uno sfasamento dell'ordine di 90° , e il numero di Strouhal, definito come il rapporto della velocità

di battito a quella di avanzamento, deve essere nell'intervallo $[0.2,0.4]$. Tentativi di migliorare l'efficienza sono stati fatti modificando il numero di Reynolds, aumentando la complessità del moto dell'ala e simulando dei periodi di volo planato. L'effetto di un aumento del numero di Reynolds risulta in perdite viscosive minori e, di conseguenza, una migliore efficienza. Allo stesso tempo, la cinematica ottima per una tale configurazione lo rimane anche nel caso di un numero di Reynolds più piccolo, col vantaggio di ridurre il costo numerico. La caduta dell'efficienza è stata limitata per le grandi forze di spinta e le moderate ampiezze di oscillazione angolare includendo delle armoniche di ordine superiore nelle oscillazioni verticali. L'approccio semplificato di volo planato non ha migliorato l'efficienza propulsiva globale però ha permesso di dimostrare la capacità degli animali o dei veicoli ad utilizzare questo modo di volo per durate abbastanza lunghe.

Introduction

Between those who say that man-made products are asymptotically tending towards their limits of perfection and those who think that we still very far from this limit, no one disagrees with the fact that any source of inspiration, allowing progress, is welcome. And what better than nature to get inspired from? 10^9 years of perpetual and infinite evolution and levels of complexity and efficiency beyond humanity's range now and for long years to come. Therefore, and increasingly in the last two decades, humanity substituted the pure biological studies on animals by the investigation of the physical mechanisms they develop and the possibility to apply them to man-made products. Nowadays, even companies which suggests to find biometric solutions to industrial problems exist.

Since the present PhD thesis is concerned with flapping foils propulsion, the focus is here on the animals using this type of locomotion, namely some categories of birds, insects and fish. In the first half of the twentieth century, interest was triggered by the observation of some animals features. Subsequently, all kinds of experiments were conducted on animals with three major targets: confirm a given high performance level, understand what allows the animal to reach this level and finally try to apply the mechanism on man made vehicles (UAVs for unmanned air vehicles, AUVs for autonomous underwater vehicles and MAVs for micro air vehicles). The last of these experiments made four godwits (*Limosa lapponica*) fly their way into the records book with a more than 10,000 kms non-stop flight between New Zealand and the Yellow Sea. The godwits, tracked by satellite transmitters, flew for 8 days at an average speed of 55 km/h without any stop to drink or eat over the Pacific Ocean in march 2007. This is an example of what nature is able to perform. An example that would highly interest micro air vehicles designers and constructors unable to make their prototypes fly for more than few minutes. It may also interest any human being living in the twenty first century, with a barrel of oil worth around 100 \$ (U.S.A), (for the moment), in a world where more efforts and investments are injected to prevent pollution and global warming than what it is done to provide drinkable water to over one billion and a half humans. This example of natural high level of performance is one of the most recent in a long list. Previous

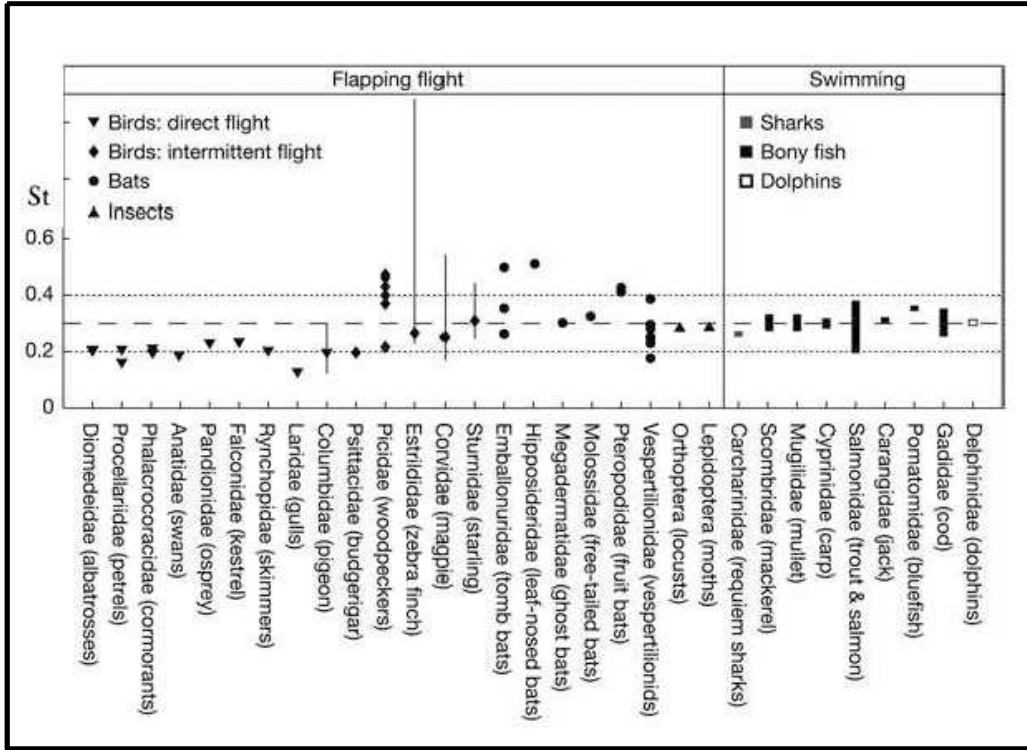


Figure 1: The natural Strouhal number for some swimming and flying species (Taylor et al., 2003).

contributions showed, for instance, that birds fly in groups because they are able to manipulate and control the shed vorticity around them by other animals in a way to limit the efforts their flight requires (Kvist et al., 2001; Weimerskirch et al., 2001). Other contributions proved a surprising low drag level for birds (Rayner, 2001) due to the elasticity of their body and the manipulation of vorticity with their tail and an excessively high lift level (Ellington and Usherwood, 2001) due to the presence of a leading edge vortex with delay stall and a very high propulsive efficiency due to minimal losses in the wake (Rayner, 1988).

Despite the various environments in which animals live and their different constraints, a large number of authors tried to justify a kind of universal law which governs the motion and the morphology of a large number of species. The first of these laws shows that animals move with a St mainly in the range $[0.2 - 0.4]$ (see figure 1) where St is the Strouhal number, a ratio between the flapping and the forward velocities. Triantafyllou et al. (1993) also proved that numerous species of fish flap their fins in this same range of Strouhal number. Subsequent works showed that the choice of these values correspond to configurations with high propulsive efficiency, i.e. configurations allowing the animal to cross the longest distance with the minimal

effort and consumption of food. Rayner (1996) treated the case of birds and Bejan and Marden (2006) generalized this principle to all kinds of living beings (see figures 2 and 3).

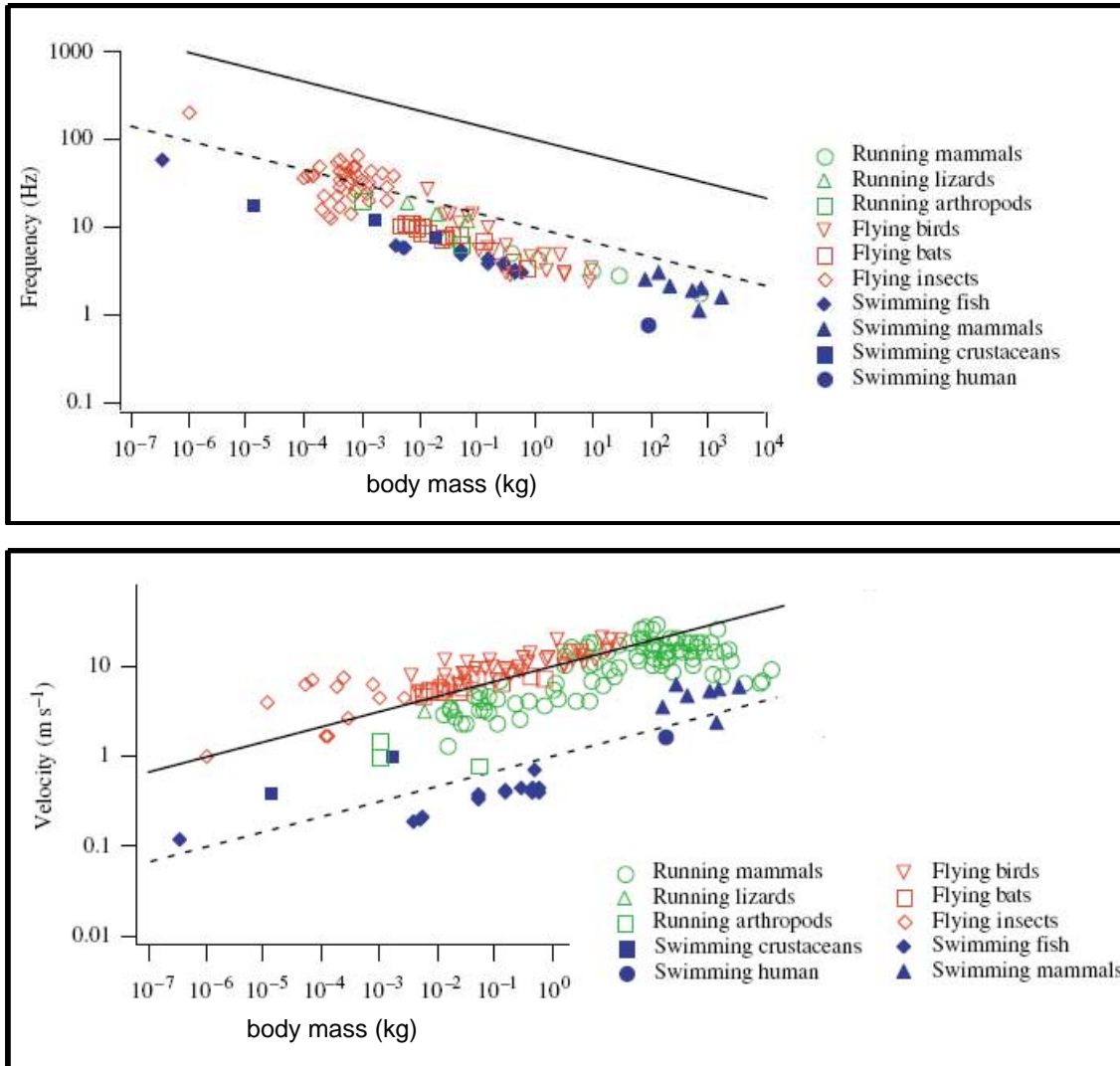


Figure 2: Universal law governing the frequency (top) and the velocity (bottom) of motions of flying, swimming and running species versus their body mass (Bejan and Marden, 2006).

They proved that the frequency of flapping, the forward velocity, the force developed by the body and the wing span follow a proportionality law with respect to the body mass.

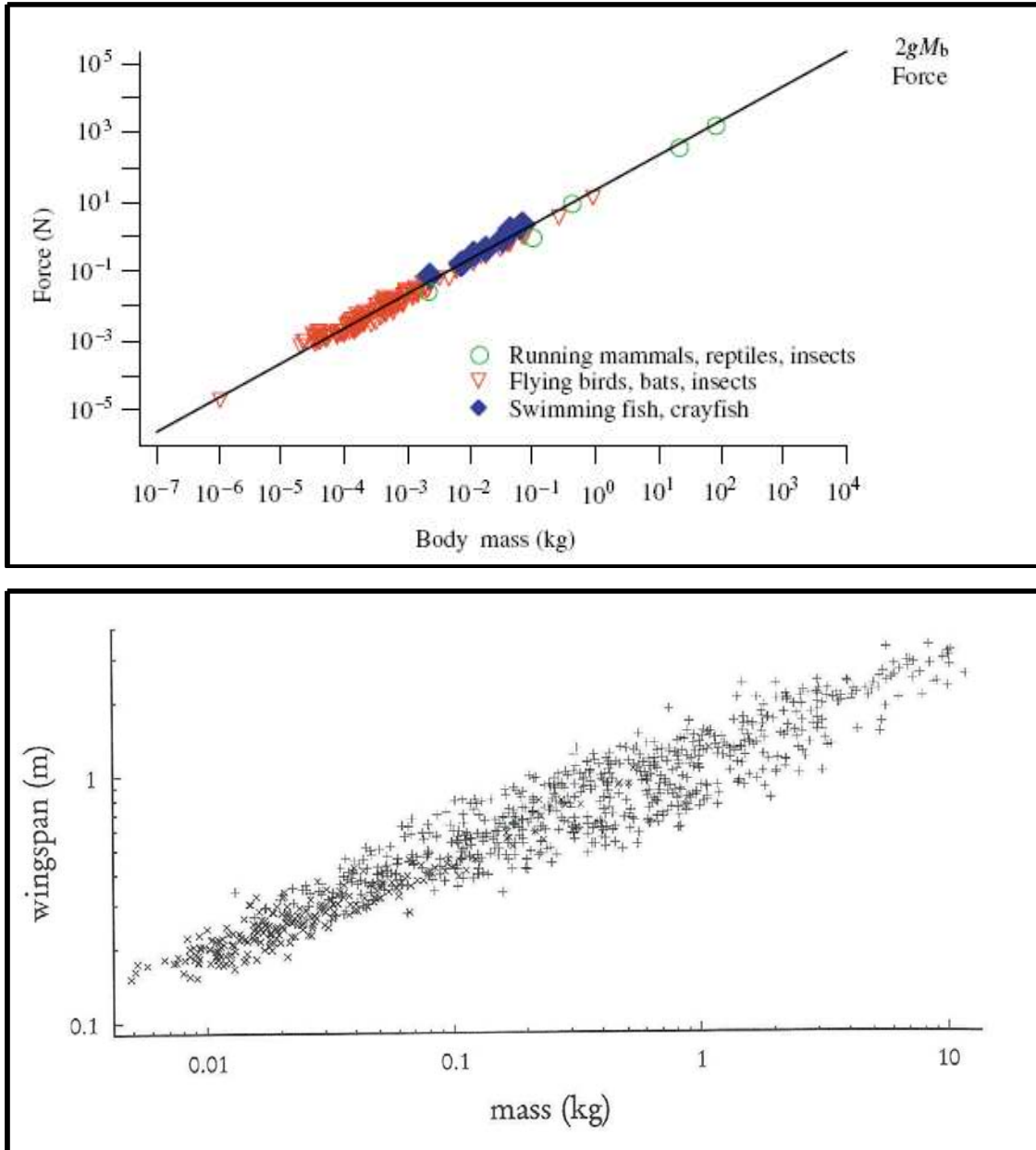


Figure 3: Universal law between the force developed by some species (Bejan and Marden, 2006) (top) and the wing span of flying animals (Rayner, 1996) (bottom) with respect to their body mass.

The idea of the present work is to show whether by optimising the motion of a flapping airfoil in a way to ensure high propulsive efficiencies, the optimal motion will be similar to that used by birds in their flight. In other words, a cost functional related

to the propulsive efficiency is defined and optimised by controlling the kinematics of a flapping airfoil, and the optimal values are compared to the characteristics of living animals. The values to be compared are the Strouhal number and other parameters that will be defined in the following including the phase angle which pilots the vorticity shedding.

To reach this target, and after a summary of previous contributions on the topic, the flow around a flapping NACA0012 airfoil is solved numerically for a two-dimensional low Reynolds number incompressible configuration. Then, the gradient of the cost functional is evaluated thanks to the sensitivity and complex step derivatives methods (CSDM). The value of the gradient is used to update the value of the control parameter by a quasi-Newton algorithm until reaching the optimal value, which is compared to the values observed in nature in living animals.

The optimal configurations are sought for different conditions including non lifting cases of fish, lifting cases of birds and high thrust cases. This case of high thrust is usually associated to a decrease of the propulsive efficiency. Therefore, more sophisticated kinematics, with higher order harmonics, are included in order to overcome this problem. Finally, the gliding configuration is studied and compared to the complex mechanisms used by birds during this phase.

Chapter 1

Flapping airfoils and applications to MAVs

Introduction

Assuming that oceans and the atmosphere are not the natural environments where human are supposed to move, the construction of man-made air and underwater vehicles should be inspired by animals. Without arguing on the evolution theory, from the philosophical point of view, one may imagine that animals optimised, or at least adapted, their motion and morphology in the course of the millennia in a way to render their motion more efficient. During the twentieth century, many efforts were concentrated on the comprehension of the mechanisms developed by animals.

The ability of reducing devices' sizes, due to electronics, gave human the opportunity to build prototypes of similar dimensions to birds, fish and, lately, insects. Nowadays, the challenge is to apply the already understood natural mechanisms on these prototypes on the one hand, and to pursue the investigation of complex mechanisms still not completely unsolved, on the other. This chapter aims at giving a non exhaustive list of the contributions made in the field of nature-mimicking for robots propulsion and lift. A special attention is given to the case of micro air vehicle and to flapping foils which are the basic configuration for the motion of birds and some types of fish.

1.1 Micro air vehicles

The present section is dedicated to the investigation of micro air vehicles. After giving their main characteristics and specific constraints, their applications are introduced

and the advantage of adopting MAVs, for given types of missions, is highlighted. Then, a comparison between different wings configurations is made to show that at bird scale, mobile-wing is more than an option. It is rather the optimal configuration adopted by animals and developed during millennia of evolution.

1.1.1 MAVs' definition and applications

MAV is the denomination used for small unmanned air vehicles (UAVs). These engines became realizable in the last decade and a half due to progress in miniaturization of propulsion and avionics devices. Typically, an MAV has a 15 cm wing-span and weighs around 100 g with a payload of roughly 20 g, usually a camera or other sensors. It flies at low altitudes, around 100 m, at a cruising speed of 50 km/h for a duration between 30 and 60 minutes. These characteristics make MAVs of similar dimensions than a large number of birds (see figure 1.1). The main application of MAVs is to operate in 3-D environments where 3-D refers to dull, dirty and dangerous. In other words, they are sent to a given location in order to establish a visual/acoustic contact. This objective can be sought in spying and surveillance missions in the battlefield, hostage rescue, fire detection or the exploration of hostile environments including the Martian atmosphere in the future. They are also used for other types of missions including weather forecast, biological/chemical elements detection, sowing of fields in agriculture, or communication "relay".

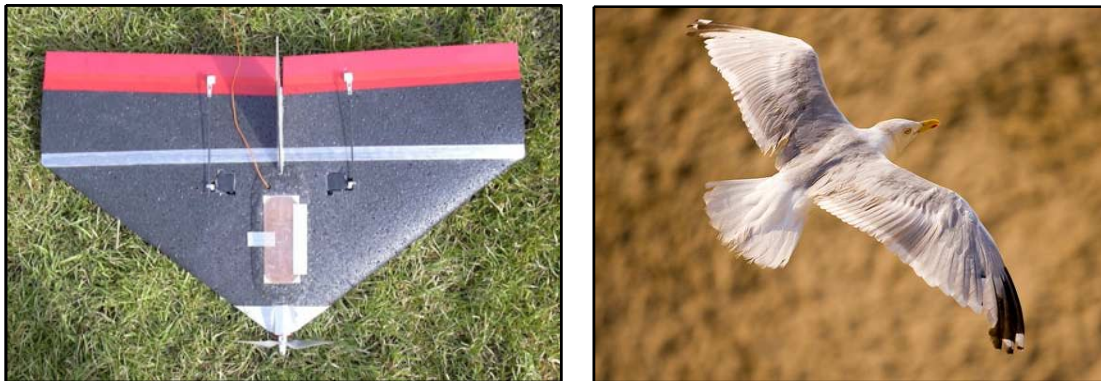


Figure 1.1: A fixed-swept-wing MAV prototype (left) and a bird of close dimensions (right)

Analysing the characteristics and the applications of MAVs allows to identify the principal constraints to be respected when they are designed:

- Low altitude cruise requires an anti-collision detection system.

- Light global mass implies high manoeuvrability, i.e. spare thrust and lift forces to overcome wind gusts and harsh atmospheric conditions.
- Small dimensions explains the reason why in MAVs some features are neglected or sacrificed, namely the autonomy, in order to fit the dimensions and weights of propulsion and avionics devices available today. Any further reduction in MAVs size is highly linked to progress in miniaturization of these devices.
- Slow cruising speeds renders MAVs an easy target once they are traced which imposes the need for real-time data acquisition systems.

1.1.2 MAVs advantages and avionics

The advantages of MAVs are directly related to their characteristics and can be summarized as:

- Low cost due to the absence of human casualties in case of an MAV loss and the low production price with respect to UAVs or full-scale military aircrafts.
- Stealth thanks to their small radar's wet surface, the low temperature they develop and their silent flight especially for fixed-wing electrically motorised configuration. However, real time data transfer increases the risk of communications interception.
- Their low speed and altitude allow better image capturing of the area to explore, despite making them easier targets once they are located.
- Their easy and fast deployment render them operative in short time including in maritime and mountainous environment.

These advantages are common to all MAVs. Some specific characteristics of mobile-wing case will be given when this configuration is compared to the fixed-wing one (cf. §1.1.3).

On the other hand, MAVs, from design and aerodynamics points of view, are not only small aircrafts, which means that considering a good airplane and reducing its dimensions does not lead necessarily to a good MAV. Two main reasons explain this fact: the first is related to the different aerodynamics for the small Reynolds number regime used by MAV (discussed in §1.2) and the second is the different mass breakdown (cf. figure 1.2) and the larger dependence to avionics that MAVs have in general.

The construction of MAVs is rendered possible thanks to the development of microelectronics and microelectromechanical systems which allowed to incorporate into the vehicle a variety of computing, communication and sensing functions. The term avionics is used to denote the set of devices which enables the control of the aircraft. It includes the processor which pilots the vehicle (automatic pilot or ground-data processing), actuators which transmit the commands of the processor, the batteries and the motor, yielding the energy needed for the mission, the sensors which verify the good response of the vehicle to the pilot commands, the communication device for data transfer and the payload, usually an infra-red video camera. The mass distribution in an MAV, with comparison to a civil aircraft, is given in figure 1.2 to show that, despite progress made, the mass of motors and especially batteries (usually 5 Watts and 9 Volts respectively) is very important representing between 50 and 60 % of the total mass of the vehicle. Despite this high percentage, autonomy of present MAVs does not exceed one hour.

To improve this measure of performance, some contributions are dedicated to build long-life and light batteries exploiting new chemical elements. The other axis of research is to improve the propulsive efficiency of flight in order to ensure that a maximal percentage of the energy is usefully employed. This is the reason why mobile-wing configurations are investigated and the motion of the wing is optimised in the present work.

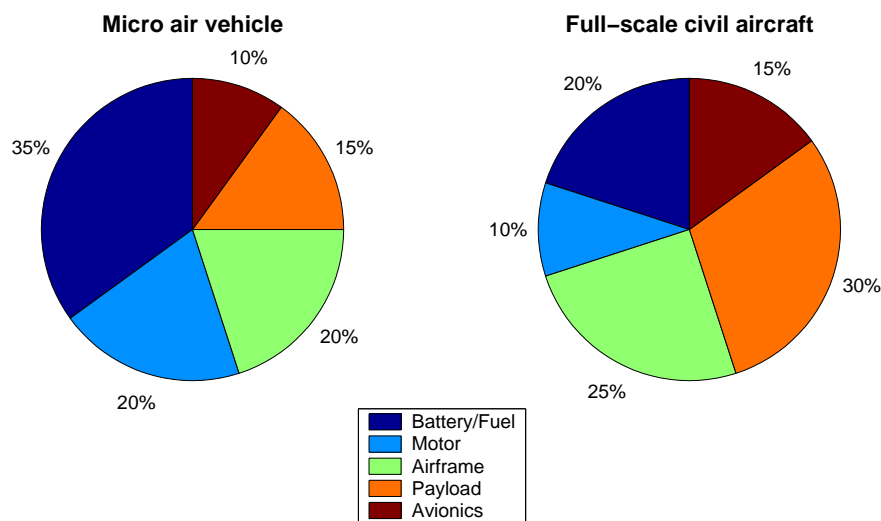


Figure 1.2: Comparison of mass breakdown between an MAV (left) and a classical civil aircraft (right).

1.1.3 Mobile- versus fixed-wing MAVs

Since the early age of humanity, flying as a bird has fascinated humans. Historically, it was thought that the movement of the wings is the main reason for flying and the only means to remain airborne, leading to numerous tragic experiences. This idea was so overspread that Da Vinci (see figure 1.3(b)) and Lilienthal mimicked birds in their own attempts to fly (Ellington and Usherwood, 2001).

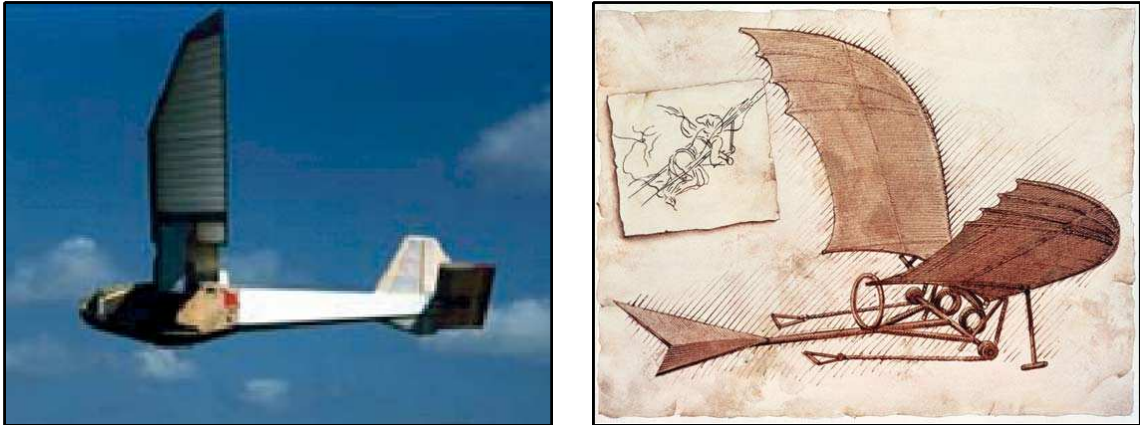


Figure 1.3: A flapping-wing MAV prototype (Ornithopter project, see www.ornithopter.ca) (left) and a sketch of a flying machine imagined by Leonardo Da Vinci (1452-1519) and based on flapping wings (right).

Cayley bypassed this assumption in 1799 with his concept of a fixed-wing airplane and a dedicated propulsion system (Gibbs-Smith, 1953). Hence, and for almost two centuries, attention was focused on fixed-wing air vehicles. At the human scale, this configuration is, undoubtedly, the best for three major reasons (Kroo and Kunz, 2001):

- The objective of human-scale aircrafts is to transport from point A to point B a given mass as fast as possible, and in term of forward speed, fixed wings are by far more efficient.
- From a pure structural point of view, the management of the movement of a wing submitted to forces of many tons, especially at the root of the wing where huge torques are present, constitutes a real challenge. Without mentioning the resonance problems if the motion has frequency close to the modes of the structure.

- At human scale, fixed-wing flight requires less power than hovering or other mobile-wing flights. Kroo and Kunz (2001) have shown that the hovering to fixed-wings ratio of required powers is roughly equal to $\left(\frac{C_L}{4}\right)^{0.5} \frac{L}{D}$ where L , D and C_L are, respectively, lift and drag forces and lift coefficient. For a large UAV or a civil airplane, $\frac{L}{D}$ is nearly 35 and $C_L = 1$ leading to a ratio of 17.5 whereas for a small UAV, $\frac{L}{D}$ is roughly equal to 5 and $C_L = 0.2$ leading to a ratio of 1.12. The ratio between required powers for flapping and fixed wings configurations can be less than one for an MAV even if the pure propulsive efficiency is lower for the mobile wing case (cf. Appendix A). The absence in nature of flying animals at human scale and the use of flapping wings by birds of similar size with respect to MAVs seem to confirm the latter statement.

In addition to the smaller power required and a good propulsive efficiency that we intend to confirm in the present work, the flapping-wing configuration presents the advantage of a bird-like stealth and a slower forward velocity which allows better image capturing. As a counterpart, the motion of the wings renders MAV more noisy and requires a stabilization system for exploitable image capturing.

1.2 Low Reynolds number aerodynamics

Early attempts to design MAVs were inspired by full-scale aircrafts methodology. However, an MAV is very different from a classical airplane and one cannot consider a full-scale aircraft and reduces it in a given proportion in order to build a successful MAV. The reasons for this are the mass breakdown mentioned in §1.1.2 and the low-Reynolds number aerodynamics both completely different and with a relevant impact. Due to their small dimensions and low forward speeds, the Reynolds number for MAVs is roughly between 5×10^4 and 10^5 (cf. figure 1.4). Despite the dearth of studies for the aerodynamics of airfoils for this regime, one can understand that phenomena as separation bubbles and transition are highly dependent on the value of the Reynolds number.

Some authors investigated low aspect-ratio airfoils at moderately low Reynolds number. We can cite the experimental contributions of Zimmerman (1932), Bartlett and Vidal (1955) and Wadlin et al. (1955), the theoretical works of Hoerner (1965), Hoerner and Brost (1975), Bollay (1939), Weinig (1947) and Polhamus (1971) and the numerical simulations of Smith (1996), Jones and Platzler (1997) and Ramamurti et al. (2000). Here, we focus on the work of McMasters and Henderson (1980) who studied the variation of lift and drag on a large range of Reynolds number for fixed airfoils. They have shown a relevant alteration of aerodynamics coefficients with

both a decrease of lift, a decrease of lift-to-drag ratio and an increase of drag when the Reynolds number is smaller than 10^5 (cf. figure 1.5). This result illustrates the difficulties for MAVs' regime of Reynolds number and renders legitimate the search for new approaches, such as the motion of the wing, to overcome this down-shoot in coefficients, in consideration of the fact that the slow velocity of MAVs and their light weight require high performances.

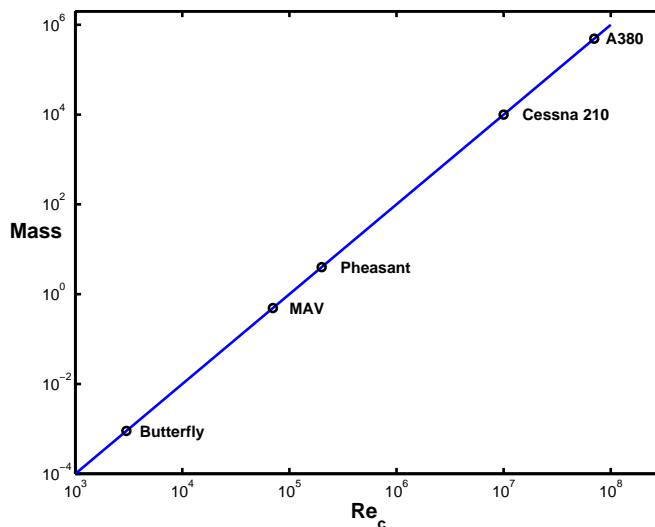


Figure 1.4: Mass (in kg) versus the Reynolds number (based on the chord length and the free stream velocity) for some flying animals and vehicles.

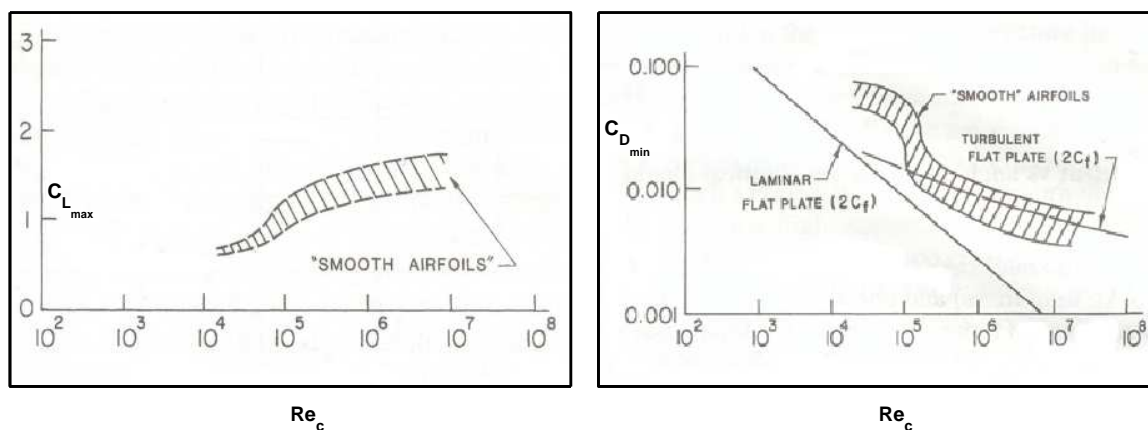


Figure 1.5: Evolution of the maximal lift coefficient (left) and the minimal drag coefficient (right) with the Reynolds number for smooth still airfoils (McMasters and Henderson, 1980).

The other main consequence of such low Reynolds number is the important viscous effects and their impact on the propulsive efficiency. Usually, when MAVs' aerodynamics is investigated numerically, the Reynolds number considered is between 10^3 and 10^4 , accentuating the viscous effects and leading to smaller values of efficiency when compared to the values obtained experimentally on airfoils and on animals such as birds and fish.

1.3 Flapping airfoils

The denomination *flapping* is usually used for a foil which accomplishes simultaneously a translational (heaving) and a rotational (pitching) motion around a point located on the foil called the pitching centre. Hence, the vertical position of the pitching centre $h^*(t)$ and the angle between the axis of the airfoil and the horizontal direction $\alpha(t^*)$ are varied in time (t^*) (cf. figure 1.6(a)), where the superscript $*$ denotes a dimensional variable. The coupling of these two motions is considered to mimic the motion of birds' wings and fish fins, normally simulated by monochromatic harmonic oscillations of heaving and pitching of the same frequency. MAVs and birds of similar size are located in a range of reduced frequency versus Reynolds number where a real dearth exists (cf. figure 1.6(b)).

For some values of the amplitudes and the frequency of oscillations, a flapping airfoil is able to reverse the classical von Karman street and to produce thrust. In this case, the wake is formed of clockwise-rotating vortices in the bottom row and counterclockwise-rotating vortices in the top row (cf. figure 1.7(b)) which induces a jet-like velocity component in the downstream direction (von Karman and Burgers, 1934). This jet-flow is convectively unstable which means that under the effect of the harmonic excitation from the airfoil, a staggered array of vortices is formed, moving downstream. The position of the vortices is inverted in the case of a wake behind a bluff body producing drag (cf. figure 1.7(a)). The classification of the structure of the wake was done, historically, with respect to the reduced frequency, f_r (Katz and Weihs, 1978; Ohmi et al., 1990), which measures the residence time of a particle convecting over the foil chord compared to the period of oscillation. Subsequent results showed that the classification should be done with respect to the value of the Strouhal number, St , (Triantafyllou et al., 1991; Anderson et al., 1998; Lai and Platzer, 1999) defined as the ratio of the velocity of oscillating to the forward velocity of the airfoil. Recent contributions tried to demonstrate that the classification cannot be based only on the Strouhal number but also in consideration with the other kinematics characteristics (Young and Lai, 2007).

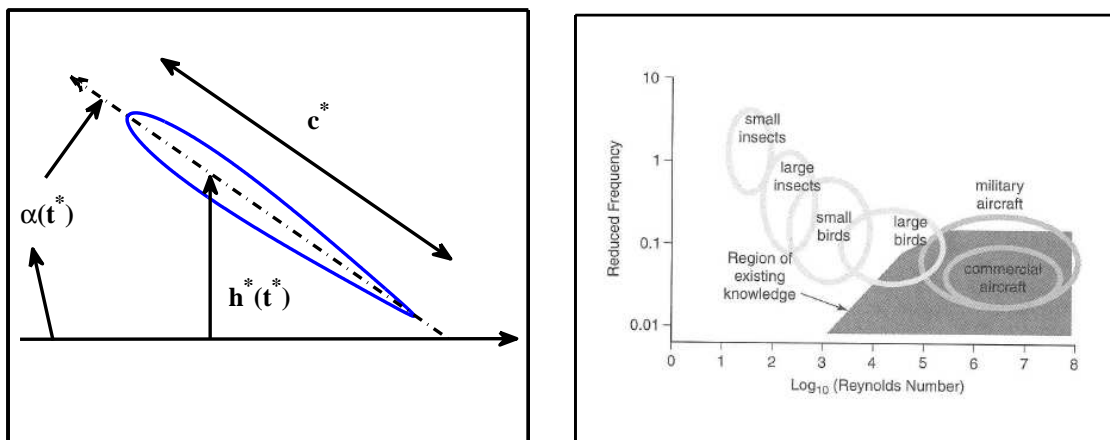


Figure 1.6: General definition of flapping (left) and reduced frequency range versus Reynolds number for flying animals and vehicles (right) (Ames et al., 2001).

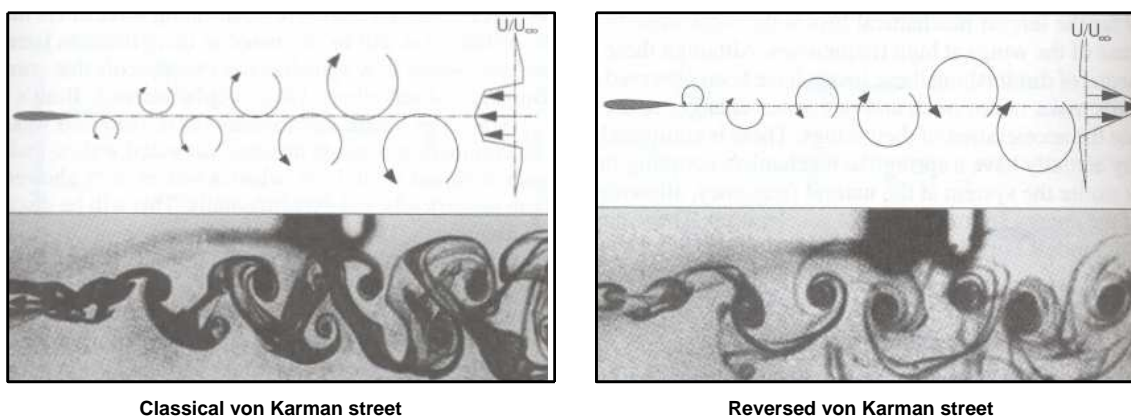


Figure 1.7: Sketch and experimental results (Jones et al., 1998) of a drag-like (left) von Karman street and a jet-like reversed von Karman street (right).

The denomination of a producing-thrust-airfoil is ambiguous, because it implies that the airfoil is not producing drag. However, and during oscillations, the unsteady horizontal force of a flapping foil experiences positive and negative values. It is the average value over a period of oscillation which classifies the type of production. Therefore, and in the remainder of this work, the denomination of an airfoil dominantly producing drag or thrust will be used. Moreover, if a non vanishing mean angle of attack exists, flapping foil can produce lift forces which is a major difference with respect to fixed-wing MAVs where thrust and lift are produced separately, without being completely independent.

Historically, the interest in propulsion by mobile wings started with the investigation of pure heaving motion with the works of Knoller (1909) and Betz (1912) who noted that the wing encounters an induced angle of attack, which inclines the normal-force vector forward such that includes both cross-stream (lift) and streamwise (thrust) force components (Jones et al., 2001). The interest of complexifying the motion was brought to light by Birnbaum (1924) who identified the conditions that lead to thrust generation and suggested the use of flapping wings as an alternative propulsive source to the conventional propeller. This proposition fostered a large interest due to the observation that the propulsive efficiency of idealized flapping wing is greater than that of a simplified propeller model which generates a disadvantageous trailing-edge vortex (Kuchemann and Weber, 1953).

1.3.1 Heaving airfoils

A heaving foil is able to produce thrust under some conditions, namely for values of the heaving amplitude and the frequency of oscillations leading to a Strouhal number greater than 0.2 (Ohashi and Ishikawa, 1972; Oshima and Oshima, 1980). During the downward plunge (cf figure 1.8(c) and 1.8(d)), a clockwise rotating vortex is generated at the leading-edge of the foil. The subsequent upward motion causes the formation of a counterclockwise rotating vortex which is deposited below and to the left of the previous one (cf. figure 1.8(a) and 1.8(b)). In addition to the separation from the trailing-edge, a separation occurs also near the leading-edge. The clockwise rotating vortex merges with the vorticity shed from the trailing-edge and reinforces it (Freymuth, 1988). The same airfoil, oscillating "slowly", would produce drag.

When the heave amplitude is increased, the airfoil experiences higher thrust for longer durations along a cycle. However, the propulsive efficiency, defined as the ratio of the useful-to-total power, decreases. The maximum efficiency occurs when the flow is fully attached all along the heaving motion, although this maximum occurs usually for insufficient thrust forces. Therefore, it is often preferable to ensure a large thrust force for a less-than-optimal efficiency. For further increase of the heaving amplitude, the flow separation at the leading-edge turns into the formation of a large-scale dynamic stall vortex which is convected downstream and shed in the wake. For higher amplitudes, secondary leading-edge vortices are generated and the thrust is increased together with a drop-off in efficiency.

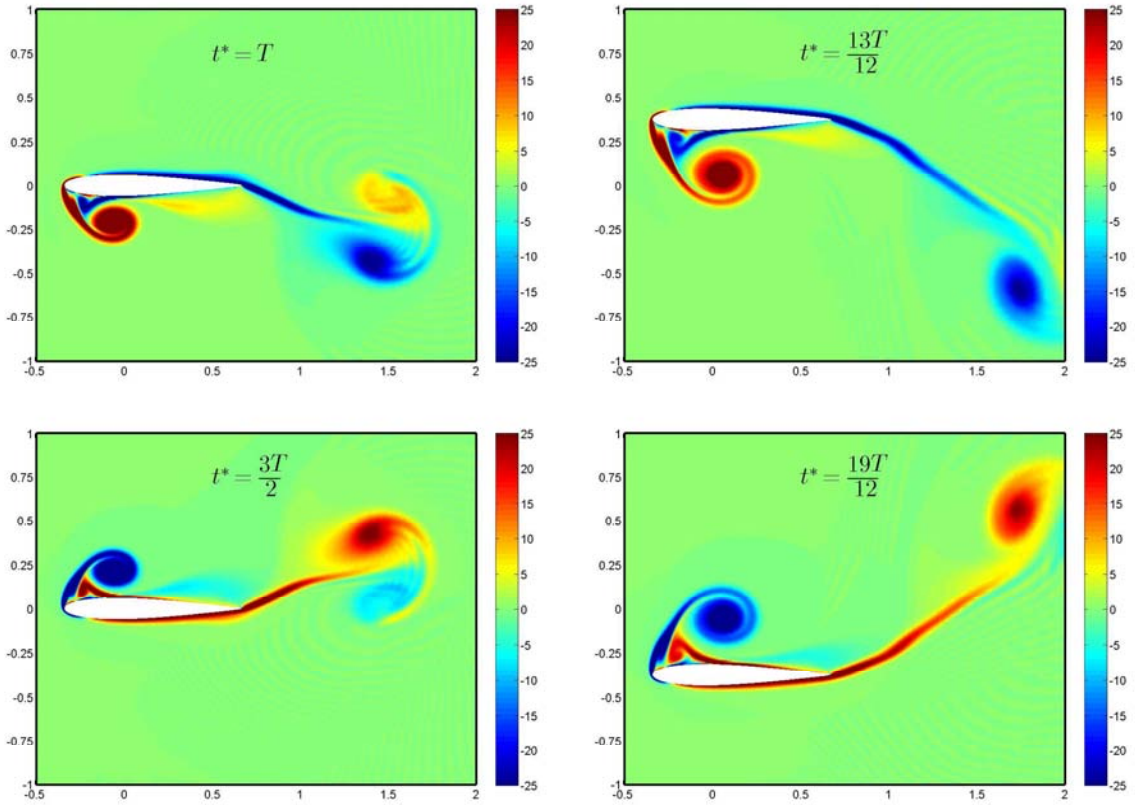


Figure 1.8: Wake structure for purely heaving airfoil producing thrust for $h^*(t^*) = \frac{3c^*}{4} \sin\left(\frac{2\pi}{T}t^*\right)$ and $St = 0.35$ during upward and downward plunging, where c^* is the chord length and St the strouhal number. The colour scale is for the vorticity field.

1.3.2 Pitching airfoils

Garrick (1936) was the first to show that propulsion is possible with purely pitching airfoils but only at "high" frequencies. The topology of the flow field is quite similar to the case of pure heaving: during the pitch-up, a counterclockwise rotating vortex is formed into the flow whereas during the pitch-down, a clockwise rotating vortex is deposited to the left and below the first one. Here, the vortex filaments leaving the trailing-edge break up into small vortices due to the Helmholtz instability, before these small vortices merge into the main vortices. As in the case of pure heaving, a weak leading-edge separation is observed which, once shed, interacts constructively with the trailing-edge vorticity.

The increase of the pitching amplitude creates severe leading-edge separations and an associated erosion in the propulsive signature of the vortex array. Here again,

the high propulsive efficiency is related to the presence of attached flow during each cycle of oscillations and a decrease of the pitching frequency increases the distance between vortices. Eventually, drag forces become overwhelming and a classical von Karman street is created.

1.3.3 Combination of heaving and pitching

Despite the fact that both pure heaving and pitching are able to yield thrust, their combination seems to give the best propulsive conditions. Numerous examples existing in nature attest to this: the heaving oscillations give rise to low values of thrust and pitching is required to model well the propulsion of swimming and flying animal since their combination helps controlling the leading-edge vortex and yields higher thrust forces (Wang, 2000; Lewin and Haj-Hariri, 2003). Once this means of propulsion had been identified, attention shifted to the determination of the effect of each parameter on a given measure of performance in order to optimise it using theoretical, experimental and numerical tools.

Theoretical contributions included the works of Theodorsen (1935) and Garrick (1936) who studied small oscillations and linearized theory in an ideal fluid. Subsequently, the theory was extended to account for the non-linear and large-amplitude motions (Lighthill, 1969, 1970; Wu, 1971; Chopra, 1974, 1976). These investigators demonstrated that, for an oscillating airfoil in an inviscid fluid, the propulsive efficiency tends to 100% when the frequency of oscillations approaches zero. Later on, the case of the Reynolds number tending to infinity was considered. Under these circumstances, the viscous effects have a negligible influence on the overall flow except during the separation process. Hence, the separation at sharp edges is approximated by the Kutta condition and the free shear layers are replaced by concentrated vortices (Choi and Landweber, 1990; Guglielmini, 2004) or by vortex panels (Streitlien and Triantafyllou, 1995; Liu and Bose, 1997; Streitlien and Triantafyllou, 1998). Lately, Hall and Hall (1996) and Hall et al. (1998) developed a vortex lattice method to determine the optimal circulation distribution for prescribed values of lift and thrust and found the unsteady distribution of circulation which minimises the loss of energy in the wake for both inviscid and viscous cases. The other axis of theoretical development was the use of the lifting-line theory in the frame of flapping airfoils. A large number of models were developed (Betteridge and Archer, 1974; Philips et al., 1981; Ahmadi and Windall, 1985; Willmott, 1988) despite numerous assumptions including the neglect of viscous effects and the focus on small-amplitude oscillations in the frame of linearized equations.

The difficulty of investigating non-linear unsteady phenomena with the previous approaches was remedied by a large number of experimental and numerical works on the topic. McKinney and DeLaurier (1981) studied experimentally the power-extraction capabilities of a flapping foil and Jones et al. (1998) confirmed experimentally and numerically their results over a large range of Strouhal numbers. The agreement they observed in the wake topology is rather interesting since Jones et al. (1998) used a panel method (inviscid) solver of the flow highlighting the fact that the evolution of the wake is primarily an inviscid issue. Koochesfahani (1989) studied experimentally the wake structure behind a flapping foil and found different topologies of the wake with associated numbers of shed vortices per cycle of oscillations as function of the amplitude and the frequency of flapping. Triantafyllou et al. (1993), based on the experimental results of Koochesfahani (1989) and on a linear stability analysis of an average velocity profile, assumed that optimal efficiency is obtained when an airfoil flaps at the frequency of maximum spatial amplification of the wake. Experiments in a water-tunnel confirmed this assumption. Anderson (1996) provided a classification of the wake and investigated the effect of the phase angle between heaving and pitching. Subsequently, Wolfgang et al. (1999a) and Pedley and Hill (1999) focussed on the separation on sharp edges and its influence on animal propulsion.

Recently, more sophisticated and powerful solvers allowed to perform potential/viscous flow analyses or a full Navier-Stokes resolution. Isogai et al. (1999) considered the dynamic stall of a flapping airfoil in a compressible flow with a Mach number equal to 0.3 and a Reynolds number equal to 10^5 and showed that the highest efficiency occurs when the pitch oscillations lead the heaving ones by a phase angle in the range $[80^\circ, 100^\circ]$. This results has been confirmed by Tuncer and Platzler (2000) and Fampton et al. (2001). Ramamurti and Sandberg (2001) studied a NACA0012 airfoil at Reynolds number equal to 1100 and 12000 and confirmed that the Strouhal number is the critical parameter for thrust generation. Lewin and Haj-Hariri (2003) used a viscous solver to evaluate thrust and efficiency over a wide range of frequencies and amplitudes reaching the conclusion that high efficiency is related to the generation of a leading-edge vortex which remains attached during the whole duration of the oscillations and which reinforces the trailing-edge vortex. Pedro et al. (2003) examined the topic with their Navier-Stokes solver and an arbitrary Eulerian Lagrangian moving mesh algorithm. Their numerical visualizations of the flow around the hydrofoil allowed to quantify the effect of the flapping parameters. Read et al. (2003) complexified the motion of the foil by adding high order terms. They highlighted the importance of the role played by the maximum value of the effective angle of attack encountered by the foil during its motion and showed that higher harmonics allow to maintain acceptable efficiencies when large thrust is needed. In a similar framework, the effect of the angle of attack and its impact on the propulsive performance was investigated by Hover et al. (2004). They found that a cosine variation of the angle of

attack yielded both acceptable thrust and efficiency whereas the sawtooth variation gave the maximal thrust force. More recently, Guglielmini (2004) solved the flow around a flapping foil and concentrated on thrust generation. She confirmed the experimental results and especially the interest of positioning the pitching centre at the third of the chord length, a result found experimentally by Anderson et al. (1998). In general, the main difference between the experimental and numerical results is the lower Reynolds number and the two-dimensionality in the numerical case. This leads to higher viscous effects and a neglect of the trailing vorticity, i.e. the vorticity parallel to the direction of the motion. The most recent contributions questioned the positive influence of the leading-edge vortex on high lift mechanism (Shyy and Liu, 2007) and investigated the transition of turbulence in the frame of flapping airfoils (Radespiel et al., 2007).

After having explored the wide space of parameters, the interest, at present, is focused on the determination of the optimal set of parameters for a given measure of performance. This target was sought in the work of Tuncer and Kaya (2005) where it was demonstrated that high efficiency is reached for reduced maximum angle of attack of the airfoil, if the formation of large leading-edge vortices is prevented. Their optimisation was done by computing a cost functional for different values of the parameters in order to evaluate the gradients, then a steepest descent method was used to converge towards the optimal values. In the present work, a similar target is sought and a wider space of control parameters is considered. The gradients are not approximated: they are computed with two different methods, the sensitivity technique and the complex step derivative method (cf. §3).

In summary, and from the different contributions mentioned earlier, one can recapitulate the important results as follows:

- The critical parameter for the wake topology behind a flapping airfoil, and consequently the efficiency, is the Strouhal number. High efficiency is observed when two vortices are shed per period of oscillations. The optimal values of St are in the range $[0.25, 0.35]$ as observed for many animals (Triantafyllou et al., 1993).
- The critical value of the Strouhal number which allows reversing the von Karman street leading to a flapping foil dominantly producing thrust is around 0.2 (Anderson et al., 1998).
- A flapping foil in the previous circumstances is more efficient when the leading-edge vortex remains attached for the whole period of oscillations and once shed it interacts constructively with the vortex shed from the trailing-edge. The timing of shedding, and consequently the nature of the interaction, is driven

by the phase angle between heaving and pitching. Optimal values correspond to pitching oscillation leading heaving ones by an angle in the range $[80^\circ, 100^\circ]$ (Isogai et al., 1999).

- High order terms allow to reach high thrust without large losses in terms of propulsive efficiency (Read et al., 2003).

In the remainder of this work, the optimal parameters will be found and related to the conclusions above by quantitative comparisons and by a description of the flow field for optimal configurations.

1.4 Birds, insects and fish

Although the level of sophistication in nature is impossible to copy for robots at present (namely their control systems in harsh atmospheric conditions, the elasticity of their muscles or the role of feathers/skin), the study of animals characteristics allows progress in the right direction towards optimised MAVs. The studies can focus on three features observed in nature: minimisation of energy losses in the wake, stall delay and drag reduction.

1.4.1 Birds

Rayner (1988) demonstrated that birds use two kinds of gaits: the *ring gait* for slow speeds and the *continuous vortex gait* for cruise (cf. figure 1.9) corresponding to two ways in which an animal can maximise the sum of the mean horizontal component of the lift with the negative induced drag while maintaining a vertical component of lift. Both gaits represent minimum energy states for the wake vortices and are conditions in which the least induced wake energy is required for momentum transport (Rayner, 2001). The explanation relies in the fact that these gaits maintain the bound circulation constant which either eliminates the spanwise shed vorticity or confines it to short periods. Consequently, high induced drag is avoided by preventing unfavourable interactions between spanwise vorticity behind the trailing-edge and the bound vorticity on the wing.

The dynamic stall is identified as the mechanism used by animals to achieve high-lift level (Ellington et al., 1996). During the downstroke, air swirls around the leading-edge and rolls up into an intense leading-edge vortex which is expected to be laminar for Reynolds number typical of flying birds. The circulation of the leading-edge increases the bound vortex which allows the wing to travel at high angle of attack for brief moments, generating extra lift force before stalling. However, the presence of a transversal flow which stabilises the leading-edge vortex is required. This highlights

the need of considering three-dimensionality in order to investigate this mechanism. Three-dimensionality is also indispensable to achieve a constant circulation for the optimised gaits in the previous mechanism, since in a two dimensional flapping airfoil, the sole source of thrust is the time-variation of circulation (von Holst and Kuchermann, 1942; DeLaurier, 1993).

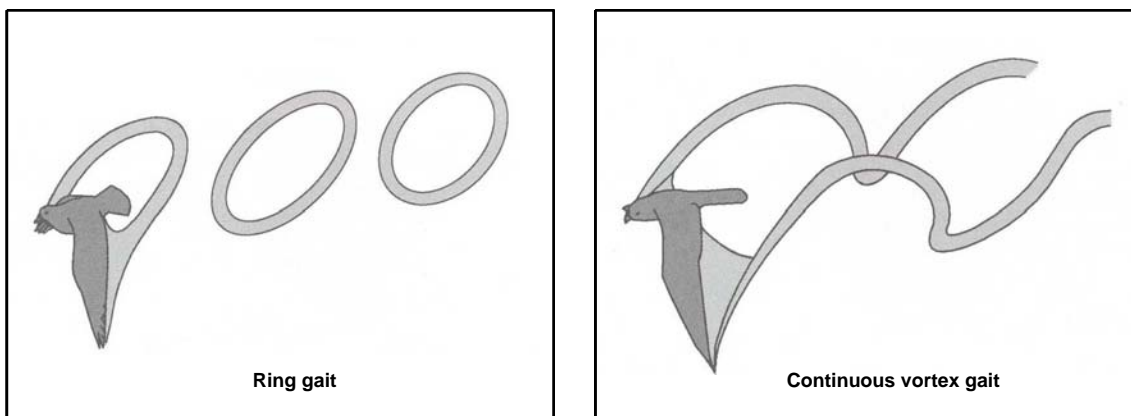


Figure 1.9: Wake vortex structure in the ring gait of birds corresponding to slow-speeds (left) and the continuous vortex gait used in cruise (right) conditions, both corresponding to minimal loss of energy in the wake (Rayner, 1988).

There are two main characteristics that render the dynamic stall different from the classical steady stall (McAlister et al., 1978). The first is that the discontinuity in lift and moment curves, as function of the angle of attack, occurs for two different values. The second is the fact that in dynamic stall, the dividing streamline from the point of zero shear into the wake encloses a narrow boundary-layer-like zone of reversed flow whereas, in steady stall, the point of separation coincides with the point of zero shear. The rate of development of the dynamic stall depends on the kinematics of the airfoil and precisely on the maximum angle of attack (McCroskey and Pucci, 1981). Hence, if a leading-edge vortex separates during the up-stroke of the airfoil, the stall is fully developed, whereas a separation when the airfoil reaches the maximum pitch leads to a less severe partially developed stall.

Birds have complex feathered shapes which do not match with the intuitive low-drag axisymmetric shape (fusiform) (Hertel, 1966). However, birds seem to be able to obtain very low drag forces and this fact has been confirmed by wind tunnel experiments on frozen animals which measured 75 % of the drag of a body of the same size and shape but with smooth surfaces (Maybury, 2000). Hence, feathers do not

play only a thermoregulation role, they participate to drag reduction probably by inducing laminar-turbulent transition and by ensuring smooth body outline eliminating potentially large and dynamic drag forces resulting from wing-body interaction (Rayner, 2001).

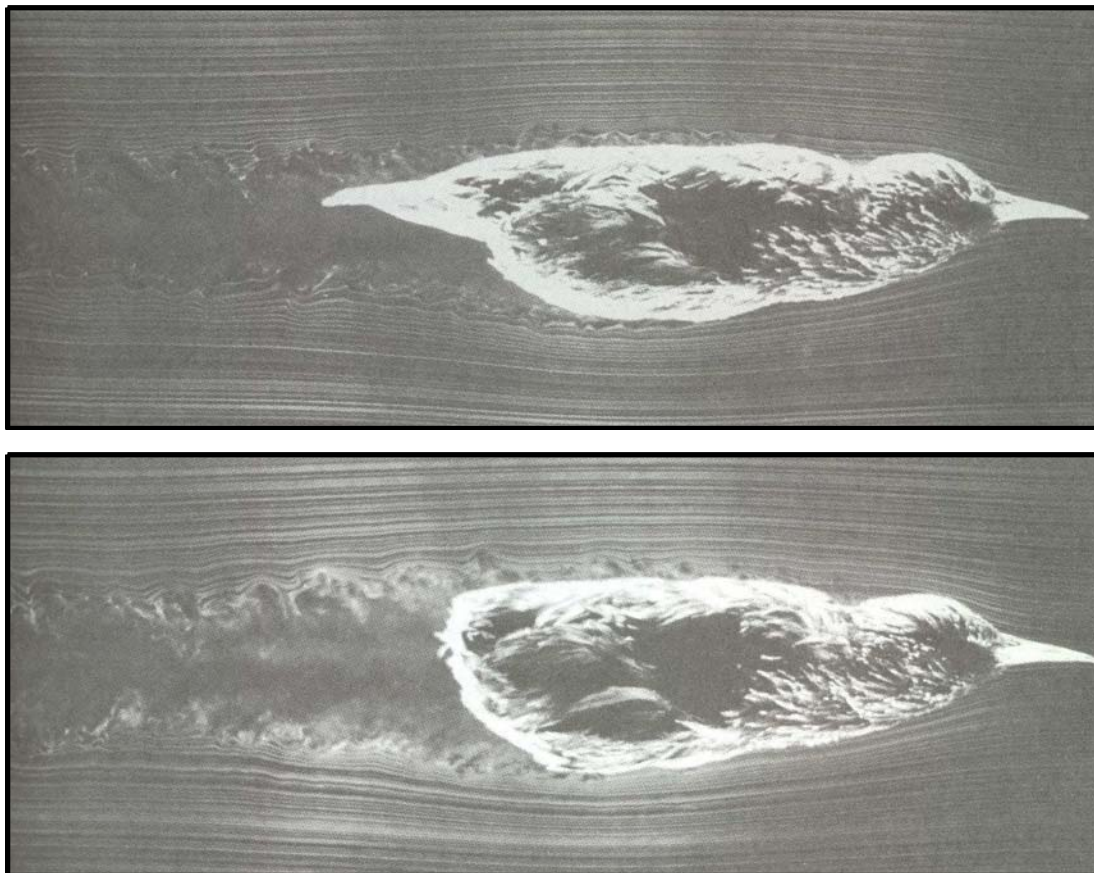


Figure 1.10: Wake behind a bird. Top: shallow regions of reattached separation on the dorsal surface and at the base of the tail due to the presence of the tail. Bottom: The separation between the ventral zone and the tail does not reattach leading to a turbulent wake and an increase of the drag due to absence of the tail (Maybury and Rayner, 2001).

Reduction of drag is also related to the presence of the animal tail. Contrarily to the intuitive idea that the tail acts as a lifting and a control surface, experiments show that it plays these roles only at low speeds. In cruise flight, the tail manipulates the boundary layer controlling separation and transition. It allows to re-attach the flow separation occurring behind the head of the bird (see figure 1.10). Measurements confirm this fact since the drag increases by 45 % when the tail is absent.

The previously evoked characteristics depend closely on three-dimensionality, the elasticity of the body, the presence of feathers and the ability of the animal to move its entire body or parts of it in order to manipulate vorticity and reduce losses. The present two-dimensional study on a rigid airfoil does not pretend to study all the mechanisms observed in flapping flight. It should be considered as a step towards the optimisation of man-made vehicles. Once, the optimal kinematics are found and the basic physical mechanisms completely analyzed, they can be correlated with the works investigating the elasticity of airfoils (Barut et al., 2006; Albertani et al., 2007) (showing that the flexibility has the double advantage of adding a relative camber and reducing the parasite three dimensional effects), the fluid-structure interactions (Gyllhem et al., 2005; Bozkurttas et al., 2006), the effect of feathers (Bannasch, 2001), or the use of actuators in a closed-loop control conditions.

1.4.2 Insects

The further miniaturizations in avionics devices, which occurred in the last few years, allowed to build a number of insect-sized prototypes of micro air vehicles (see figure 1.11). This was possible thanks to a large number of contributions which focused on insects' flights in the last two decades. The case of insects is quite close to birds' and similar mechanisms can be observed. However, three major features can distinguish insects from birds:

- The size: obviously, the biggest insects have dimensions which are close to those of the smallest birds but, in general, insects are much smaller than birds since some of them can have a wing span of more than three meters. The consequence of this observation is that birds may achieve normal flight with quasi-steady aerodynamics mechanisms, contrarily to insect where unsteady effects cannot be neglected.
- Elasticity: birds flap with actively deformed wings with muscles and joints within the wing surface whereas insects use deformable wings controlled by the base of the wing.
- Drag reduction: birds are more concerned with drag reduction and the improvement of aerodynamics performances. Hence, the mechanism they develop and their flight is adapted to these constraints whereas the requirements of insects in this field are less constraining.

On the other hand, insects can hover when momentum and forces balance during flight. This feature can be mimicked to design very small aerial vehicles for given missions. However, at this scale, other options , like rotary wings, micro-helicopters

(cf. figure 1.12) or rotatable tail (Praga et al., 2005), seem more suitable than flapping wings. The reasons are the very high flapping frequencies required (around 150 Hz (Ellington and Usherwood, 2001) still out of reach) to sustain the weight and the more severe constraints on weight and volume. Hence, any reduction in MAVs' scale passes by a better comprehension of insects' flight.

The leading description of the fluid dynamics for insects' flight is due to Maxworthy (1981). The lift generation mechanism in insect flight was investigated by Ellington (1984) and Spedding (1992). It has been shown that insects generate lift on both downstroke and upstroke and the examination of wings demonstrated that they are twisted along their length like a propeller blade since the angle of attack at the wing base is 10° to 20° larger than at the wing tip (Ellington, 1984; Willmott and Ellington, 1997). This justifies the use of the blade-element-theory for simple studies of the aerodynamics of an insect flight.

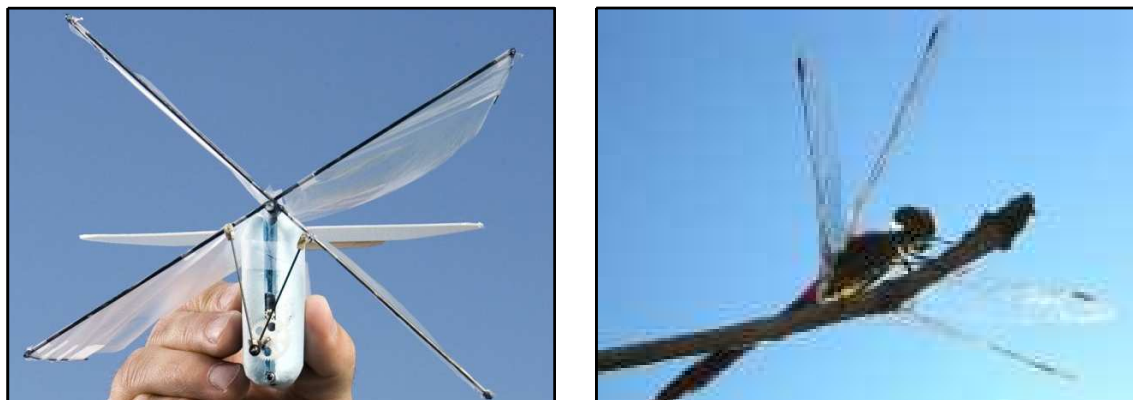


Figure 1.11: An insect-like micro air vehicle developed in Brigham Young University, Utah, U.S.A. (left) compared to its source of inspiration, the dragonfly (right).

More recently, experiments and numerical simulations were applied to this configuration and the aerodynamics and precisely the unsteady evolution of forces during insect flight was explored (Willmott and Ellington, 1997; Liu et al., 1998; Liu and Kawachi, 1998). Subsequent results (Ramamurti and Sandberg, 2002; Sun and Tang, 2002) confirmed numerically the experimental data by Dickinson et al. (1999). Lately, much effort was injected into the comprehension of the high unsteady mechanisms and to model the forces in hovering configurations (Wang et al., 2004; Zuo et al., 2006; Berman and Wang, 2007). In hovering conditions, the presence of pitching in the motion of the wings is crucial. A solely heaving airfoil in hovering conditions turns to a symmetric problem with a vanishing averaged thrust.

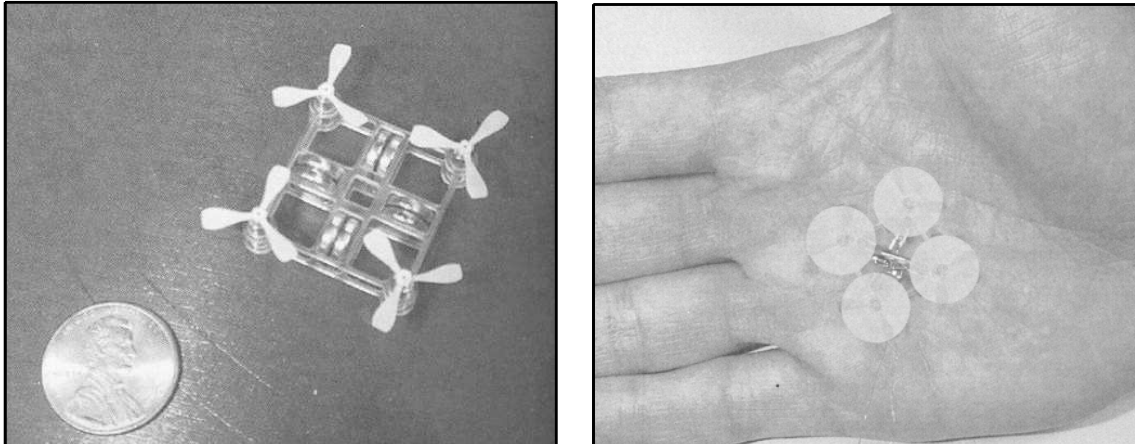


Figure 1.12: The mesicopter: a micro air vehicle prototype based on the rotating wings principle developed at Stanford university, California, U.S.A. (Kroo and Kunz, 2001).

1.4.3 Aquatic animals

The interest in aquatic animals' propulsion was fostered by the observations of Gray (1936) who highlighted the large thrust force developed by a dolphin with respect to the body mass. This was subsequently termed the "Gray's paradox" and the effect was ascribed to the compliant properties of the skin of dolphins. However, the most recent studies demonstrated that the compliant skin of dolphins plays no role (Fish, 2006). Lighthill (1960) applied the slender body theory of hydrodynamics to transverse oscillatory motions of slender fish revealing the high propulsive efficiency of fish. Subsequently, further investigations were made on the topic to elucidate Gray's paradox (Wu, 1961; Lighthill, 1969; Blake, 1983) and optimal shape problems were addressed (Wu, 1971). At that time, two-dimensional (Wu, 1961; Siekmann, 1962), and then three-dimensional (Cheng et al., 1991; Bandyopadhyay et al., 1997) potential flow models over a thin waving plate were built in order to compare the values of force coefficients between swimming animals and man-made underwater vehicles (see figure 1.13). The recent results focused on the generation of thrust by hydrofoils and on the attempt to reach the propulsive efficiency of swimming animals (Koochesfahani, 1989; Triantafyllou et al., 1991; Gopalkrishnan et al., 1994; Anderson, 1996; Guglielmini, 2004).

Fish propel themselves in water by generating a transverse wave which moves backward along the body from head to tail. This propulsion can be *anguilliform* when the whole body of the fish is flexible or *carangiform* where the amplitude of the

wave is significant only on the posterior part of the fish whereas the rest of its body remains relatively rigid (Blondeaux et al., 2005). This latter case implies that the thrust generation is almost confined to the caudal fin which can be modelled as a flapping foil moving with a constant forward speed in an undisturbed free stream. Hence, the study of the carangiform propulsion of some fish and the flight of birds can be very close. However, fish are much less concerned by the problem of lift due to Archimedes' force. In counterpart, side forces which produce lateral motions should be addressed. Other less widespread modes of propulsion exist in nature for fish including *rowing* with lateral fins and *vortex rings* mode whereby an aquatic animal (squid, salps) propels itself by expelling fluid from a tube thus producing vortex rings (Linden and Turner, 2001).



Figure 1.13: An autonomous underwater vehicle using carangiform propulsion mode developed in University of Essex, U.K. (left) compared to a fish (right).

Results show that fish use both heaving and pitching to reach high thrust forces since heaving alone requires frequencies physically unacceptable (Wang, 2000; Lewin and Haj-Hariri, 2003). Measurements on live animals show that a large species of fish move such that their Strouhal number is in the range $[0.25, 0.35]$ (Triantafyllou et al., 1993) and use a phase angle between pitching and heaving close to 90° . One may also notice the high aspect ratio of the tail and its flexibility and the ability of the fish to manipulate ambient vorticity with their caudal fin allowing them to extract energy that would otherwise be lost in wake (Streitlien et al., 1996).

Conclusion

The review of past contributions on the study of the propulsion of flying and swimming animals drives us towards clear and precise conclusions that we may summarize here. If fixed-wing configuration is probably the right one for human scale, flapping-wing at micro air vehicles' scale is not just a fantasy. Mobile-wings have the feature of requiring less power and yielding better performances if the motion is optimised and if some very complex mechanisms are employed. Even if nobody is able today to build a "perfect man-made bird", the optimisation of wings' kinematics is a step in the right direction.

Therefore, and in the remainder of the present work, the motion of a flapping airfoil will be studied and optimised in a way to favour sufficient thrust and lift forces with good propulsive efficiencies. This requires the numerical solution of the flow field around a flapping airfoil (cf. chapter 2) and an optimisation approach (cf. chapter 3). The interest resides in the fact that once the optimal kinematics are identified, they can be linked with natural observations and with laboratory measurements. This link is highlighted especially concerning the role of the Strouhal number and the effect of its values as mentioned in §1.3.3. The role of the separation and the interaction between the shed vortices is also emphasized.

Chapter 2

Problem formulation

Introduction

After having briefly described the context of the present work and the previous contributions related to the topic of propulsion for MAVs/AUVs or birds/fish, we present here the general formulation of the study. A special emphasis is given for the flow resolution around a flapping foil, the motivations for optimisation and the tools employed to achieve this optimisation.

The flow field around a flapping airfoil is nowadays easier to obtain due to a number of commercial CFD solvers. For instance, one may use OpenFoam¹, Overture² or Fluent³ even if this latter is quite hard to adapt to mobile surfaces configuration. OpenFoam (for *Open field operator and manipulator*) is a partial differential equations solver based on finite volumes and unstructured mesh. It is written in C++ and computes solutions for pressure and velocity fields using implicit schemes. Overture is also a PDE solver in C++. It is object-oriented and based on both finite differences and volumes. It is well adapted for complex and moving geometries and require the construction of structured meshes. Despite the high precision of these solvers (when the mesh is well designed), it is hard to update them for the present study since modifications in the source files of these solvers are very hard to implement if not impossible. Therefore, they can be adapted for validation reasons or for preliminary studies of the wake patterns or separation. But in the case where optimisation is asked for, the only way of doing it with these kind of solvers is to perform a very large number of runs and to post-process them. Here, the solution of the flow field around a flapping airfoil is based on the solver developed by Guglielmini (2004) during her

¹www.open CFD.co.uk/openfoam/index.html

²www.lnll.gov/casc/overture

³www.fluent.com

PhD thesis. Modifications are done to make it suitable to the configuration studied here and a solver for the sensitivity equations is developed to evaluate the gradients and reach the optimal kinematics.

After describing the geometry studied and defining the different reference systems and transformations used, the scales are introduced enabling to render the equations of the flow non-dimensional. The choice of the scales is discussed and the vorticity-stream function formulation is employed with the associated boundary conditions. The flow solution yields the flow field around the flapping airfoil and the main aerodynamic characteristics. At this point, an optimisation approach is built by defining an objective function which specifies the target to reach, and the tools to fulfil it, including choice of control parameters and the methodology of gradients computation.

2.1 The geometry

We address the problem of the numerical resolution of an incompressible flow around a two-dimensional flapping airfoil at low Reynolds number. Under these conditions, it is convenient to reduce the dimension of the problem from three variables (u^* , v^* , p^*), the horizontal and vertical components of velocity and the pressure respectively, to two variables (ω^* , ψ^*), the vorticity and the stream function respectively defined as:

$$\omega^* = \frac{\partial v^*}{\partial x^*} - \frac{\partial u^*}{\partial y^*}, \quad u^* = \frac{\partial \psi^*}{\partial y^*}, \quad v^* = -\frac{\partial \psi^*}{\partial x^*}$$

where (x, y) are the horizontal and the vertical directions of the laboratory fixed reference and the superscript $*$ denotes a dimensional variable. The resolution of the flow in this reference requires to locate the position of the airfoil in the grid instantaneously in order to impose the unsteady boundary conditions. It would lead to a model characterised by relatively simple equations but requiring in counterpart a moving mesh algorithm (Ramamurti and Sandberg (2001), Pedro et al. (2003), Smith and Wright (2005)). Another approach for numerical resolution of the flow around moving solid bodies is the immersed boundary technique (Mittal et al., 2005; Bozkurttas et al., 2005; Blondeaux et al., 2005). The key feature of this approach is that simulations with complex boundaries, including multiple bodies cases, can be done on stationary non-body conformal Cartesian grid and this eliminates the need for complicated remeshing algorithms that are usually employed with conventional body Lagrangian body-conformal methods. However, the immersed boundary technique method still can be seen as an Eulerian Lagrangian formulation where the immersed boundary are tracked as real surfaces in a Lagrangian way whereas the flow is solved on a fixed Eulerian grid (Bozkurttas et al., 2005).

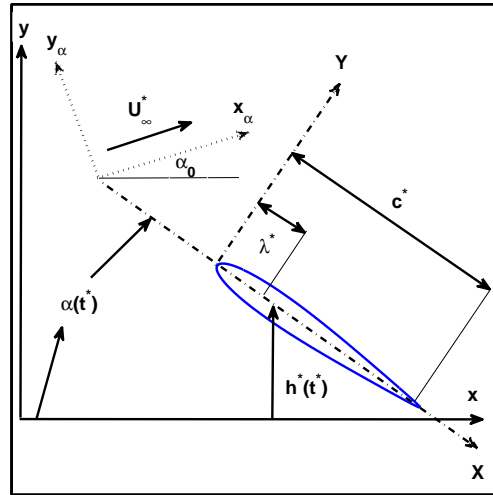


Figure 2.1: Definition of flapping and of the different frame references used.

Here, we write the governing equations in the reference (X, Y) which moves with the airfoil, where X is parallel to the airfoil chord length and Y remains perpendicular to it during the motion (cf. figure 2.1). This approach leads to relatively complicated equations of the flow but offers the advantage of easy imposition of the boundary conditions since the position of the airfoil in the moving reference is well-identified.

The airfoil is chosen such as a Joukowski transformation is possible so as to replace the flow resolution around the airfoil by a resolution around a circle of given radius (cf. Appendix B). However, the airfoil chosen remains, from a geometric point of view, very similar to a NACA0012 airfoil since the difference in shape is smaller to 1%, and mainly located near the trailing-edge (cf. figure 2.2). Comparisons of lift and drag coefficients, using Fluent solver, for the present airfoil and a NACA0012 airfoil, have shown small discrepancies on the aerodynamics forces. The moving reference (X, Y) is mapped by means of the Joukowski transformation into the plane (ξ, χ) where a polar coordinates system (r, θ) is defined. A logarithmic transformation (Braza et al., 1986) is applied for the distribution of points in the radial direction in order to refine the grid in the boundary layer where large gradients occur. The case of different possible stretching laws is not investigated, because it is not the main issue of the present work. Furthermore, this law has proved its efficiency in the past (Borthwick, 1986), and the validity of the flow solution has been verified on such a grid on the other (Guglielmini and Blondeaux, 2004). The impact of this refinement law is addressed in §4.1. More details on reference frames

and transformations employed can be found in Appendix B and in the Ph.D. thesis by Guglielmini (2004). A plot of a coarse grid showing the geometry of the grid and the distribution of points around the airfoil is given in figure 2.3.

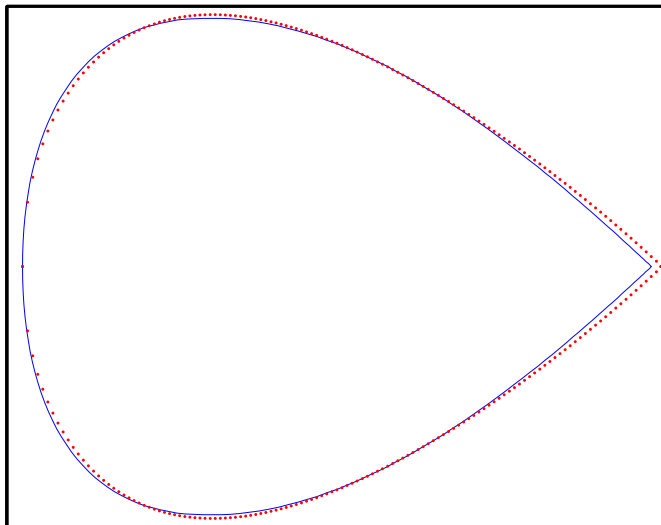


Figure 2.2: A Zoomed plot in the vertical direction of the NACA0012 airfoil (dots) and the one used in the present study (solid line), obtained by means of a Joukowski transformation.

The motion of the airfoil is defined as a combination of heaving and pitching movements. Hence, the vertical position of the pitching centre, the point around which the airfoil pitches, is varied in time as $h^*(t^*)$. In the present work, the pitching centre is located at one third of the chord length starting from the leading-edge. The position of the pitching centre will remain the same for all the simulations of the present work. Normally, the aerodynamic centre, located close to the quarter of the chord for a still airfoil, is supposed to be a good location for the pitching centre knowing that in this point the pitching torque is constant. However, previous results (Anderson et al., 1998; Guglielmini, 2004) showed that, for a flapping airfoil, the location adopted here is optimal in terms of propulsive efficiency.

On the other hand, the angle between the frames (x, y) and (X, Y) is the pitching angle $\alpha(t^*)$, also variable in time. The velocity at infinity is inclined of a constant angle α_0 with respect to the reference (x, y) . This defines the aerodynamic reference (x_α, y_α) (cf. figure 2.1) with respect to which the lift and the drag/thrust of the airfoil should be calculated. When $\alpha(t)$ is periodic in time, α_0 turns to be the mean angle of attack of the airfoil. It is possible to build another formulation in which α_0 is included inside the pitching angle $\alpha(t)$ leading to a new set of equations.

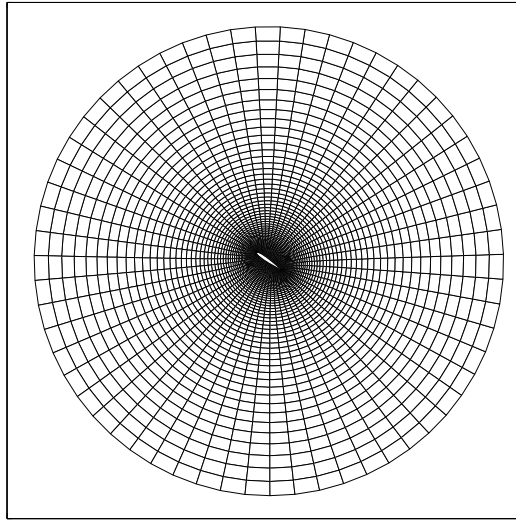


Figure 2.3: Plot of a coarse grid showing the circular form of the computational domain and the effect of the stretching law in the radial direction.

2.2 The scaling

For the problem of flapping airfoil two scales can be adopted for both length and time:

- As length scale, one can choose between the airfoil chord or the heaving amplitude corresponding to the maximal value of $h^*(t^*)$ reached during oscillations. In the present study, we aim at optimising the heaving amplitude, which means that this quantity will be variable. Therefore, the chord of the airfoil c^* or more precisely the distance λ^* (cf. Appendix B) is chosen as length scale. This distance corresponds roughly to the position of the aerodynamic centre of a NACA0012 airfoil which does not flap. Obviously, a factor of about 4 can be applied and c^* can be used as a length scale. However, because of the Joukowski transformation, we prefer to maintain λ^* as the suitable scale. On the other hand, the comparison of present results with those of literature are made upon non-dimensional coefficients, adapting the scaling effects.
- As time scale, the inverse of the frequency of flapping or the ratio of the length scale to the velocity at infinity U_∞^* can be used. Both choices present advantages and disadvantages. The choice of $\frac{\lambda^*}{U_\infty^*}$ as a scale of time allows to recover the classical Reynolds number. However, it prevents the consideration of hovering situation wherein the MAV has no forward speed and consequently U_∞^* vanishes. This problem can be overcome by considering $\frac{1}{\sigma^*}$ as a time scale

where $\sigma^* = 2\pi f^*$ and f^* is the frequency of flapping in Hertz. In this case, the optimisation of the flapping frequency is not straightforward, and includes a variation of the reduced frequency (as shown below). Another solution for this problem consists in considering a reference constant frequency σ_0^* as the inverse of time scale. In the remainder of this work, the consequences of considering σ^* , σ_0^* or U_∞^* are highlighted.

The third fundamental scale is mass scale and here it is included by the use of the density of air ρ^* . Based on these three scales, and introducing ν^* , the kinematic viscosity of air, we can render non-dimensional all flow variables.

\mathbf{t}^*	$\mathbf{x}^*, \mathbf{y}^*$	$\mathbf{u}^*, \mathbf{v}^*$	\mathbf{p}^*	$\boldsymbol{\omega}^*$	$\boldsymbol{\psi}^*$	\mathbf{Re}
$\frac{1}{\sigma^*}$	λ^*	$\lambda^* \sigma^*$	$\rho^* (\lambda^* \sigma^*)^2$	σ^*	$\sigma^* \lambda^{2*}$	$\frac{\sigma^* \lambda^{2*}}{\nu^*}$

Table 2.1: Scaling quantities based on the frequency of flapping

If the first scaling is employed, we obtain a Reynolds number Re which depends mainly on the flapping frequency and will be referred as the flapping Reynolds number. In table 2.1, σ^* may be the angular frequency of flapping or a reference constant value σ_0^* and the physical frequency of flapping σ^* is a multiple of it, belonging to the set of real numbers.

\mathbf{t}^*	$\mathbf{x}^*, \mathbf{y}^*$	$\mathbf{u}^*, \mathbf{v}^*$	\mathbf{p}^*	$\boldsymbol{\omega}^*$	$\boldsymbol{\psi}^*$	\mathbf{Re}_c
$\frac{c^*}{U_\infty^*}$	c^*	U_∞^*	$\rho^* (U_\infty^*)^2$	$\frac{U_\infty^*}{c^*}$	$U_\infty^* c^*$	$\frac{U_\infty^* c^*}{\nu^*}$

Table 2.2: Scaling quantities based on velocity at infinity

Thanks to the second scaling, we recover the classical Reynolds number Re_c based on the chord length and the velocity at infinity. A connection between the two proposed scales exists. Therefore, we introduce two important parameters in flapping foil problems, the Strouhal number, St and the reduced frequency, f_r . As mentioned earlier (cf. §1.3), the values of these parameters are used to determine the flapping régime. They represent the ratio of the velocity of flapping to flight forward velocity

and the ratio of the residence time of a particle along the airfoil chord to the period of oscillations, respectively. Hence, they are defined as:

$$St = \frac{f^* A^*}{U_\infty^*} \quad \text{and} \quad f_r = \frac{\sigma^* \lambda^*}{U_\infty^*},$$

where A^* is the width wake usually unknown *a priori*. It is often approximated by the double of the heaving amplitude $\| h^*(t^*) \|$ where the norm $\| \cdot \|$ corresponds to $\max(\cdot)$ for $t^* \in [0, T^*]$ and T^* is the period of oscillations. Under these conditions, we can give another expression of the Strouhal number and relate it to the reduced frequency. A relation between the flapping and the classical Reynolds number exists also through f_r as :

$$St = \frac{\sigma^* \| h^*(t^*) \|}{\pi U_\infty^*}, \quad St = \frac{\| h(t) \| f_r}{\pi} \quad \text{and} \quad Re_c = \frac{4Re}{f_r}.$$

The heave amplitude is considered in the following as a control parameter (see §2.5.2). Hence, in this case, it is preferable to perform the computations for a constant reduced frequency f_r rather than a constant Strouhal number. On the other hand, when the frequency of flapping is optimised, f_r will be varied. In both cases, we impose the classical Reynolds number Re_c . Then, in the first case, we impose also the reduced frequency, and we compute the value of the flapping Reynolds number which appears in the equations. For a given value of the heaving amplitude, the Strouhal number can be also recovered and the optimisation is done by updating the heave amplitude and, consequently, the Strouhal number. In the second case, we impose the heave amplitude and for a given value of the reduced frequency we compute the flapping Reynolds and the Strouhal numbers. Optimisation is done by updating f_r and, consequently, Re and St .

From what precedes, we can notice that there is some kind of hierarchy of the problem's parameters, with Re_c on a different level than Re , f_r or St . The reason for this choice is the secondary importance of Re_c , as shown by Ohmi et al. (1990). The classical Reynolds number has undoubtedly an effect on the results, especially on the values of the propulsive efficiency η , defined as the ratio of useful-to-total required powers. A low value of Re_c implies higher viscous effects and as a consequence a smaller η . However, the conjecture is that the thrust force depends mainly on the pressure distribution and the latter is much less affected by the value of Re_c as long as it remains in the range $[10^3 - 10^5]$ (Anderson et al., 1998; Guglielmini and Blondeaux, 2004). In other words, if we optimise the flapping kinematics for a low Reynolds number, we expect to find the optimal parameters to remain valid for this range of Reynolds numbers but with lower propulsive efficiency. This underestimation of the propulsive efficiency counterbalances the effect of performing

two-dimensional simulations: the approach adopted here, neglects a part of the vorticity shed in the wake, namely the trailing vorticity, i.e. the vorticity parallel to the direction of the flow. Consequently, a 2-D approach is expected to yield higher values of η than real 3-D cases. However, for low Re_c , the viscous effect is dominant. Therefore, even three-dimensional published numerical simulations failed to appropriately quantify the effective efficiency of thrust-producing-foils as argued by Pedro et al. (2003) due to a small Re_c and an overestimation of the viscous forces .

In nature, the wings/fins span (between 10 cm and 3 m for some species of hawks), the forward velocity (between 0.5 and 15 m/s) and flapping frequency (up to 60 Hz for hummingbirds) observed for birds, insects and fish cover a wide range (see figures 2(a) and 3(b)). The majority of the numerical simulations performed in the present work have been done for $f_r = 0.3665$ and $Re_c = 1100$, and consequently, $Re = 100.79$. If we refer to figure 1.6(b), the value of f_r corresponds to that of small birds and large insects (the y-axis scale in this figure should be divided by two if we want to compare, since in Ames et al. (2001)'s work, the reduced frequency is defined by: $f_r = \frac{\pi f^* c^*}{U_\infty^*}$). However, the Reynolds number used here is quite low for a bird configuration. It has been chosen because it corresponds to a much used configuration in the literature (Anderson et al., 1998; Ramamurti and Sandberg, 2001; Pedro et al., 2003; Guglielmini and Blondeaux, 2004). This choice is numerically advantageous, since the spatial and temporal steps of discretization depend directly on the value of Re_c . A larger value of Re_c would be more realistic. For instance, a bird having a wing of 0.1m chord length, flapping at 3.5 Hz and moving with a forward speed of 1.5 m/s, gives $f_r = 0.3665$ and $Re_c = 10274$ (assuming a value of the air kinematic viscosity, $\nu^* = 1.46 \times 10^{-5} m/s^2$). Since the kinematic viscosity of water is 10 times larger than that of air, our value is more adapted for a fish. However, and as mentioned before, we assume that the optimal kinematics for $Re_c = 1100$ are not too far from the optimal values at a larger Reynolds number, and that the relevant physical phenomena and mechanisms are captured, at least qualitatively.

2.3 The flow equations

The flow is governed by the system 2.1 which expresses the equations of continuity and Navier-Stokes in the vorticity-stream function formulation in the polar coordi-

nate system (r, θ) :

$$\begin{cases} \frac{\partial \omega^*}{\partial t^*} + \frac{1}{\sqrt{J}} \left[v_r^* \frac{\partial \omega^*}{\partial r^*} + \frac{v_\theta^*}{r^*} \frac{\partial \omega^*}{\partial \theta^*} \right] = \frac{\nu^*}{J} \left[\frac{\partial^2 \omega^*}{\partial r^{*2}} + \frac{1}{r^*} \frac{\partial \omega^*}{\partial r^*} + \frac{1}{r^{*2}} \frac{\partial^2 \omega^*}{\partial \theta^{*2}} \right], \\ \frac{\partial^2 \psi^*}{\partial r^{*2}} + \frac{1}{r^*} \frac{\partial \psi^*}{\partial r^*} + \frac{1}{r^{*2}} \frac{\partial^2 \psi^*}{\partial \theta^{*2}} = -J\omega^*. \end{cases} \quad (2.1)$$

where v_r^* and v_θ^* are the velocities in the radial and azimuthal directions respectively. Applying the first scale to these equations leads to the non-dimensional system of flow equations:

$$\begin{cases} \frac{\partial \omega}{\partial t} + \frac{1}{\sqrt{J}} \left[v_r \frac{\partial \omega}{\partial r} + \frac{v_\theta}{r} \frac{\partial \omega}{\partial \theta} \right] = \frac{1}{ReJ} \left[\frac{\partial^2 \omega}{\partial r^2} + \frac{1}{r} \frac{\partial \omega}{\partial r} + \frac{1}{r^2} \frac{\partial^2 \omega}{\partial \theta^2} \right], \\ \frac{\partial^2 \psi}{\partial r^2} + \frac{1}{r} \frac{\partial \psi}{\partial r} + \frac{1}{r^2} \frac{\partial^2 \psi}{\partial \theta^2} = -J\omega, \end{cases} \quad (2.2)$$

where,

$$\begin{aligned} v_r &= \frac{1}{\sqrt{J}} \left[\frac{1}{r} \frac{\partial \psi}{\partial \theta} - \left(\dot{h}(t) \sin(\alpha(t)) - \dot{\alpha}(t)Y \right) \left(\frac{\partial X}{\partial \xi} \cos \theta + \frac{\partial X}{\partial \chi} \sin \theta \right) \right. \\ &\quad \left. - \left(\dot{h}(t) \cos(\alpha(t)) + \dot{\alpha}(t)X \right) \left(\frac{\partial Y}{\partial \xi} \cos \theta + \frac{\partial Y}{\partial \chi} \sin \theta \right) \right], \\ v_\theta &= \frac{1}{\sqrt{J}} \left[-\frac{\partial \psi}{\partial r} - \left(\dot{h}(t) \sin(\alpha(t)) - \dot{\alpha}(t)Y \right) \left(\frac{\partial X}{\partial \chi} \cos \theta - \frac{\partial X}{\partial \xi} \sin \theta \right) \right. \\ &\quad \left. - \left(\dot{h}(t) \cos(\alpha(t)) + \dot{\alpha}(t)X \right) \left(\frac{\partial Y}{\partial \chi} \cos \theta - \frac{\partial Y}{\partial \xi} \sin \theta \right) \right]. \end{aligned}$$

Dots denote derivation with respect to time t and J is the Jacobian of the Joukowski transformation which maps the coordinates of the Cartesian plane (X, Y) into the plane (ξ, χ) (cf. Appendix B). The same equations can be obtained if the second scaling is applied, with a main difference though, that in this latter case, Re should be substituted by Re_c .

The first equation in the system 2.2 is solved thanks to an alternate direction implicit (ADI) method which decouples the azimuthal direction from the radial one. First, a half temporal step is accomplished in the θ direction, leading to a tridiagonal linear system solved with a Thomas-like algorithm and periodic boundary conditions. The tridiagonal system is a direct result of the choice of the discretization schemes, here second order centred schemes. A second half step is performed

for the r direction resulting in a new tridiagonal system, solved with a similar algorithm but with Dirichlet- and Neumann-like boundary conditions in this case. The Poisson-like equation ($\Delta\psi = -J\omega$, where Δ is the Laplacian operator, here in polar coordinates) is solved by a Fourier transform. We assume the two equations to be uncoupled. Thus, we solve the first equation (referred to as ω equation) for the value of ψ for the previous temporal step. Then, once ω is evaluated, it is used to compute ψ , using the second equation (called Poisson-like equation). Details on the tridiagonal systems, Fourier transformation and algorithms are given in Appendix D.

We associate to the flow equations the flow boundary conditions on ω and ψ . The conditions on the airfoil express a vanishing velocity for the fluid. This results from the fact that the numerical resolution is done in the moving reference system fixed on the airfoil. The relation between the stream function and the radial and azimuthal velocities allows to reach a condition on ψ on the airfoil. Moreover, the value of vorticity on the airfoil is evaluated using a Taylor development on one hand, and the Poisson-like equation between ω and ψ , on the other. For the outflow, three boundary conditions were tested.

- The first is the one used by Guglielmini (2004) and expresses the fact that vorticity is constant when progressing in the radial direction near the computational domain limit: $\left(\frac{\partial\omega}{\partial r}\right)_{outflow} = 0$. This condition is the easiest to implement but it is called "perfectly reflecting condition" since it can possibly reflect back outgoing waves when the shed vorticity reaches the boundary of the computational domain. This imposes the choice of a large domain and increases the nodes number and consequently the computational cost.
- The second is proposed by Tezduyar and Liou (1991) and may be seen as a higher order and less constraining condition than the previous one. It is written as: $\left(\frac{\partial^2\omega}{\partial r^2}\right)_{outflow} = 0$ and $\left(\frac{\partial^2\psi}{\partial r^2}\right)_{outflow} = 0$. It has been reported that this condition allows waves to smoothly leave the domain at the exit boundary.
- The third, referred to as convective outflow condition is the most realistic. It expresses the fact that the shed vorticity from the airfoil will cross the computational domain with a constant velocity equal to the free stream velocity U_0 where U_0 is the non-dimensional value of U_∞^* since $U_0 = \frac{U_\infty^*}{\lambda^*\sigma^*} = \frac{1}{f_r}$. Hence, we write that on the outflow boundary:

$$\frac{\partial\omega}{\partial t} + U_0\frac{\partial\omega}{\partial r} = 0, \frac{\partial\psi}{\partial t} + U_0\frac{\partial\psi}{\partial r} = 0.$$

Even if the interest of implementing this condition is concentrated inside a solid angle behind the airfoil where the wake crosses the computational domain (see figure 2.4), it is valid for the whole outflow boundary. It allows to reduce the computational cost by reducing the size of the grid and it remains valid even if the vorticity shed does not translate with a velocity perfectly equal to U_0 (Bottaro, 1990).

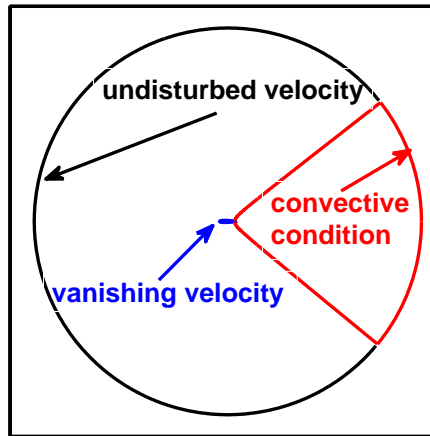


Figure 2.4: Location of the imposed boundary conditions.

The validity of the outflow boundary conditions with respect to the computational domain size is verified in §4.2. More details on the boundary conditions for the flow equations are given in Appendix E.1.

Finally, ω equation is time-dependent, i.e. solving it requires an initial condition. The system is advanced in time starting from an initial condition of vanishing vorticity and stream function thanks to a first order upwind scheme split into two sub-iteration because of the ADI method.

2.4 Direct variables

We denote by *direct* any variable computed through the resolution of the flow equations as opposed to gradients (sensitivity and imaginary variables) obtained by solving the sensitivity and the complex equations (see chapter 3). The problem studied is highly unsteady which means that all forces and moments are time-dependent.

Therefore, mean variables are introduced. They correspond to the average value of a variable over a period of oscillation, T . The superscript $\bar{\cdot}$ is used to denote this average since $\bar{(\cdot)} = \frac{1}{T} \int_0^T (\cdot) dt$.

The main direct variables of interest in the present work are:

- The mean power required to sustain the motion of the airfoil, typically the energy extracted from the batteries to perform the flapping, if we do not account for losses. It is defined as:

$$\bar{P} = -\frac{1}{T} \int_0^T \left[F_y(t) \dot{h}(t) + M_z(t) \dot{\alpha}(t) \right] dt;$$

- The mean horizontal force \bar{F} corresponding to thrust or drag produced by the flapping airfoil:

$$\bar{F} = \frac{1}{T} \int_0^T F_{//}(t) dt;$$

- The mean vertical force \bar{L} representing the lift force of the airfoil:

$$\bar{L} = \frac{1}{T} \int_0^T F_{\perp}(t) dt;$$

where $F_{//}$ and F_{\perp} are respectively the parallel and perpendicular forces with respect to the velocity at infinity. Obviously, when $\alpha_0 = 0$, they correspond to the horizontal and vertical forces F_x and F_y in the fixed reference frame (x, y) . Looking at the definition in figure 2.1, we note that negative values of \bar{F} are associated to an airfoil dominantly producing thrust whereas positive values refer to drag. Moreover, the positive values of \bar{L} correspond to a lifting airfoil. M_z is the pitching torque acting on the airfoil. We associate to these mean quantities the mean power, thrust and lift coefficients:

$$C_P = \frac{\bar{P}^*}{\frac{1}{2} \rho^* c^* U_{\infty}^{*3}} = \frac{\bar{P}}{2U_0^3}, \quad C_T = -\frac{\bar{T}^*}{\frac{1}{2} \rho^* c^* U_{\infty}^{*2}} = -\frac{\bar{F}}{2U_0^2}, \quad C_L = \frac{\bar{L}^*}{\frac{1}{2} \rho^* c^* U_{\infty}^{*2}} = \frac{\bar{L}}{2U_0^2}$$

We also define the pressure coefficient, C_{pr} as: $C_{pr} = \frac{p^* - p_0^*}{\frac{1}{2} \rho^* U_{\infty}^{*2}}$ where p^* is the pressure and p_0^* a reference pressure. The pressure coefficient is not a global variable since it is computed on a discrete set of points located on the airfoil and corresponding to the grid nodes. Finally, we introduce the propulsive efficiency as the ratio of the useful power (used to fly straightforward) to the total required power:

$$\eta = -\frac{\bar{F}U_0}{\bar{P}} = \frac{C_T}{C_P}.$$

Obviously, the definition of a propulsive efficiency loses interest when the airfoil is mostly producing drag ($\eta < 0$). More details about the expressions of these direct variables in the moving frame and the relations allowing to compute them from the variables ω and ψ are given in appendix C.1.

2.5 The optimisation approach

At this point, the questions, which constitute the three components of the optimisation problem, may be addressed. First, what do we want to optimise? In other words, what is the measure of performance or more generally the "cost functional" whose optimum is sought? Second, what are we acting on? Or in other words, what are the "control parameters" to manipulate to reach our target. Third, what method are we going to use in order to drive the control parameters towards their optimal values, i.e. what method are we using to "evaluate the gradient" of the cost functional with respect to the control parameters and to drive it to zero? The investigation of these three points, one by one, constitutes the core of this section.

2.5.1 Cost functional

The measure of performance to be optimised is directly related to the type of mission the MAV is expected to perform. The main problem of nowadays MAVs is their autonomy, typically between 30 and 60 minutes (cf. §1.1.2). This duration is not sufficient for military spying missions in a battlefield. Hence, one may be tempted, for such a mission, to optimise the propulsive efficiency. MAVs are also small, slow and light. This make them very sensitive to gust and harsh atmospheric conditions in general. Under these circumstances, one may try to ensure a large lift and thrust in a way to have spare forces for manoeuvring. Besides, thrust, lift and propulsive efficiency are dependent in a complex way. This illustrates the difficulty of considering a simple aerodynamic coefficient as the cost functional to be optimised. Actually, considering η as cost functional may seem suitable. However, it is not the case since it has been reported in previous contributions (Triantafyllou et al., 1993; Anderson et al., 1998; Read et al., 2003) that the peak of efficiency is located for small values of the Strouhal number corresponding to very small values of the thrust insufficient to move the vehicle. Therefore, it is preferable to seek a sufficient value of the thrust within an acceptable value of efficiency, exploiting the fact that the curve of η versus C_T decreases typically more or less slowly after the peak value. Considering the thrust force as a cost functional is not adapted neither, because it can lead to solution with very poor efficiencies or with very large oscillations. Consequently, in the present work, we aim at optimising, i.e. minimizing the functional \mathcal{L} defined as:

$$\mathcal{L} = \beta_P^2 \bar{P} + \beta_F^2 \bar{F} U_0 + \epsilon_\alpha^2 \bar{\alpha}^2(t) + \epsilon_h^2 \bar{h}^2(t) \quad (2.3)$$

where β_P^2 , β_F^2 , ϵ_α^2 and ϵ_h^2 are positive coefficients giving different weights to the different components of the cost functional. The four weights can not be reduced to three by a simple division by one of them because in some computations in the following, these weights will vanish. The first two terms represent a balance between the required and the useful powers and yield, thus, a link with the propulsive efficiency. A quadratic functional is not considered to properly account for the sign of the horizontal force ($\bar{F} < 0$ when thrust is produced) avoiding optimal solutions corresponding to drag producing kinematics. This choice has an impact on the optimisation update algorithm discussed in §4.4. A higher weight will be given to thrust with respect to power ($\beta_F^2 > \beta_P^2$) to favour an optimal solution with a large thrust. This also prevents the optimisation process to be driven towards the trivial solution of a still airfoil requiring vanishing power and producing drag. The last two terms will be referred to as the cost of the control⁴. They are integrated into the cost functional to avoid optimal solution with very large amplitudes of heaving or pitching: it is known that the thrust coefficient increases when the heave amplitude and, consequently, the Strouhal number increases. Hence, adding these two terms ensure an optimal solution with realistic oscillations preventing large constraints from the structural dynamics point of view. Furthermore, a larger weight is given to $\bar{\alpha}^2(t)$ with respect to $\bar{h}^2(t)$ ($\epsilon_\alpha^2 > \epsilon_h^2$) to ensure giving an equivalent weight to these two terms since the angle $\alpha(t)$ is in radians.

The lift force has not been included in the cost functional because lift depends mainly on the mean angle of attack α_0 and preliminary results showed that optimal values for efficiency are obtained for non-lifting configurations ($\alpha_0 = 0$). In other words, if we include lift in the previous cost functional, a local optimum might be reached for vanishing lift. We thus prefer to seek the optimal kinematics for a non-lifting configuration and then add a mean angle of attack to ensure a sufficient lift (cf. §5.6). Furthermore, the cost functional in this form, can be applied to fish propulsion optimisation, where lift issue is secondary.

In the configuration studied, as long as the classic Reynolds number is constant, the velocity at infinity U_0 is constant as if the optimal performance is sought for a given translational velocity of the vehicle. Therefore, U_0 does not admit variations and its presence in equation 2.3 ensures a balance between two powers. The physical configuration in which the velocity of the airfoil depends on its kinematics would be hard to simulate since it requires a relation of the type: $U_0 = U_0(\alpha_0, h(t), \alpha(t), \dots)$. It would give rise to a more realistic study in which the optimal kinematics may lead to higher forward speed of the MAV.

⁴The time average is done for the square of $\alpha(t)$ and $h(t)$. For a dimensional version of equation 2.3, the weights of these two terms have a dimension in a way to have a sum of powers.

2.5.2 Control parameters

Control, in general, is divided into two categories, passive and active; each one may be subdivided into two sub-categories of open- and closed-loop. The denomination of *passive control* refers to the case where no supplementary energy is injected into the system in order to control it, as in the case where the shape of the airfoil is optimised (Amoignon et al., 2006), whereas the term *active control* is the opposite, including for instance suction to control disturbances in a boundary layer (Walther et al., 2001; Pralits and Hanifi, 2003; Airiau et al., 2003). The *open-loop control* is the configuration in which the control is imagined and applied to the system, like the case in which the position and intensity of suction is previously defined and applied, whereas in *closed-loop control*, sensors detect the situation of the system in real-time and adapt the control to the requirements (Alam et al., 2006). In the present work, we aim at identifying the motion of the wing which gives a good thrust force and an acceptable efficiency and then applying those kinematics to the MAV. We employ optimal control theory, however, no classical flow control is done. This work must be considered as a step towards more sophisticated control systems where the vehicle, like the animal it is supposed to mimic, adapts its motion to the type of mission or to the atmospheric conditions.

Here, we impose the motion of the wing by providing analytical expressions for $\alpha(t)$ and $h(t)$. This is fundamentally different from what is done experimentally by some authors (Silin et al., 2006) who build elastic wings and put them in a wind tunnel giving rise to a free undetermined motion of the wings. The imposed kinematics is supposed to mimic the motion of birds'/insects' wings and fish fins. Historically, birds' flight and fish swimming were modelled by means of simple heaving. The poor thrust developed in these conditions and its absence in hovering conditions (Wang, 2000; Lewin and Haj-Hariri, 2003; Guglielmini, 2004) suggested the inclusion of pitching. This allows a higher thrust production by controlling the leading-edge vortex formation and development. Recently, in literature, these motions have been simulated by monochromatic harmonic heaving and pitching oscillations of the same frequency (Anderson et al., 1998; Read et al., 2003; Pedro et al., 2003; Lewin and Haj-Hariri, 2003; Guglielmini, 2004). An illustration of such a motion is given in figure 2.5 for $h(t) = c \sin(\frac{2\pi t}{T})$, $\alpha_0 = 0^\circ$ and $\alpha(t) = -35^\circ \sin(\frac{2\pi t}{T} + \frac{\pi}{2})$.

Here, we formally generalise this motion by writing a sum of harmonics as:

$$\begin{cases} h(t) = \sum_{k=1}^N h_k \sin(\sigma_k t + \tau_k) \\ \alpha(t) = \sum_{k=1}^N \alpha_k \sin(\sigma_k t + \phi_k) \end{cases} \quad (2.4)$$

where h_k , α_k , τ_k and ϕ_k are heaving and pitching amplitudes and phases respectively, N is the number of considered modes and σ_k the angular frequency of oscillation of each mode. In the case in which σ^* is the opposite of time scale, σ_k are integer numbers equal to k , whereas they are real if a reference frequency σ_0^* is adopted for time scale. Such a choice of a sum of harmonics present three major advantages. The first is that by imposing $N = 1$, we recover the classical case studied in literature. Secondly, it allows to simulate a very wide space of motions since a large number of analytical functions can be projected on an infinite sum of sine functions. Third, it provides the opportunity to consider higher order harmonics as in Read et al. (2003). We note that, since the average over one period of $\alpha(t)$ vanishes, α_0 is the value of the angle of attack of the airfoil. Regardless of the value of N , the flapping motion is periodic in time with a dimensionless period equal to 2π . Thus, the numerical simulations will be carried out for a non dimensional time multiple of 2π representing an integer number of periods.

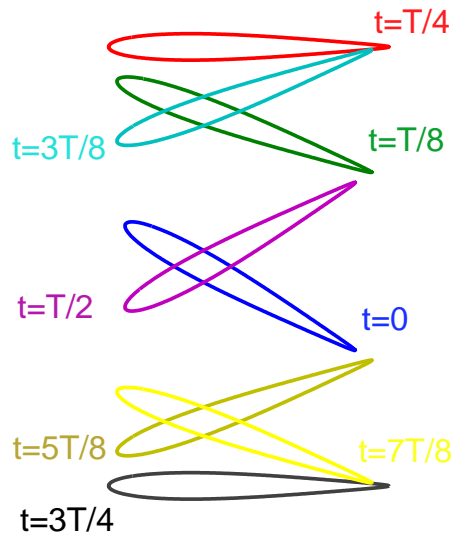


Figure 2.5: Different position of an airfoil at uniform intervals over a period of oscillation for a classical flapping motion.

The flapping characteristics are considered as control parameters. Hence, the vari-

ables α_0 , h_k , α_k , ϕ_k and τ_k and the temporal frequency σ_k for $k = 1, N$ are the parameters for which the gradients of the cost functional will be computed. Amplitudes and phases have a crucial impact on propulsion performances since they drive the timing of the vortex shedding and propagation in the wake whereas the average angle of attack is important for lift generation. The letter g will denote in the following any generic control parameter of the $5N + 1$ possible ones.

If we exclude the purely geometric parameters related to the form of the airfoil, its thickness and/or camber and we focus on the flight conditions, the flapping airfoil depends on a set of 7 relevant parameters:

- The Strouhal number, classifying whether the airfoil is producing drag or thrust and in which conditions,
- the heaving amplitude,
- the pitching amplitude,
- the phase angle between heaving and pitching. For $N = 1$, one angle ϕ_1 or τ_1 is sufficient to simulate this phase angle,
- the Reynolds number or equivalently the free stream velocity,
- the mean angle of attack α_0 and
- the position of the pitching centre.

According to our choice of control parameters, only the position of the pitching centre is not controlled since in all simulations, the airfoil pitches around a point located at one third the chord length. Guglielmini (2004) has shown the positive impact of considering a pitching centre in this position. This configuration is also adopted in Anderson et al. (1998), in which a propulsive efficiency as high as 87% is achieved. Moreover, the effect of the Reynolds number at infinity is briefly studied due to its secondary role (Ohmi et al., 1990). All the other parameters are directly investigated. The Strouhal number is related to the frequency of flapping and to the heaving amplitude. It has not been considered as a control parameter by itself. However, by controlling the flapping frequency and the heaving, we modify the Strouhal number, showing its effect.

2.5.3 Evaluating the gradient

The third component of the optimisation problem deals with the technique used in order to find the optimal control parameters and consequently the optimal cost

functional. The principle of the technique is very simple. If we consider constant the other parameters, the cost functional depends on $5N + 1$ control parameters. For its optimal value, the gradient of the cost with respect to any generic control parameter g should vanish. Thus, the main question is how to evaluate the gradient of \mathcal{L} with respect to g . The simplest and most rudimentary way is to evaluate \mathcal{L} for various values of g and to deduce the gradient by a simple finite differences approach. The main advantage of this method is avoiding further computations than the strict solution of the flow equations. However, it is not suited for a large space of parameters. On the other hand, it requires a previous knowledge of the range in which the optimal values are, in order to vary the parameters inside this range. This technique of varying the control parameter, one by one, and observing the effect of the measure of performance is very widespread in literature (Triantafyllou et al., 1993; Anderson, 1996; Isogai et al., 1999; Read et al., 2003; Pedro et al., 2003; Lewin and Haj-Hariri, 2003; Guglielmini and Blondeaux, 2004; Tuncer and Kaya, 2005).

In the present work, a different approach is adopted and the gradients of the cost functional are evaluated with high precision, rather than approximated. Sensitivity technique and the complex step derivative method (see chapter 3) are applied. This methodology enables us to perform a multi-parameters optimisation in a wide space. Despite the computational cost needed to evaluate these gradients, the high precision of these two methods and their ability to drive several parameters towards their optimal values, make them more efficient than what previous contributions has accomplished.

Conclusions

We address the problem of solving the flow around a two-dimensional flapping airfoil. A vorticity-stream function formulation is used in a circular computational domain resulting from the application of the Joukowski transformation on the airfoil. Once solved, the flow equations enable us to recover the aerodynamic characteristics of the flapping airfoil. We propose to optimise these characteristics by acting directly on the motion of the foil. Hence, a cost functional has been defined: it represents the objective of producing sufficient thrust and lift with acceptable propulsive efficiency and without very large oscillations. The control is done on the kinematics of flapping, a generalised formulation of simple monochromatic harmonic oscillations mimicking birds' wings and fish fins motion. The next step consists in writing the equations which compute the gradients of the objective functional with respect to the control parameters and to create the solver which estimates them. This is the aim of chapter 3.

Chapter 3

Gradient evaluation

Introduction

The gradient evaluation is required to drive the control parameters towards their optimal values. The value of the gradient and its sign indicates, in the case of a monotonous function, from which side and how far the considered value is from the optimal one. For a complex functional and flow like those concerned here, this may not be always true due to the eventual presence of local optima. Nonetheless, a vanishing value of the gradient should be found for the optimum, even if it is a local one.

Two techniques are adopted for the estimation of the gradient of the cost functional. The first is the sensitivity technique. It necessitates the solution for the sensitivity equations obtained by deriving the flow equations. The second is the complex step derivative method, where the flow equations are solved in the complex space and the imaginary part of the solution is related to the gradient. While the complex method is more accurate for a small number of discretization points, both yield very close results for refined grids. This can be explained by the existence of a tight relation between these two methods. An alternative to the method based on the evaluation of sensitivities is the adjoint method, which is also very efficient for the calculation of gradients and which has been used in recent references (Iollo and Zannetti, 2000; Bottaro et al., 2006). The adjoint approach has the advantage of lower memory penalty for a large number of control parameters, with respect to automatic differentiation softwares, for instance. However, a different set of adjoint equations must be derived and solved for each different cost function. Otherwise, one may estimate the gradients by a simple finite differences approach. However, compared to the other three methods, this one is slower and less accurate. All these approaches yield local extrema; global ones can be obtained by stochastic methods, like genetic algorithms for instance.

In what follows, the expressions of the gradients are given for a generic control parameter g . In practice, for the sensitivity method, the optimisation can be done for one or many parameters at the same time. In this latter case, the flow equations are common and the sensitivity equations differ from case to case by a source term. Computational time may be spared if the gradient for two or more control parameters is evaluated together. Another possibility is to parallelize the computations by delegating the computations of each gradient to a processor and putting in common the flow solution. In the case of the complex step method, the computation of several gradients at the same time is also possible but filters should be injected into the equations to distinguish the real terms of the complex terms. This is compulsory since the non-controlled parameters should be real.

3.1 Sensitivity technique

The basics of the sensitivity technique are described by Gunzburger (1997). The idea is to compute for a physical variable its sensitivity (total derivative) to a given parameter. The term of sensitivity is meaningful because it emphasises the idea of how much the physical variable is sensitive to the parameter, i.e. how much the physical variable is affected when the parameter is varied?

As far as the cost functional is concerned, the answer of the latter question requires first to compute the sensitivity of the governing variables (here ω and ψ) with respect to control parameters and then use them to deduce the cost functional gradient. If we denote by g a generic control parameter, the sensitivity of ω and ψ with respect to g will be referred by $\omega_{,g}$ and $\psi_{,g}$. They are evaluated by solving the sensitivity equations, obtained by deriving the flow equations with respect to g . In practice, we start by writing the sensitivity equations, we then solve them and finally use the solution for the computation of the gradient.

3.1.1 Sensitivity equations

We consider the non-dimensional equations governing the flapping airfoil problem presented in §2.3:

$$\begin{cases} \frac{\partial \omega}{\partial t} + \frac{1}{\sqrt{J}} \left[v_r \frac{\partial \omega}{\partial r} + \frac{v_\theta}{r} \frac{\partial \omega}{\partial \theta} \right] = \frac{1}{ReJ} \left[\frac{\partial^2 \omega}{\partial r^2} + \frac{1}{r} \frac{\partial \omega}{\partial r} + \frac{1}{r^2} \frac{\partial^2 \omega}{\partial \theta^2} \right], \\ \frac{\partial^2 \psi}{\partial r^2} + \frac{1}{r} \frac{\partial \psi}{\partial r} + \frac{1}{r^2} \frac{\partial^2 \psi}{\partial \theta^2} = -J\omega, \end{cases} \quad (3.1)$$

where

$$\begin{aligned}
 v_r &= \frac{1}{\sqrt{J}} \left[\frac{1}{r} \frac{\partial \psi}{\partial \theta} - \left(\dot{h}(t) \sin(\alpha(t)) - \dot{\alpha}(t) Y \right) \left(\frac{\partial X}{\partial \xi} \cos \theta + \frac{\partial X}{\partial \chi} \sin \theta \right) \right. \\
 &\quad \left. - \left(\dot{h}(t) \cos(\alpha(t)) + \dot{\alpha}(t) X \right) \left(\frac{\partial Y}{\partial \xi} \cos \theta + \frac{\partial Y}{\partial \chi} \sin \theta \right) \right], \\
 v_\theta &= \frac{1}{\sqrt{J}} \left[-\frac{\partial \psi}{\partial r} - \left(\dot{h}(t) \sin(\alpha(t)) - \dot{\alpha}(t) Y \right) \left(\frac{\partial X}{\partial \chi} \cos \theta - \frac{\partial X}{\partial \xi} \sin \theta \right) \right. \\
 &\quad \left. - \left(\dot{h}(t) \cos(\alpha(t)) + \dot{\alpha}(t) X \right) \left(\frac{\partial Y}{\partial \chi} \cos \theta - \frac{\partial Y}{\partial \xi} \sin \theta \right) \right]
 \end{aligned}$$

The derivative of 3.1 with respect to g yields the sensitivity equations of the flow with respect to a generic control parameter:

$$\begin{aligned}
 \frac{\partial \omega_{,g}}{\partial t} + \frac{1}{\sqrt{J}} \left[v_r \frac{\partial \omega_{,g}}{\partial r} + \frac{v_\theta}{r} \frac{\partial \omega_{,g}}{\partial \theta} + \underbrace{\frac{\partial v_r}{\partial g} \frac{\partial \omega}{\partial r} + \frac{1}{r} \frac{\partial v_\theta}{\partial g} \frac{\partial \omega}{\partial \theta}} \right] &= \frac{1}{ReJ} \left[\frac{\partial^2 \omega_{,g}}{\partial r^2} + \frac{1}{r} \frac{\partial \omega_{,g}}{\partial r} + \frac{1}{r^2} \frac{\partial^2 \omega_{,g}}{\partial \theta^2} \right], \\
 \frac{\partial^2 \psi_{,g}}{\partial r^2} + \frac{1}{r} \frac{\partial \psi_{,g}}{\partial r} + \frac{1}{r^2} \frac{\partial^2 \psi_{,g}}{\partial \theta^2} &= -J \omega_{,g},
 \end{aligned} \tag{3.2}$$

where

$$\begin{aligned}
 \frac{\partial v_r}{\partial g} &= \frac{1}{\sqrt{J}} \left[\frac{1}{r} \frac{\partial \psi_{,g}}{\partial \theta} - \frac{\partial}{\partial g} \left(\dot{h}(t) \sin(\alpha(t)) - \dot{\alpha}(t) Y \right) \left(\frac{\partial X}{\partial \xi} \cos \theta + \frac{\partial X}{\partial \chi} \sin \theta \right) \right. \\
 &\quad \left. - \frac{\partial}{\partial g} \left(\dot{h}(t) \cos(\alpha(t)) + \dot{\alpha}(t) X \right) \left(\frac{\partial Y}{\partial \xi} \cos \theta + \frac{\partial Y}{\partial \chi} \sin \theta \right) \right], \\
 \frac{\partial v_\theta}{\partial g} &= \frac{1}{\sqrt{J}} \left[-\frac{\partial \psi_{,g}}{\partial r} - \frac{\partial}{\partial g} \left(\dot{h}(t) \sin(\alpha(t)) - \dot{\alpha}(t) Y \right) \left(\frac{\partial X}{\partial \chi} \cos \theta - \frac{\partial X}{\partial \xi} \sin \theta \right) \right. \\
 &\quad \left. - \frac{\partial}{\partial g} \left(\dot{h}(t) \cos(\alpha(t)) + \dot{\alpha}(t) X \right) \left(\frac{\partial Y}{\partial \chi} \cos \theta - \frac{\partial Y}{\partial \xi} \sin \theta \right) \right].
 \end{aligned}$$

The main difference between flow and sensitivity equations is the source term underbraced in equation 3.2. It depends on the choice of the control parameter among the $5N + 1$ possible ones (cf. Appendix C.2). The computation of the sensitivity equations require a prior resolution of the flow equations 3.1. However, and due to the particularity of deriving the product of two terms, the sensitivity equations are

always linear, which facilitates their resolution. Thus, for a given instant, the solver treats the flow equation first, then the sensitivity equations before moving to the next instant. The same numerical approach applied for the flow equation system is used for the sensitivity system. The two equations are assumed to be uncoupled. This assumption is valid when the temporal step is small enough, like in the present work. Hence, the equation for $\omega_{,g}$ is solved using the value of $\psi_{,g}$ from the previous temporal step and then it is injected into the second equation to evaluate the new value of $\psi_{,g}$. The same ADI method is applied to the first equation to decouple the two directions, with first, a half temporal step in the θ direction and then in the r direction. In each case, we recover a tridiagonal linear system. The tridiagonality is due to the choice of a second order centred scheme in the discretization. The linear systems are solved with a Thomas-like algorithms. On the other hand, the Poisson-like equation ($\Delta\psi_{,g} = -J\omega_{,g}$, where Δ is the Laplacian operator in the polar coordinates) is solved by a Fourier transformation, usually very suitable for handling this kind of equations. Details on discretization schemes and the associated tridiagonal systems and their resolution are given in Appendix D.

The solution of the flow equations provides the fields of vorticity and stream function in the whole computational domain. Consequently, the rest of the physical variables can be obtained, including the two components of velocity and pressure. Analyzing these fields allows to investigate the physical mechanisms which take place inside the flow. Phenomena like flow separation, leading- and trailing-vorticity can be observed and their impact on lift, thrust and propulsive efficiency may be studied. The interpretation of the sensitivity fields is not straightforward. These fields have rather a mathematical sense than a physical sense, since they are the derivative of physical quantities. They provide a map of the spots where vorticity or stream function (and consequently velocity components and pressure) are more/less sensitive to the control parameter g . This implies that it is hard to explain why the optimal kinematics are optimal by looking at the sensitivity fields. It would be more interesting to use the sensitivity variables in order to reach the optimal kinematics and then analyze the physical variables of these optimal kinematics in order to justify the optimality. Plots of these fields are shown in §5.2 providing the position of the points where vorticity is most sensitive to the kinematics of the airfoil. These points are, unsurprisingly, located near the airfoil's tips and in its wake.

The boundary conditions for system 3.2 are obtained by the derivation of the boundary conditions of system 3.1 with respect to the control parameter g (cf. Appendix E.2). They depend, thus, on the choice of the control parameter. In the same way than the flow equations, the equation for $\omega_{,g}$ is unsteady, requiring an initial condition and time advancement. The condition of vanishing sensitivities at initial time are imposed. This choice does not affect the final flow fields of sensitivity functions

once the flow is established. Time advancement is performed with a first order up-wind scheme. Unlike adjoint methods, where the adjoint system is advanced from the final towards the initial instant, time advancement in sensitivity and complex step derivative methods is done in the same way than for the flow equations.

3.1.2 Sensitivity gradient

Once the sensitivity of the vorticity and stream function are evaluated, they are used to compute the gradient of the cost functional. Formally, the gradient computed with the sensitivity is similar to any gradient of a multi-variable function. Thus, logically assuming that the cost functional depends on the flow variables ω and ψ and on the control parameter ($\mathcal{L} = \mathcal{L}(\omega, \psi, g)$), the gradient can be expressed as:

$$\frac{d\mathcal{L}}{dg} = \frac{\partial\mathcal{L}}{\partial\omega} \frac{d\omega}{dg} + \frac{\partial\mathcal{L}}{\partial\psi} \frac{d\psi}{dg} + \frac{\partial\mathcal{L}}{\partial g}. \quad (3.3)$$

The last term in equation 3.3 is a classical partial derivative calculated by isolating the terms inside \mathcal{L} which depend on g and applying a partial derivation. The first two terms on the right hand side of the equations 3.3 are computed by isolating the terms of \mathcal{L} which depend on ω (respectively ψ) and substituting the vorticity (respectively the stream function) by its sensitivity $\omega_{,g}$ (respectively $\psi_{,g}$) inside these terms. This justifies the need to solve the sensitivity equations before being able to evaluate the sensitivity gradient. In our case, the cost functional is a sum of four terms so what precedes is applied to each of them:

$$\frac{d\mathcal{L}}{dg} = \beta_P^2 \frac{d\bar{P}}{dg} + \beta_F^2 \frac{d\bar{F}}{dg} U_0 + \epsilon_\alpha^2 \frac{d\bar{\alpha}^2}{dg} + \epsilon_h^2 \frac{d\bar{h}^2(t)}{dg} \quad (3.4)$$

Expressing the terms involved in \mathcal{L} in the moving reference frame (X, Y) and isolating the parts which depend on vorticity, stream function and control parameter, we reach

the formal expression of the gradient with respect to a generic control parameter g :

$$\begin{aligned}
 2\pi \frac{d\mathcal{L}}{dg} = & - \beta_P^2 \int_0^{2\pi} \left[\left(\frac{\partial F_X}{\partial g} + \frac{\partial F_X}{\partial \omega} \frac{d\omega}{dg} + \frac{\partial F_X}{\partial \psi} \frac{d\psi}{dg} \right) \sin(\alpha(t)) \dot{h}(t) \right] dt \\
 & - \beta_P^2 \int_0^{2\pi} \left[\left(\frac{\partial F_Y}{\partial g} + \frac{\partial F_Y}{\partial \omega} \frac{d\omega}{dg} + \frac{\partial F_Y}{\partial \psi} \frac{d\psi}{dg} \right) \cos(\alpha(t)) \dot{h}(t) \right] dt \\
 & - \beta_P^2 \int_0^{2\pi} \left[\left(\frac{\partial M_z}{\partial g} + \frac{\partial M_z}{\partial \omega} \frac{d\omega}{dg} + \frac{\partial M_z}{\partial \psi} \frac{d\psi}{dg} \right) \dot{\alpha}(t) + M_z \frac{\partial \dot{\alpha}(t)}{\partial g} \right] dt \\
 & - \beta_P^2 \int_0^{2\pi} \left[F_X \frac{\partial (\sin(\alpha(t)))}{\partial g} \dot{h}(t) + F_X \sin(\alpha(t)) \frac{\partial \dot{h}(t)}{\partial g} \right] dt \\
 & - \beta_P^2 \int_0^{2\pi} \left[F_Y \frac{\partial (\cos(\alpha(t)))}{\partial g} \dot{h}(t) + F_Y \cos(\alpha(t)) \frac{\partial \dot{h}(t)}{\partial g} \right] dt \quad (3.5) \\
 & + \beta_F^2 \int_0^{2\pi} \left[\left(\frac{\partial F_X}{\partial g} + \frac{\partial F_X}{\partial \omega} \frac{d\omega}{dg} + \frac{\partial F_X}{\partial \psi} \frac{d\psi}{dg} \right) \cos(\alpha(t) - \alpha_0) \right] dt \\
 & - \beta_F^2 \int_0^{2\pi} \left[\left(\frac{\partial F_Y}{\partial g} + \frac{\partial F_Y}{\partial \omega} \frac{d\omega}{dg} + \frac{\partial F_Y}{\partial \psi} \frac{d\psi}{dg} \right) \sin(\alpha(t) - \alpha_0) \right] dt \\
 & + \beta_F^2 \int_0^{2\pi} \left[F_X \frac{\partial (\cos(\alpha(t) - \alpha_0))}{\partial g} - F_Y \frac{\partial (\sin(\alpha(t) - \alpha_0))}{\partial g} \right] dt \\
 & + \epsilon_\alpha^2 \frac{\partial \bar{\alpha}^2(t)}{\partial g} + \epsilon_h^2 \frac{\partial \bar{h}^2(t)}{\partial g},
 \end{aligned}$$

where F_X , F_Y and M_Z are the horizontal and vertical forces in the moving frame (X, Y) and the pitching torque respectively. The detailed expressions of each term in equation 3.5 and the different values of the derivative terms according to the control parameter are given in appendix C.2.

3.2 Complex step derivative method

In order to evaluate, in a different manner, the gradient of the cost functional with respect to the control parameters, we adopt the complex step derivative method (CSDM). This relatively new method for computing gradients is not very widespread in literature despite its powerful ability to handle sophisticated computations. The

first contribution evoking the use of complex variables to estimate derivatives of real function seems to be that by Lyness and Moler (1967). However, the fundamentals of the method were written in the last decade (Squire and Trapp, 1998) and its application to problems in fluids mechanics has been done only for few years (Vatsa, 2000; Martins et al., 2003) including extensions to the pseudospectral algorithms (Cerviño and Bewley, 2003).

3.2.1 The principle of the method

The principle of the complex step derivative method can be understood by performing a Taylor development with a complex step. Normally, to approximate the derivative of a given functional, one may use a first or a second-order finite differences method:

First-order finite difference:
$$\frac{\partial \mathcal{L}}{\partial g}(g, \cdot) = \frac{\mathcal{L}(g + \delta g, \cdot) - \mathcal{L}(g, \cdot)}{\delta g} + O(\delta g),$$

Second-order finite difference:
$$\frac{\partial \mathcal{L}}{\partial g}(g, \cdot) = \frac{\mathcal{L}(g + \delta g, \dots) - \mathcal{L}(g - \delta g, \dots)}{2\delta g} + O(\delta g^2).$$

Now if instead of a step δg , we apply a complex step $i\delta g$, where i is the square root of -1, we obtain:

Complex Step method:
$$\frac{\partial \mathcal{L}}{\partial g}(g, \cdot) = \frac{1}{\delta g} \text{Imag} \left[\tilde{\mathcal{L}}(g + i\delta g, \cdot) \right] + O(\delta g^2),$$

where Imag refers to the imaginary part and the superscript $\tilde{\cdot}$ indicates that the functional \mathcal{L} is now a complex dependent function. Three major advantages can be cited for this method. First, its simplicity, since no further computations are required. It is enough to declare complex all the variables of a given problem and solve the same equations governing the physical quantities in the complex space and to adapt the solver (see §3.2.2 for details). The real part of the complex solution corresponds to the physical solution whereas the imaginary part is the gradient with respect to the control g . Second, this method is, by construction, of second-order since the second-order derivative is real and hence is not involved in the imaginary part of $\tilde{\mathcal{L}}$. Third, this method eliminates the cancellation error, a well-known phenomenon in the finite difference method. For a large step δg , the error is dominated by the truncation error. For a very small step, the error does not tend to zero due to the vanishing of both numerator and denominator of the finite-difference formulas. Previous results have shown that there is an optimal step size when applying finite difference schemes. When the step tends to zero, the error saturates to a value higher than the one obtained by CSDM (cf. figure 3.1). However, in the present work, the very high accuracy is not of so-much concern. Therefore, the cancellation error is not a real issue. A more interesting question to address is the comparison between first-order, second-order finite difference schemes on the one hand, and the complex

3.2 Complex step derivative method

step derivative method on the other for reasonably, and usual, small steps.

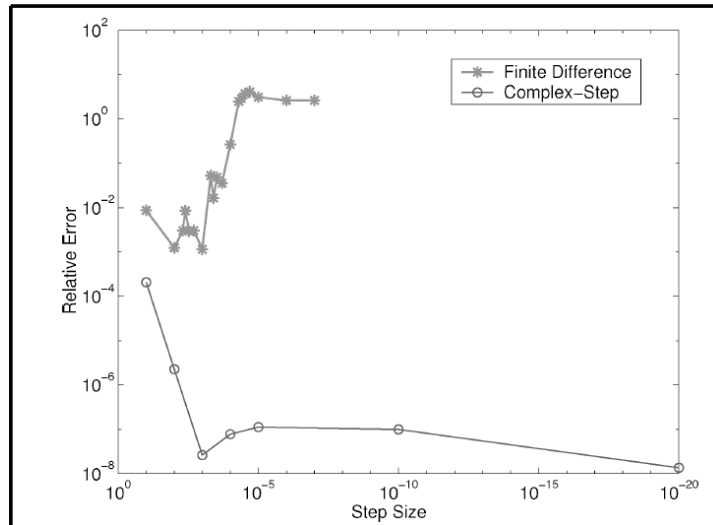


Figure 3.1: Plot of the relative error for skin friction drag of an aircraft in a supersonic laminar flow versus the step size for finite difference and complex step methods (Martins et al., 2003).

In this optics, we consider the simple function: $f(g) = 3 \sin(g^2) - 2g$ on the interval $[-\pi, \pi]$ and its derivative $f'(g) = 6g \cos(g^2) - 2$ that we approximate with the three approaches. In figure 3.2(a), we plot the exact and approximated derivatives for 100 nodes and in figure 3.2(b), we show the relative error.

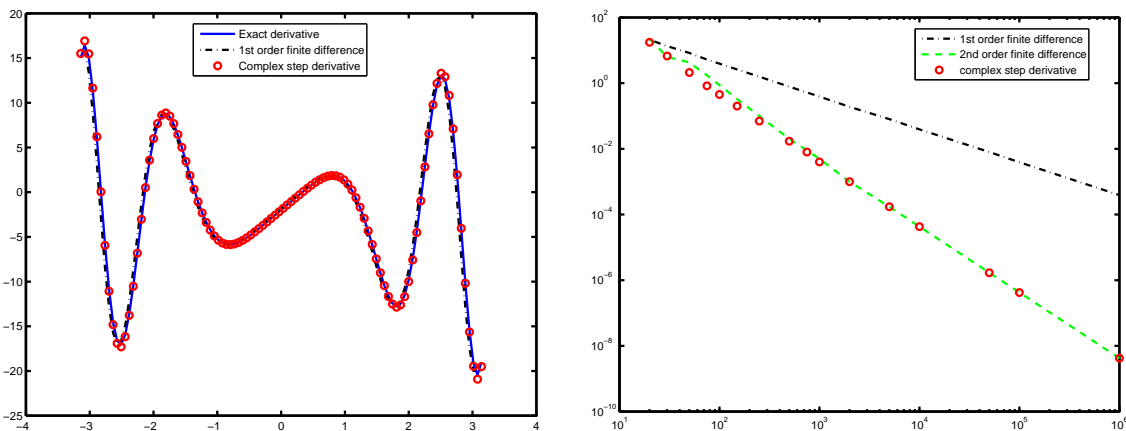


Figure 3.2: Comparison between the exact and approximated derivatives (left) and a plot of the relative error versus the number of discretization points (right).

Two results should be highlighted from this comparison, the first is that for such a simple function no cancellation error problem is observed and that as soon as we exceed 10^3 discretization points, the second-order finite difference method is as accurate as the CSDM (and obviously, much more than the first-order scheme). Despite the simplicity of the considered function, this result suggests that for refined grids second order schemes used in sensitivity methods and complex derivative method should provide close gradients. This is confirmed by the results of the present study. The equivalence of results is even less surprising after showing the link between the two approaches (cf. §3.3).

3.2.2 Coding tricks

Thirty years were needed after the first contribution mentioning the possibility of using the complex variables to estimate gradients of real function (Lyness and Moler, 1967) to apply numerically this principle Squire and Trapp (1998). The main reason is the inability of compilers to deal effectively with complex arithmetic. However, the procedure for converting an existing real Fortran code into complex one is relatively simple:

- Declare all the variables as complex adding, for instance, "implicit complex ($a - h, o - z$)" in the main program and the subroutines.
- Modify the declaration of variables by substituting double precision to double complex variables.
- Create a complex equivalent for all the intrinsic routines used. As an example, the *max* and *min* routines should refer to the norm of the complex number. Furthermore, all trigonometric functions should be defined using complex exponentials.
- Replace in each unit of the program the real function by its correspondent complex one.
- Modify the syntax for the logical functions in a way to position the condition on the real part of the complex number or on its norm. This should be done for commands such as: *if*, *LE*, *GT*.
- Adapt the format of input and output data to fit with the actual size of the complex variables.

The main disadvantage of the complex step derivative method is nearly the double of the original memory of the real code and between 2 and 3 longer duration of simulations. Moreover, the conversion to complex variables requires human intervention, which may lead to user-induced errors.

3.2.3 Application to flapping airfoil

Applying the complex step derivative method to flapping airfoil problem consists in simply rendering complex the governing flow equations. Hence, we render all the variables complex (formally, by adding a tilde) and we solve the complex system:

$$\begin{cases} \frac{\partial \tilde{\omega}}{\partial t} + \frac{1}{\sqrt{J}} \left[\tilde{v}_r \frac{\partial \tilde{\omega}}{\partial r} + \frac{\tilde{v}_\theta}{r} \frac{\partial \tilde{\omega}}{\partial \theta} \right] = \frac{1}{ReJ} \left[\frac{\partial^2 \tilde{\omega}}{\partial r^2} + \frac{1}{r} \frac{\partial \tilde{\omega}}{\partial r} + \frac{1}{r^2} \frac{\partial^2 \tilde{\omega}}{\partial \theta^2} \right], \\ \frac{\partial^2 \tilde{\psi}}{\partial r^2} + \frac{1}{r} \frac{\partial \tilde{\psi}}{\partial r} + \frac{1}{r^2} \frac{\partial^2 \tilde{\psi}}{\partial \theta^2} = -J\tilde{\omega}, \end{cases} \quad (3.6)$$

where

$$\begin{cases} \tilde{v}_r = \frac{1}{\sqrt{J}} \left[\frac{1}{r} \frac{\partial \tilde{\psi}}{\partial \theta} - \left(\dot{\tilde{h}}(t) \sin(\tilde{\alpha}(t)) - \dot{\tilde{\alpha}}Y \right) \left(\frac{\partial X}{\partial \xi} \cos \theta + \frac{\partial X}{\partial \chi} \sin \theta \right) \right] \\ \quad - \frac{1}{\sqrt{J}} \left[\left(\dot{\tilde{h}}(t) \cos(\tilde{\alpha}(t)) + \dot{\tilde{\alpha}}X \right) \left(\frac{\partial Y}{\partial \xi} \cos \theta + \frac{\partial Y}{\partial \chi} \sin \theta \right) \right], \\ \tilde{v}_\theta = \frac{1}{\sqrt{J}} \left[-\frac{\partial \tilde{\psi}}{\partial r} - \left(\dot{\tilde{h}}(t) \sin(\tilde{\alpha}(t)) - \dot{\tilde{\alpha}}Y \right) \left(\frac{\partial X}{\partial \chi} \cos \theta - \frac{\partial X}{\partial \xi} \sin \theta \right) \right] \\ \quad - \frac{1}{\sqrt{J}} \left[\left(\dot{\tilde{h}}(t) \cos(\tilde{\alpha}(t)) + \dot{\tilde{\alpha}}X \right) \left(\frac{\partial Y}{\partial \chi} \cos \theta - \frac{\partial Y}{\partial \xi} \sin \theta \right) \right]. \end{cases} \quad (3.7)$$

The same method used for the flow equations is applied to system 3.6 in the complex space. This illustrates the power of this method, since for a given solver of a mathematical problem, transforming the variables into complex and solving the same problem yields the solution and its gradient. The choice of the parameter for which the gradient is computed is imposed by the expressions of $\tilde{h}(t)$ and $\tilde{\alpha}(t)$. A small complex step is added to the control parameter. Hence, for instance, to control the first heave amplitude harmonic h_1 , we write that :

$$\tilde{h}(t) = (h_1 + i\delta h_1) \sin(\sigma_1 t + \tau_1) + \sum_{k=2}^N h_k \sin(\sigma_k t + \tau_k),$$

and

$$\tilde{\alpha}(t) = \alpha(t) = \sum_{k=1}^N \sin(\sigma_k t + \phi_k).$$

In the same way, and by adding a small complex step to the control parameter inside the boundary conditions of the flow equation, we obtain the complex boundary conditions for system 3.6.

3.2.4 Complex-step gradient

The gradient of the cost functional \mathcal{L} with respect to a generic control parameter g is simply obtained by computing the complex cost $\tilde{\mathcal{L}}$ and isolating the imaginary part since:

$$\frac{d\mathcal{L}}{dg} = \frac{1}{\delta g} \text{Imag} [\tilde{\mathcal{L}}] = \frac{1}{\delta g} \text{Imag} \left[\beta_P^2 \tilde{P} + \beta_F^2 \tilde{F}U_0 + \epsilon_\alpha^2 \overline{(\tilde{\alpha})^2} + \epsilon_h^2 \overline{(\tilde{h})^2} \right],$$

where $\tilde{\mathcal{L}} = \mathcal{L}(g + i\delta g)$. The expression of this gradient in the general case is rather long but straightforward. An example, for the control of h_k is given in Appendix C.3.

3.3 From CSDM to sensitivity

For a "sufficiently" refined grid, the numerical values of gradients are similar with the sensitivity approach and the complex step method. This is due to a link between these two methods. As shown below, this link can be brought to light by splitting the equations of CSDM into real and imaginary parts. Under these conditions, the real part can be seen as a second order approximation of the flow equations and the imaginary part corresponds exactly to the sensitivity system. For the sake of clarity, the relation between the two approaches is demonstrated first for the simple case of Burgers' equation, then for the problem of the flapping foil.

3.3.1 Burgers' equation

Consider the mono-dimensional Burgers' equation expressed as:

$$\frac{\partial u}{\partial t} + u \frac{\partial u}{\partial x} = \frac{1}{Re} \frac{\partial^2 u}{\partial x^2}$$

where $u = u(x, t, \cdot)$, $x \in [0, 1]$ and $t \in [0, T]$ and the associated generic boundary conditions written as:

$$\begin{cases} u(0, x) &= f_0(x), \\ u(t, x_1) &= f_1(t), \\ u(t, x_2) &= \frac{df_2(t)}{dt}. \end{cases}$$

We apply the sensitivity method to this equation for the control parameter g . We denote by u_g the sensitivity of u with respect to any variable g upon which u depends.

The sensitivity equation is obtained by deriving Burgers' equation with respect to g :

$$\frac{\partial u_g}{\partial t} + u \frac{\partial u_g}{\partial x} + u_g \frac{\partial u}{\partial x} = \frac{1}{Re} \frac{\partial^2 u_g}{\partial x^2}$$

Thus, a system for the flow and sensitivity equations is reached. The flow equations must be solved first for a temporal step recovering u before using it to solve the sensitivity system:

$$\begin{cases} \frac{\partial u}{\partial t} + u \frac{\partial u}{\partial x} & = \frac{1}{Re} \frac{\partial^2 u}{\partial x^2} \\ \frac{\partial u_g}{\partial t} + u \frac{\partial u_g}{\partial x} + u_g \frac{\partial u}{\partial x} & = \frac{1}{Re} \frac{\partial^2 u_g}{\partial x^2} \end{cases} \quad (3.8)$$

Now, apply the complex step derivative method to the same 1D Burgers' equation to compute the gradient of u with respect to g . Therefore, the real variable u is replaced by a complex variable \tilde{u} and the following complex equation is numerically solved in the complex space:

$$\frac{\partial \tilde{u}}{\partial t} + \tilde{u} \frac{\partial \tilde{u}}{\partial x} = \frac{1}{Re} \frac{\partial^2 \tilde{u}}{\partial x^2} \quad (3.9)$$

If the complex variable \tilde{u} is decomposed into a real part u and an imaginary part u_g as $\tilde{u} = u + iu_g$, and injected into 3.9, then by separating the real part from the imaginary one, two equations are recovered:

$$\begin{cases} \frac{\partial u}{\partial t} + u \frac{\partial u}{\partial x} - u_g \frac{\partial u_g}{\partial x} & = \frac{1}{Re} \frac{\partial^2 u}{\partial x^2} \\ \frac{\partial u_g}{\partial t} + u \frac{\partial u_g}{\partial x} + u_g \frac{\partial u}{\partial x} & = \frac{1}{Re} \frac{\partial^2 u_g}{\partial x^2} \end{cases} \quad (3.10)$$

The comparison between the systems 3.8 and 3.10 shows a perfect match between the sensitivity equation and the imaginary part of the csdm method. The term $-u_g \frac{\partial u_g}{\partial x}$ which renders the flow equation and the real part of the complex equation of the CSDM method different can be neglected, when δg is small, since a simple Taylor development applied to the term $\tilde{u}(g + i\delta g, \cdot)$ yields:

$$\tilde{u}(g + i\delta g, \cdot) = u(g, \cdot) + i\delta g \frac{\partial u}{\partial g}(g, \cdot) + O(\delta g^2) - iO(\delta g^3) = u + iu_g$$

which implies that $u_g = \delta g \frac{\partial u}{\partial g}(g, \dots) - O((\delta g)^3)$. Hence, as long as u is a C^1 function having limited derivatives in the whole domain of variables, u_g and $\frac{\partial u_g}{\partial x}$ are $O(\delta g)$

and the term $u_g \frac{\partial u_g}{\partial x}$ can be neglected. Thus, when we split the complex variables, the CSDM turns to be an $O(\delta g^2)$ approximation of the sensitivity system 3.8.

The correspondence exists also for the boundary conditions. If we consider the case in which $g = t$, the boundary conditions for the sensitivity equations are:

$$\begin{cases} \frac{\partial u}{\partial g}(0, x) = 0, \\ \frac{\partial u}{\partial g}(t, x_1) = f_1'(t), \\ \frac{\partial u}{\partial g}(t, x_2) = f_2''(t). \end{cases}$$

For $g = t$, the boundary conditions for the complex equation 3.9 are:

$$\begin{cases} \tilde{u}(0, x) = f_0(x), \\ \tilde{u}(\tilde{t}, x_1) = \tilde{f}_1(\tilde{t}), \\ \tilde{u}(\tilde{t}, x_2) = \frac{d\tilde{f}_2(\tilde{t})}{dt}. \end{cases}$$

By writing $\tilde{t} = t + i\delta t$, achieving a Taylor development and separating the real and the imaginary parts, we reach the same boundary conditions for both Burgers' equation and its derivative:

$$\begin{cases} u(0, x) = f_0(x), & \frac{\partial u}{\partial g}(0, x) = 0, \\ u(t, x_1) = f_1(t), & \frac{\partial u}{\partial g}(t, x_1) = f_1'(t), \\ u(t, x_2) = f_2'(x), & \frac{\partial u}{\partial g}(t, x_2) = f_2''(t). \end{cases}$$

The same agreement can be found if g is equal to x or any generic parameter on which u depends.

3.3.2 Flapping airfoil

The same principle may be applied to the problem of flapping airfoil. It has been shown (cf. §3.1.1) that the system of flow and sensitivity equations can be written

as:

$$\left\{ \begin{array}{l}
 \frac{\partial \omega}{\partial t} + \frac{1}{\sqrt{J}} \left[v_r \frac{\partial \omega}{\partial r} + \frac{v_\theta}{r} \frac{\partial \omega}{\partial \theta} \right] \\
 \frac{\partial^2 \psi}{\partial r^2} + \frac{1}{r} \frac{\partial \psi}{\partial r} + \frac{1}{r^2} \frac{\partial^2 \psi}{\partial \theta^2} \\
 \frac{\partial \omega_g}{\partial t} + \frac{1}{\sqrt{J}} \left[v_r \frac{\partial \omega_g}{\partial r} + \frac{\partial v_r}{\partial g} \frac{\partial \omega}{\partial r} + \frac{v_\theta}{r} \frac{\partial \omega_g}{\partial \theta} + \frac{1}{r} \frac{\partial v_\theta}{\partial g} \frac{\partial \omega_g}{\partial \theta} \right] \\
 \frac{\partial^2 \psi_g}{\partial r^2} + \frac{1}{r} \frac{\partial \psi_g}{\partial r} + \frac{1}{r^2} \frac{\partial^2 \psi_g}{\partial \theta^2}
 \end{array} \right. = \begin{array}{l}
 \frac{1}{ReJ} \left[\frac{\partial^2 \omega}{\partial r^2} + \frac{1}{r} \frac{\partial \omega}{\partial r} + \frac{1}{r^2} \frac{\partial^2 \omega}{\partial \theta^2} \right], \\
 -J\omega, \\
 \frac{1}{ReJ} \left[\frac{\partial^2 \omega_g}{\partial r^2} + \frac{1}{r} \frac{\partial \omega_g}{\partial r} + \frac{1}{r^2} \frac{\partial^2 \omega_g}{\partial \theta^2} \right], \\
 -J\omega_g,
 \end{array} \quad (3.11)$$

where

$$\left\{ \begin{array}{l}
 v_r = \frac{1}{\sqrt{J}} \left[\frac{1}{r} \frac{\partial \psi}{\partial \theta} - \left(\dot{h}(t) \sin(\alpha(t)) - \dot{\alpha}(t) Y \right) \left(\frac{\partial X}{\partial \xi} \cos \theta + \frac{\partial X}{\partial \chi} \sin \theta \right) \right. \\
 \qquad \qquad \qquad \left. - \left(\dot{h}(t) \cos(\alpha(t)) + \dot{\alpha}(t) X \right) \left(\frac{\partial Y}{\partial \xi} \cos \theta + \frac{\partial Y}{\partial \chi} \sin \theta \right) \right], \\
 v_\theta = \frac{1}{\sqrt{J}} \left[-\frac{\partial \psi}{\partial r} - \left(\dot{h}(t) \sin(\alpha(t)) - \dot{\alpha}(t) Y \right) \left(\frac{\partial X}{\partial \chi} \cos \theta - \frac{\partial X}{\partial \xi} \sin \theta \right) \right. \\
 \qquad \qquad \qquad \left. - \left(\dot{h}(t) \cos(\alpha(t)) + \dot{\alpha}(t) X \right) \left(\frac{\partial Y}{\partial \chi} \cos \theta - \frac{\partial Y}{\partial \xi} \sin \theta \right) \right],
 \end{array} \right.$$

and

$$\left\{ \begin{array}{l}
 \frac{\partial v_r}{\partial g} = \frac{1}{\sqrt{J}} \left[\frac{1}{r} \frac{\partial \psi_g}{\partial \theta} - \frac{\partial}{\partial g} \left(\dot{h}(t) \sin(\alpha(t)) - \dot{\alpha} Y \right) \left(\frac{\partial X}{\partial \xi} \cos \theta + \frac{\partial X}{\partial \chi} \sin \theta \right) \right. \\
 \qquad \qquad \qquad \left. - \frac{\partial}{\partial g} \left(\dot{h}(t) \cos(\alpha(t)) + \dot{\alpha} X \right) \left(\frac{\partial Y}{\partial \xi} \cos \theta + \frac{\partial Y}{\partial \chi} \sin \theta \right) \right], \\
 \frac{\partial v_\theta}{\partial g} = \frac{1}{\sqrt{J}} \left[-\frac{\partial \psi_g}{\partial r} - \frac{\partial}{\partial g} \left(\dot{h}(t) \sin(\alpha(t)) - \dot{\alpha} Y \right) \left(\frac{\partial X}{\partial \chi} \cos \theta - \frac{\partial X}{\partial \xi} \sin \theta \right) \right. \\
 \qquad \qquad \qquad \left. - \frac{\partial}{\partial g} \left(\dot{h}(t) \cos(\alpha(t)) + \dot{\alpha} X \right) \left(\frac{\partial Y}{\partial \chi} \cos \theta - \frac{\partial Y}{\partial \xi} \sin \theta \right) \right].
 \end{array} \right.$$

The application of the complex step derivative method to this problem, introducing the complex variables $\tilde{\omega}$ and $\tilde{\psi}$ yields the following complex system:

$$\begin{cases} \frac{\partial \tilde{\omega}}{\partial t} + \frac{1}{\sqrt{J}} \left[\tilde{v}_r \frac{\partial \tilde{\omega}}{\partial r} + \frac{\tilde{v}_\theta}{r} \frac{\partial \tilde{\omega}}{\partial \theta} \right] = \frac{1}{ReJ} \left[\frac{\partial^2 \tilde{\omega}}{\partial r^2} + \frac{1}{r} \frac{\partial \tilde{\omega}}{\partial r} + \frac{1}{r^2} \frac{\partial^2 \tilde{\omega}}{\partial \theta^2} \right], \\ \frac{\partial^2 \tilde{\psi}}{\partial r^2} + \frac{1}{r} \frac{\partial \tilde{\psi}}{\partial r} + \frac{1}{r^2} \frac{\partial^2 \tilde{\psi}}{\partial \theta^2} = -J\tilde{\omega}, \end{cases} \quad (3.12)$$

where

$$\begin{cases} \tilde{v}_r = \frac{1}{\sqrt{J}} \left[\frac{1}{r} \frac{\partial \tilde{\psi}}{\partial \theta} - \left(\dot{h}(t) \sin(\tilde{\alpha}(t)) - \dot{\alpha}Y \right) \left(\frac{\partial X}{\partial \xi} \cos \theta + \frac{\partial X}{\partial \chi} \sin \theta \right) \right] \\ \quad - \frac{1}{\sqrt{J}} \left[\left(\dot{h}(t) \cos(\tilde{\alpha}(t)) + \dot{\alpha}X \right) \left(\frac{\partial Y}{\partial \xi} \cos \theta + \frac{\partial Y}{\partial \chi} \sin \theta \right) \right], \\ \tilde{v}_\theta = \frac{1}{\sqrt{J}} \left[-\frac{\partial \tilde{\psi}}{\partial r} - \left(\dot{h}(t) \sin(\tilde{\alpha}(t)) - \dot{\alpha}Y \right) \left(\frac{\partial X}{\partial \chi} \cos \theta - \frac{\partial X}{\partial \xi} \sin \theta \right) \right] \\ \quad - \frac{1}{\sqrt{J}} \left[\left(\dot{h}(t) \cos(\tilde{\alpha}(t)) + \dot{\alpha}X \right) \left(\frac{\partial Y}{\partial \chi} \cos \theta - \frac{\partial Y}{\partial \xi} \sin \theta \right) \right]. \end{cases}$$

Now, all the complex variables are split into real and imaginary parts by writing:

$$\begin{cases} \tilde{\omega} = \omega + i\omega_g, & \tilde{\psi} = \psi + i\psi_g, \\ \tilde{v}_r = v_r + iv_{rg}, & \tilde{v}_\theta = v_\theta + iv_{\theta g}, \\ \tilde{h}(t) = h(t) + ih_g(t), & \tilde{\alpha}(t) = \alpha(t) + i\alpha_g(t) \end{cases}$$

so that we obtain the system:

$$\left\{ \begin{array}{l}
 \frac{\partial \omega}{\partial t} + \frac{1}{\sqrt{J}} \left[v_r \frac{\partial \omega}{\partial r} + \frac{v_\theta}{r} \frac{\partial \omega}{\partial \theta} - \underbrace{v_{rg} \frac{\partial \omega_g}{\partial r} - \frac{v_{\theta g}}{r} \frac{\partial \omega_g}{\partial \theta}} \right] = \frac{1}{ReJ} \left[\frac{\partial^2 \omega}{\partial r^2} + \frac{1}{r} \frac{\partial \omega}{\partial r} + \frac{1}{r^2} \frac{\partial^2 \omega}{\partial \theta^2} \right], \\
 \frac{\partial^2 \psi}{\partial r^2} + \frac{1}{r} \frac{\partial \psi}{\partial r} + \frac{1}{r^2} \frac{\partial^2 \psi}{\partial \theta^2} = -J\omega, \\
 \frac{\partial \omega_g}{\partial t} + \frac{1}{\sqrt{J}} \left[v_r \frac{\partial \omega_g}{\partial r} + \frac{v_\theta}{r} \frac{\partial \omega_g}{\partial \theta} + v_{rg} \frac{\partial \omega}{\partial r} + \frac{v_{\theta g}}{r} \frac{\partial \omega}{\partial \theta} \right] = \frac{1}{ReJ} \left[\frac{\partial^2 \omega_g}{\partial r^2} + \frac{1}{r} \frac{\partial \omega_g}{\partial r} + \frac{1}{r^2} \frac{\partial^2 \omega_g}{\partial \theta^2} \right], \\
 \frac{\partial^2 \psi_g}{\partial r^2} + \frac{1}{r} \frac{\partial \psi_g}{\partial r} + \frac{1}{r^2} \frac{\partial^2 \psi_g}{\partial \theta^2} = -J\omega_g.
 \end{array} \right. \quad (3.13)$$

As discussed for Burgers' equation, the underbraced terms $v_{rg} \frac{\partial \omega_g}{\partial r}$ and $\frac{v_{\theta g}}{r} \frac{\partial \omega_g}{\partial \theta}$ can be neglected because their order of magnitude is $O(\delta g^2)$. This leads to the same equations than flow equations in the system 3.11. Moreover, the terms v_{rg} and $v_{\theta g}$ correspond exactly to the terms $\frac{\partial v_r}{\partial g}$ and $\frac{\partial v_\theta}{\partial g}$ in the sensitivity equations. As a proof for the former statement, we consider, for instance, the case in which we are controlling the heaving amplitude. Under these conditions, and if we denote $\frac{\partial \dot{h}(t)}{\partial g}$ by $\dot{h}_g(t)$, we obtain:

$$\left\{ \begin{array}{l}
 \frac{\partial v_r}{\partial g} = \frac{1}{\sqrt{J}} \left[\frac{1}{r} \frac{\partial \psi_g}{\partial \theta} - \left(\dot{h}_g(t) \sin(\alpha(t)) \right) \left(\frac{\partial X}{\partial \xi} \cos \theta + \frac{\partial X}{\partial \chi} \sin \theta \right) \right] \\
 \quad - \frac{1}{\sqrt{J}} \left[\left(\dot{h}_g(t) \cos(\alpha(t)) \right) \left(\frac{\partial Y}{\partial \xi} \cos \theta + \frac{\partial Y}{\partial \chi} \sin \theta \right) \right], \\
 \frac{\partial v_\theta}{\partial g} = \frac{1}{\sqrt{J}} \left[-\frac{\partial \psi_g}{\partial r} - \left(\dot{h}_g(t) \sin(\alpha(t)) \right) \left(\frac{\partial X}{\partial \chi} \cos \theta - \frac{\partial X}{\partial \xi} \sin \theta \right) \right] \\
 \quad - \frac{1}{\sqrt{J}} \left[\left(\dot{h}_g(t) \cos(\alpha(t)) \right) \left(\frac{\partial Y}{\partial \chi} \cos \theta - \frac{\partial Y}{\partial \xi} \sin \theta \right) \right].
 \end{array} \right.$$

On the other hand,

$$\left\{ \begin{array}{l} \tilde{v}_r = \frac{1}{\sqrt{J}} \left[\frac{1}{r} \frac{\partial \tilde{\psi}}{\partial \theta} - \left(\dot{h}(t) \sin(\alpha(t)) - \dot{\alpha} Y \right) \left(\frac{\partial X}{\partial \xi} \cos \theta + \frac{\partial X}{\partial \chi} \sin \theta \right) \right] \\ \quad - \frac{1}{\sqrt{J}} \left[\left(\dot{h}(t) \cos(\alpha(t)) + \dot{\alpha} X \right) \left(\frac{\partial Y}{\partial \xi} \cos \theta + \frac{\partial Y}{\partial \chi} \sin \theta \right) \right], \\ \tilde{v}_\theta = \frac{1}{\sqrt{J}} \left[-\frac{\partial \tilde{\psi}}{\partial r} - \left(\dot{h}(t) \sin(\alpha(t)) - \dot{\alpha} Y \right) \left(\frac{\partial X}{\partial \chi} \cos \theta - \frac{\partial X}{\partial \xi} \sin \theta \right) \right] \\ \quad - \frac{1}{\sqrt{J}} \left[\left(\dot{h}(t) \cos(\alpha(t)) + \dot{\alpha} X \right) \left(\frac{\partial Y}{\partial \chi} \cos \theta - \frac{\partial Y}{\partial \xi} \sin \theta \right) \right], \end{array} \right. \quad (3.14)$$

and splitting into real and imaginary parts, we find a perfect equivalence since:

$$\left\{ \begin{array}{l} v_{rg} = \frac{1}{\sqrt{J}} \left[\frac{1}{r} \frac{\partial \psi_g}{\partial \theta} - \left(\dot{h}_g(t) \sin(\alpha(t)) \right) \left(\frac{\partial X}{\partial \xi} \cos \theta + \frac{\partial X}{\partial \chi} \sin \theta \right) \right] \\ \quad - \frac{1}{\sqrt{J}} \left[\left(\dot{h}_g(t) \cos(\alpha(t)) \right) \left(\frac{\partial Y}{\partial \xi} \cos \theta + \frac{\partial Y}{\partial \chi} \sin \theta \right) \right], \\ v_{\theta g} = \frac{1}{\sqrt{J}} \left[-\frac{\partial \psi_g}{\partial r} - \left(\dot{h}_g(t) \sin(\alpha(t)) \right) \left(\frac{\partial X}{\partial \chi} \cos \theta - \frac{\partial X}{\partial \xi} \sin \theta \right) \right] \\ \quad - \frac{1}{\sqrt{J}} \left[\left(\dot{h}_g(t) \cos(\alpha(t)) \right) \left(\frac{\partial Y}{\partial \chi} \cos \theta - \frac{\partial Y}{\partial \xi} \sin \theta \right) \right]. \end{array} \right.$$

The equivalence can be demonstrated for the other control parameters and for the boundary conditions in the same way it has been done for Burgers' equation. This explains the reason why gradients computed with both approaches, sensitivity and complex step methods, are identical. This fact is valid for "sufficiently" refined grids (see §4.1). The length of the computations is also very close for identical grids. Obviously, one system is solved in the complex method instead of two in the sensitivity technique, but this single system is complex and the dimension of the problems are the same. The main advantage of CSDM is its good accuracy for coarse grids. In this case, there can be a large difference between the gradients, and the complex step's gradient is closer to the converged value. In the remainder of this work, and since all results are done on refined grids, no distinction will be made between the results obtained with one method or the other.

Conclusions

The third component of an optimisation problem has been addressed. The computation of the gradients of the cost functional with respect to the control parameters has been accomplished with two different approaches. The first requires the solution of two real systems, the second of one complex system. Simulations have shown very close results for the two methods. Beyond the fact that the same quantity is computed in two different manners, a link between the sensitivity method and the complex step derivative method is brought to light by the decomposition of the complex system into a real and imaginary parts. Under this decomposition, the CSDM turns out to be a second-order approximation of the sensitivity system of equations. Having achieved presenting the tools needed to optimise the airfoil kinematics, we focus now on the numerical aspects and the validation of the solver.

Chapter 4

Numerical aspects

Introduction

Having established the motivations of the present study and the tools to accomplish the announced targets, attention shifts to the solver used. The usual topics arising in all numerical simulations are covered here, ranging from the adequacy of the grid, to the quality of the boundary conditions to the solver validation. The first point addresses the consistency of the numerical results by confirming converged results. The unsteady equations for the flapping airfoil are solved by means of an alternate direction implicit method. A large number of grids were built and employed to verify the independence of the results on the mesh. The use of valid and realistic boundary conditions ensures the elimination of numerical boundary errors which may influence the quality of the results. This is done *a posteriori* by the investigation of the flow fields. The validation of the solver is done by computing the gradient for various values of the parameters, and thus of the cost functional and verifying the coherence between the values of the cost functional and its gradient. Once the value of the gradients is confirmed for an iteration (solving the flow and the gradient equations), an update algorithm, based on a quasi-Newton method, is implemented to drive the control parameters towards their optimal values. The aim of this algorithm is to reach the optimal configuration for the smallest possible number of iterations and without additional relevant computations.

Moreover, the stability of the numerical simulation depends also on the kinematics of the airfoil. The cases of high levels of shed vorticity or of small time scales, due to the presence of motions of high frequencies, require smaller time steps.

4.1 On the grid adequacy

The grid choice is a fundamental and indispensable issue in every numerical simulation. The dilemma consists in finding a grid providing accurate results with acceptable computational time. Two main topics may be addressed: the number of discretization points and the way in which they are distributed.

As far as the distribution is concerned, a logarithmic law which stretches the points in the radial direction was adopted. In addition to r_0 , the radius of the circle obtained when the Joukowski transformation is applied to the airfoil, two radii should be chosen: R_{max} , the radius of the circular computational domain and R_{int} an intermediate radius within which half of the points in the radial direction are distributed (see figure 4.2). The refinement of points near the wall, i.e. in the boundary layer where large spatial gradients subsist, is done by writing $z = \ln(r + a)$ where

$$a = \frac{R_{int}^2 - R_{max}r_0}{R_{max} + r_0 - 2R_{int}}.$$

This choice of a ensures that the cell size near the wall is at least 10 times smaller than the thickness of the boundary layer approximated by the relations of Stokes and Blasius. This implies having at least 10 nodes inside the boundary layer. In practice, and despite the difficulty to identify properly a boundary layer thickness for a flapping airfoil configuration, the number of points inside this region was at least threefold the mentioned limit (see figure 4.7(a)). Obviously, different stretching laws are possible including hyperbolic refinements $z = \frac{C_1}{C_2 + C_3r^2}$ or $z = \frac{C_1r}{C_2 + C_3r^2}$ where C_1, C_2 and C_3 are adapted constants. However, these choices have not been investigated in the present work because the previously mentioned logarithmic law showed its ability to perform accurate computations with acceptable computational cost (Braza et al., 1986; Borthwick, 1986; Guglielmini and Blondeaux, 2004). The effect on the results of the distribution parameters, R_{max} and R_{int} was studied. On the other hand, and due to the symmetry of the problem in the azimuthal direction, a uniform distribution law has been employed in the θ -direction. Distributing the points along the radial direction of a circle ensures the orthogonality of the mesh on the airfoil surface (see figure 4.1) and this characteristic is usually considered as a positive quality for the grid.

Concerning the choice of the number of nodes and of the time step choices, Basic constraints such as $\Delta t \leq \frac{Re(\Delta z)^2}{4}$, $\Delta t \leq \frac{Re(\Delta \theta)^2}{4}$ and $\Delta t \leq \frac{2}{Re|V_{max}|^2}$ should be respected, where Δz is the spatial step in the radial direction (the radial step in terms of r is logarithmically variable whereas it is uniform in terms of z), $\Delta \theta$ is the

grid step in the azimuthal direction, Δt is the time step and $|V_{\max}|$ is the norm of the maximal velocity vector encountered within the computational domain. These constraints ensure that the particle of fluid will remain within the same cell during one time step (Braza, 1981). Despite being necessary, these conditions are not sufficient. In addition to being highly unsteady, the flow field of a flapping airfoil, depends on the kinematics of the airfoil. Configurations with high heaving amplitudes, for instance, favours intense vorticity shedding, whereas the case of a bad phase angle between heaving and pitching leads to a non-synchronisation of the shedding. Those are examples of cases where the constraints on the stability of computations are more severe. Therefore, a thorough investigation is required and a large number of grids is considered to study the effect of each parameter.

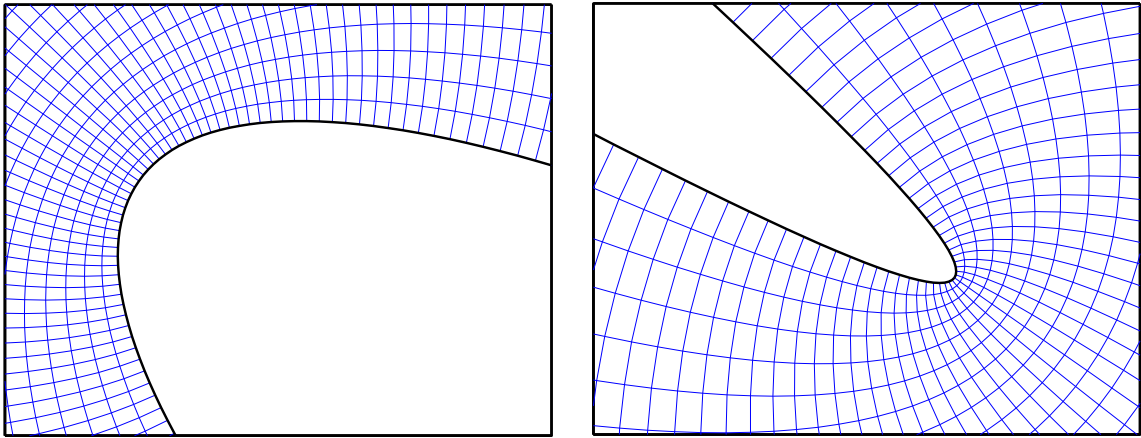


Figure 4.1: Plot of the mesh topology at the airfoil surface near the leading and trailing edges.

Accepting the logarithmic stretching, the mesh quality depends on five parameters already mentioned and summarized here:

- R_{max} , the circular radius corresponding to the size of the computational domain. The choice of this radius is a compromise between the will to limit the computational cost and to apply physically valid boundary conditions. The unsteady configuration studied here requires to push the numerical simulations beyond the time of flow establishment by at least one period of oscillation to compute the average quantities. In the meanwhile, the shed vorticity propagates towards R_{max} . Therefore, a large computational domain or good boundary conditions are needed.
- R_{int} , the parameter of the stretching law. Half the points in the radial direction are located between the airfoil and R_{int} and the other half between R_{int} and

R_{max} . The value of R_{int} is a compromise between an accurate resolution of the boundary layer and of the wake. As mentioned before, a large number of points should be in the close-wall region, and at the same time the shed vorticity propagates far in the wake and should be accurately computed (see figure 4.6). The choice of R_{int} influences these two aspects.

- N_r , the number of points in the radial direction, since

$$\Delta z = \frac{\ln(R_{max} + a) - \ln(r_0 + a)}{N_r - 1}.$$

The index on N_r is directed for increasing distance with respect to the airfoil, i.e. the value 1 of this index corresponds to the airfoil and the value N_r corresponds to the outflow boundary.

- N_θ , the number of points in the azimuthal direction with $\Delta\theta = \frac{2\pi}{N_\theta}$. A relation exists between the accuracy of computations, the computational cost and the number of radial and azimuthal points.
- N_T , the number of time steps in one period of oscillation, with $\Delta t = \frac{2\pi}{N_T}$. Here, 2π refers to the non-dimensional value of a period. The value of N_T is related to the stability of the computation since exceeding a given threshold on the time step, the simulation diverges. This parameter is highly affected by the kinematics of the airfoil.

A large number of grids were studied by modifying one single parameter from case to case. A representative set of grids tested is given in table 4.1. They are ordered by decreasing relative error of the gradient.

For the flapping configuration with $N = 1$, $\alpha_0 = 0$, $h_1 = 3 \sin(t)$, $\alpha = -35^\circ \sin(t + \frac{\pi}{2})$, $f_r = 0.3665$ and $Re_c = 1100$, the percentage of error of the thrust force and its gradient with respect to h_1 is plotted in figure 4.3. The relative error is with respect to the very refined grid # 20, considered as a reference case. We note that the number of points in θ -direction is always a power of two due to the subroutine chosen to perform the fast Fourier transformation. The choice of showing the error on the thrust is due to the fact that \bar{F} seems to be more dependent on the grid than power \bar{P} . A large number of grid refinement studies was carried out and in all of them, the maximal error on the power was smaller than errors on the thrust. On the other hand, and as mentioned in details in §4.3, the flow solver has been already validated, which means that the converged values of the thrust are considered correct.

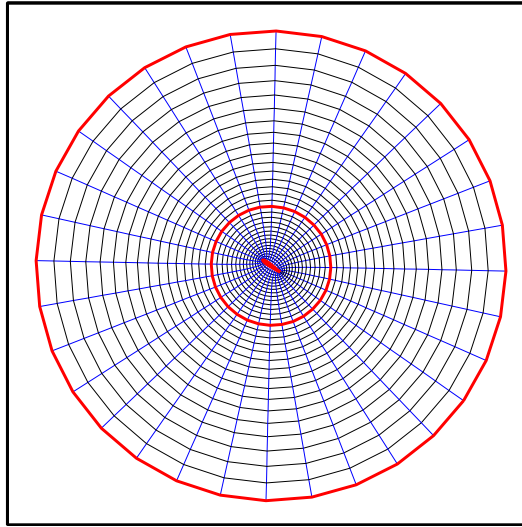


Figure 4.2: Plot of a coarse grid showing the position of R_{int} and R_{max} (red circles) and the associated distribution of points.

#	R_{max}	R_{int}	N_θ	N_r	N_T	#	R_{max}	R_{int}	N_θ	N_r	N_T
1	45	12	256	250	10^4	11	60	15	512	500	10^4
2	45	12	512	250	10^4	12	60	15	1024	500	10^4
3	70	20	512	500	10^4	13	70	20	1024	800	10^4
4	60	15	512	350	10^4	14	45	12	1024	500	10^4
5	30	10	512	300	10^4	15	45	12	512	500	$6 \cdot 10^3$
6	70	20	1024	600	10^4	16	45	12	512	500	10^4
7	45	15	512	500	10^4	17	45	12	512	500	$1.5 \cdot 10^4$
8	45	12	512	350	10^4	18	45	12	512	500	$2 \cdot 10^4$
9	70	20	1024	700	10^4	19	45	12	512	600	10^4
10	80	25	1024	1000	10^4	20	100	30	2048	2000	$2 \cdot 10^4$

Table 4.1: The grid parameters for a selection of the tested meshes.

A plot of examples of the distribution of points inside the computational domain is given in figure 4.4. As expected, the gradient, in figure 4.3, is more dependent on the grid choice than the direct variable but the grids which estimate the best \bar{F} (grids 11 and 12) are not the optimal for the gradient estimation (grid 19). The effect of a large computational domain can be highlighted by observing the bad ranking of grids 3, 6, 9 and 10. Even if these grids ensure valid boundary conditions (cf. §4.2), and despite a large number of points, they fail in providing a good approximation of $\frac{d\bar{F}}{dh_1}$. Comparing, for instance, grids 5 and 6 shows that considering a small R_{max} , and despite the larger constraints on the outflow boundary conditions, may yield a

much better accuracy-to-computational cost ratio. This demonstrates that efforts should be concentrated on small domains and realistic boundary conditions rather than large domains with heavy costs.

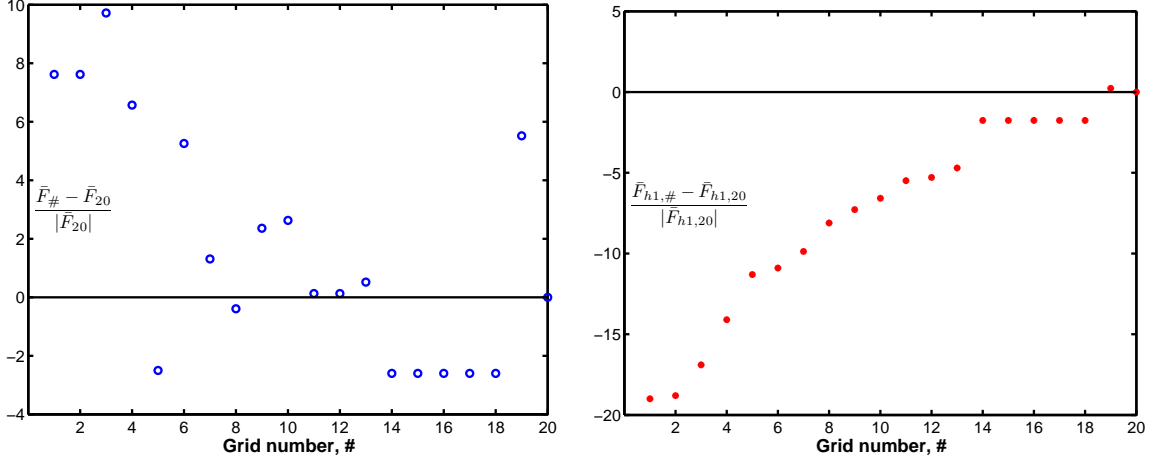


Figure 4.3: Effect of the grid choice on the relative error (in percentage) for thrust (left) and its gradient with respect to the heave amplitude (right) for the case $N = 1, \alpha_0 = 0^\circ, h_1 = 3, \tau_1 = 0^\circ, \alpha_1 = -35^\circ, \phi_1 = 90^\circ, f_r = 0.3665$ and $Re_c = 1100$.

The effect of R_{int} is observed by comparing grid 7 to grids 8 and 16. The more accurate estimation of the gradient with grid 8, despite a smaller number of points, proves that the good resolution of the boundary layer region is very important. This is even more clear by looking to the results of grids 7 and 16, which show that good solution of the boundary layer is preferable to good solution of the wake (see figure 4.4). Obviously, one may think that the quantity compared here is the thrust, directly related to the pressure on the airfoil, and this may justify the importance of the boundary layer with respect to the wake. This logic is misleading, because during the ascent phase of the flow (and gradient) solution, the step forward is done from the outflow towards the airfoil. Hence, the values inside the boundary layer are far from being independent from those in the wake. However, the comparison suggests that there is a bigger influence of the boundary layer and this implies putting enough points in this region, without exaggerating to prevent the need of a very small time step Δt .

The effect of the time step arises out of the comparison of grids 15, 16, 17 and 18. The main conclusion is that as long as the stability of the computation is ensured, considering a time step smaller than a given threshold, the value of the time step has no influence on the results. Clearly, for a time step larger than the threshold, the computations diverges, but within the threshold any value is acceptable.

However, the threshold depends on the kinematics of the airfoil. The cases of large heaving amplitudes, of small pitching amplitudes and of absence of phase angle between heaving and pitching require lower time step. A small Δt is also required when high order harmonics are considered ($N > 1$). This is the direct consequence of having higher frequencies in the motion of the airfoil and consequently the time scale of the flow field is reduced.

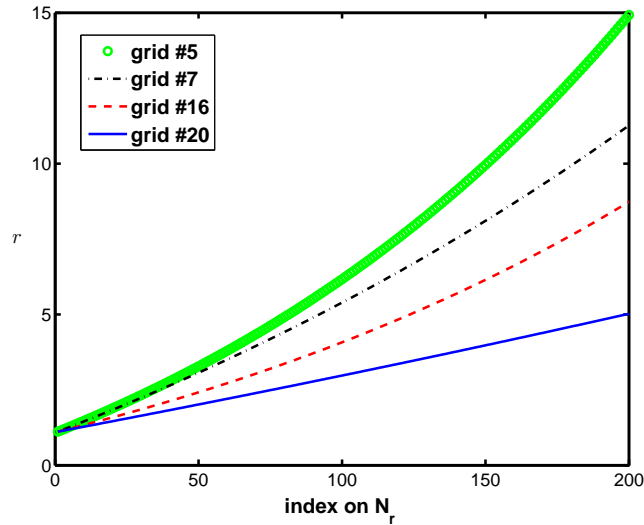


Figure 4.4: Distribution of the first 200 points in the radial direction for grids 5, 7, 16 and 20.

On the basis of the results above, grids 15-18 seem to give the best ratio of accuracy to cost. These grids yield also good results when the control of the other parameters is done and for different configurations. The estimation of power and thrust and their gradients with respect to h_1 , h_2 , α_1 and ϕ_1 in the case where $\alpha_0 = 0^\circ$, $h(t) = 2 \sin(t) + 0.5 \sin(2t)$ and $\alpha(t) = -25^\circ \sin(t + \frac{\pi}{2})$, $f_r = 0.3665$ and $Re_c = 1100$ has been performed for the twenty grids. For all these cases, grid 16 gave acceptable errors (within 5%) for the gradient and realistic flow fields. Finally, we note that for these grids no significant differences were observed between the sensitivity and the complex step derivative method. Differences may be observed for grids less refined than grid 1 and in this case, the complex step derivative method yielded smaller errors of roughly 15 %. In the remainder of this work, the grid 16 was adopted and time step was adapted to the kinematics of the airfoil. This corresponds roughly to consider a 0.25 million nodes distributed in a domain as big as 11 times the airfoil chord, with half of them within a 3 chord length distance, and to solve the flow and gradient equations 10000 times for every period of oscillations.

4.2 Boundary conditions validity

The relatively large errors observed on small grids and the desire to perform computations physically coherent with the flow and relatively free of numerical errors shifted our attention towards the boundary conditions. The question should particularly concern the outflow boundary conditions (cf. Appendix E.1). Before answering this issue, the duration of the simulations should be defined, since as long as the wake remains far away from the outflow boundary, the validity of the boundary conditions is obvious. Therefore, long-term simulations on grid 16 are performed, and the evolution of the instantaneous vertical force (lift) and its gradient with respect to h_1 are plotted in figure 4.5.

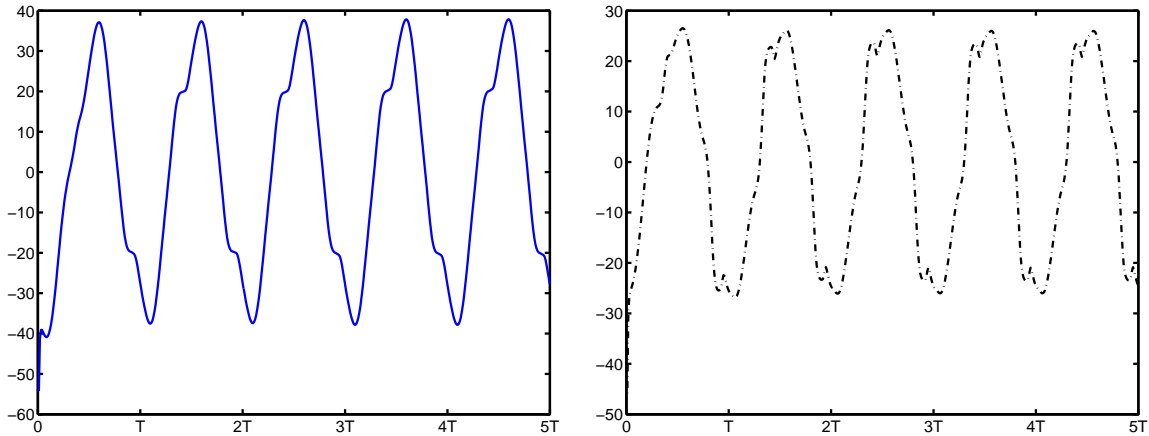


Figure 4.5: Evolution of the instantaneous lift force (left) and its gradient (right) with respect to the heave amplitude h_1 for the configuration $N = 1, \alpha_0 = 0^\circ, h_1 = 3, \tau_1 = 0^\circ, \alpha_1 = -35^\circ, \phi_1 = 90^\circ, f_r = 0.3665$ and $Re_c = 1100$.

The temporal evolution of various quantities for different configurations (including large oscillations and high order harmonics) showed that the initial transient lasts one period of oscillation since results are perfectly periodic starting from the second period of oscillations. Hence, in the remainder of the present work, numerical simulations are carried out for two periods and the mean quantities are averaged on the second one. An exception to this rule is done in §5.6 where very large angles of attack are considered leading to highly unsteady flows, which establish slowly.

The original question can be addressed now: "How valid the boundary conditions are for $t = 4\pi$?" and the answer depends on the grid selection and the choice of the boundary conditions. We consider the small grid # 5 and the intermediate grid #

16. The vorticity fields, for these grids, are plotted at the moment where the first shed vortices reach the outflow boundary (see figure 4.6). This occurs for roughly $t = 12$ for grid 5 and roughly $t = 18$ for grid 16. We note that this value is within the simulation duration for the small grid on one hand, and that it corresponds to the same ratio $\frac{R_{max}}{t} = 2.5 = 0.9U_0$ since $U_0 = \frac{1}{f_r} = 2.73$, on the other. This yields an estimation of the forward velocity of propagation of the shed vorticity in the wake.

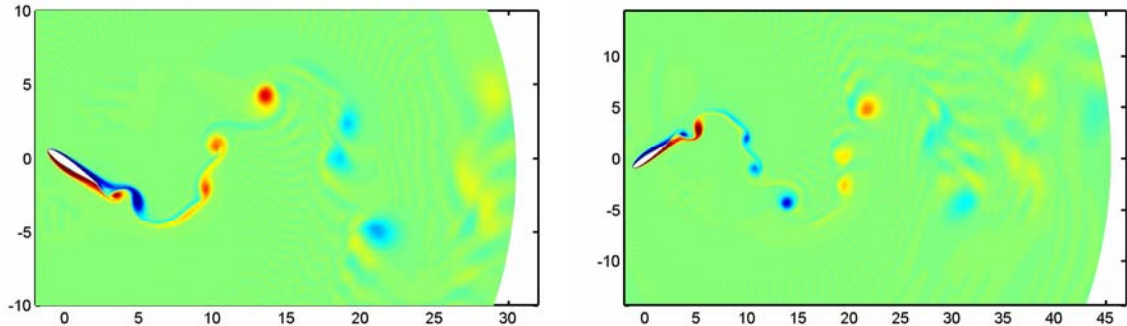


Figure 4.6: Propagation of the shed vorticity in the wake towards the limit of the computational domain for grid 5 at $t = 12$ (left) and grid 16 at $t = 18$ (right) for the configuration $N = 1, \alpha_0 = 0^\circ, h_1 = 3, \tau_1 = 0^\circ, \alpha_1 = -35^\circ, \phi_1 = 90^\circ, f_r = 0.3665$ and $Re_c = 1100$.

For the small grid # 5, the condition $\left(\frac{\partial\omega}{\partial r}\right)_{outflow} = 0$ is satisfied, even if it is not perfectly respected, since near the outflow boundary the vorticity tends to a constant level, close to a vanishing value (see figure 4.8(a)). On the other hand, the condition of undisturbed velocity equal to free stream velocity is far from being satisfied. In figure 4.7(a), the horizontal velocity is plotted in the whole computational domain at $t = 2T$ for grid 5. Furthermore, 4 angles are chosen and the horizontal velocities are plotted for these angles in figure 4.8(b).

For the angles $\theta = 70^\circ$ and $\theta = 145^\circ$, the flow is not perturbed by the airfoil flapping and the boundary condition is valid. However, for $\theta = 5^\circ$, the velocity profile is submitted to a steep down-shoot near the outflow boundary in order to reach the value of U_0 imposed in $r = R_{max}$. This kind of discontinuity affects the validity of the solution qualitatively in terms of flow fields and quantitatively in terms of aerodynamic coefficients. To avoid this behaviour, the size of the computational domain should be increased, paying the price of increased computational costs, or better boundary conditions, such as convective conditions should be adopted (cf. §2.3).

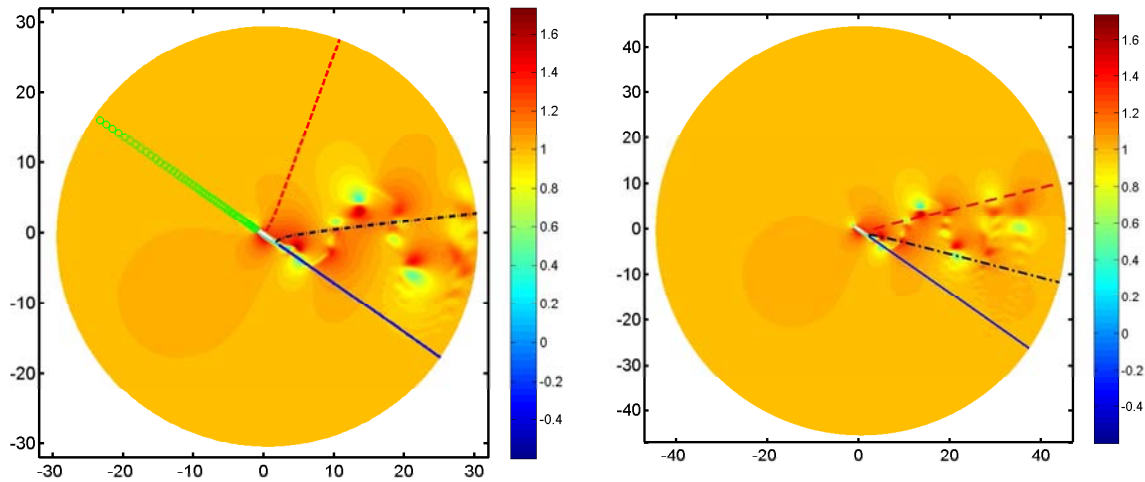


Figure 4.7: The horizontal velocity field for grid #5 (left) and grid #16 (right) and the radii along which vorticity and velocity are plotted in figures 4.8 and 4.9, at $t = 4\pi$ for $N = 1$, $\alpha_0 = 0^\circ$, $h_1 = 3$, $\tau_1 = 0^\circ$, $\alpha_1 = -35^\circ$, $\phi_1 = 90^\circ$, $f_r = 0.3665$ and $Re_c = 1100$. The colour scale is for $\frac{u}{U_0}$. Angles are given with respect to the horizontal axis at $y = 0$.

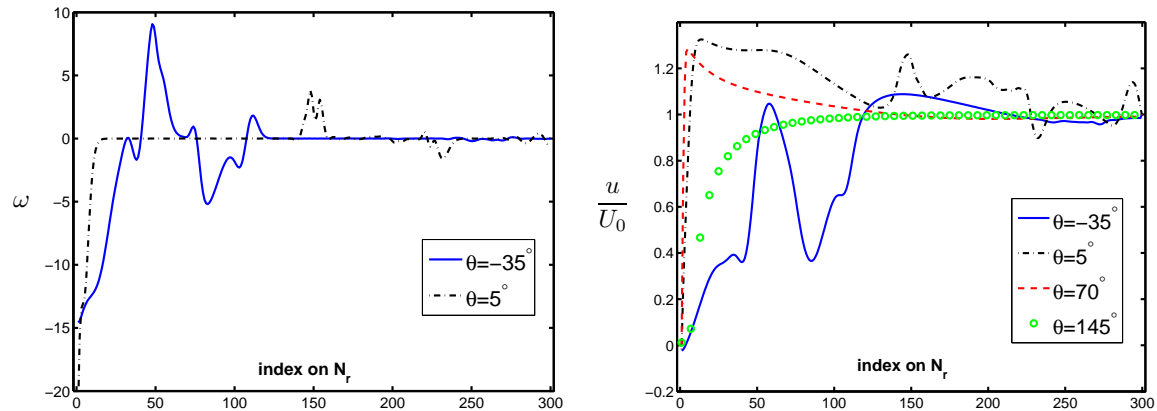


Figure 4.8: Validity of the boundary condition on ω (left) and on ψ (right) for grid #5 at $t = 4\pi$ for $N = 1$, $\alpha_0 = 0^\circ$, $h_1 = 3$, $\tau_1 = 0^\circ$, $\alpha_1 = -35^\circ$, $\phi_1 = 90^\circ$, $f_r = 0.3665$ and $Re_c = 1100$. The minimal and maximal values of the index on N_r correspond to the airfoil and the outflow boundary, respectively.

Therefore, the same principle was applied to grid # 16. In figure 4.7(b), the horizontal velocity was plotted for the whole domain for the same configuration than figure 4.7(a) and at the same instant $t = 4\pi$. Beyond the visual observation of a

less significant influence of the outflow boundary condition, the plot of vorticity and horizontal velocity along three angles shows a much better validity of the imposed boundary conditions, including for the most unfavourable angle $\theta = 13^\circ$. This may be an explanation of the smaller errors obtained with grids 15-18, and proves that the large errors of grids 3, 6, 9 and 10 is mainly due to a bad resolution of the boundary layer and that more points should be used there.

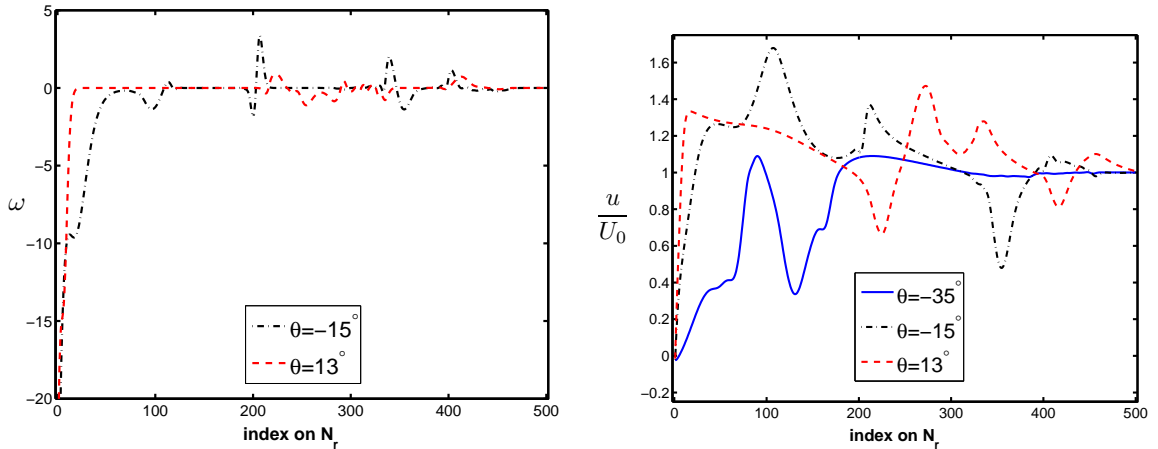


Figure 4.9: Validity of the boundary condition on ω (left) and on ψ (right) for grid #16 at $t = 4\pi$ for $N = 1, \alpha_0 = 0^\circ, h_1 = 3, \tau_1 = 0^\circ, \alpha_1 = -35^\circ, \phi_1 = 90^\circ, f_r = 0.3665$ and $Re_c = 1100$. The minimal and maximal values of the index on N_r correspond to the airfoil and the outflow boundary, respectively.

The other way to avoid this problem is by imposing more realistic boundary condition in $r = R_{max}$, i.e. a convective condition:

$$\frac{\partial \omega}{\partial t} + 0.9U_0 \frac{\partial \psi}{\partial r} = 0, \quad \frac{\partial \psi}{\partial t} + 0.9U_0 \frac{\partial \omega}{\partial r} = 0,$$

which requires a modification of the Thomas algorithm. The velocity of advection of the flow structures has been chosen equal to $0.9U_0$. Different choices modify only slightly the fields in the vicinity of R_{max} .

4.3 Solver validation

The flow solver has been validated by Guglielmini (2004) by comparison to the experimental results for a fixed airfoil by Guermond and Quartapelle (1997) and for a flapping foil by Anderson et al. (1998) and Wang (2000). The comparison

concerned mainly the flow fields, and also the aerodynamic coefficients agreed for similar Reynolds numbers configurations. Further validations of the flow solver has been done in the present work by comparison with numerical results from commercial CFD tools as discussed in §5.6. Here, the validation of the gradient computation was deeply studied. The principle of the validation is simple: assuming the flow results valid, the value of the cost function is accurate. Considering the control parameters one by one and by modifying each of them separately, the minimum of the cost functional is found and the condition of vanishing gradient is verified. Moreover, having the value of the cost functional for different values of the parameter, a gradient may be estimated by simple finite difference approximation.

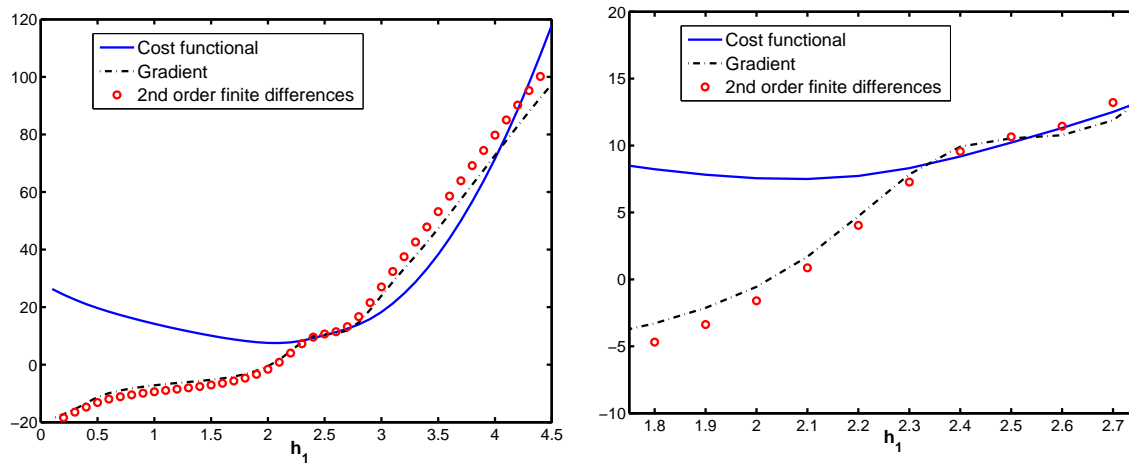


Figure 4.10: Plot of the cost functional and its gradient with respect to h_1 computed with the present solver and compared to the approximated second order finite differences gradient (left) and zoom near the optimal values (right) for $N = 1$, $\alpha_0 = 0^\circ$, $\tau_1 = 0^\circ$, $\alpha_1 = -25^\circ$, $\phi_1 = 90^\circ$, $f_r = 0.3665$ and $Re_c = 1100$.

The solvers validity is tested for the cost functional \mathcal{L} defined as:

$$\mathcal{L} = \bar{P} + 2\bar{F}U_0 + 15.14\bar{\alpha}^2 + \bar{h}^2(t)$$

The choice of the weight for $\bar{\alpha}^2$ is related to the desire to give equivalent importance to the terms of the control cost. The validity of the solver which computes the gradient with respect to h_1 can be analysed on figure 4.10. A very good agreement exists especially near the optimal value (coinciding with a vanishing gradient), which is the region of interest for the optimisation problem. Some discrepancies between the gradient computed with the sensitivity or complex step techniques on the one hand, and those approximated with finite differences method on the other, exist

for large heaving amplitudes. These discrepancies seem more related to the mesh quality rather than to the solver validity. Configurations with heaving amplitudes larger than the chord length require smaller time step and eventually more refined grids. Furthermore, the value of the gradient and even the optimal value of h_1 are not sought with 8 or 16 digits. A very accurate computation of the gradient is not a real issue. The importance is mostly on the sign of the gradient and its vanishing. Therefore, methods where incomplete gradients are computed flourished in the last decade (Mohammadi and Pironneau, 2004). In these methods, the terms of the gradient with high computational cost and small effect on the value of the gradient are purely neglected, leading to approximate value of the gradient, with the exact sign though. Hence, the small discrepancies observed here can be accepted.

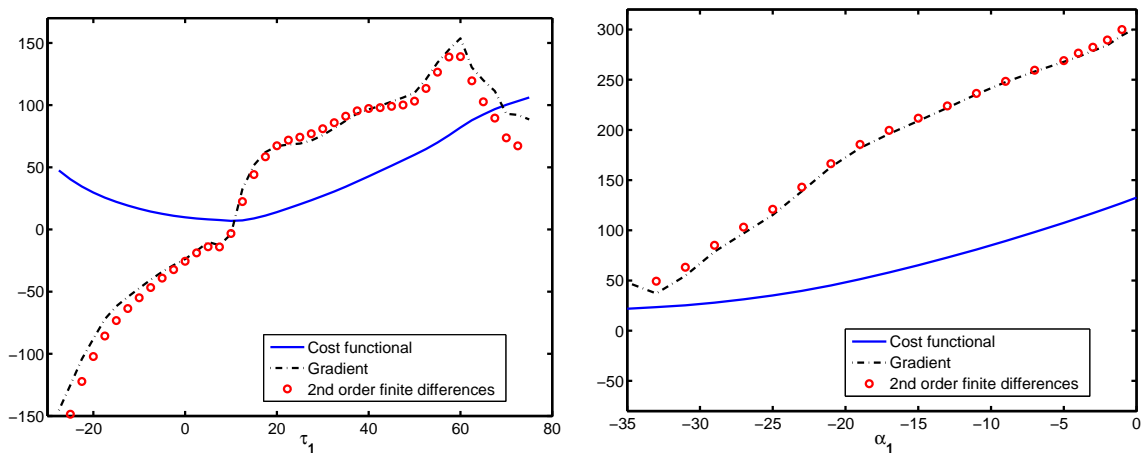


Figure 4.11: Plot of the cost functional and its gradient computed with the present solver and compared to the approximated second order finite differences gradient with respect to τ_1 for $N = 1$, $\alpha_0 = 0^\circ$, $h_1 = 3$, $\alpha_1 = -40^\circ$, $\phi_1 = 90^\circ$, $f_r = 0.3665$, and $Re_c = 1100$ (left) and with respect to α_1 for $N = 1$, $\alpha_0 = 8^\circ$, $h_1 = 3$, $\phi_1 = 90^\circ$, $f_r = 0.3665$, and $Re_c = 1100$ (right).

The same methodology is applied for the other parameters. In figure 4.11(a), the phase angle τ_1 is controlled whereas an example of the control of α_1 is shown in figure 4.11(b). Despite the absence of minimum in the range studied in this latter case, a very good agreement between the two methods of evaluation of the gradient persists. This agreement is rather interesting since the considered configuration has a non vanishing mean angle of attack α_0 which renders the flow harder to simulate. The condition of vanishing gradient is respected for the control of τ_1 in figure 4.11(a), validating the solver. Moreover, theoretical and evaluated gradients coincides except for the region of large τ_1 . Flows with very large τ_1 are also, from the numerical point of view, more unstable. They require a smaller time step like in the case of large

heaving amplitudes.

The numerical problems occurring for large τ_1 are found also for small phase angle ϕ_1 when this latter is controlled (see figure 4.12). The reason is related to the fact that in the case $N = 1$, one angle τ_1 or ϕ_1 is enough to model the phase angle between heaving and pitching. From the mathematical point of view, this corresponds to a change of variables since we can move from:

$$\begin{aligned} h(t) &= h_1 \sin(t) & \text{to} & & h(t) &= h_1 \sin(t + \tau_1) \\ \alpha(t) &= \alpha_1 \sin(t + \phi_1) & & & \alpha(t) &= \alpha_1 \sin(t + \frac{\pi}{2}) \end{aligned}$$

by introducing $t' + \frac{\pi}{2} = t + \phi_1$, which implies that $\tau_{1opt} = \frac{\pi}{2} - \phi_{1opt}$. This relation is verified when comparing figures 4.11(a) and 4.12(a) despite a slightly different pitching amplitude for the two cases. Obviously, in the case of $N = 1$, the gradient with respect to τ_1 solver is not indispensable, although it has been written and validated, in the present section, and will be useful for the high order harmonics configurations. The discrepancies subsist when a mean angle of attack is included (figure 4.12(b)). However, in all the cases presented here for the phase angle control, the gradient is perfectly evaluated in the optimal region and the condition of vanishing is fulfilled validating the solvers.

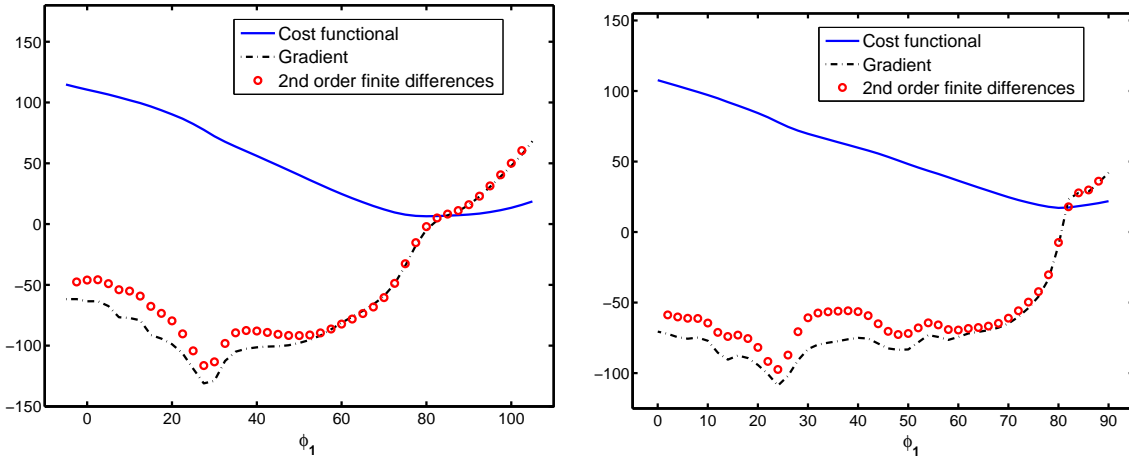


Figure 4.12: Plot of the cost functional and its gradient with respect to ϕ_1 computed with the present solver and compared to the approximated second order finite differences gradient for $N = 1, h_1 = 3, \tau_1 = 0^\circ, \alpha_1 = -35^\circ, f_r = 0.3665, Re_c = 1100$ and $\alpha_0 = 0^\circ$ (left) and $\alpha_0 = 8^\circ$ (right).

4.4 Optimisation update

Once the gradient is evaluated for a given value of the control parameter, the normal question to address is: "how to use the value of the gradient to update the control parameter towards its optimal value?". A large number of methods exist in literature to handle this problem. The idea is to limit the number of iterations before reaching the optimal value. However, the computational cost of this update method must not exceed what it is spared by limiting the number of iterations. For the flapping airfoil problem considered here, and in the case in which one parameter is controlled, an iteration consists in the computation of the flow and sensitivity equations (or the complex system). We want to reach the optimal parameter performing this iteration as few times as possible.

The conjugate gradient is one of the most popular and efficient methods. However, it is suitable for quadratic cost functional and this kind of functional is not adopted here to account for the sign of the vertical force favouring configurations dominantly producing thrust. A different version of the gradient conjugate (Polak-Ribière method) adapted for non quadratic functionals exists but the computational cost of this method is judged too heavy so as to counterbalance the benefit of the reduction in the number of iterations. Therefore, two simpler update algorithms are considered here:

- The steepest descent method: $g^{(n+1)} = g^{(n)} - s_d \nabla \mathcal{L}_g^{(n)}$ where s_d is a positive relaxation parameter which can be optimised by further sub-iterations or simply kept constant. The principle of this method is to perform a small variation of the parameter when the gradient is small, i.e. when a relative optimum is being reached. An example of the application of this method to flapping foil optimisation with an optimal step can be found in Tuncer and Kaya (2005).
- The quasi-Newton algorithm: $g^{(n+1)} = g^{(n)} - \frac{g^{(n)} - g^{(n-1)}}{\nabla \mathcal{L}_g^{(n)} - \nabla \mathcal{L}_g^{(n-1)}} \nabla \mathcal{L}_g^{(n)}$. In this case, a first order finite difference approximation of the second derivative is used to enrich the search of the optimal direction of update. The denomination "quasi" refers to the fact that the second derivative is approximated rather than computed (Newton update algorithm) avoiding relevant supplementary computations.

The negative signs in the expressions above ensure that a minimum of the functional is being pursued. These algorithms present the advantage of not requiring any further computations than those needed to compute the gradient (unless if the relaxation parameter s_d is optimised, alternatively, it is possible to use a small constant step,

albeit with considerable increase of the number of iterations). Therefore, the quasi-Newton method turns to be more efficient, because there is no relaxation parameter to optimise. It cannot be applied starting from the first iteration because it requires the value of the gradients for two values of the control parameter before indicating the optimal direction. To overcome this minor difficulty, the steepest descent may be adopted for the first iteration, or a constant step of the control parameter can be done between the first two iterations.

An illustration of what precedes is given by optimising, with respect to h_1 , the functional:

$$\mathcal{L} = \bar{P} + \bar{F} + \bar{\alpha}^2(t) + \bar{h}^2(t);$$

We consider the case $N = 1, h_1^{(0)} = 4.25, \alpha_0 = \tau_1 = 0^\circ, \alpha_1 = -25^\circ, \phi_1 = 90^\circ$. For the steepest descent method, the update algorithm employs a constant relaxation step $s_d = 0.01$, whereas for the quasi-Newton method we use:

$$\begin{cases} g^{(1)} = g^{(0)} - 0.25 \text{sign}(\nabla \mathcal{L}_g^{(0)}), \\ g^{(n+1)} = g^{(n)} - \frac{g^{(n)} - g^{(n-1)}}{\nabla \mathcal{L}_g^{(n)} - \nabla \mathcal{L}_g^{(n-1)}} \nabla g^{(n)}, \end{cases} \quad \text{for } n \geq 1.$$

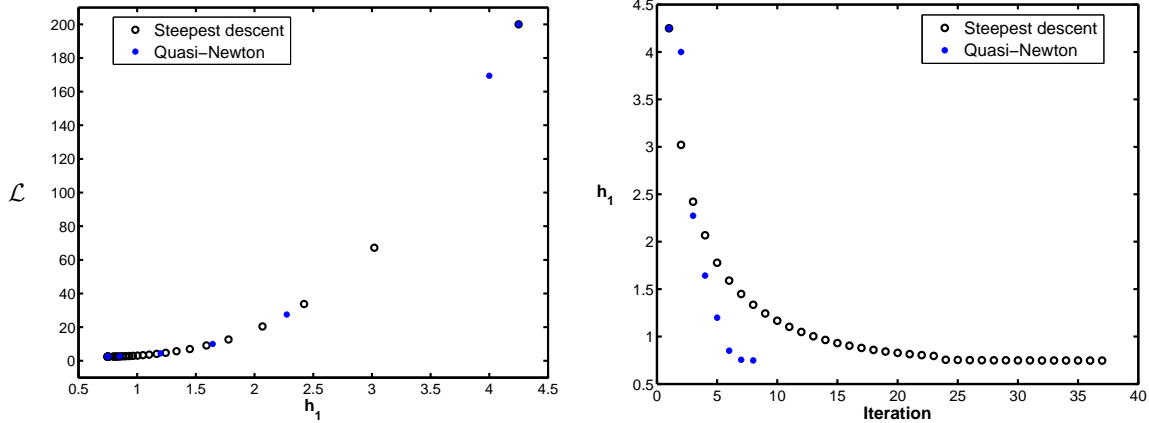


Figure 4.13: Comparison of the cost function evolution (left) and the number of iterations (right) between the steepest descent and quasi-Newton algorithms for control parameter update finite differences gradient for $N = 1, \alpha_0 = 0^\circ, \tau_1 = 0^\circ, \alpha_1 = -25^\circ, \phi_1 = 90^\circ, f_r = 0.3665$ and $Re_c = 1100$.

This implies that $h_1^{(1)} = h_1^{(0)} \pm 0.25$ according to the sign of $\nabla \mathcal{L}_g^{(0)}$. Otherwise, the steepest descent method may be used for this first iteration update. The same minimum for $h_1 = 0.748$ ($St = 0.087$) is reached after 8 iterations with the quasi-Newton

methods versus 37 iterations for the steepest descent method (figure 4.13). This discrepancy in performance could be reduced through a better choice of the constant update step s_d or thanks to sub-iterations optimising it but the speed of the quasi-Newton method is such that it has been the method of choice for all further calculations. The choice of this form of \mathcal{L} was done to highlight the importance of the cost functional and the weights. The optimal solution found here corresponds to a dominantly drag producing airfoil, whereas multiplying \bar{F} by U_0 and adapting the weights, leads to an optimum with $h_1 = 2.03$ (cf. figure 4.10(b)) and a thrust producing flapping airfoil consequently.

Conclusion

The choice of an adequate grid is made by building a 0.256 million nodes mesh distributed in a circular computational domain of a radius equal to 11 chord lengths. This grid, with an adapted time step, related to the kinematics of the airfoil, ensures accurate results and accurate treatment of the boundary conditions for the duration of the simulation, typically two periods of oscillations.

The gradient solver has been validated and a quasi-Newton descent algorithm is selected to update the control parameter. Hence, the algorithm of optimisation consists in:

- 1- Impose initial values for the control parameters.
- 2- For two periods of oscillations, solve the flow equations at each temporal step.
- 3- Solve the gradient equation for the same temporal step, using the results of the flow solution.
- 4- Compute the average quantities including the cost functional and its gradient.
- 5- When the gradient vanishes, the parameter is optimal; otherwise, use the value of the gradient to update the control parameter and continue iterating.

Now that the grid is chosen, the solver validated, the update method approved and the algorithm of optimisation defined, we move to the exploitation of the solver for the optimisation of the flapping airfoil kinematics in chapter 5.

Chapter 5

Kinematics optimisation

Introduction

After writing the equations allowing to solve the flow and estimate the gradient of the cost functional with respect to the control parameters, after choosing the grids which ensure good accuracy-to-computational cost yielding physically valid results and after validating the solvers, attention now turns towards the optimisation of the kinematics of the flapping airfoil.

The final target being to answer which motion the airfoil should adopt, first of all, the mechanism by which it produces lift and thrust should be addressed. This requires to determine the critical Strouhal number beyond which the von Karman street is inverted and the airfoil stops receiving energy from the flow and starts producing thrust. Afterwards, the effect of each control parameter is studied. First, focus is on the amplitudes and the phase angles of monochromatic oscillations for non-lifting configurations. The reason is due to the higher propulsive efficiency achievable under these conditions and the possibility to apply the results to fish-like locomotion. The term *flapping foil* will be used for statements common for airfoils and hydrofoils. Then, the mean angle of attack is investigated to ensure a sufficient lift force. Subsequently, the optimal configurations, by acting on all the variables of the kinematics simultaneously, is sought for various cost functionals. The choice of the functionals covers the possible missions the vehicle should fulfil, ranging from high propulsive efficiency with sufficient lift and thrust forces to high thrust generation. The optimal kinematics are linked to natural observations on the one hand (Triantafyllou et al., 1993; Taylor et al., 2003; Bejan and Marden, 2006) and to the results obtained numerically and experimentally by varying the parameters over given ranges (Anderson, 1996; Lewin and Haj-Hariri, 2003; Pedro et al., 2003; Guglielmini, 2004).

The decrease of the propulsive efficiency η for high thrust forces is recovered by including and optimising higher harmonics of the kinematics. In total, five harmonics are considered and the optimisation is done over the odd ones to ensure better efficiency for high thrust coefficient C_T than in the case characterised by monochromatic oscillations. The influence of the other parameters (the Reynolds number and the reduced frequency) is studied to understand the relatively low optimal values for η obtained in the present study. Finally, a simple gliding configuration is analysed, showing no increase of the global efficiency. This may imply that the main reason for gliding is to relax the muscles of the birds; however, more investigations onto gliding are called for.

5.1 Thrust and lift generation

For adequate kinematics, a flapping airfoil is able to produce both thrust and lift forces. This is a main difference with respect to the fixed airfoil case, where lift is generated over the wing and thrust is due to the motor. Here, the motor (electric DC device) produces the motion of the wing, which generates lift and thrust. However, as for fixed airfoils, both forces are influenced by the effects of pressure and viscosity. The thrust generation is due to the momentum injected in the flow resulting from the acceleration of the fluid around the airfoil, whereas lift is a consequence of a different pressure distribution between the upper side (suction side) and the lower side (pressure side) of the airfoil. The symmetry of the motion during upstroke and downstroke renders double the frequency of the thrust signal. In figure 5.1, the heaving and the pitching position, for a configuration with $\alpha_0 = 0^\circ$, and the associated forces and moment acting on the airfoil are plotted. The instantaneous values of forces and moment correspond to the integral of the pressure distribution and the viscous effects over the whole airfoil. We note that the positive lift force corresponds to the period where $h(t)$ decreases (downstroke) associated with a positive pitching angle.

When a vanishing mean angle of attack is considered, there is no difference between the forces in the laboratory frame (x, y) and the aerodynamic frame (x_α, y_α) and the average lift force vanishes over a period. During the upstroke, a high pressure zone is observed on the suction side of the airfoil and inversely a low pressure zone is created on the pressure side of the airfoil leading to a negative lift force. During the downstroke, the mechanism is inverted and an equivalent positive lift force is generated compensating the previous one. When an angle α_0 is included, the symmetry is broken, like for thrust, and the average value of the vertical force yields a net positive lift. The symmetry of the lift force when $\alpha_0 = 0^\circ$, due to the symmetry of the motion and of the airfoil, may be also observed by looking at the

pressure coefficient. In figure 5.2(a), the pressure coefficient is plotted for three instants during the upstroke. The C_{pr} curve is equivalent during the downstroke, with inverted values for the suction side and the pressure side. As it can be seen in figure 5.1(b), the lift force is negative for $t \in [2\pi, 2.5\pi]$ (corresponding to $\frac{t}{T} \in [0, 0.25]$). Therefore, and despite the upward direction of the vertical axis in figure 5.2(a), the plot is done in the classical way, with the suction side above the pressure side. On the other hand, the lift force can be plotted versus the pitching angle as in figure 5.2(b). In this configuration, the viscous effects are negligible for both thrust and lift.

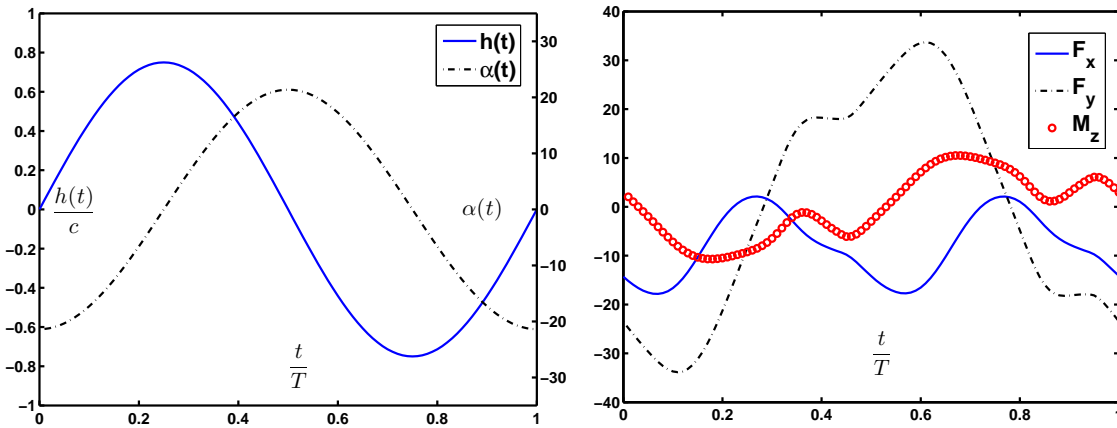


Figure 5.1: Temporal evolution of the heave distance and the pitch angle and the associated forces and torque acting on the airfoil for $N = 1, \alpha_0 = 0^\circ, h_1 = 3, \tau_1 = 0^\circ, \alpha_1 = -35^\circ, \phi_1 = 90^\circ, f_r = 0.3665$ and $Re_c = 1100$.

The thrust for a flapping airfoil is produced with a similar mechanism than that described for pure heaving in §1.3.1. During the downstroke, a clockwise rotating vortex is generated at the leading-edge and it is paired with a counterclockwise rotating vortex shed from the trailing-edge. The position of this pair of vortices in the wake is such that a jet-like velocity is induced downstream.

A plot of the stream function at $t = 2.25\pi$ in figure 5.3(a) shows a flow separation over a large percentage of the suction side of the airfoil. This is coherent with the plateau of the pressure coefficient observed in figure 5.2(a). On the other hand, the vorticity field at $t = 2.5\pi$ in figure 5.3(b) suggests that the bump in the pressure coefficient near the trailing-edge is related to the presence of a counterclockwise rotating vortex at the pressure side of the airfoil. In the remainder of this chapter, vorticity field will be used to illustrate the topology of the wake, whereas the stream

function and the horizontal velocity fields will interfere in the investigation of flow separation.

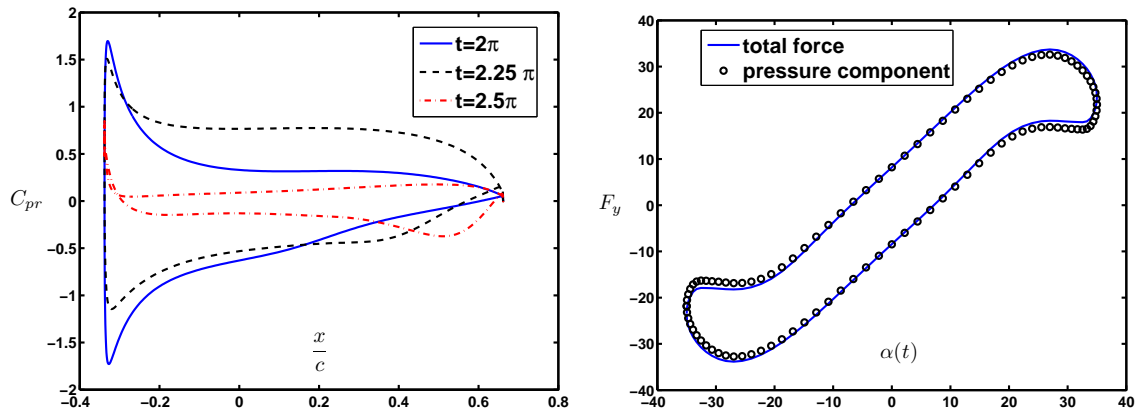


Figure 5.2: Pressure coefficient for a non-lifting configuration during the upstroke (left) and average lift total force and pressure component versus the pitching angle (right) for $N = 1, \alpha_0 = 0^\circ, h_1 = 3, \tau_1 = 0^\circ, \alpha_1 = -35^\circ, \phi_1 = 90^\circ, f_r = 0.3665$ and $Re_c = 1100$.

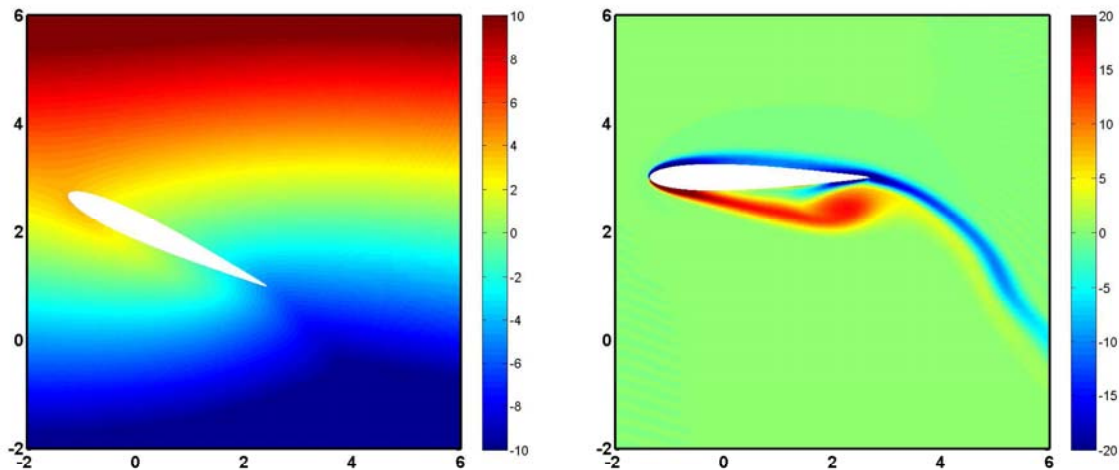


Figure 5.3: Stream function at $t = 2.25\pi$ (left) and vorticity at $t = 2.5\pi$ (right) fields for a flapping airfoil with $N = 1, \alpha_0 = 0^\circ, h_1 = 3, \tau_1 = 0^\circ, \alpha_1 = -35^\circ, \phi_1 = 90^\circ, f_r = 0.3665$ and $Re_c = 1100$.

For a vanishing mean angle of attack and for a Reynolds number equal to 1100, the drag coefficient of the airfoil used here is $C_D = -C_T = 0.12$ and it increases for

increasing mean angle of attack. This value is considered as a reference value for thrust generation. Therefore, values of C_T in the range $[0, 0.25]$ will be considered as small thrust forces, whereas thrust coefficients exceeding 1 will be referred to as large thrust forces.

5.2 Sensitivity fields

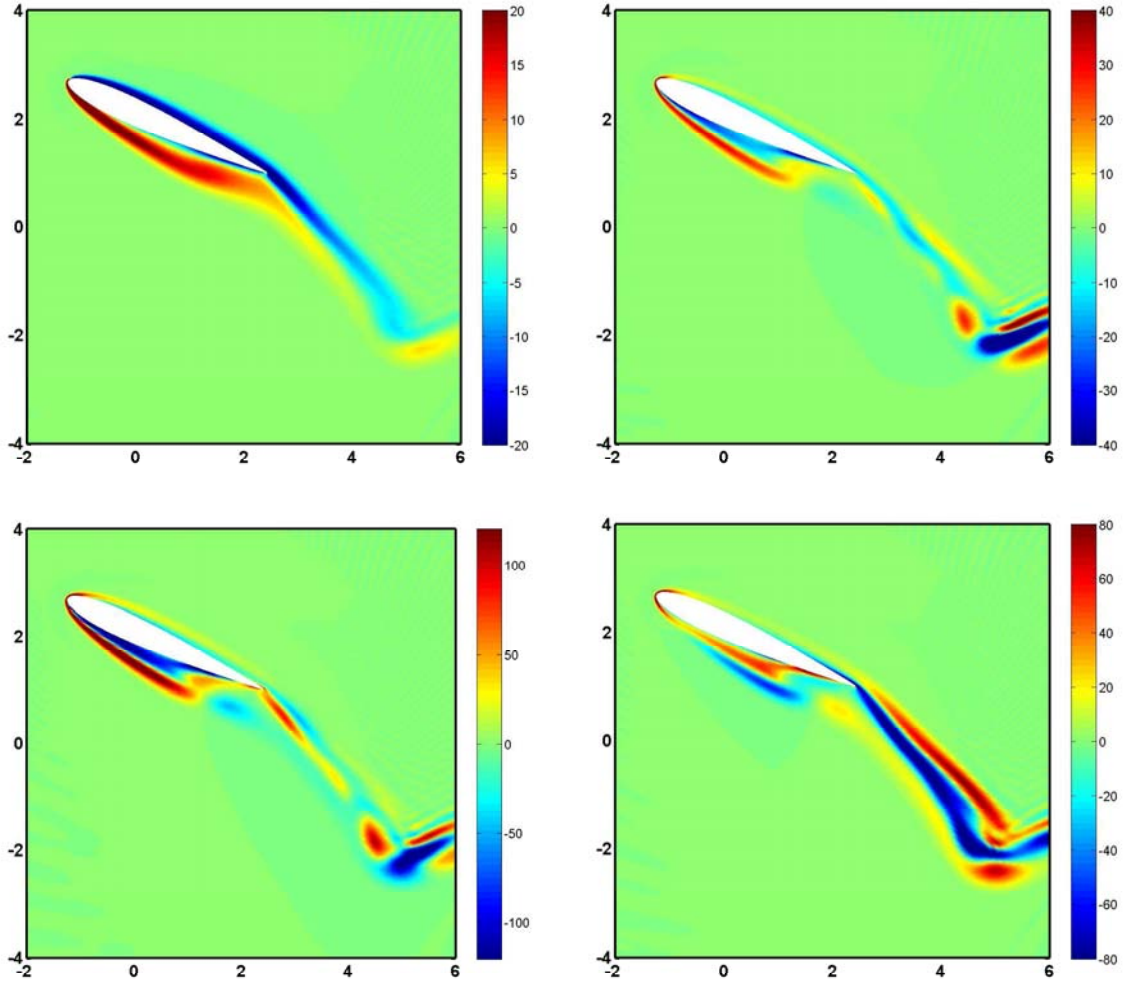


Figure 5.4: Comparison of the vorticity field (top left) to its sensitivity fields with respect to the heaving amplitude (top right), the pitching amplitude (bottom left) and the phase angle (bottom right) during the upstroke at $\frac{t}{T} = 1.125$ for $N = 1$, $\alpha_0 = 0^\circ$, $h_1 = 3$, $\tau_1 = 0^\circ$, $\alpha_1 = -35^\circ$, $\phi_1 = 90^\circ$, $f_r = 0.3665$ and $Re_c = 1100$.

By solving the sensitivity equations or by isolating the imaginary part of the solution of the complex system, the fields of $\omega_{,g}$ and $\psi_{,g}$ may be investigated. If the computation of these fields, referred to as sensitivity fields, is indispensable for the gradient evaluation, their interpretation is not straightforward. As their name indicates, they point out in which regions of the computational domain, the flow variables are most sensitive to the control parameter g . They correspond to the fields of the derivative of the flow variable with respect to the control parameter. In this sense, they should be considered from the mathematical point of view rather than the physical one. An example of sensitivity fields of the vorticity ω with respect to heave and pitching amplitudes and the phase angle is given in figure 5.4.

The topology of the sensitivity fields for the three control parameters are quite similar: vanishing values where the vorticity vanishes far from the airfoil and non vanishing values on the surface of the airfoil and in its wake. The main difference between the three fields is the numerical order of magnitude. The colour scale in figure 5.4 shows that the pitching amplitude α_1 has higher maximal values (and lower minimal values) with respect to the phase angle ϕ_1 . This implies that vorticity in this configuration is more sensitive to the pitching amplitude.

The regions where maximal (and minimal) sensitivity values occur vary from one kinematics to another. However, as a general rule, they are naturally located where vorticity is created and shed. Therefore, they remain close to the airfoil's leading- and trailing-edges, highlighting the important role played by the near-wake and by the tips of the airfoil in generating vorticity. The sensitivity fields of the stream function are harder to interpret as one can see in figure 5.5. However, the higher sensitivity to the pitch amplitude with respect to the phase angle subsists.

5.3 Critical Strouhal number

The Strouhal number is a crucial parameter for flapping foils configurations. Its value indicates whether the foil is dominantly producing drag (small values of St) or thrust (Triantafyllou et al., 1991) and it correlates to the wake topology, i.e. to the number of vortices shed per cycle of oscillation and consequently to the flapping efficiency (Anderson et al., 1998; Lai and Platzer, 1999). For large values of St , a symmetrical problem results in a non symmetric solution since *deflected wakes* are observed (see figure 5.6). The denomination *deflected* is related to the angle which exists between the wake and the horizontal direction.

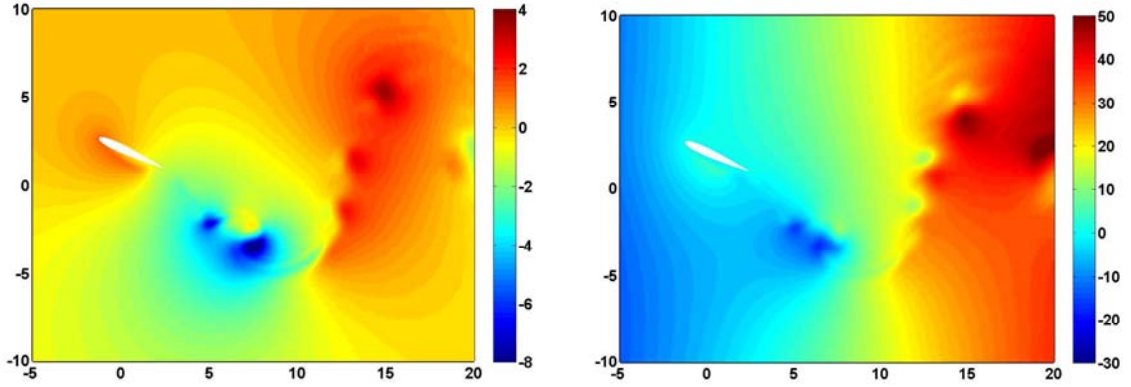


Figure 5.5: Sensitivity fields of the stream function at $\frac{t}{T} = 1.125\pi$ with respect to the heave amplitude (left) and the pitch amplitude (right) for a flapping airfoil with $N = 1, \alpha_0 = 0^\circ, h_1 = 3, \tau_1 = 0^\circ, \alpha_1 = -35^\circ, \phi_1 = 90^\circ, f_r = 0.3665$ and $Re_c = 1100$.

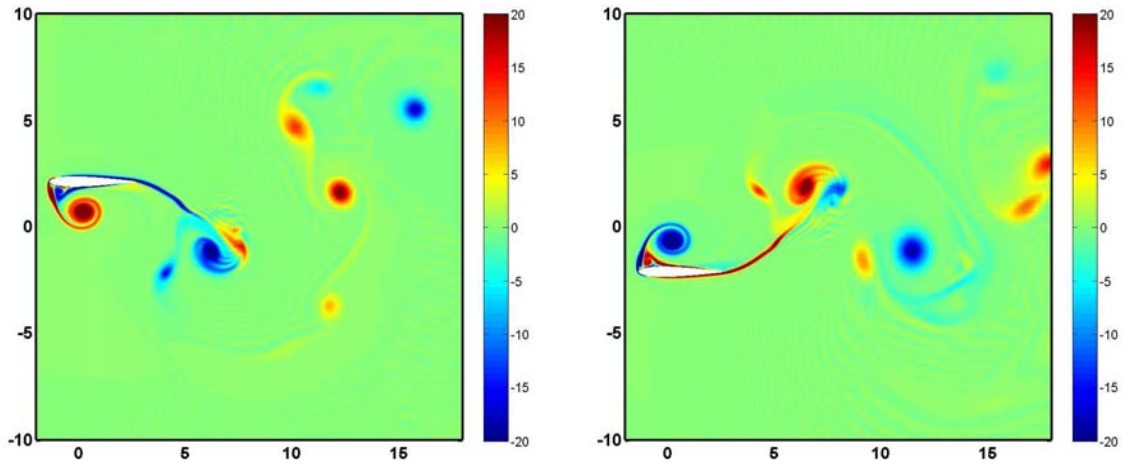


Figure 5.6: Vorticity fields for a deflected wake behind an airfoil flapping at Strouhal number ($St = 0.48$) during upstroke at $t = \frac{9\pi}{4}$ (left) and downstroke at $t = \frac{13\pi}{4}$ (right) for $N = 1, \alpha_0 = 0^\circ, h_1 = 3, \tau_1 = 0^\circ, \alpha(t) = 0, f_r = 0.5$ and $Re_c = 1100$.

The Strouhal number for a flapping airfoil is defined as the ratio of two velocities, the velocity of flapping versus the velocity of moving forward, and may be written as:

$$St = \frac{f^* A^*}{U_\infty^*} = \frac{\sigma^* \|h^*(t)\|}{\pi U_\infty^*} = \frac{\|h(t)\| f_r}{\pi}$$

where A^* is the wake width very often approximated by the double of the heave amplitude. Increasing the Strouhal number of the flapping motion allows to invert

the von Karman classic street and to produce thrust. The value beyond which this inversion happens is called the critical Strouhal number. For a two-dimensional airfoil which oscillates exactly at this critical value, a neutral wake, defined as an alternance of clockwise and counterclockwise aligned vorticity, is observed (see figure 5.7).

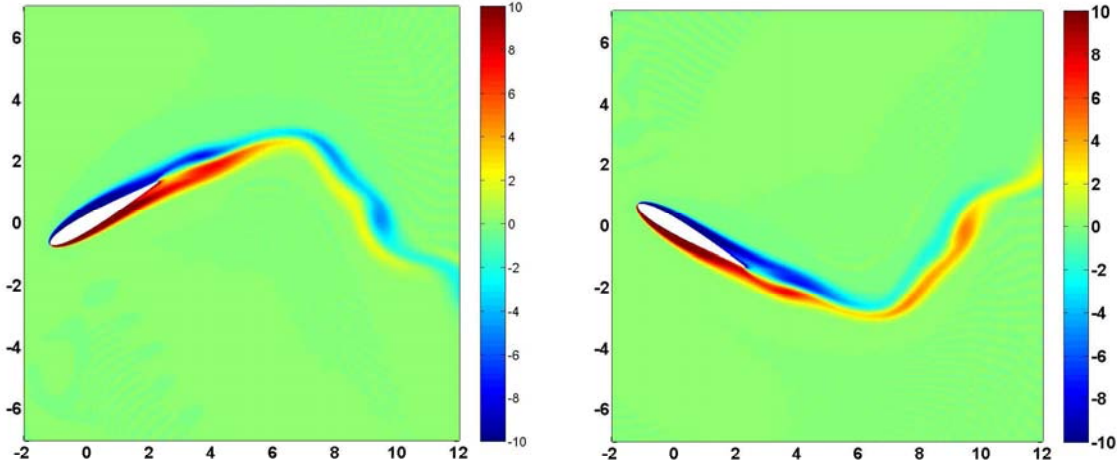


Figure 5.7: Vorticity fields for a neutral wake behind an airfoil flapping at the critical value of the Strouhal number ($St=0.214$) during downstroke at $t = 3\pi$ (left) and upstroke at $t = 4\pi$ (right) for $N = 1, \alpha_0 = 0^\circ, \tau_1 = 0^\circ, \alpha_1 = -30^\circ, \phi_1 = 90^\circ, f_r = 0.3665$ and $Re_c = 1100$.

For a fixed free stream velocity (and hence constant Reynolds number), St increases when the flapping frequency increases or when the wake width (due to heaving amplitude) increases. In the present section, we suggest to find the critical Strouhal number for a monochromatic motion and a fixed reduced frequency $f_r = 0.3665$, acting solely on the heave amplitude, h_1 . The tools already defined bring all the elements necessary for these computations. The cost functional is adapted by imposing vanishing values to $\beta_P^2, \epsilon_\alpha^2$ and ϵ_h^2 , and by considering the gradient as $2 \bar{F} \nabla \bar{F}$. This corresponds to a cost functional equal to $\mathcal{L} = \bar{F}^2$. By controlling the heave amplitude, h_1 , the optimal value yielding the minimal \mathcal{L} (consequently, vanishing horizontal force \bar{F}) is found and the correspondent Strouhal number is identified. What precedes has been done for various pitching amplitudes α_1 in the range $[-45^\circ, 0^\circ]$ and various phase angles ϕ_1 in the range $[0^\circ, 90^\circ]$.

For the reduced frequency used here, results in figure 5.8 indicate that for a purely heaving airfoil, thrust production requires a Strouhal number greater than 0.152 independently of the phase angle (since ϕ_1 has no influence when α_1 vanishes). This

value is close to that found experimentally by Anderson (1996) (roughly 0.2) at a Reynolds number equal to 40,000. For a flapping airfoil, thrust production is less constraining in terms of Strouhal number for small pitching angles, since a minimal critical Strouhal number of 0.133 is observed for a pitching angle close to -7.5° when a 90° phase difference between heaving and pitching is considered. Large pitching amplitudes require larger Strouhal numbers to reverse the von Karman street. The critical values increase when the phase ϕ_1 decreases from 90° towards 0° . The interest of considering a phase close to 90° , confirmed in §5.5, has been highlighted by Streitlien et al. (1996) and Isogai et al. (1999); this configuration supports the reduction of flow separation and increases flight efficiency by driving the timing of vortex shedding from the airfoil tips so that leading edge vortex interacts constructively with the trailing edge vortex leading to two vortices deposited per flap (Anderson et al., 1998; Lewin and Haj-Hariri, 2003).

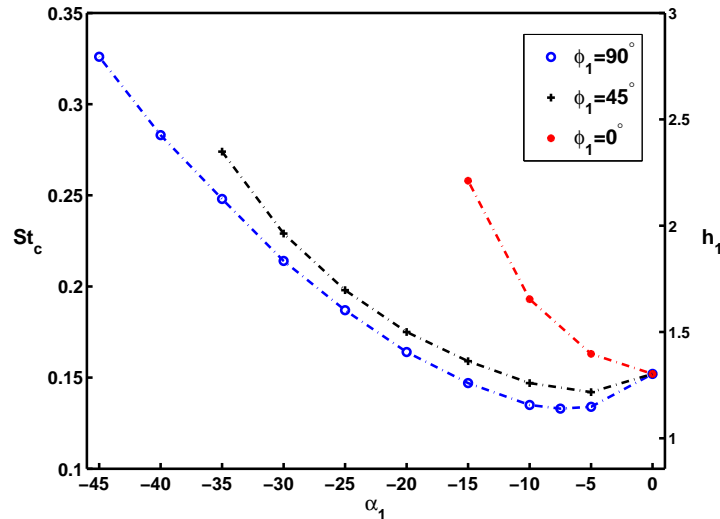


Figure 5.8: Values of the critical Strouhal for various pitching amplitudes and various phase angles.

In conclusion, for acceptable pitching angles no thrust production can be observed for $h_1 < 1$ which corresponds to an airfoil with a heaving amplitude smaller than a quarter of its chord. If a vanishing phase angle has to be studied, a pitching amplitude in the interval $[-20^\circ, 0^\circ]$ must be considered. Beyond this range, no thrust production has been observed. In the same way, and for $\phi_1 = 45^\circ$, there is no possible thrust production for $\alpha_1 < -35^\circ$. The critical Strouhal numbers for $\phi_1 = 45^\circ$ are closer to the values for $\phi_1 = 90^\circ$ than to those for $\phi_1 = 0^\circ$. In the remainder of this work, we will focus on control parameters within favourable ranges for thrust production.

5.4 Effect of heaving and pitching amplitudes

The attention shifts in the present section to the effect of the heaving and pitching amplitudes in the case of monochromatic oscillations. Since the other parameters should be fixed, a constant phase angle $\phi_1 = 90^\circ$ is imposed. This choice is a consequence of the results reported in the previous section. In the case $N = 1$, one phase angle is sufficient, hence a vanishing phase angle τ_1 is considered. Moreover, for constant values of the reduced frequency $f_r = 0.3665$ and of the mean angle of attack $\alpha_0 = 0^\circ$, two sets of computations are done.

- In the first, the pitching amplitude α_1 is varied in the range $[-45^\circ, 0^\circ]$, with an increment of 5° and the optimal values of h_1 are sought.
- In the second, the heaving amplitude h_1 is varied in the range $[0, 4]$, with an increment of 0.5 and the optimal α_1 is computed.

The optimisation is done for the cost functional:

$$\mathcal{L} = \bar{P} + 2\bar{F}U_0 + \bar{\alpha}^2 + \bar{h}^2(t)$$

5.4.1 Optimal amplitudes

The results in figure 5.9 show a linear dependence between the optimal amplitudes for heaving and pitching in the ranges considered. Controlling a single parameter may be misleading. Two examples of this may be seen when considering solely one amplitude as control parameter. The first is that for a vanishing pitching amplitude, the optimal h_1 is equal to zero corresponding to an airfoil which does not flap, the second is that optimal values of h_1 obtained for $\alpha_1 \in [-20^\circ, 0^\circ]$ yield dominantly drag-producing configurations (cf. figure 5.8). This may suggest that the cost functional was poorly chosen. However, deeper investigation of the results contradicts this statement. Even if the motionless configuration is optimal, the value of the cost functional is not minimal with respect to the values for non-vanishing pitching amplitudes (see figure 5.10). This implies that if the two amplitudes are controlled together, the optimal solution will not be the configuration of a still airfoil.

The global minimum of the cost function, over the ranges concerned, when controlling h_1 is obtained for the couple $(h_1, \alpha_1) = (2.321, -30^\circ)$ yielding a propulsive efficiency $\eta = 0.398$ and a thrust coefficient $C_T = 0.229$. Higher η and C_T are obtained for relatively large optimal amplitudes since for $(h_1, \alpha_1) = (3.651, -45^\circ)$ we have $\eta = 0.466$ giving rise to $C_T = 0.601$. However, large amplitudes of oscillations are not desired since they engender high structural constraints. This highlights the impact of including the last two terms in the cost functional to limit the cost of the

control.

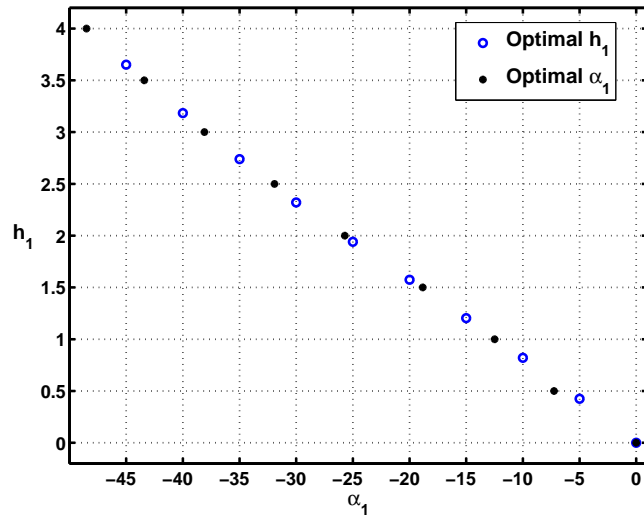


Figure 5.9: Optimal heaving amplitudes (empty circles) and optimal pitching amplitudes (filled circles) for $N = 1, \alpha_0 = 0^\circ, \tau_1 = 0^\circ, \phi_1 = 90^\circ, f_r = 0.3665$ and $Re_c = 1100$.

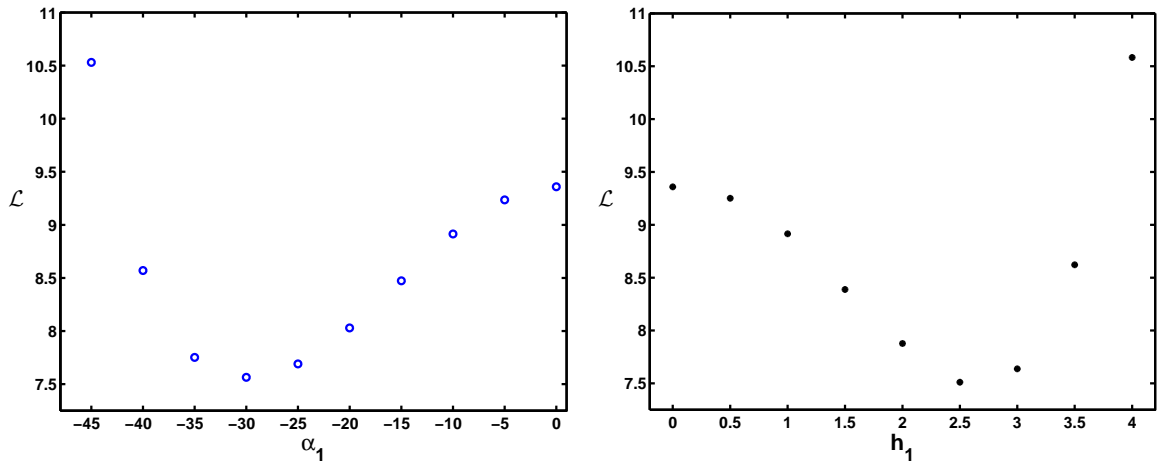


Figure 5.10: Values of the cost functional for optimal heaving amplitudes h_1 (left) and optimal pitching amplitudes α_1 (right) for $N = 1, \alpha_0 = 0^\circ, \tau_1 = 0^\circ, \phi_1 = 90^\circ, f_r = 0.3665$ and $Re_c = 1100$.

When controlling α_1 , the global minimum of the cost functional is obtained for the couple $(h_1, \alpha_1) = (2.5, -31.91^\circ)$, obviously very close to the one obtained by controlling h_1 . This configuration is characterised by $\eta = 0.423$ and $C_T = 0.28$. Here

again, for large amplitudes, for instance for $(h_1, \alpha_1) = (4, -48.50^\circ)$, larger efficiency and thrust can be recovered ($\eta = 0.485$ and $C_T = 0.90$), but the choice of the cost functional prevents these high-constraints configurations from becoming the global optimum. The optimal cases with dominantly drag producing flapping airfoils are also related to the choice of the cost functional and the associated weights. With the present choice, the optimisation process is directed towards pitching amplitudes in the range $[-35^\circ, -25^\circ]$. This should be seen as a feature of the considered cost functional. A deep investigation for $\alpha_1 \in [-20^\circ, 0^\circ]$ has shown that in this range, the thrust generated is very small and the efficiency really poor for any heaving amplitude. Thus, by converging to drag-producing kinematics leading to larger values of the cost functional, the choice adopted here avoids a zone of the control parameters with no practical interest.

The physical reason for the high efficiency in the optimal configuration may be addressed by comparing the vorticity and the velocity fields to a bad-efficiency configuration. Therefore, in figures 5.11 and 5.12 fields are plotted for the case $(h_1, \alpha_1) = (2.5, -31.91^\circ)$ and the configuration $(h_1, \alpha_1) = (4, -5^\circ)$ yielding a $C_T = 0.52$ with a very poor propulsive efficiency $\eta = 8.7\%$. The symmetry of the motion during the upstroke and the downstroke leads to fields which are the mirror images of one another. The bad efficiency is related to the presence of widespread (larger dimensions) vortices and to secondary structures. The more compact and coherent vortices in the optimal configuration are created with less wasted energy whereas the break up of shed vorticity increases the loss of energy. In the optimal configuration, the airfoil "snakes" its way through the fluid, displacing it less in both the horizontal and vertical direction. This implies a decrease of the horizontal and the vertical forces, but the decrease in the required power is larger than the decrease of the thrust, and the efficiency is increased.

The other main reason for the high η is the rate of separation of the flow over the airfoil during the stroke. The same colour scale is used for the two configurations in figure 5.12. A large separation bubble can be observed on the pressure side during the upstroke (and on the suction side, during the downstroke) which increases the pressure drag forces as for fixed airfoils and thus decreases the thrust forces and consequently the efficiency.

The two global optimal solutions for heaving and pitching amplitudes control corresponds respectively to values of the Strouhal number of 0.27 and 0.29. The values are perfectly inside the optimal range $St \in [0.25, 0.35]$ as shown by Triantafyllou et al. (1993) and observed on a very large flying and swimming animals in nature (Taylor et al., 2003). This confirms the ability of the optimisation approach and the chosen cost functional to drive the parameters towards physically optimal values,

encountered in nature.

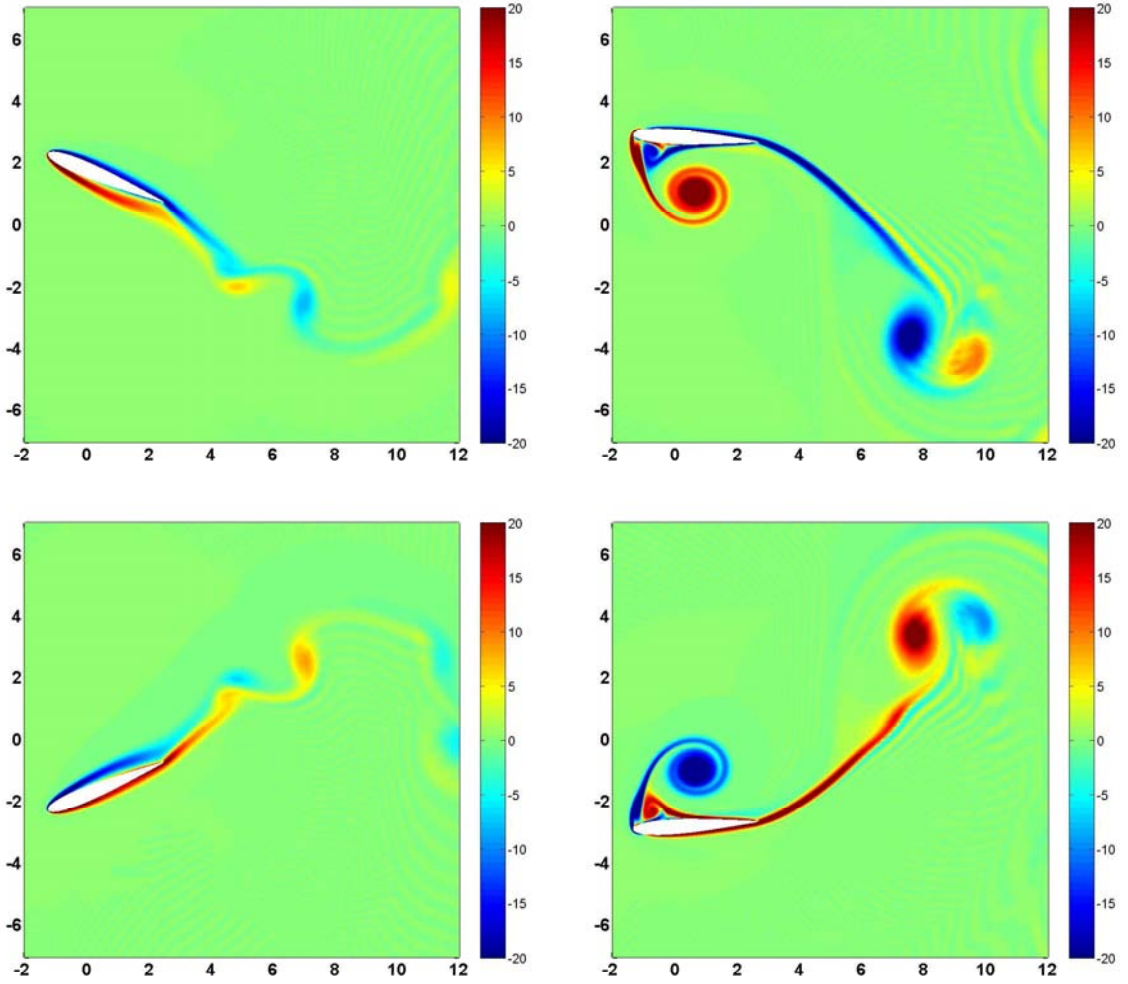


Figure 5.11: Comparison of vorticity fields during upstroke at $\frac{t}{T} = 1.125$ (top row) and downstroke at $\frac{t}{T} = 1.625$ (bottom row) for $N = 1, \alpha_0 = 0^\circ, \tau_1 = 0^\circ, \phi_1 = 90^\circ, f_r = 0.3665, Re_c = 1100$ and $(h_1, \alpha_1) = (2.5, -31.91^\circ)$ (left) and $(h_1, \alpha_1) = (4, -5^\circ)$ (right).

5.4.2 Effective angle of attack

The effect of both amplitudes, and the significance of the linear dependence is studied by introducing the effective angle of attack γ . For a non flapping airfoil, the angle of

attack is the real angle between the airfoil and the flow whereas for a flapping one, the vertical motion induces an angle and the effective angle of attack "seen" by the airfoil is:

$$\gamma(t^*) = \alpha_0 + \arctan\left(\frac{\dot{h}^*(t^*)}{U_\infty^*}\right) + \alpha(t^*),$$

or in non-dimensional form:

$$\gamma(t) = \alpha_0 + \arctan\left(\frac{\dot{h}(t)}{U_0}\right) + \alpha(t).$$

The variation in time over one period for two optimal configurations are given in figure 5.13. We note that in the case $\alpha_0 = 0^\circ$ and $\phi_1 = 90^\circ$, and thanks to the properties of the arctan function, each half period can be divided into 2 quarters where the variation of γ is antisymmetric. Furthermore, the global minimum is characterised by an effective angle of attack divided into two *plateaux* (cf. figure 5.13(a)) whereas the other optimal configurations present a number of peaks (cf. figure 5.13(b)).

The maximal value of $\gamma(t)$ over one period of oscillation γ_{\max} plays a crucial role since it governs the rate of the flow separation over the foil and consequently, the thrust generation and the propulsive efficiency. According to the value of the angle, a flapping airfoil can create thrust or extract power from the flow. In between, it is said that the wings *feathers* through the flow without disturbing it. For $N = 1$, one may write that:

$$\gamma_{\max} \leq \alpha_0 + \arctan\left(\frac{h_1}{U_0}\right) + \alpha_1.$$

As it can be observed in figure 5.13, the two optimal configurations have very close values of γ_{\max} . By extending to the other cases, we notice that all optimal configurations corresponding to thrust generation have a maximal effective angle of attack in the range $[10^\circ, 12.25^\circ]$ as it can be seen in figure 5.14. Hence, the linear dependence between optimal heaving and pitching amplitudes results in a roughly constant maximal value for the effective angle of attack equal to 11° . This observation is rather interesting, especially because this value corresponds to a high lift-to-drag ratio and it is within the stall angle for the same airfoil at the same Reynolds number when it does not flap, as shown in §5.6. If we admit that γ_{\max} plays a similar role than the angle of attack for a still airfoil, the latter result confirms the fact that optimal kinematics are directly related to attached flows, as discussed by Tuncer and Platzer (2000). A summary of the characteristics of the optimal configurations, when controlling the amplitudes, is given in table 5.1.

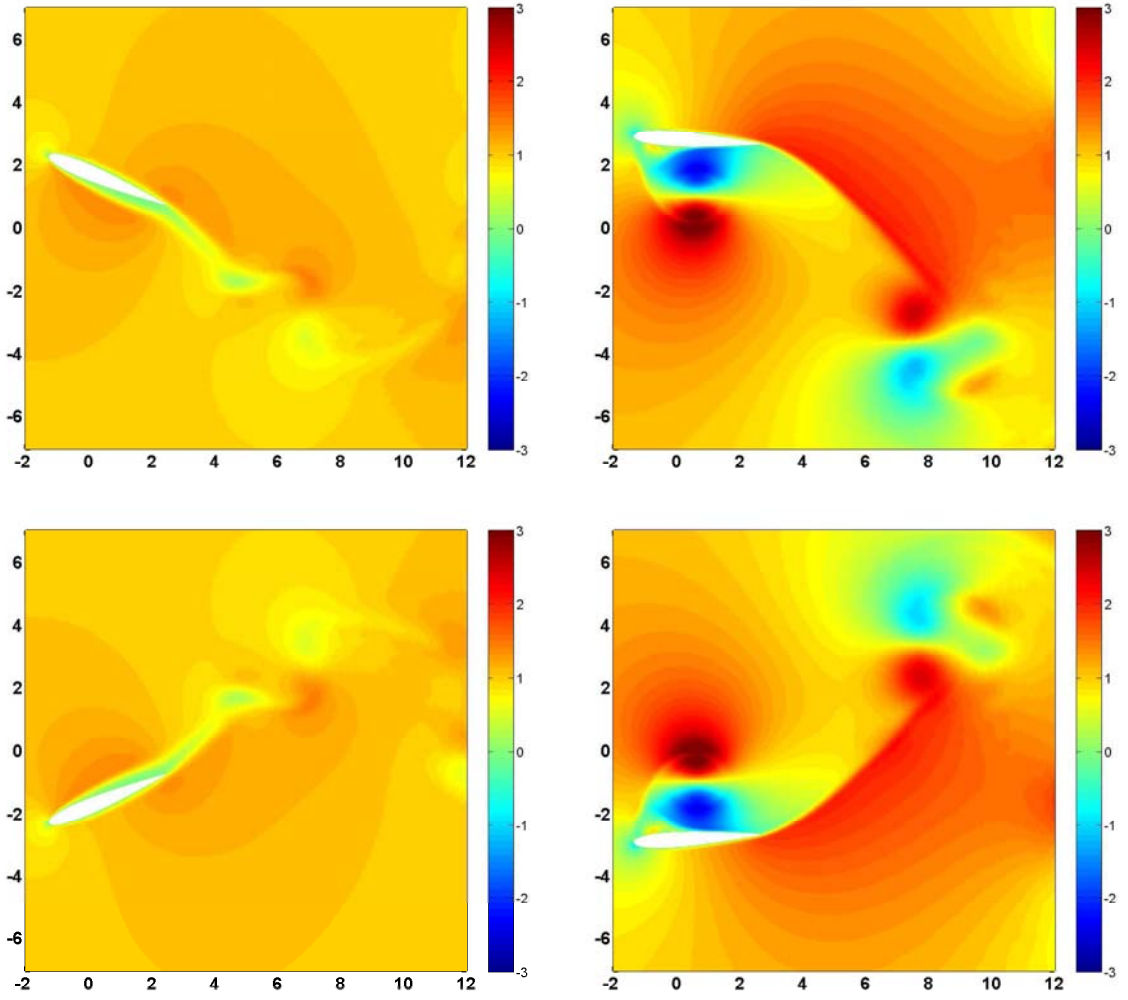


Figure 5.12: Comparison of the relative velocity $\frac{u}{U_0}$ fields during upstroke at $\frac{t}{T} = 1.125$ (top row) and downstroke at $\frac{t}{T} = 1.625$ (bottom row) for $\alpha_0 = 0^\circ$, $\tau_1 = 0^\circ$, $\phi_1 = 90^\circ$, $f_r = 0.3665$, $Re_c = 1100$ and $(h_1, \alpha_1) = (2.5, -31.94^\circ)$ (left) and $(h_1, \alpha_1) = (4, -5^\circ)$ (right).

α_0	h_1	α_1	ϕ_1	St	γ_{\max}	C_L	C_P	C_T	η
0°	2.321	-30.00°	90.00°	0.271	10.43°	0	0.575	0.229	0.398
0°	2.500	-31.91°	90.00°	0.291	10.81°	0	0.492	0.280	0.423

Table 5.1: Optimal kinematics when controlling the heaving and pitching amplitudes for $N = 1$, $f_r = 0.3665$ and $Re_c = 1100$.

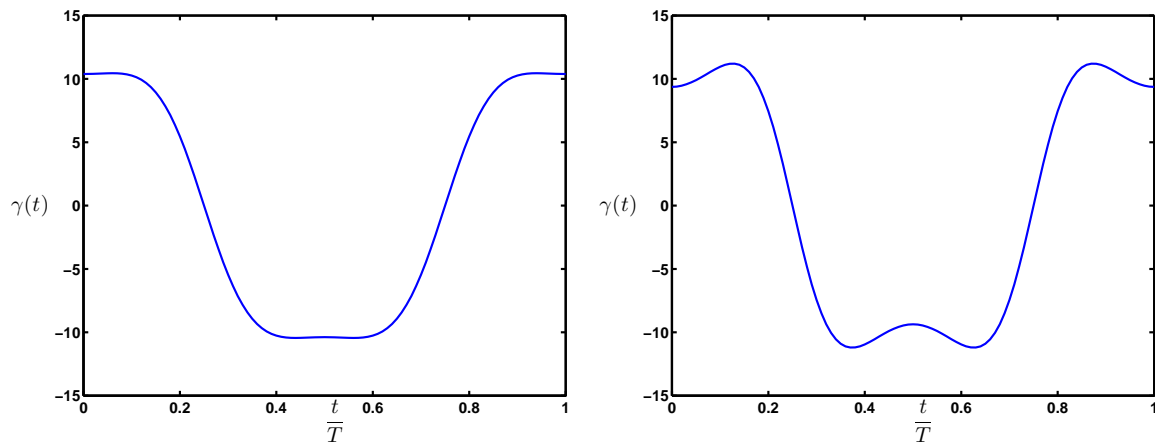


Figure 5.13: Evolution over one period of the effective angle of attack $\gamma(t)$ for $N = 1, \alpha_0 = 0^\circ, \tau_1 = 0^\circ, \phi_1 = 90^\circ, f_r = 0.3665, Re_c = 1100$ and $(h_1, \alpha_1) = (2.321, -30^\circ)$ (left) and $(h_1, \alpha_1) = (3.180, -40^\circ)$ (right).

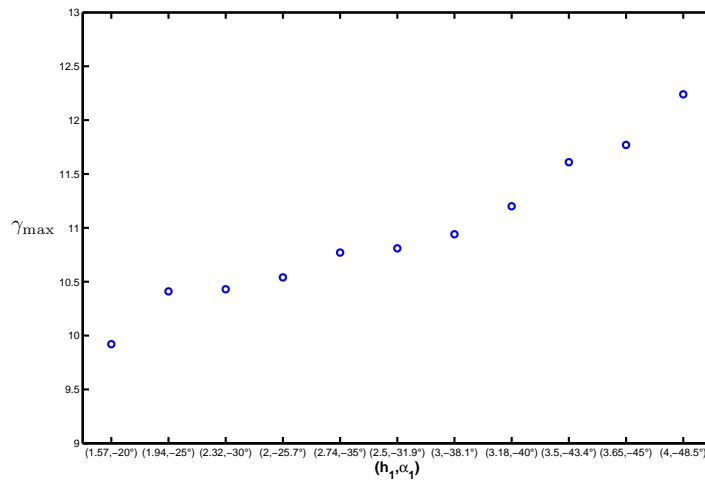


Figure 5.14: Values of the maximal effective angle of attack for optimal amplitudes for $N = 1, \alpha_0 = 0^\circ, \tau_1 = 0^\circ, \phi_1 = 90^\circ, f_r = 0.3665$ and $Re_c = 1100$.

5.5 Effect of the phase angle

Here, the effect of the phase angle between heaving and pitching oscillations is studied. This angle drives the timing of shed vorticity and governs consequently the type of interaction which occurs between leading-edge and trailing-edge vortices. In the case $N = 1$, and as demonstrated earlier, one angle ϕ_1 or τ_1 is sufficient to describe the phase between the two motions. In literature, including the phase angle inside

the pitching oscillations is the most widespread practice. However, and for solver validation reasons, the optimal angles τ_1 are also computed. Hence, we start by controlling the angle ϕ_1 . The other parameters are maintained constant with the imposed values of $\alpha_0 = \tau_1 = 0^\circ$, $f_r = 0.3665$ and $Re_c = 1100$. Two values are considered for the heaving amplitude ($h_1 = 2$ and $h_1 = 3$). For each heaving amplitude, the pitching amplitude α_1 is varied in the range $[-45^\circ, -5^\circ]$, with an increment of 5° . For each of these configurations, the phase angle ϕ_1 is optimised so as to minimise the cost functional:

$$\mathcal{L} = \bar{P} + 2\bar{F}U_0 + \bar{\alpha}^2 + \bar{h}^2(t)$$

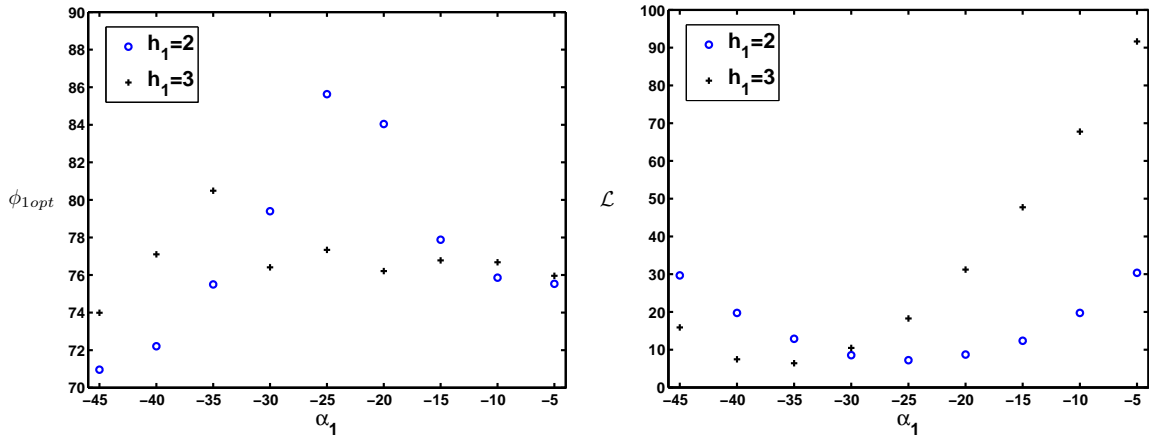


Figure 5.15: Values of the optimal phase angles (left) and the associated values of the cost functional (right) for various heaving and pitching amplitudes for $N = 1$, $\alpha_0 = 0^\circ$, $\tau_1 = 0^\circ$, $f_r = 0.3665$ and $Re_c = 1100$.

Obviously, no optimal ϕ_1 is sought for a vanishing pitching amplitude. Results in figure 5.15(a) show that for any plausible amplitude for pitching and heaving, the optimal phase angle is in the range $[70^\circ, 90^\circ]$. This means that the propulsive efficiency is favoured when the motion of the airfoil is such that the maximum angle occurs for a vanishing heave and *viceversa* (see figure 2.5). The good influence on the propulsive efficiency of considering pitching oscillations leading the heaving ones by an angle roughly equal to 90° has been mentioned in previous contributions (Streitlien et al., 1996; Isogai et al., 1999). The physical explanation for this high η is the mostly attached flow under these conditions since the separation is confined to a small region near the trailing-edge. The leading-edge vortex remains attached during the whole stroke and once it is shed it interacts constructively with the vortex shed from the trailing-edge (see figure 5.16). The optimisation approach used here allows to find these results with a new methodology and confirms that the cost functional

adopted is well linked to a high generation of thrust with acceptable propulsive efficiencies.

The global minimum of the cost functional is given for the kinematics $(h_1, \alpha_1, \phi_1) = (3, -35^\circ, 80.5^\circ)$ corresponding to $\eta = 0.481$ and $C_T = 0.526$ (see figure 5.15(b)). For the same values of f_r, Re_c, α_0, h_1 and α_1 , the angle ϕ_1 was imposed equal to 90° and the optimal values found for τ_1 verified the relation $\tau_{1opt} = \frac{\pi}{2} - \phi_{1opt}$. A summary of the characteristics of the optimal configurations, when controlling the phase angle, is given in table 5.2.

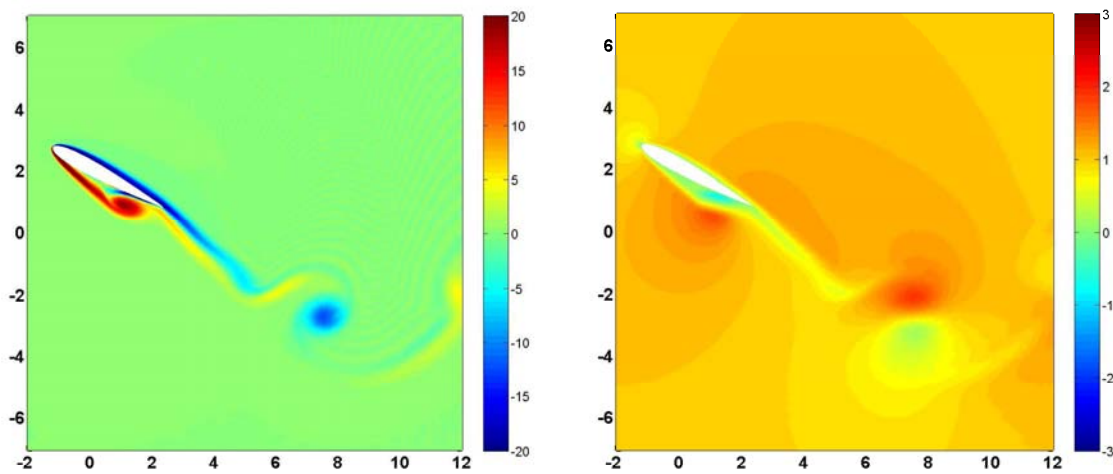


Figure 5.16: Vorticity (left) and relative horizontal velocity fields $\frac{u}{U_0}$ (right) during upstroke at $\frac{t}{T} = 1.125$ for an optimised phase angle: $N = 1, \alpha_0 = 0^\circ, h_1 = 3, \tau_1 = 0^\circ, \alpha_1 = -35^\circ, \phi_1 = 80.5^\circ, f_r = 0.3665$ and $Re_c = 1100$.

α_0	h_1	α_1	ϕ_1	St	γ_{\max}	C_L	C_P	C_T	η
0°	3.000	-35.00°	80.50°	0.350	17.55°	0	1.093	0.526	0.481

Table 5.2: Optimal kinematics when controlling the phase angle for $N = 1, f_r = 0.3665$ and $Re_c = 1100$.

5.6 Lift analysis

In the present section, we focus on the effect of the mean angle of attack α_0 and its influence on the lift force. Regardless of the value of N , the pitching angle $\alpha(t)$ is periodic in time with a non dimensional period equal to 2π . Therefore, the average value of $\alpha(t)$ over a period of oscillation vanishes and no average lift is produced in the absence of a mean angle of attack α_0 . The average lift force \bar{L} was not included inside the cost functional for the main reason that the non-lifting configurations provide better propulsive efficiencies. Lift depends mainly on α_0 and when an average lift force is generated, the power required is increased without substantial increase (and even decrease in most of the cases) in the thrust force. This favours flow separation and implies a decrease of η . In other word, if the lift is linearly added to the cost functional with an associated negative weight, and the optimisation approach is applied acting on the mean angle of attack, the optimal values would be reached for a vanishing α_0 . More complex cost functionals could be adopted, but the adaptability to the different configurations studied here would be less straightforward. The main target being to produce high thrust forces with acceptable efficiency, both for micro air and autonomous underwater vehicles, it is preferable to study the lift force separately and ensure a sufficient lift force for the optimal kinematics.

5.6.1 Lift of a flapping airfoil

As shown in §5.3, 5.4 and 5.5, a roughly 90° phase angle, a heaving amplitude in the range $[2, 3]$ and a pitching amplitude in the range $[-25^\circ, -35^\circ]$ are optimal. For these values, the mean angle of attack α_0 , lift, thrust (or drag) and efficiency are investigated. Results in figure 5.17(a) show the ability of flapping airfoils to produce high lift coefficients, since a coefficient as high as $C_L = 3$ can be achieved. Micro air vehicles are generally light, i.e. very sensitive to harsh atmospheric conditions, which means that high lift and thrust forces are welcome to enable manoeuvring. On the other hand, the slow velocity of the micro air vehicle requires a high lift coefficient to sustain the weight of the vehicle. High values of lift are obtained for large angles of attack. They are found in the range $[24^\circ, 36^\circ]$ when the mean angle of attack is considered. However, the three configurations $(h_1, \alpha_1) = (2, -25^\circ)$, $(2, -35^\circ)$ and $(3, -35^\circ)$ yield the first peak of C_L for the same value of $\gamma_{max} = 39^\circ$, whereas the fourth configuration $(h_1, \alpha_1) = (3, -25^\circ)$ yields the first peak for $\gamma_{max} = 48^\circ$. Unfortunately, this range of angles for α_0 cannot be used since under these conditions the flapping airfoil does not produce thrust. As shown in figure 5.17(b), when the mean angle of attack is increased, the von Karman street is not reversed and drag is produced ($C_T = -\frac{\bar{F}}{2U_0^2}$, i.e. negative values of C_T are relative to drag production).

For the configurations considered, no thrust production is possible beyond $\alpha_0 = 20^\circ$, and the drag coefficient increases very fast beyond this threshold reaching values preventing any practical application of this range. A polar may be plotted for the case of a flapping airfoil, but special attention should be done to vanishing values of the horizontal force when the wake is inverted.

In the same way, starting from a vanishing mean angle of attack, the propulsive efficiency decreases until drag replaces thrust as shown in figure 5.18(a). The good correlation between the propulsive efficiency and the cost functional is demonstrated by plotting in figure 5.18(b) the variation of

$$\mathcal{L} = \bar{P} + 2\bar{F}U_0 + \bar{\alpha}^2 + \bar{h}^2(t).$$

The comparisons between the two configurations for constant α_0 , and within one configuration when varying α_0 , prove that by minimising the cost functional a high propulsive efficiency is reached. The impact of the weights of the last two terms corresponds mostly to a shift of the cost functional values, and thus when these weights will be varied in the following, this good correlation is maintained. The minimal value of the cost functional obtained for $\alpha_0 = 0^\circ$ justifies what has been mentioned earlier about not considering the lift force inside the cost functional. Hence, in the following, instead of optimising the lift, the optimal kinematics are sought, imposing a given α_0 , and the lift force is deduced. Therefore, a first conclusion is that flapping airfoils are able to produce large lift coefficients for large angles of attack but it is preferable to consider smaller angles when a reasonable of lift is sufficient and thrust is produced.

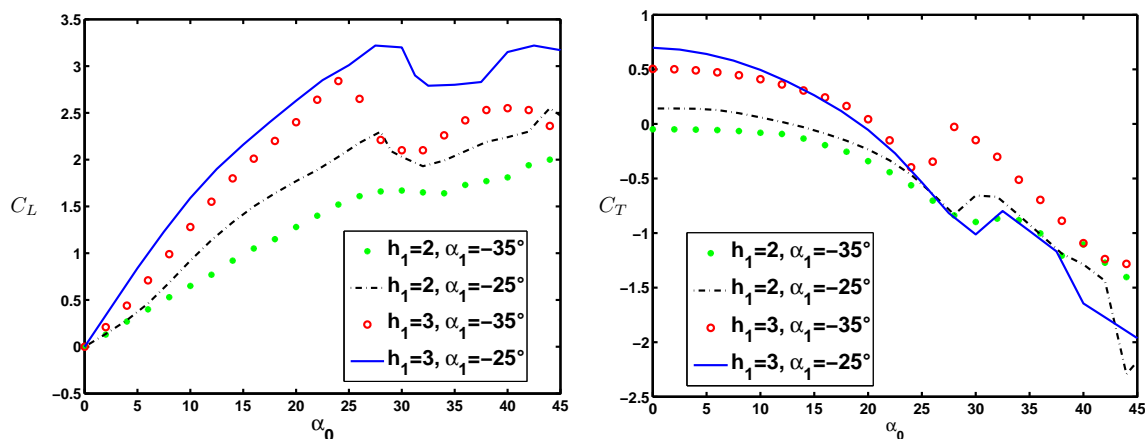


Figure 5.17: Lift (left) and thrust/drag (right) coefficients versus mean angle of attack α_0 for $N = 1$, $\tau_1 = 0^\circ$, $\phi_1 = 90^\circ$, $f_r = 0.3665$, $Re_c = 1100$ and various amplitudes.

The second topic investigated refers to the stall of flapping airfoil. It is well known that for a fixed airfoil, the lift coefficient increases almost linearly when the angle of attack increases. For a given value of the angle of attack, the adverse pressure gradient on the suction side becomes too strong, and the boundary layer separates leading to a down-shoot of the lift force. This phenomenon is referred to as *static stall*. For the NACA airfoils family used here, and for high Reynolds numbers, it takes places for a relatively small angle of attack, in the range $[12^\circ, 18^\circ]$, according to the value of Re_c . For flapping airfoils, the peak value is obtained for a much larger angle of attack, and interestingly, the lift coefficient increases after the down-shoot following the first peak, giving rise to multiple peaks. Numerical simulations have been carried out for angles of attack as large as 90° and lift still can be generated under these conditions. This result was also observed experimentally by Silin et al. (2006) who observed a lift force for a flapping airfoil with a 90° angle of attack. However, in their case, the lift coefficient saturated to an asymptotic value after the first peak, which they also obtained for angles of attack in the range $[40^\circ, 50^\circ]$. This discrepancy can be related to the elasticity of the wings in their study.

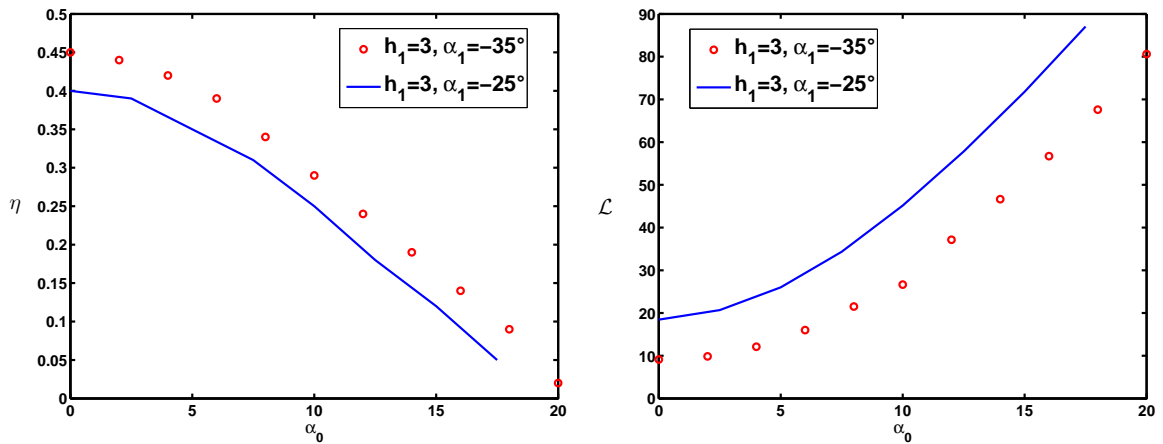


Figure 5.18: Efficiency (left) and cost functional (right) variation with the mean angle of attack α_0 for $N = 1, \tau_1 = 0^\circ, \phi_1 = 90^\circ, f_r = 0.3665, Re_c = 1100$ and various amplitudes.

5.6.2 Comparison of still and flapping airfoils

The high value of the angle of attack yielding the maximal lift is related to the low value of the Reynolds number rather than the wing motion. In figure 5.19(b), the lift coefficient is plotted for the same NACA0012 profile at the same Reynolds number of $Re_c = 1100$ for α_0 in the range $[0^\circ, 90^\circ]$ when it does not flap. The maximal

lift ($C_L = 1.8$) is obtained for $\alpha_0 = 47^\circ$. The maximal lift-to-drag ratio is equal to 2.43 and it occurs for $\alpha_0 = 11^\circ$. We notice that this angle is in the same range for which the maximum effective angle of attack $\gamma_{\max} (\in [10^\circ, 12.25^\circ])$ should be, for the optimal kinematics of the flapping airfoil. The comparison may seem ambitious since the problems are different; in one case we have an optimal lift-to-drag ratio for a fixed airfoil optimising the mean angle of attack, whereas in the other, we have an optimal propulsive efficiency for a flapping airfoil optimising the amplitudes and consequently the effective angle of attack. However, this fact confirms that γ plays the same role for a flapping airfoil than α_0 for a fixed one. It also proves that the optimisation of lift-to-drag and the propulsive efficiency are not contradictory, both being large in case of minimal separations and small losses of energy in the wake.

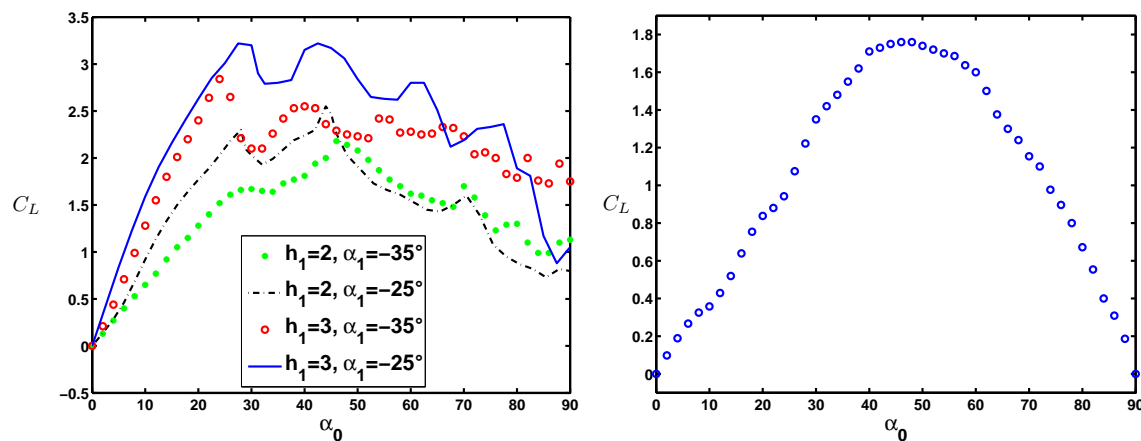


Figure 5.19: Lift coefficients at $Re_c = 1100$ for a fixed (left) and flapping (right) NACA0012 airfoil for $N = 1, \tau_1 = 0^\circ, \phi_1 = 90^\circ, f_r = 0.3665$ and various amplitudes over wide range of angle of attack α_0 .

The same range of α_0 was investigated in figure 5.19(a) for flapping configurations. The results were confirmed by computations performed with Fluent for the fixed airfoil and with the Overture software for the fixed and flapping configurations. A very good agreement was statistically found for both aerodynamic coefficients and flow fields confirming that the maximum lift is in the range $[40^\circ, 50^\circ]$ for such a low Re_c . The term "statistically" is very important because for such high angles of attack, the flow around the airfoil is very unsteady and consequently very long to establish towards an unsteady periodic solution. Following the choice of time interval on which the averaging is done, the lift coefficient may slightly vary. To illustrate the difficulty of the flow establishment, the temporal evolution of C_L is plotted in the case of a 30° angle of attack in figure 5.20(a) for the still airfoil. Under these conditions, there

is no sense to refer to the period of oscillations but the same time scaling, based on flapping frequency, has been nonetheless chosen for comparison reasons.

For such high angles of attack, two periods of oscillations are not enough to establish the flow like previously mentioned in §4.2. Even after 6 periods, small discrepancies may be observed in figure 5.20(a). However, when averaging on such a long duration, those variations are smoothed and the value of the aerodynamic coefficient is reliable. The flow is harder to establish for higher angles of attack and for a flapping configuration as shown in figure 5.20(b). In this case, after 8 periods of oscillations, perfect periodic unsteady flow is not yet established. Therefore, very long duration of the simulations (between 12 and 15 periods) were needed for such configurations. The possibility to smooth even more the lift curves in figure 5.19(a) exists if infinite time simulations are carried out, but there is no interest in determining the lift with high accuracy in a range of angles of attack where drag is too large.

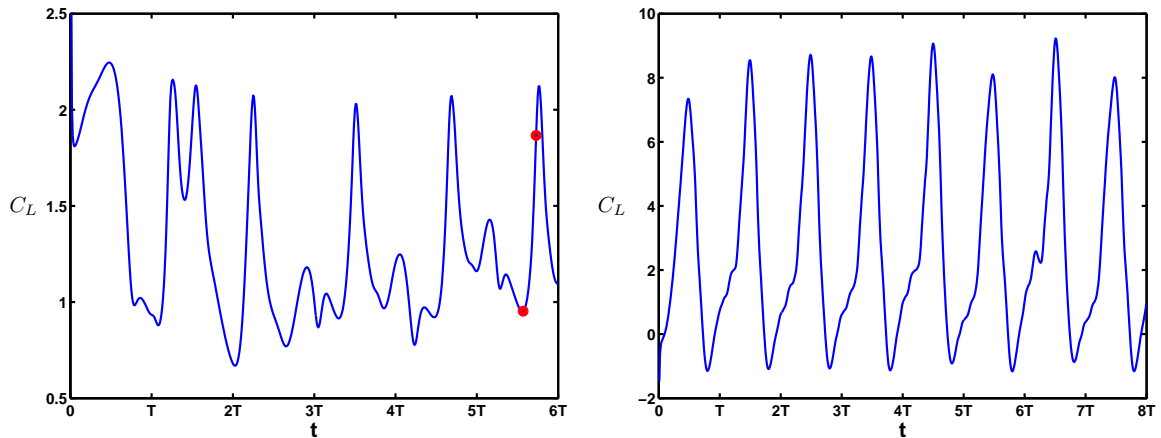


Figure 5.20: Evolution for a NACA0012 of the lift coefficient in time at $Re_c = 1100$ for a fixed airfoil at $\alpha_0 = 30^\circ$ (left) and flapping airfoil at $\alpha_0 = 40^\circ$ (right) for $N = 1, h_1 = 3, \tau_1 = 0^\circ, \alpha_1 = -35^\circ, \phi_1 = 90^\circ$, and $f_r = 0.3665$.

In figure 5.21, the velocity fields are plotted for two instants at $t = 35$ and $t = 36$ corresponding to high and low lift configurations, and pointed out by two circles in figure 5.20(a). As one may expect, for such large α_0 , the flow is separated over a large majority of the airfoil. However, the position of the separation bubble is closer to the airfoil at $t = 35$, when the lift force is small and consequently, more negative velocities are available near the airfoil surface, influencing both lift and drag forces. For all these reasons, in the following, lift will be ensured by considering an angle of attack in the range of $[8^\circ, 12^\circ]$, and the optimisation will be carried out by acting on the other control parameters.

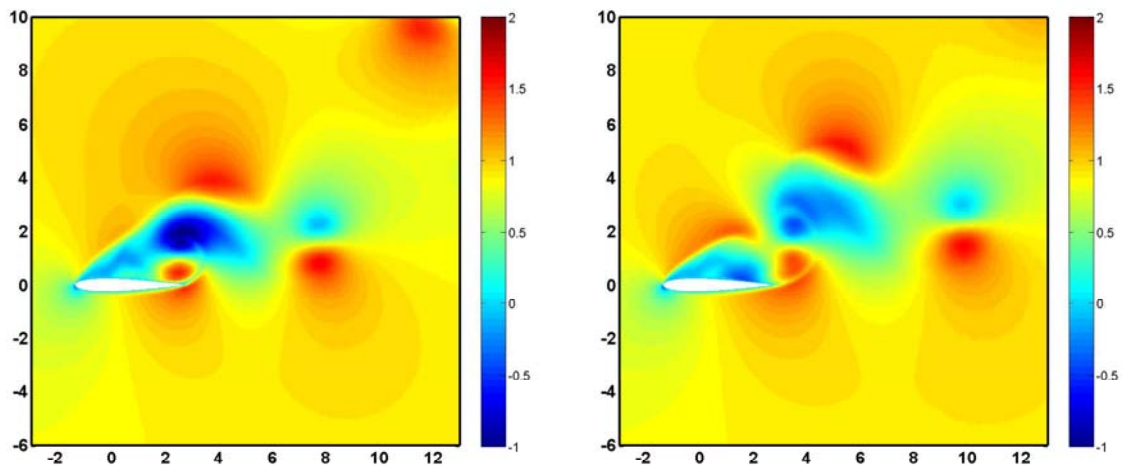


Figure 5.21: Relative horizontal velocity ($\frac{u}{U_0}$) fields for a fixed NACA0012 airfoil at 30° angle of attack at $Re_c = 1100$ at $t=35$ (left) and $t=36$ (right).

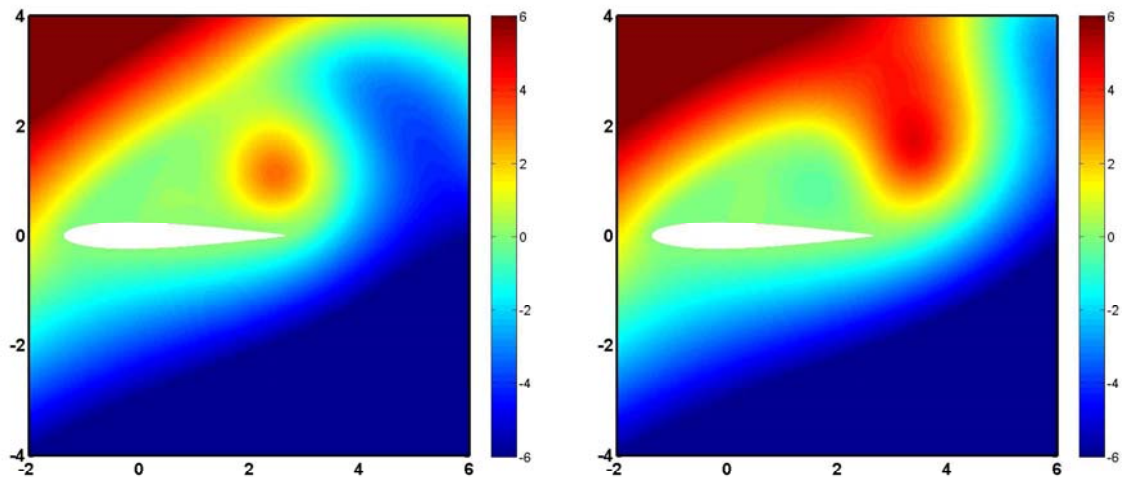


Figure 5.22: Stream function fields for a fixed NACA0012 airfoil with 30° angle of attack at $Re_c = 1100$ at $t=35$ (left) and $t=36$ (right).

The plot of the stream function in figure 5.22(a) shows clearly the presence of a vortex at the suction side near the trailing edge and which may be linked to the altered lift force at $t = 35$.

5.7 Optimal configurations

After analysing the effect of each control parameter separately, attention shifts now on the optimal configurations obtained acting on multiple parameters. From the numerical point of view, the choice was made to solve the flow and the sensitivity equations for a set of parameters and to use the gradients to update all the parameters together. Another possible approach could be to wait for each parameter until it reaches its optimal value and then to move to another and then to restart the process until all gradients vanish, but this approach requires a larger total number of iterations. Hence, for various forms of the cost functional, the amplitudes and the phase angle were optimised. The choice of the cost functional is related to the missions of the vehicle and the possible conditions it may encounter. Therefore, three main cases are considered.

- The first corresponds to an autonomous underwater vehicle, where lift is not required and thrust with good propulsive efficiency is the main target (*basic* configuration).
- The second is the case of high thrust forces required. This may be useful in harsh atmospheric conditions (*thrust* configuration).
- The third is the case of an MAV where both lift and thrust are sought, with good propulsive efficiency (*practical* configuration).

As discussed in section 5.6, the mean angle of attack is imposed and the control is done on the other parameters.

5.7.1 Basic configuration

The best propulsive efficiency is usually obtained for very small thrust forces. Therefore, we aim at optimising the kinematics of a hydrofoil which may be used for an UAV to ensure both good thrust force and propulsive efficiency. The mean angle of attack is imposed equal to zero and the considered cost functional is:

$$\mathcal{L} = \bar{P} + 2\bar{F}U_0 + \epsilon_\alpha^2 \bar{\alpha}^2 + \epsilon_h^2 \bar{h}^2(t).$$

The weights ϵ_α^2 and ϵ_h^2 are set to 15.14 and 1, respectively, to avoid very large amplitudes of oscillations. The value of ϵ_α^2 is obtained by imposing that a heave amplitude $h_1 = 4$ has the same weight than a pitching amplitude $\alpha_1 = -45^\circ$ so as to give equivalent importance to the two terms of the cost of the control. The control is done in the case $N = 1$ for $f_r = 0.3665$ and $Re_c = 1100$, by acting on h_1 , α_1 and ϕ_1 . The optimal triplet is $(h_1, \alpha_1, \phi_1) = (2.82, -32.15^\circ, 85.45^\circ)$, yielding the triplet

$(C_T, C_L, \eta) = (0.512, 0, 0.502)$. The associated Strouhal number is equal to 0.329 inside the optimal range observed for a large number of animals in nature as discussed by Triantafyllou et al. (1993) and Taylor et al. (2003). This proves on the one hand that animals have naturally the ability to tune their motion to optimal kinematics and that the cost functional and the optimisation approach employed here, achieve successfully their principal target.

α_0	\mathbf{h}_1	α_1	ϕ_1	\mathbf{St}	γ_{\max}	\mathbf{C}_L	\mathbf{C}_P	\mathbf{C}_T	η
0°	2.820	-32.15°	85.45°	0.329	15.45°	0	1.020	0.512	0.502

Table 5.3: Optimal kinematics yielding good efficiency with limitation on the cost of the control for $N = 1$, $f_r = 0.3665$ and $Re_c = 1100$.

The optimal efficiency and thrust in table 5.3 is directly linked to the reduced flow separation during the motion of the wing and to the leading-edge vortex which remains attached during the whole stroke, before being shed and interacting constructively with the trailing-edge vortex, as discussed in §5.4 and 5.5.

The relatively small optimal efficiency is related to the low Reynolds number as discussed in §5.9 whereas the relatively moderate thrust is due to the constraints imposed on the cost of the control. It can be increased by eliminating the limitation on the cost of the control. Hence, by imposing $\epsilon_\alpha^2 = \epsilon_h^2 = 0$, we reach a new optimal solution summarized in table 5.4.

α_0	\mathbf{h}_1	α_1	ϕ_1	\mathbf{St}	γ_{\max}	\mathbf{C}_L	\mathbf{C}_P	\mathbf{C}_T	η
0°	3.926	-45.24°	83.13°	0.458	16.17°	0	1.641	0.806	0.491

Table 5.4: Optimal kinematics yielding good efficiency without limitation on the cost of the control for $N = 1$, $f_r = 0.3665$ and $Re_c = 1100$.

The consequence of eliminating the cost of the control is large-amplitude oscillations. However, higher thrust force is obtained without substantial decrease of the propulsive efficiency.

5.7.2 Thrust configuration

Here, high thrust coefficients are sought both in lifting and non-lifting configurations. The cost functional used is:

$$\mathcal{L} = (\bar{F} - F_0)^2,$$

where F_0 is an imposed value of the thrust force. Hence, for a given value of the thrust coefficient, the associated thrust force is evaluated and the optimisation is done on h_1 , α_1 and ϕ_1 until the required C_T is obtained. The mean angle of attack is imposed together with $f_r = 0.3665$ and $Re_c = 1100$. A summary of the results is given in table 5.5.

α_0	h_1	α_1	ϕ_1	St	γ_{\max}	C_L	C_P	C_T	η
0°	3.535	-32.12°	91.79°	0.412	31.25°	0	2.320	1.000	0.431
0°	4.063	-26.79°	87.16°	0.474	29.77°	0	3.956	1.500	0.341
0°	4.512	-33.45°	89.68°	0.526	26.27°	0	5.249	2.000	0.381
8°	3.477	-44.73°	90.19°	0.406	18.39°	0.606	1.202	0.500	0.416
10°	4.170	-43.59°	92.96°	0.487	28.24°	1.694	2.786	1.000	0.359
10°	4.341	-29.54°	91.89°	0.506	38.95°	1.861	5.208	1.500	0.288

Table 5.5: Optimal kinematics yielding imposed thrust coefficients for $N = 1$, $f_r = 0.3665$ and $Re_c = 1100$.

When the constraints on the cost of the control are eliminated, higher thrust coefficients are accessible but the strain, to which the wing is submitted, becomes a real issue. For such moderately large C_T , the propulsive efficiency remains acceptable for monochromatic oscillations. The values of St and γ_{\max} for the optimal configurations are not in the range of high propulsive efficiencies. In nature, animals employ two modes to optimise either their thrust or their efficiency. In the first mode, the interaction between the vortices generated by those shed from the flapping surface (wings or fish fins) is constructive. This implies that body vortices are paired with wing vortices of the same sign resulting in a stronger reverse von Karman street and better thrust. In the second mode, the interaction occurs between paired vortices of opposite signs. Hence, the foil extracts less energy increasing the efficiency. This refers to the vorticity shed from the body and the moving surface and confusion should not be made with the constructive interactions of the vorticity shed from the leading- and trailing-edges of the moving surface. The same principle may be applied to man-made vehicles. In the part of the mission when the duration of flight is favoured, the efficiency should be optimised, considering the *basic* configuration kinematics. Once the image capturing process is over or when the vehicle is tracked, kinematics may switch to the *thrust* configuration, favouring manoeuvring and/or high forward velocities.

Vorticity and relative horizontal velocity fields are plotted in figures 5.23 and 5.24 for a thrust coefficient $C_T = 1$ at $\alpha_0 = 10^\circ$. Due to the presence of a non-zero mean angle of attack, the symmetry is broken and the fields at $\frac{t}{T} = 1.625$ are not perfectly

the mirror image of those at $\frac{t}{T} = 1.125$.

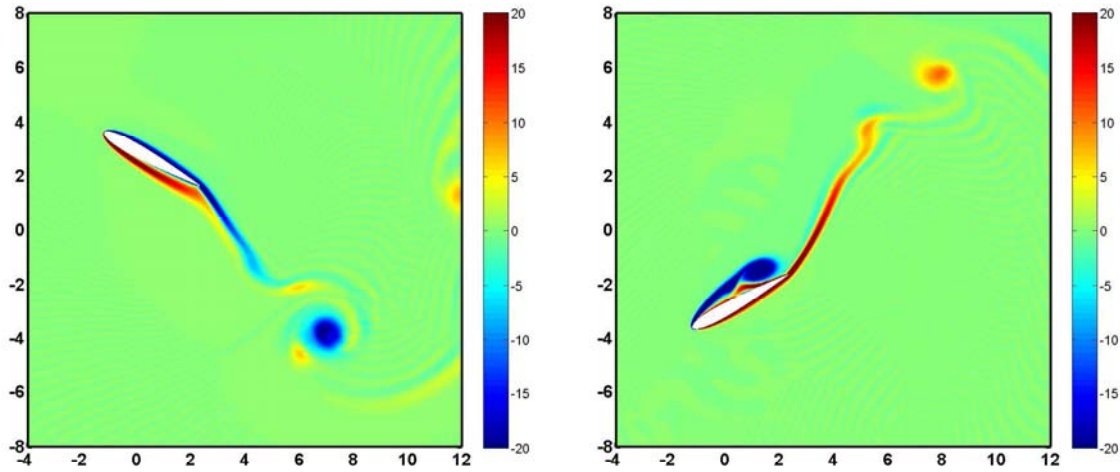


Figure 5.23: Vorticity fields during upstroke at $\frac{t}{T} = 1.125$ (left) and downstroke at $\frac{t}{T} = 1.625$ (right) for an optimised thrust coefficient $C_T = 1$ for $N = 1, \alpha_0 = 10^\circ, h_1 = 4.170, \tau_1 = 0^\circ, \alpha_1 = -43.59^\circ, \phi_1 = 92.96^\circ, f_r = 0.3665$ and $Re_c = 1100$.

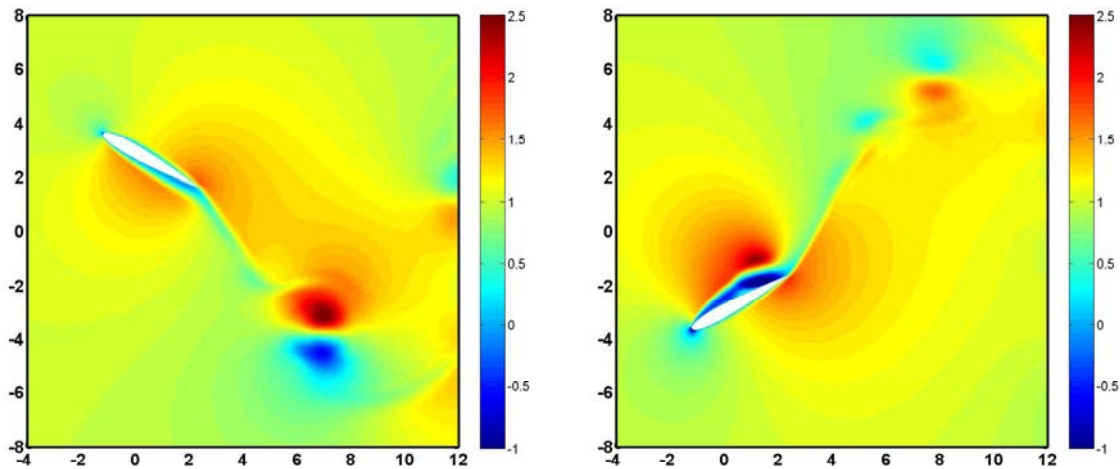


Figure 5.24: Relative horizontal velocity fields $\frac{u}{U_0}$ during upstroke at $\frac{t}{T} = 1.125$ (left) and during downstroke at $\frac{t}{T} = 1.625$ (right) for an optimised thrust coefficient $C_T = 1$ for $N = 1, \alpha_0 = 10^\circ, h_1 = 4.170, \tau_1 = 0^\circ, \alpha_1 = -43.59^\circ, \phi_1 = 92.96^\circ, f_r = 0.3665$ and $Re_c = 1100$.

Despite the high lift and thrust coefficients, the propulsive efficiency remains acceptable due to the leading-edge vortex which remains attached during the downstroke (see figure 5.23(b)) and due to the relatively confined regions or separated flow during the upstroke (see figure 5.24(a)). The relatively high γ_{\max} for the optimal thrust cases is not surprising since high thrust is related to large-amplitude oscillations. Likewise, it is not surprising to observe a decrease of the propulsive efficiency with respect to the latter case due to a larger region of separated flow.

5.7.3 Practical configuration

The *practical* solution is the one adapted to a micro air vehicle configuration. It implies sufficient lift and thrust forces, together with good propulsive efficiency. Therefore, the angle of attack is maintained constant equal to 8° and then to 10° , together with $f_r = 0.3665$ and $Re_c = 1100$. The values for the angles of attack are chosen in the range where thrust production is still possible and flow separation is limited, resulting in good propulsive efficiency. The optimisation is done with respect to the cost functional written as:

$$\mathcal{L} = \bar{P} + 2\bar{F}U_0 + \epsilon_\alpha^2 \bar{\alpha}^2 + \epsilon_h^2 \bar{h}^2(t).$$

First, the weights ϵ_α^2 and ϵ_h^2 are set to 15.14 and 1, respectively, to avoid very large amplitudes of oscillations. The optimal results are summarized in table 5.6. The thrust forces and the propulsive efficiency are moderate in this case.

α_0	\mathbf{h}_1	α_1	ϕ_1	St	γ_{\max}	\mathbf{C}_L	\mathbf{C}_P	\mathbf{C}_T	η
8°	3.397	-41.15°	84.95°	0.396	23.10°	0.790	1.240	0.516	0.419
10°	3.577	-45.47°	91.35°	0.417	19.95°	0.764	1.402	0.572	0.408

Table 5.6: Optimal kinematics yielding good thrust, lift and efficiency with limited oscillations for $N = 1$, $f_r = 0.3665$ and $Re_c = 1100$.

Second, vanishing values are given to ϵ_α^2 and ϵ_h^2 eliminating thus the limitations on the amplitudes of oscillations and giving rise to higher thrust coefficient and eventually higher propulsive efficiency.

The consequence is slightly larger η and relatively high thrust coefficient and, in counterpart, large amplitudes both for heaving and pitching as shown in table 5.7. The Strouhal number observed is not perfectly inside the range used by a large number of birds. This demonstrates that the motion of animals is adapted to fulfil more complex criteria than a simple high lift, thrust or efficiency. In addition, they should

be also able to manoeuvre, "battle" against wind gust, avoid fatigue and all this in the presence of elastic feathered surfaces which are not taken into account in the present study. Nonetheless, the optimal configurations described still can be applied to vehicles achieving the desired performances and further progress can be done consequently by including factors not yet accounted for.

α_0	h_1	α_1	ϕ_1	St	γ_{\max}	C_L	C_P	C_T	η
8°	3.957	-45.22°	90.85°	0.461	24.45°	0.874	2.063	0.885	0.429
10°	3.756	-46.29°	91.25°	0.438	22.59°	0.786	1.620	0.682	0.421

Table 5.7: Optimal kinematics yielding good thrust, lift and efficiency without limitation on oscillation amplitudes for $N = 1$, $f_r = 0.3665$ and $Re_c = 1100$.

5.8 High order harmonics

As observed in §5.7.2, the propulsive efficiency decreases when high thrust forces are sought. This behaviour is general since the maximum of η occurs often for very small values of C_T and then decreases for larger thrust forces. This explains also why the optimal C_T is relatively low when the high efficiency was favoured in the *basic* configuration. The reason is that at high Strouhal numbers, the effective angle of attack "seen" by the airfoil does not vary sinusoidally anymore and multiple peaks appear together with sharp variations altering the vortical dynamics in a relevant way. These irregularities in the effective angle of attack may be eliminated through modifications to either or both the heaving and the pitching motions. Here, we consider a correction on the heave in the same way as Read et al. (2003). In their experimental work, they imposed an effective angle of attack $\gamma(t)$ and they computed the super-harmonics components in $\dot{h}(t)$ which may cancel the undesirable variation in the pitching angle $\alpha(t)$. They demonstrated that eliminating the multiple peaks is possible by acting on the odd harmonics, namely the third and the fifth ones. Here, a different approach, in the same spirit, is done to recover the decrease of η . First, we impose that the heaving motion is monochromatic and we seek the heaving amplitude h_1 which yields a given thrust force. This work is done for various pitching amplitudes, and for each one of them, the propulsive efficiency is reported. Then, the heaving motion is imposed as:

$$h(t) = h_1 \sin(t + \tau_1) + h_3 \sin(3t + \tau_3) + h_5 \sin(5t + \tau_5),$$

together with

$$\alpha(t) = \alpha_1 \sin(t + \phi_1).$$

The angles $\alpha_0, \alpha_1, \phi_1$ and τ_k for $k \in \{1, 3, 5\}$ are imposed and the amplitudes h_1, h_3 and h_5 are optimised to yield a given thrust force as in §5.7.2. This is also done for various values of the pitching amplitude and the propulsive efficiency is compared to the monochromatic case.

The impact of the high order terms is to include higher frequencies components in the foil motion. This renders the numerical stability condition more severe by imposing a smaller threshold for the time step and leads to high-frequency oscillations for the aerodynamic forces (cf. the vertical force in figure 5.25). This is another reason for limiting the amplitudes of oscillations since very large amplitudes would lead to a sinusoidal trajectory of the vehicle rather than straightforward motion.

However, the transient is not longer and one period of oscillation remains sufficient for the flow establishment. Despite the excessively high lift forces in this case, the average lift coefficient vanishes due to the fact that the mean angle of attack α_0 is zero.

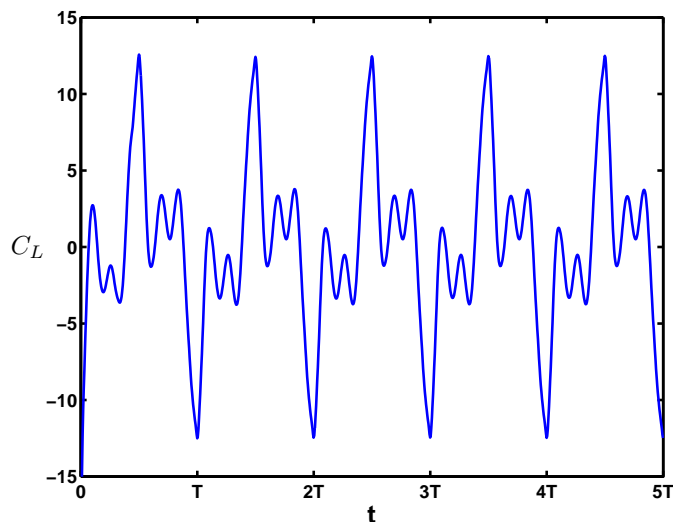


Figure 5.25: Temporal evolution of vertical force for long simulations with high order harmonics in the case $N = 3, \alpha_0 = 0^\circ, h_1 = 3.524, h_3 = 0.719, h_5 = 0.212, \tau_1 = \tau_3 = \tau_5 = 0^\circ, \alpha(t) = -35^\circ \sin(t + 90^\circ), f_r = 0.3665$ and $Re_c = 1100$.

5.8.1 Optimised high order harmonics configurations

For the case of monochromatic oscillations, figures 5.26 and 5.27 show the variations of the propulsive efficiency and the thrust coefficient with respect to the Strouhal number for various pitching angles. As described previously, for a given pitching

angle, the control is done on the heaving amplitude until a given value of the thrust is found. This is done for a constant reduced frequency, i.e. the variations of the Strouhal number are purely due to the variations of h_1 . While C_T increases with St , η has a maximum for an increasing Strouhal number when the pitching amplitude is varied from -15° to -45° . Higher thrust coefficients are also obtained for large-amplitude oscillations. For small pitching amplitudes ($\alpha_1 \in [-15^\circ, -25^\circ]$), and due to relatively smaller peak value, the decrease of η is very fast preventing the possibility of using this range of angles in high thrust configurations. The values of η for high thrust coefficients are better for $\alpha_1 = -35^\circ$ and especially for $\alpha_1 = -45^\circ$. To improve this loss of performance, the high order terms are included.

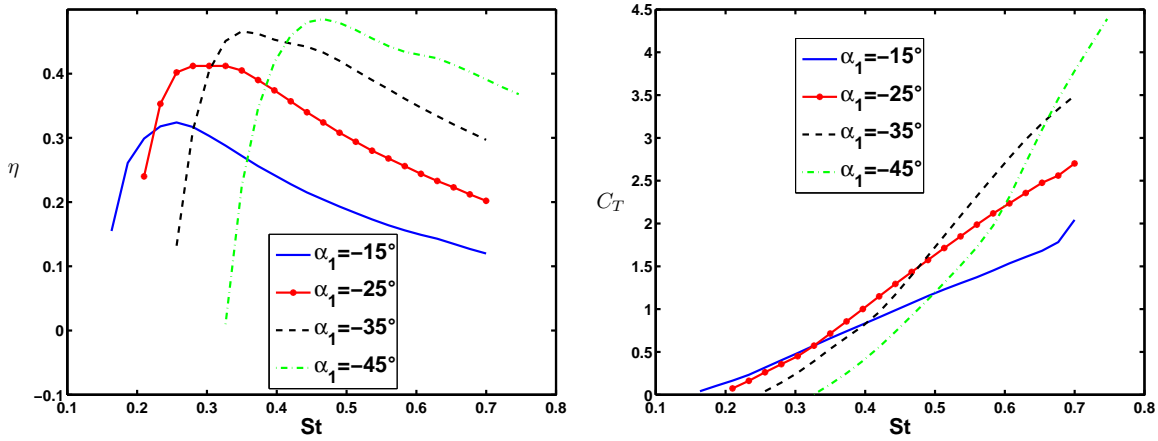


Figure 5.26: Variation of the propulsive efficiency (left) and the thrust force (right) with the Strouhal number for various pitching amplitudes and $N = 1$, $\alpha_0 = 0^\circ$, $0^\circ\tau_1 =$, $\phi_1 = 90^\circ$, $f_r = 0.3665$ and $Re_c = 1100$.

In figure 5.28, the efficiency is plotted versus the thrust coefficient for $\alpha_1 = -25^\circ$ and $\alpha_1 = -35^\circ$, with and without the higher order terms. For $\alpha_1 = -25^\circ$, results shows clearly that for C_T larger than 1, the odd harmonics yield a better efficiency than the monochromatic oscillations. The improvement can climb up to 21%, as in the case of $C_T = 2.75$. The difference is even larger when smaller amplitudes of pitching are considered ($\alpha_1 \in [-5^\circ, -15^\circ]$). However, even the improved efficiency for these cases is too low, which makes non-practical any use of this range. Moreover, the inclusion of high order terms allows reaching more easily higher C_T , since, for instance, in the case $\alpha_1 = -25^\circ$, a $C_T = 3$ was not accessible with monochromatic oscillations. The summary of the kinematics yielding the imposed thrust coefficient for the $N = 5$ case are given in table 5.8.

The importance of the amplitude of the higher order terms increases when the required thrust increases. This implies a higher Strouhal number due to larger maximal amplitude of oscillations and a higher effective angle of attack γ_{\max} . Naturally, the power required to the engine becomes very important for such thrust forces, but it is smaller when the higher harmonics are included.

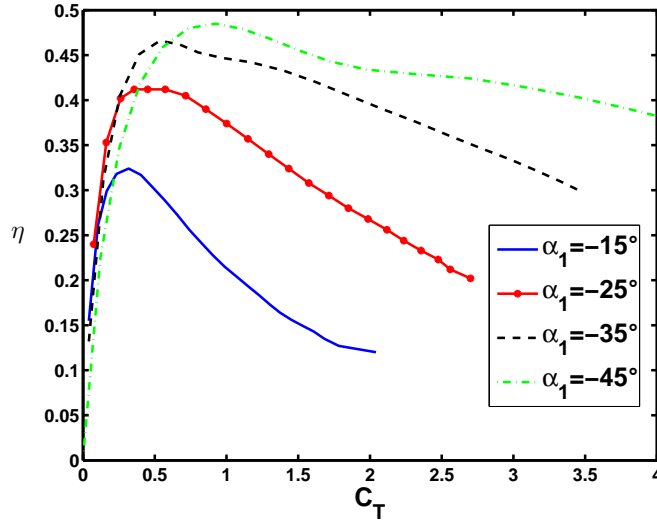


Figure 5.27: Variation of the propulsive efficiency with the thrust force for various pitching amplitudes and $N = 1$, $\alpha_0 = 0^\circ$, $\tau_1 = 0^\circ$, $\phi_1 = 90^\circ$, $f_r = 0.3665$ and $Re_c = 1100$.

h_1	h_3	h_5	α_1	ϕ_1	St	γ_{\max}	C_T	η
3.247	0.452	0.012	-25°	90°	0.330	34.67°	1.300	0.374
3.505	0.503	0.104	-25°	90°	0.362	38.75°	1.600	0.323
3.589	0.608	0.223	-25°	90°	0.374	42.32°	2.000	0.280
3.670	0.681	0.225	-25°	90°	0.375	43.25°	2.250	0.265
4.102	0.694	0.144	-25°	90°	0.414	43.43°	2.500	0.258
4.241	0.720	0.195	-25°	90°	0.433	44.70°	2.750	0.245
4.352	0.833	0.211	-25°	90°	0.435	45.96°	3.000	0.243

Table 5.8: Optimal kinematics yielding imposed thrust for $N = 5$ acting on odd harmonics together with $\alpha_0 = 0^\circ$, $f_r = 0.3665$ and $Re_c = 1100$.

The comparison is less advantageous in the case $\alpha_1 = -35^\circ$ since some high order optimised configurations are found they yield a smaller efficiency than monochromatic oscillations, and since the maximal increase of η , observed in the case of $C_T = 3$, does not exceed 7%. This is due to the relatively higher efficiency obtained for this

pitching angle for large thrust forces, highlighted by the slower decrease of η (cf. figure 5.27). The other possible reason is the possibility to find a different combination of h_1 , h_3 and h_5 giving rise to the same thrust force but with higher efficiency. The solutions, summarized in table 5.9, are obtained starting from a given set of initial values and the optimal result is that having the initial conditions sufficiently close to the local optimal solution. Despite the fact that starting from different initial conditions yielded always the same optimum, there is no proofs of the uniqueness. The higher efficiency in this case is due to lower maximum effective angle of attack limiting the flow separation and to values of the Strouhal number closer to the optimal range.

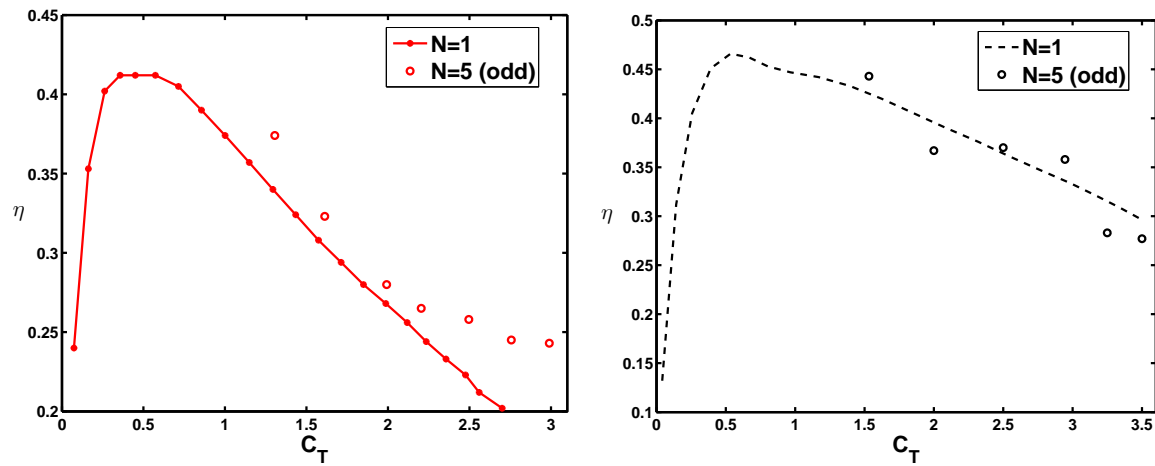


Figure 5.28: Influence of the high order terms on the efficiency versus thrust coefficient variations for $\alpha_1 = -25^\circ$ (left) and $\alpha_1 = -35^\circ$ (right) for $\alpha_0 = 0^\circ$, $\tau_1 = \tau_3 = \tau_5 = 0^\circ$, $\phi_1 = 90^\circ$, $f_r = 0.3665$ and $Re_c = 1100$.

We notice that the behaviour of the high order terms is quite similar for these two angles, with an increasing amplitudes for increasing thrust forces. We may highlight, for instance, that almost the same heaving motion is needed for both angles to produce a thrust coefficient equal to 2.5. The inclusion of the higher order terms is even less interesting in the case $\alpha_1 = -45^\circ$, where only the case $C_T = 1.75$, yielded a 1.8% increase of η by passing from 0.443 in the monochromatic case to 0.451 for $N = 5$. The associated optimal amplitudes are $h_1 = 4.032$, $h_2 = 0.703$ and $h_3 = 0.200$. The inclusion of the higher order terms for $\alpha(t)$ and/or the optimisation of the pitching amplitudes and phase angles is possible, however, the computational cost will be even more relevant.

In figure 5.29, the heaving motion $h(t)$ and the associated effective angle of attack γ yielding a thrust coefficient $C_T = 2.75$ at $\alpha_1 = -25^\circ$ are plotted for both $N = 1$ and $N = 5$. The heaving motion becomes flattened out when high order terms are included and the norm of the heaving motion, based on the maximal value reached over a period, decreases implying a smaller Strouhal number closer to the most efficient range; consequently, a higher η is observed. The effective angle of attack experiences steepest variations and a multi-peak configuration. This result is also different from the shape of the effective angle of attack observed when the heaving and pitching amplitudes were optimised in §5.4. However, in that case, the optimal cost function was in a range of thrust forces much lower than here, which may explain this difference.

h_1	h_3	h_5	α_1	ϕ_1	St	γ_{\max}	C_T	η
3.748	0.506	0.017	-35°	90°	0.330	27.98°	1.500	0.443
3.524	0.719	0.212	-35°	90°	0.352	32.96°	2.000	0.367
4.078	0.708	0.140	-35°	90°	0.410	33.43°	2.500	0.370
4.501	0.696	0.103	-35°	90°	0.456	33.99°	3.000	0.358
3.998	0.748	0.496	-35°	90°	0.437	37.63°	3.250	0.283
3.942	0.943	0.438	-35°	90°	0.401	39.93°	3.500	0.277

Table 5.9: Optimal kinematics yielding imposed thrust for $N = 5$ acting on odd harmonics together with $\alpha_0 = 0^\circ$, $f_r = 0.3665$ and $Re_c = 1100$.

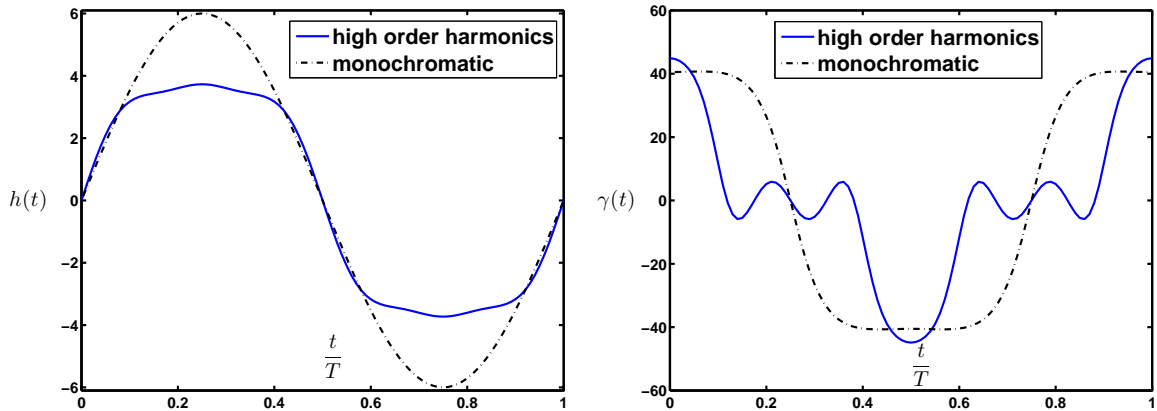


Figure 5.29: Influence of the high order terms on the heaving motion (left) and on the effective angle of attack (right).

This is not in contradiction with what Read et al. (2003) obtained experimentally, because in their case, $\gamma(t)$ was imposed and they found that multiple peaks and sharp variations should be eliminated in $\alpha(t)$. In our case, $\alpha(t)$ is imposed, and the efficiency increases when the heave motion is smooth and flat. This conclusion, highlighted by figure 5.29(a) can be generalised. Therefore, computations of high order oscillations have been performed (without the optimisation approach) to understand the influence of heave motion profiles on both thrust and efficiency.

5.8.2 Non-optimised configurations

Here, the heave motion is written more generally as:

$$h(t) = h_1 \sin(t) + h_2 \sin(2t) + h_3 \sin(3t) + h_4 \sin(4t) + h_5 \sin(5t),$$

together with:

$$\alpha(t) = -35^\circ \sin(t + 90^\circ).$$

A sample of the computations performed is given in table 5.10. The last column is the value of the efficiency for the monochromatic oscillations extrapolated from the curve for $\alpha_1 = -35^\circ$ in figure 5.27. The symbol $-$ is given when no such high thrust forces have been obtained for $N = 1$.

#	h_1	h_2	h_3	h_4	h_5	St	γ_{\max}	C_T	η	$\eta_{(N=1)}$
1	3.40	0	0.50	0	0.1	0.35	28.19°	1.32	0.443	0.436
2	2.75	0.50	0.50	0.50	0.50	0.35	39.36°	1.94	0.198	0.399
3	4.00	0.95	0.50	0	0	0.50	35.95°	2.16	0.307	0.385
4	2.00	0	1.75	0	0.50	0.35	80.61°	2.63	0.143	0.356
5	4.50	0	0.75	0	0.20	0.47	36.17°	3.30	0.326	0.317
6	4.00	1.00	0.62	0.62	0	0.50	40.22°	3.62	0.266	-
7	4.80	0	0.75	0	0.25	0.50	36.80°	3.68	0.315	-
8	1	0	1.825	0	1	0.35	94.57°	4.85	0.144	-
9	2.70	0	2.70	0	0.5	0.50	89.00°	8.89	0.187	-

Table 5.10: Non-optimised kinematics for high order harmonics together with $\alpha_0 = 0^\circ, \alpha_1 = -35^\circ, \phi_1 = 90^\circ, f_r = 0.3665$ and $Re_c = 1100$.

The comparison of the motion $h(t)$ and $\gamma(t)$, between the case 1, where the high order terms increases the efficiency, and cases 2 and 4, where they highly decrease it, confirms the interest of flat function without multiple peaks (see figure 5.30(a)). In general, favourable cases are observed when the amplitude of the terms $N > 1$ are smaller than the fundamental amplitude. Consequently, the higher terms should

be seen as a correction of the heave motion. When the terms are of the same order of magnitude, larger thrust forces are generated such as the extremely high value observed in case number 9. Despite this, the efficiency is very low, like in all the other cases where γ_{\max} exceeds 40° see figure 5.30(b). Even if the number of peaks in the curve of $\gamma(t)$ is increased with respect to the monochromatic oscillations, it is clear in figure 5.30(b) that case 1, which increased the efficiency, corresponds to smoother function (independently from the figure scale).

In conclusion, the high orders terms may be advantageous for small pitching angles, where the decrease of the efficiency is much faster when the thrust increases. They can also be applied for large amplitudes of pitching oscillations, but in all cases, higher harmonics should be a small correction of the fundamental, flattening the heave motion and avoiding a relevant increase to the maximal effective angle of attack.

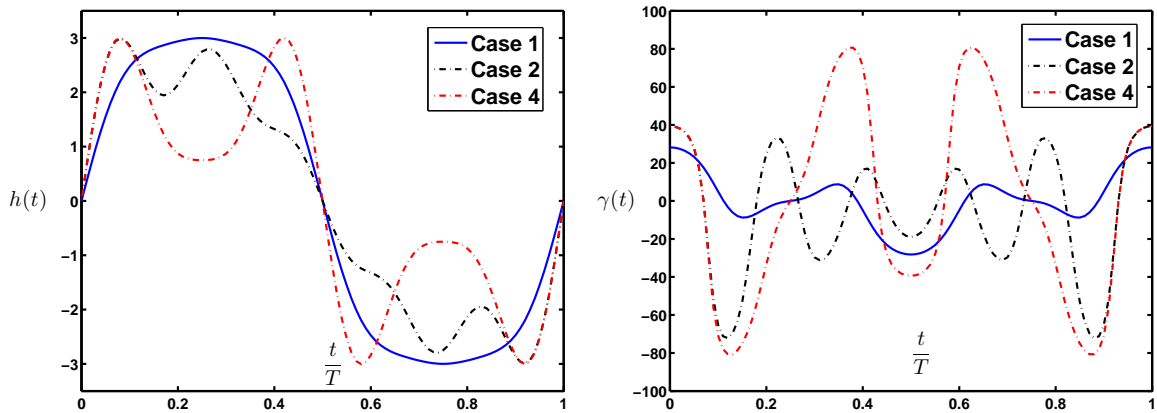


Figure 5.30: Heave motion (left) and effective angle of attack (right) for various high-order configurations.

5.9 Frequency and Reynolds number effects

The value of the propulsive efficiency reached in the optimal configurations may seem small since the highest value was roughly 50%, obtained for vanishing mean angle of attack α_0 . Furthermore, the thrust coefficients may also seem modest for configurations supposed to be optimal. This may be misleading by implying that the optimisation approach is not efficient or that propulsion by flapping foils is not as reliable as expected. A rebuttal to the second statement can be made by citing

the numerous experimental measurements accomplished on animals and foils where flapping resulted in propulsive efficiencies as high as 87% (Anderson, 1996; Read et al., 2003). On the other hand, two main reasons justify the relatively low maximal efficiency in the present work. The first is that the maximal efficiency was not at any moment the real target of the optimisation, i.e. the efficiency was not considered directly in the cost functional. As discussed in §5.8 and shown in figure 5.27, the peak of η occurs for low thrust coefficients and a more or less slow decay follows. Consequently, it is more interesting to set the motion slightly beyond this peak value, where higher thrust forces are accessible without relevant loss of the efficiency. The second reason is the low Reynolds number of the present simulations. The value of $Re_c = 1100$ has been chosen because it is a well documented case in the literature which requires an affordable computational cost. However, for such a value of the Reynolds number, the viscous effects are very important and they influence the flow around the airfoil and the vortical patterns. One consequence of viscosity is the high angle of attack for which the peak of the lift occurs (cf. figure 5.19) and another is a lower propulsive efficiency. Moreover, both thrust and efficiency depend on the physical frequency of flapping, which has been maintained constant in time for the moment, and should instead be varied. High frequencies of oscillations produce much larger thrust forces.

5.9.1 Reynolds number effect

Fixing all the other parameters, the Reynolds number is varied in the range [1000,4000] and the propulsive efficiency is plotted in figure 5.31. Results for the configuration $N = 1, \alpha_0 = 0^\circ, h_1 = 3, \tau_1 = 0^\circ, \alpha_1 = -35^\circ, \phi_1 = 90^\circ$ and $f_r = 0.3665$ show an increase of 8.7% of the propulsive efficiency when the Reynolds number increases from 1000 to 4000. The increase of η is due mainly to the increase of the thrust force when $Re_c \in [1000, 1500]$, whereas it is due to the decrease of the required power for $Re_c \in [1500, 4000]$.

The higher efficiency is related to more concentrated vortices in the wake. These vortices are less spread and closer to each others as shown in figure 5.32(a) where favourable interactions occur between the leading- and trailing-edges vorticity. Naturally, the boundary layer thickness decreases and further increase of the Re_c would transform the wake into a sheet of vorticity.

The variation in terms of C_T between the maximal and minimal values for $Re_c \in [1000, 4000]$ is of the same order of magnitude than the variation of η . Consequently, the natural question to answer is whether the optimal kinematics, found for $Re_c = 1100$, remains optimal for higher Reynolds number of practical use, since both the efficiency and the thrust forces depend on the Re_c . The answer is probably

positive. Comparisons in the literature between experiments and numerical simulations for $Re_c = 40000$ and 1000 respectively, showed a much higher dependence of η with respect to Re_c than C_T (Anderson et al., 1998; Guglielmini and Blondeaux, 2004). The reason is that the thrust force is related to the pressure distribution whereas the propulsive efficiency is related to both pressure and viscosity. The conjecture is that the pressure fields depend less on the Reynolds number than the viscous effects as long as Re_c remains in the range $[10^3, 10^5]$.

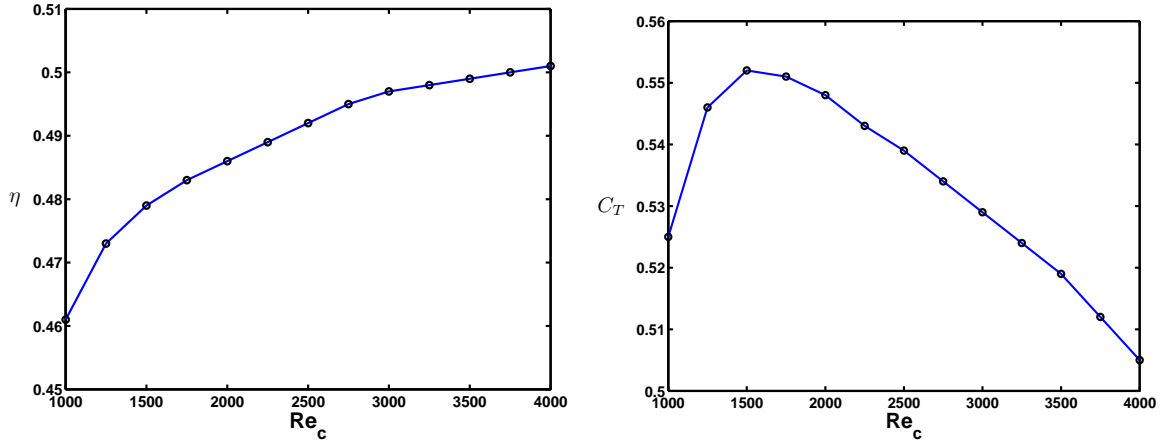


Figure 5.31: Variation of the propulsive efficiency (left) and the thrust force (right) with the Reynolds number for $N = 1, \alpha_0 = 0^\circ, h_1 = 3, \tau_1 = 0^\circ, \alpha_1 = -35^\circ, \phi_1 = 90^\circ$ and $f_r = 0.3665$.

The pressure distributions over the airfoil are plotted for $Re_c = 1100$ and $Re_c = 3500$ in figure 5.33. Here again, and despite the positive value of the coefficient, the upper curve corresponds to the suction side. The pressure coefficient experiences higher values and steepest compressions are observed in the case of high Re_c . The plateau followed by a second compression at the pressure side at $t = 1.125T$ is related to the presence of a separation bubble which reattaches as one may see in figure 5.32. The variation in C_{pr} is in contradiction with the fact that the pressure fields are less dependent on Re_c . A first explanation can be that the size of the investigated range of Reynolds numbers is limited. Over larger ranges, the variations of η are expected to be larger reaching roughly the value of 90%, observed experimentally. Over the same wide range, C_T should be less sensitive. The more plausible explanation is that when Re_c is increased, the hierarchy remains respected: if the thrust force for a first set of parameters is higher than the thrust force for a second set of parameters at $Re_c = 1100$ this is also true at $Re_c = 3500$, despite the different values of C_T together with a larger η for the larger Re_c .

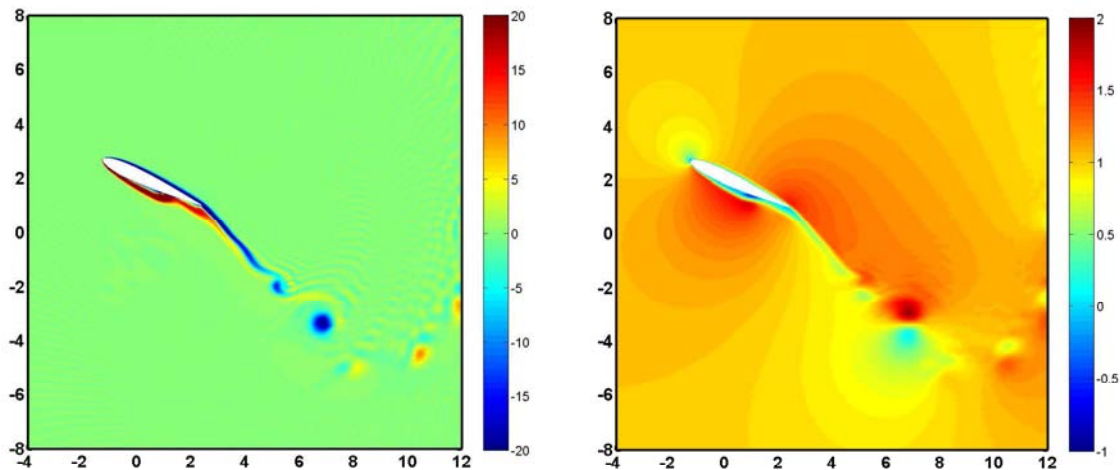


Figure 5.32: Vorticity and relative horizontal velocity ($\frac{u}{U_0}$) fields at $\frac{t}{T} = 1.125$ for $N = 1, \alpha_0 = 0^\circ, h_1 = 3, \tau_1 = 0^\circ, \alpha_1 = -35^\circ, \phi_1 = 90^\circ, f_r = 0.3665$ and $Re_c = 3500$.

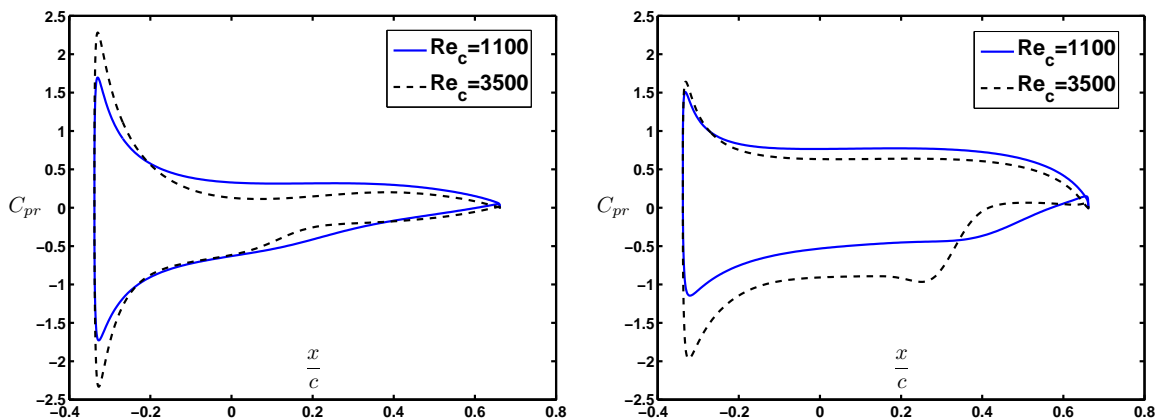


Figure 5.33: Comparison of the pressure coefficient on the airfoil for $Re_c = 1100$ and $Re_c = 3500$ at $t = 2\pi$ (left) and $t = 2.25\pi$ (right) for $N = 1, \alpha_0 = 0^\circ, h_1 = 3, \tau_1 = 0^\circ, \alpha_1 = -35^\circ, \phi_1 = 90^\circ$ and $f_r = 0.3665$.

No simulations were carried out for Reynolds number larger than 4000 due to their prohibitive computational cost, but the optimisation for the *basic* configuration has been carried out for $Re_c = 3000$. The cost functional is the same with the weights (1,2,15,14,1) respectively. The time-step was further reduced for this case. Close optimal kinematics are reached since the triplet $(h_1, \alpha_1, \phi_1) = (2.854, -34.28^\circ, 83.90^\circ)$ has

been found, yielding $C_T = 0.532$ and $\eta = 0.573$. Compared to the case $Re_c = 1100$, the increase of the propulsive efficiency is equal to 14% whereas the variation on the thrust force is within 4%.

In conclusion, the optimal configurations found in §5.7 should remain optimal for higher Reynolds number with the advantage of higher η . Moreover, even without reaching very high values of η and remaining in the range of 50% – 60%, the flapping flight has advantages over the fixed-wing flight as further discussed in Appendix A.

5.9.2 Reduced frequency effect

The physical frequency of oscillations f^* has a direct influence on whether the airfoil produces thrust or drag and on the general topology of the wake. Two non-dimensional numbers depend on this frequency: the Strouhal number and the reduced frequency, defined as:

$$St = \frac{f^* A^*}{U_\infty^*} = \frac{\sigma^* \|h^*(t^*)\|}{\pi U_\infty^*} = \frac{f_r \|h(t)\|}{\pi}, \quad f_r = \frac{\sigma^* \lambda^*}{U_\infty^*}.$$

On the other hand, two Reynolds number were defined and related to each others:

$$Re_c = \frac{U_\infty^* c^*}{\nu^*}, \quad Re = \frac{\sigma^* \lambda^{2*}}{\nu^*}, \quad Re_c = \frac{4Re}{f_r}.$$

Until now, the Strouhal number variations were due to modification of the heave amplitude and consequently the wake width. Here, the physical frequency of the motion is varied. This modifies the reduced frequency, and consequently, the Strouhal number and the flapping Reynolds, while Re_c is maintained constant equal to 1100. This is done for three configurations that have already been optimised in §5.4, 5.5 and 5.7.2 for constant reduced frequency $f_r = 0.3665$.

- Configuration 1: optimised pitching amplitude: $\alpha_0 = 0^\circ, h_1 = 2.5, \alpha_1 = -31.91^\circ$ and $\phi_1 = 90^\circ$, yielding $C_T = 0.280$ and $\eta = 0.423$.
- Configuration 2: optimised phase angle: $\alpha_0 = 0^\circ, h_1 = 3, \alpha_1 = -35^\circ$ and $\phi_1 = 80.5^\circ$, yielding $C_T = 0.526$ and $\eta = 0.481$.
- Configuration 3: optimised thrust force: $\alpha_0 = 8^\circ, h_1 = 3.477, \alpha_1 = -44.74^\circ$ and $\phi_1 = 90.19^\circ$, yielding $C_T = 0.500$ and $\eta = 0.416$.

In figure 5.34, the reduced frequency is varied in the range $[0, 1]$. Results show a large increase of the thrust coefficient with the reduced frequency, due to an increase of the Strouhal number, as in figure 5.26(b). The high values reached are very attractive but the associated efficiencies render them less applicable.

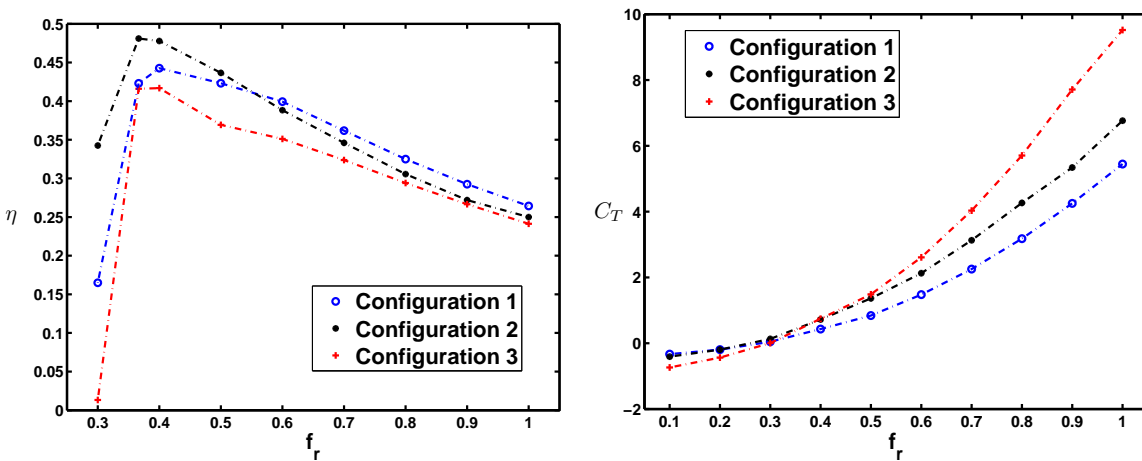


Figure 5.34: Effect of the reduced frequency on the the propulsive efficiency (left) and thrust coefficient (right) for $Re_c = 1100$.

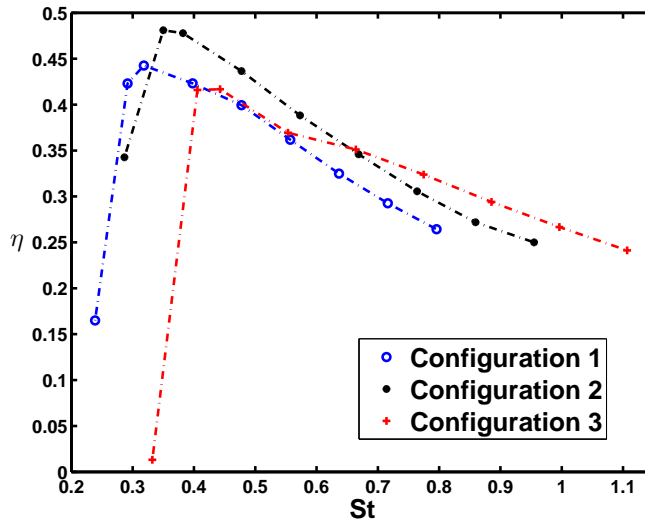


Figure 5.35: Effect of the Strouhal number on the propulsive efficiency by modifying the flapping frequency.

For small reduced frequencies ($f_r < 0.3$), and for the kinematics imposed here, a classical von Karman street is produced together with a drag force. Furthermore, the maximal propulsive efficiency is in the range, $f_r \in [0.3, 0.4]$. This justifies the choice of carrying out the case of constant $f_r = 0.3665$, when the other control parameters are studied. In terms of the Strouhal number, this corresponds to $St \in [0.3, 0.4]$ close to the optimal range found by Triantafyllou et al. (1993) and used by a many

animals as shown by Taylor et al. (2003) and Bejan and Marden (2006) (see figure 5.35).

5.10 Gliding

Birds' flight can be divided into four categories which are *flapping*, *soaring*, *gliding* and *hovering*. The main difference between these modes is the number of cycles the wings achieve per unit of time. Some birds are more adapted to some configurations. For instance, the hummingbirds are true hoverers, able to flap their wings with a frequency in the vicinity of 60 Hz to produce enough lift to sustain their weight, without any forward speed. Eagles and hawks are very good in soaring configuration, since they may use their wings motion occasionally with one or two minutes between beats. They use the thermal difference of air, rising with warm air and descending with cold one. The gliding configuration is used by a large number of birds, even though, some species, like albatross, are real gliders since they use the motion of their wings almost only during landing and take-off. The principle is that the bird uses its weight to overcome air resistance to its forward motion. The aim is to cover the maximal distance losing the smallest possible height. This ratio can reach one meter of height lost for 20 meters of forward motion on species like the black vultures. The increase of the forward speed during gliding results in a faster descent. However, the distance travelled remains almost constant, a result of the principle of energy conservation and the equilibrium between potential and kinetic energies. Birds may also gain height during gliding phases due to vertical air columns. This same mechanism, used by gliders' pilots, is accessible in presence of hills or thermal plumes.

In the present section, a non-exhaustive investigation of this mechanism is carried out. The solver allows to impose the heave and pitching motion of the wing. Therefore, the flow is solved over an airfoil which performs an alternance of flapping motion and gliding. A large number of parameters could be taken into account, and eventually optimised in the future. The most important between them are the duration of the motion and the gliding phases, the position in which the wing stops to flap and the way in which it does it. The variation of the bird's mass of the body can also be taken into account since gliding birds travel long distances with a stored amount of energy within their body, a mass that they lose progressively. The first parameter concerning the duration is governed by the will to avoid the fall down of the bird. This implies a sufficient forward speed ensuring lift and thrust. Birds are perfect closed-loop controlled system. They stop their wing in the optimal position avoiding fast losses of height, forward velocity or lift. They adapt the angle of attack and the camber of their wings during gliding in a way to accomplish the maximal distance

before restarting to flap. Here, the bird is supposed to fly with the same velocity during the flapping and the gliding phases. This means that, for an adequate angle of attack, the lift force is ensured, but the thrust force of the bird, during the flapping phase, will decrease due to the loss of energy of the drag forces. Therefore, we may estimate the duration of the gliding phase at a given velocity before the thrust force vanishes. Furthermore, the airfoil may stop flapping at any position thanks to a slowing law. In the present work, and since gliding is not the core of this manuscript, the stop is done impulsively, i.e. with a discontinuity of a kinematic variable. This discontinuity can be for the acceleration or the velocities following the position of the still airfoil. Consider the heave and the pitch motion written as:

$$\begin{cases} h(t) = h_1 \sin(t), & \dot{h}(t) = h_1 \cos(t), & \ddot{h}(t) = -h_1 \sin(t), \\ \alpha(t) = \alpha_1 \sin(t + \phi_1), & \dot{\alpha}(t) = \alpha_1 \cos(t + \phi_1), & \ddot{\alpha}(t) = -\alpha_1 \sin(t + \phi_1). \end{cases}$$

If $\phi_1 = 90^\circ$, stopping at $t = \frac{\pi}{2}$ (or $t = \frac{3\pi}{2}$) implies a discontinuity on the heaving acceleration and the pitching velocity, whereas stopping at $t = \pi$ (or $t = 2\pi$) leads to discontinuity on heaving velocity and pitching acceleration. A vanishing value of ϕ_1 leads to discontinuity on the same variables of heaving and pitching. Preliminary computations showed a divergence in the case of a discontinuity of the heave velocity. This corresponds to stopping in the position of a vanishing $h(t)$ where the heaving velocity is maximal in amplitude. Therefore, the airfoil was stopped at $h(t) = \pm h_1$. Moreover, the position ($h(t)$ and $\alpha(t)$) were maintained constant during the gliding duration. Consequently, the angle of attack is constant equal to α_0 if we stop at $t = \frac{\pi}{2}$ or $t = \frac{3\pi}{2}$ for $\phi_1 = 90^\circ$. The main target is to estimate the gliding duration and to infer whether the gliding phase increases the global propulsive efficiency of the animal. Therefore, we consider, for the case $N = 1, h_1 = 3, \tau_1 = 0^\circ, \alpha_1 = -35^\circ, f_r = 0.3665$ and $Re_c = 1100$, a series of simulation summarized in table 5.11 where T_{stop} is the instant when the airfoil stops flapping, $T_{restart}$ is the instant of in which it restarts to flap from the same position where it stopped and T_{finish} is the final instant, indicating the total duration of the simulation.

C_T and η in figure 5.36 are averaged values at the generic time t_0 obtained as:

$$C_T(t_0) = \frac{1}{t_0} \int_0^{t_0} C_T(t) dt, \quad \eta(t_0) = \frac{1}{t_0} \int_0^{t_0} \eta(t) dt.$$

A long time, corresponding to 5 times the flapping duration, is required before the thrust force vanishes, when the airfoil is moving at a constant forward velocity. However, it is rather deceiving to observe that the propulsive efficiency drops as soon as the flapping motion stops. In the gliding phase, the power required for flapping

vanishes and the non-averaged instantaneous horizontal force corresponds to the drag of the NACA0012 airfoil at this Reynolds number. Therefore, η is influenced by both the advantageous effect on the power and the negative effect on the thrust. In this case, the effect of the drag is dominant, leading to an average decrease of the propulsive efficiency. This imply that the bird would stop flapping for the only reason of stopping the consumption of energy and relaxing its muscles. However, the real configuration is much more complex than those simulated here, since the angle of attack of the wing, its position and the velocity of the bird are modified and adapted during the gliding period. A bird would favour during its gliding period the mean angle of attack yielding the maximum lift-to-drag ratio. On the other hand, a decrease of the forward velocity implies a decrease of the lift force that the animal should recover with an increase of the angle of attack to sustain its weight. This behaviour is also recovered for the case 2, 3 and 4.

Case	α_0	ϕ_1	\mathbf{T}_{stop}	$\mathbf{T}_{\text{restart}}$	$\mathbf{T}_{\text{finish}}$	Gliding position
1	0°	90°	4.5π	N/A	20π	$h(t) = 3, \alpha(t) = 0^\circ$
2	10°	0°	4.5π	10.5π	20π	$h(t) = 3, \alpha(t) = -35^\circ$
3	10°	90°	6.5π	12.5π	20π	$h(t) = 3, \alpha(t) = 0^\circ$
4	10°	90°	7.5π	13.5π	20π	$h(t) = -3, \alpha(t) = 0^\circ$

Table 5.11: List of the gliding configuration simulated for $N = 1, h_1 = 3, \tau_1 = 90^\circ, \alpha_1 = -35^\circ, f_r = 0.3665$ and $Re_c = 1100$.

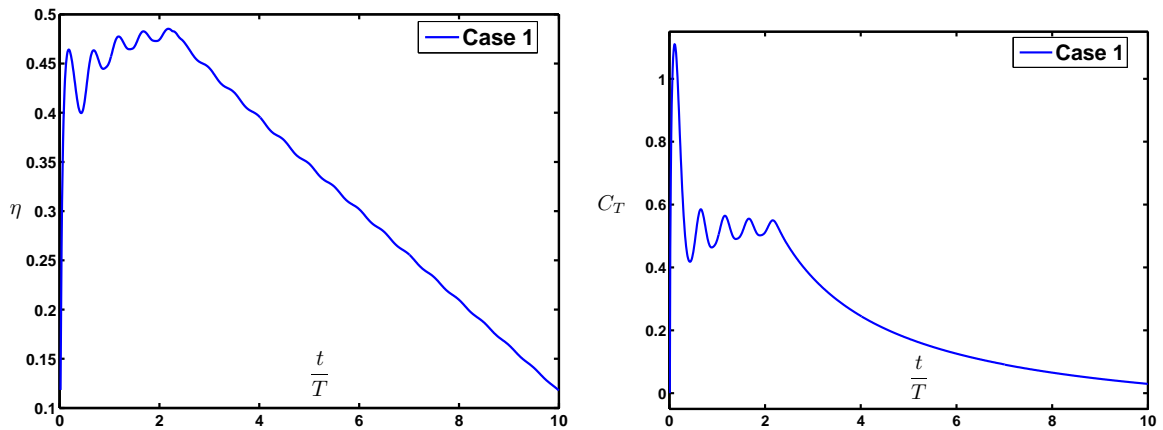


Figure 5.36: Temporal evolution of the propulsive efficiency (left) and the thrust force (right) during the gliding phase for Case 1.

In figure 5.37, the instantaneous lift and thrust forces are plotted for the whole duration of the simulations. We noted that 8 periods of oscillation time were necessary before the vanishing of C_T . Here, and due to the presence of a mean angle of attack α_0 , a shorter time of 6π was considered for gliding. Cases 3 and 4 differ from each others by a simple time translation of the curves showing the perfect establishment of a periodic flow after the transients. This is not surprising since the angle of attack of the airfoil is the same, whether it stops at the maximal or the minimal heave position. Case 2 is very different since a vanishing phase angle leads to a maximal angle of attack equal to $\alpha_0 + \alpha_1$ during the gliding phase. Consequently, the lift forces are much larger during gliding but the drag forces increases to non affordable levels. In this case, the average horizontal force changes sign even in less than 6π time. This can be seen as another advantage of considering pitching oscillations which lead the heaving one by an angle of 90° , or a consequence of the higher thrust forces reached in this case.

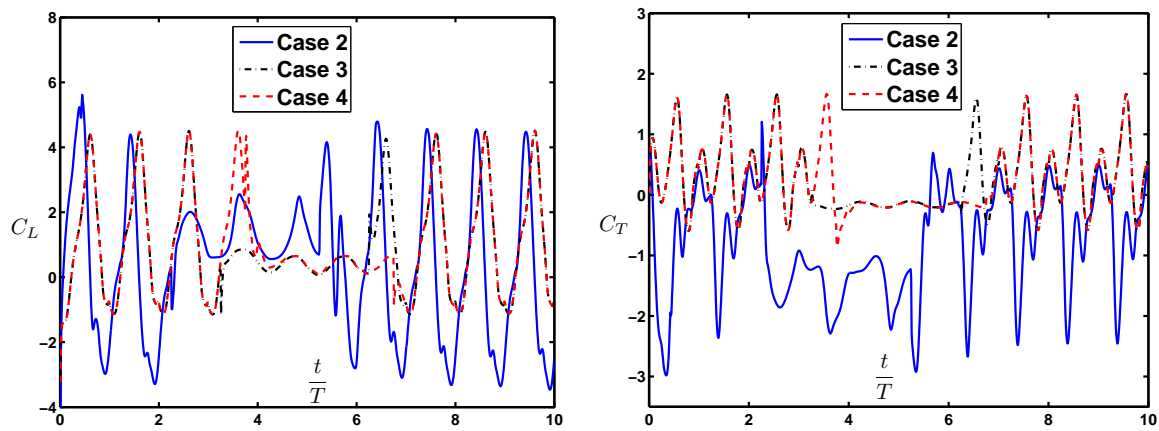


Figure 5.37: Temporal evolution of the lift force (left) and the thrust force (right) during the gliding phase for Case 2, 3 and 4.

This brief investigation of the gliding motion answers the two main questions addressed. The gliding time can be longer than the flapping time or at least of the same order of magnitude. On the other hand, it is preferable to stop in the position where the heaving velocity vanishes and with a very small pitching angle. The lift in this case is due to the mean angle of attack. In the bird case, α_0 is included inside $\alpha(t)$ and the stop is done much more smoothly. An optimisation of the various parameters during gliding could be a very interesting topic, aiming at proving an increase of the global efficiency.

Conclusion

The results presented in this section allow to provide answers to the main issues encountered in flapping airfoils. They showed that the optimisation approach is efficient in driving the control parameters towards their optimal values known in nature and literature. Hence, they have confirmed the optimal range for the Strouhal number used by animals. This has been done by modifying the wake width for a constant flapping frequency and then inversely, by maintaining the wake width and modifying the flapping frequency. A linear relation is found between the optimal amplitudes for heaving and pitching, corresponding to a constant effective angle of attack. The optimal range for the phase angle was also recovered here, in agreement with the literature. This proves the adequacy of the cost functional adopted. Optimisation of lift has produced very high lift coefficients. However, the flapping airfoil does not produce thrust for the associated angles of attack. Therefore, small mean angles of attack were considered, ensuring sufficient lift and thrust. The multi-parameters optimisation has led to optimal configurations with high aerodynamic measures of performances according to the mission of the vehicle. Then, high order harmonics oscillations have been included to recover the loss of efficiency for high thrust coefficients. This has been done successfully for average amplitudes of pitching. Finally, the effect of the Reynolds number and some representative gliding configurations have been investigated, showing a positive influence on η by increasing Re_c and that, despite the possibility of long periods of gliding, the global efficiency does not increase with the simple approach adopted.

Summary and concluding remarks

During the last two decades, the skills and knowledge developed in the frame of micro aircrafts and animals flights were joined to build man-made vehicles based on locomotion available in nature. The case of flapping-wing micro air vehicles is the perfect example of this union between two fields, the final goal being to produce improved robots. The main motivation is to mimic some levels of performance not reached yet by fixed-wing vehicles. The ability of birds to fly over very long distances, without interruptions, inspired the idea of building birds-like locomotion vehicles. The aim of the present work has been to accomplish a step towards the improvement of a vehicle autonomy by optimising the flapping motion. Once found, the optimal parameters are compared to those observed in nature, in order to show the natural evolution of animals towards optimised configuration. In practice, the set of optimal kinematics can be then stored in the processor which pilots the vehicle and used for different phases of the flight, including take-off, landing, cruise and high speed phases. To reach this target, the principle is to construct an optimisation approach which yields the optimal parameters, mainly in terms of lift and thrust forces.

A large number of contributions on flapping foils exist in the literature. The effect of the various parameters has been largely studied by exploring the space of variation of each. The originality of the present contribution resides in rendering automatic the search of the optimal kinematics. This implies that one may impose a given measure of performance and the solver, written during this thesis, will identify the adequate kinematics. The measure of performance is directly related to the mission of the vehicle. Therefore, investigations of lift, thrust, propulsive efficiency or any possible functional combining these measures has been carried out. The other originality resides in the techniques of optimisation which has been applied to the flapping airfoil problem, namely the sensitivity approach and the complex step derivative method.

The principles of the optimisation are based on the direct numerical solution of the flow field around a flapping airfoil in an incompressible low Reynolds number configuration. Then, and according to the specific the mission to be accomplished,

a cost functional is defined and its gradients, with respect to the physical variables influencing the kinematics, are evaluated. This is done by solving a similar system to the flow equations (sensitivity technique) or by writing the direct system of equations in complex space (complex step derivative method). The value and the sign of the gradients are used to update the control parameters with a quasi-Newton algorithm. Vanishing gradients ensure the optimum of the cost function and the associated kinematics can be applied to the micro air vehicle.

After having summarized the previous contributions, analysed the natural mechanisms and described the flapping motion, the pure mathematical problem has been set by writing its five components: the non-dimensional equations solving the flow field around the airfoil, the cost functional, the control parameters, the equations computing the gradient of the cost functional with respect to the kinematics and the parameters' update algorithm. The problem is solved in the moving reference frame which renders the equations more complex, while simplifying the boundary conditions. The numerical issues have been addresses and a grid yielding a good accuracy-to-computational cost has been identified. It ensures a physical validity of the boundary conditions for the duration of the unsteady numerical simulations, typically equal to two periods of oscillations. It is built with roughly 0.25 million nodes distributed in a domain equal to 11 chord lengths. Spatial discretization is done with centred finite differences scheme and time advancement with first-order upwind scheme, performing between 10000 and 20000 temporal steps for each period of oscillations.

Sensitivity fields of a variable have a similar topology of the field of this same variable. They highlight the important role played by the airfoil's leading- and trailing-edges. Optimisation of amplitudes showed that the high efficiency is related to limited separation of the flow during the flapping motion. This is observed through a linear dependence between the optimal heaving and pitching amplitudes leading to a roughly constant maximal effective angle of attack in the range $[10^\circ, 12^\circ]$. Optimisation of the phase angle proved the interest of considering pitching oscillations leading the heaving ones by an angle in the range $[70^\circ, 90^\circ]$ in agreement with the results of Isogai et al. (1999) and Fampton et al. (2001). This is due to the positive interactions of the vorticity shed by the airfoil leading- and trailing-edges. Investigation of lift demonstrated the ability of flapping airfoil to produce high lift coefficients. This is useful due to their light mass and sensitivity to harsh atmospheric conditions and their relatively slow forward velocity. The peak of lift is observed for relatively high maximal effective angles of attack in the range $[39^\circ, 48^\circ]$. This is mainly related to the low Reynolds number used here. The peak of lift-to-drag ratio for the same airfoil when it does not flap is obtained for an angle of attack equal to 11° . This shows a correspondence between the mean angle of attack and the maximal effec-

tive angle for still and flapping airfoils, respectively. It also shows that lift-to-drag and propulsive efficiency are favoured by similar conditions. The optimisation of the non-dimensional frequency of flapping, the Strouhal number (St), has been achieved by acting on both the physical frequency of flapping and the wake width. Both attempts have yielded an optimal St in the range $[0.25, 0.40]$, close to the values for optimal efficiency found numerically and experimentally (Triantafyllou et al., 1993) and widely spread in nature (Taylor et al., 2003; Bejan and Marden, 2006).

Having studied the effect of each parameter separately, a multi-parameters optimisation is carried out to find the optimal kinematics for various missions. The optimisation is always carried out for one single adapted functional by acting on many parameters, in opposition to a multi-functional optimisation. Results have demonstrated the ability of a flapping airfoil to fulfil its duties in terms of aerodynamic forces production. The real dilemma is to ensure both high thrust and propulsive efficiency. The first is favoured by large-amplitude oscillations, leading to high Strouhal number and maximal effective angle of attack, the second is favoured by small oscillations with minimum flow separation. Additionally, the constraints acting on the airfoil, such as the limitation on the maximal amplitude of the oscillations are contained in the cost functional adopted. Acceptable combinations of flapping parameters have been identified but the optimal efficiency has been found smaller than values reported in the literature and observed in nature. Three attempts were done to increase this maximal efficiency.

First, more complex motions were used, including high order harmonics oscillations. The effect of this approach is interesting for high thrust coefficients and for moderate pitching amplitude in the vicinity of -25° . For larger amplitudes, the decrease of efficiency is slower for high thrust and the approach is not justified. For smaller amplitudes, efficiencies and associated thrust coefficients are very poor. Second, the effect of increasing the Reynolds number, Re_c , is analysed. Reducing the viscous forces improved the efficiency but the prohibitive computational cost prevented the study of realistic Reynolds numbers. However, it is discussed that the optimal kinematics found here would remain valid for higher Reynolds number configurations, with higher efficiency. This is confirmed by the agreement of the optimal kinematics with those of the literature obtained experimentally for higher Re_c . Third, the impact of gliding phases was observed by applying very simple alternance law of flapping and gliding. Results showed the ability of the two-dimensional airfoil to use gliding for long duration but the global efficiency decreased. This is probably due to the simplicity of the configuration analysed, since the forward speed and the position of the airfoil were maintained constant during the gliding phase, whereas in reality the velocity of the bird is variable and the position of its wing is adapted.

It may be stated that that the present study has fulfilled its principal objectives. However, extensions of the present work can be carried out and divided into two categories. First, the perspectives directly related to the present work, as a deeper insight of the Reynolds number effect in the same way than Ohmi et al. (1990) should be done for the optimised configurations. This is valid also for the higher order harmonics, where the works of Read et al. (2003) can be extended and generalised for better improvements of the efficiency by including higher terms for pitching motions and by controlling the pitching amplitudes and the phases angles. The three-dimensional effects should also be addressed. Here, we focused on the case of a two-dimensional airfoil where no tips vortices and induced drag are included. This aspect is very important since birds wings and especially fish fins have an aspect ratio close to one, amplifying the role of the tips. Furthermore, a three dimensional approach would favour the investigation of the lateral forces and flight stability with a thorough analysis of the role of torques, which has been mainly neglected in the present study. Finally, a gliding optimisation may be carried out by controlling the parameters influencing this phase, precisely the gliding duration, and the position and behaviour of the wing during this period. Secondly, Other perspectives linked to the present work but with major variations of the solver may be done. This refers to taking into account the elasticity, the presence of feathers and their influence on the shape of the wing tips. Such a study requires the resolution of fluid-structure interaction problems. It may be done in a compressible flow configuration where a noise-linked cost functional can possibly be defined and optimised, or in an incompressible solver with noise propagation laws for the far-field. In fact, noise generated by flapping wings is a real issue due to large fluctuations of the pressure and consequently to unsteady forces on the airfoil. This renders prototypes very noisy, whereas they are supposed to be stealthy.

In conclusion, the efforts done in various domains should be put together to build, in the near future, vehicles with better levels of performances and especially with longer autonomy. Despite still being far away from performances achieved by animals in nature, things are evolving in the right direction. The proof that animals are still more evolved than man-made vehicles in this PhD thesis should not be seen as a pessimist message. The future contributions should probably focus on the elasticity and its role, the ultimate objective being to build, someday, micro air vehicles with performances as good as mounting a camera on a living bird.

Conclusions finales

Durant les deux dernières décennies, les progrès accomplis au niveau des micro-robots et de la mécanique animale ont été mis en commun pour produire des micro-véhicules améliorés. Le cas d'un micro-drone à ailes battants est le parfait exemple de cette union entre les deux domaines. L'objectif principal étant d'atteindre les hauts niveaux de performance observés dans la nature chez des animaux ayant une dimension et un mode de propulsion similaires. En particulier, le but de cette thèse a été de contribuer à l'amélioration de l'autonomie d'un micro-véhicule en optimisant le battement de l'aile en terme de forces de poussée, de portance et d'efficacité propulsive. Une fois identifiée, ces cinématiques optimales sont comparées à ce qu'on observe dans la nature chez les oiseaux, les insectes et les poissons. Une correspondance entre les deux montrent que les animaux ont naturellement optimisé leur mouvement de sorte à limiter les pertes d'énergie, leur permettant ainsi de parcourir des distances maximisées.

Un grand nombre de contributions existe dans la littérature et traite le sujet du battement d'aile. L'effet de chaque paramètre a été identifié par le balayage dans l'espace des paramètres. L'originalité de l'étude actuelle réside dans l'automatisme de la recherche des paramètres optimaux. Pour chaque phase ou mission du micro-drone correspond une fonctionnelle coût à qui correspond une cinématique optimale. Ainsi, pour la croisière, l'efficacité propulsive peut être avantagée alors qu'un accent est mis sur la poussée dans les phases d'accélération. L'autre originalité provient de l'utilisation de techniques nouvelles comme la sensibilité et le pas complexe dans le cadre de l'optimisation du battement d'une aile.

Le principe de l'optimisation est basé sur la résolution numérique de l'écoulement autour d'un profil d'aile soumis à des oscillations de translation et de rotation combinées à un faible nombre de Reynolds. Par la suite, et suivant l'objectif requis, une fonctionnelle coût est définie et son gradient par rapport aux paramètres de contrôle est calculé. Le contrôle est réalisé notamment sur les amplitudes des oscillations, leur déphasage et leur fréquence. Enfin, le signe et la valeur du gradient permet à travers un algorithme du type quasi-Newton d'actualiser la valeur du paramètre de contrôle jusqu'à ce que la valeur optimale soit atteinte. La simulation numérique est effectuée sur un maillage d'environ 0.25 million de mailles distribuées dans un domaine circulaire de rayon supérieur à 11 cordes et dont la moitié est dans un cercle de rayon inférieur à 3 cordes. L'aspect instationnaire du problème exige une résolution temporelle avec 10000 à 20000 pas de temps requis pour chaque période d'oscillation.

L'optimisation des amplitudes a montré que la haute efficacité propulsive est liée au cas de séparation minimale de l'écoulement durant le battement du profil.

Ceci est confirmé par une valeur maximale de l'angle d'attaque effectif "vu" par l'aile et qui doit rester dans l'intervalle $[10^\circ, 12^\circ]$. D'autre part, des oscillations angulaires qui précèdent celles verticale d'un angle dans l'intervalle $[70^\circ, 90^\circ]$ a un impact positif sur le rendement en accord avec les résultats de Isogai et al. (1999) et Fampton et al. (2001). Ceci est notamment dû à une interaction constructive entre le tourbillon du bord d'attaque qui reste attaché durant presque tout le cycle du battement avant de venir renforcer le tourbillon du bord de fuite.

En outre, un profil d'aile battue est capable de produire des larges forces de portance et même si l'angle de portance maximale pour une aile battue à faible nombre de Reynolds est assez élevé, l'angle donnant un rapport de portance et traînée maximal pour un profil fixe est de 11° . Comparant cette valeur à l'intervalle optimale pour le maximum de l'angle d'attaque effectif pour une aile battue montre que les 2 angles jouent le même rôle et que l'optimisation de la portance et celle de la poussée sont complémentaires nécessitant une réduction des zones de séparation de l'écoulement. D'autre part, l'optimisation de la fréquence adimensionnelle du battement a montré qu'en terme d'efficacité propulsive, l'intervalle optimal est celui qu'on observe chez un grand nombre d'êtres vivants, à savoir un nombre de Strouhal entre 0.25 et 0.40 en accord avec Taylor et al. (2003) et Bejan and Marden (2006).

Après avoir étudié l'effet séparé de chaque paramètre, une optimisation multi-paramètres a été réalisée pour des objectifs liés à la poussée, la portance et le rendement. Un compromis doit être trouvé vu que l'augmentation de la poussée s'accompagne par une chute plus ou moins rapide de l'efficacité propulsive. Un moyen de réduire cette chute est d'inclure les termes d'ordre supérieur dans les oscillations de translation. Ceci a été fait avec succès dans le cas d'une amplitude de tangage dans le voisinage de -25° . D'autre part, le cas d'un plus grand nombre de Reynolds a permis d'augmenter le rendement en limitant les pertes visqueuses. En revanche, les variations sur la cinématique optimale en augmentant le nombre de Reynolds sont assez limitées. Enfin, une étude simpliste du vol plané a permis de démontrer l'aptitude d'un profile battant à adopter cette configuration durant une longue durée avant que sa poussée ne s'annule. Cependant, le rendement global n'a pas été amélioré durant cette phase.

Dans le futur, cette configuration de vol plané peut être étudiée en considérant l'ensemble des paramètres présents notamment le ralentissement du véhicule ou l'animal durant cette phase et la manière dont l'animal arrête son battement et le reprend. En outre, le cas d'une aile tridimensionnelle serait plus réaliste notamment à cause du rapport d'aspect des ailes chez les animaux qui rendent les effets de bord très importants. Enfin, cette étude peut être corrélée à d'autres contributions traitant l'élasticité des ailes, la forme des plumes ou la manipulation de la vorticit 

pour réaliser à l'avenir des meilleurs véhicules.

Appendix A

Comparison of fixed- and mobile-wing powers

Kroo and Kunz (2001) compared the power required for a forward flight of a full-scale aircraft with fixed wings and for hovering conditions at small scale. They showed that hovering requires substantially more power than does forward flight at human scale since a fixed wing aircraft needs to produce a thrust equal to $\frac{W^*}{\frac{L^*}{D^*}}$ whereas a mobile-wing aircraft require a thrust equal to W^* , where W^* is the weight of the aircraft, L^* its global lift force, D^* the global drag force and the superscript $*$ denotes a dimensional quantity. This implies that if the wing lift-to-drag ratio is small, the difference between the required powers for forward and hovering flights is less significant.

The power required by a fixed-wing aircraft to maintain its level flight is:

$$P_{fixed}^* = \frac{T^* U_{\infty}^*}{\eta_p} = \frac{\left[\frac{W^*}{\frac{L^*}{D^*}}\right] \left(\frac{2W^*}{\rho^* S_0^* C_L}\right)^{0.5}}{\eta_p}$$

and the power required for hover is:

$$P_{hover}^* = \frac{T^* V_h^*}{M} = \frac{[W^*] \left(\frac{W^*}{2\rho^* S_0^*}\right)^{0.5}}{M}$$

where T^* is the thrust force, U_{∞}^* the forward speed of the fixed-wing aircraft, η_p the propulsive efficiency of the aircraft propeller, ρ^* is the air density, S_0^* a reference surface, C_L the lift coefficient, V_h^* the induced velocity in hover and M the rotor figure of merit. Hence, the ratio of these two powers is:

$$\frac{\left(\frac{P^*}{W^*}\right)_{hover}}{\left(\frac{P^*}{W^*}\right)_{fixed}} = \frac{[(L^*/D^*)\eta_p(W^*/2\rho^*S_0^*)^{0.5}]}{[M(2W^*/\rho^*S_0^*C_L)^{0.5}]}$$

So if we consider the same density of air and the same reference surfaces, this ratio becomes:

$$\frac{\left(\frac{P^*}{W^*}\right)_{hover}}{\left(\frac{P^*}{W^*}\right)_{fixed}} = \frac{L}{D} \left(\frac{C_L}{4}\right)^{0.5} \frac{\eta_p}{M}.$$

Moreover, if the rotor figure of merit and the propeller efficiency is of the same order of magnitude (roughly between 0.75 and 0.8), we reach the relation:

$$\frac{\left(\frac{P^*}{W^*}\right)_{hover}}{\left(\frac{P^*}{W^*}\right)_{fixed}} \frac{L}{D} \left(\frac{C_L}{4}\right)^{0.5}.$$

Hence, for an MAV of 15-cm wing span a lift-to-drag ratio $\frac{L}{D} = 5$ and a lift coefficient $C_L = 0.2$, a hovering vehicle would require only 12% more power than the fixed wing device; whereas for a full scale prototype, $\frac{L}{D} = 35$ and $C_L = 1$ which implies that hovering require 17.5 times the power needed for straightforward flight.

We address now the configuration of straightforward flight on both a full scale aircraft and a flapping-wing MAV. We can show that a flapping-wing configuration requires less power than a fixed-wing one and that even if the pure propulsive efficiency is lower. The latter statement does not mean that flapping-wing is less efficient. It means that due to flapping, the thrust generated by the wing counterbalance its drag and there is no need for supplementary power from the motors to overcome this drag like in the fixed-wing configuration. Consider the case of forward flight with a constant velocity for the two configurations. A constant velocity implies a vanishing acceleration, and thus a balance of forces. Hence, neglecting the drag due to interactions of body and wings, we have:

For fixed-wing configuration: $T_{fixed} = D_{wing} + D_{body}$

For flapping-wing configuration: $T_{mobile} = D_{body}$

where T refers to the thrust developed by the vehicle in each configuration and D denotes the drag. Now and for simplification, assume that the drag of the body is the same when the MAV flaps or not. This leads to:

$$T_{fixed}V_0 = T_{flapping}V_0 + D_{wing}V_0,$$

where V_0 is the constant forward velocity of the vehicle in both cases. If we denote by $\eta_{flapping}$ and η_{fixed} the propulsive efficiencies, we can substitute the latter equation by :

$$\eta_{fixed}P_{fixed} = \eta_{flapping}P_{flapping} + P_{wing},$$

where P is the power supply. This implies that:

$$\frac{P_{flapping}}{P_{fixed}} = \frac{\eta_{fixed}}{\eta_{flapping}} - \frac{1}{\eta_{flapping}} \frac{P_{wing}}{P_{fixed}}$$

If we assume typical performances of the fixed-wing configuration, where $\eta_{fixed} = 0.8$ and the power dissipated to overcome the wing drag almost 0.3 of the total required power, the latter equations implies that a flapping efficiency $\eta_{flapping} = 50\%$ is enough to have a comparable required powers in the two cases. This shows that even if the flapping efficiency is lower, the required power is still smaller in this configuration. However, experimental data proved that the efficiency of flapping can be as high as roughly 90%. Consequently, in addition to higher efficiency, the ratio of the required powers $\frac{P_{flapping}}{P_{fixed}}$ becomes equal to 0.55.

Obviously, this demonstration is rendered simple by a lot of arguable assumptions. Nonetheless, it still provides an idea about the benefit of flapping-wing configuration.

Appendix B

Reference systems and transformations

(x, y) is the laboratory fixed reference, (X, Y) the moving reference related to the motion of the airfoil whereas (x_α, y_α) is the aerodynamic reference. The relation between these frames is:

$$\begin{cases} X &= x_\alpha \cos(\alpha(t) - \alpha_0) + (y_\alpha - h(t)) \sin(\alpha(t) - \alpha_0), \\ Y &= -x_\alpha \sin(\alpha(t) - \alpha_0) + (y_\alpha - h(t)) \cos(\alpha(t) - \alpha_0). \end{cases} \quad (\text{B.1})$$

To obtain the relations between the frames (x, y) and (X, Y) , it is enough to impose $\alpha_0 = 0$ in the above equations.

$$\begin{cases} x_\alpha &= X \cos(\alpha(t) - \alpha_0) - Y \sin(\alpha(t) - \alpha_0), \\ y_\alpha &= h(t) + X \sin(\alpha(t) - \alpha_0) + Y \cos(\alpha(t) - \alpha_0). \end{cases} \quad (\text{B.2})$$

By assuming the airfoil to be a Joukowski profile, the domain around the airfoil is mapped onto the field external to a circle of radius $r_0 = \lambda + e + s$ by means of the transformation:

$$\begin{cases} X &= \xi + \lambda^2 \frac{\xi - e}{(\xi - e)^2 + \chi^2} + d - e \\ Y &= \chi - \lambda^2 \frac{\chi}{(\xi - e)^2 + \chi^2} \end{cases} \quad (\text{B.3})$$

where λ , d and e are distances which depend on the chord length of the airfoil, the position of the pitching centre and the thickness of the airfoil respectively, whereas s is a small value which allows to round off the trailing-edge of the airfoil. The dimensionless values for all computations were taken as $\lambda = 1$, $d = 0.667$, $e = 0.075$ and $s = 0.038$ when the scale length is λ^* such as $\lambda^* = 0.248c^*$ and c^* the dimensional

chord length of the airfoil. This value corresponds roughly to the position of the aerodynamic centre of the airfoil. The Jacobian which allows the transformation between the (X, Y) and (ξ, χ) is expressed as:

$$J = 1 + \frac{1 - 2(\xi - e)^2 + 2\chi^2}{[(\xi - e)^2 + \chi^2]^2}.$$

A polar reference (r, θ) is used in the Joukowski plane with:

$$\begin{cases} \xi &= r \cos \theta, \\ \chi &= r \sin \theta. \end{cases} \quad (\text{B.4})$$

A logarithmic law (Braza et al., 1986) is introduced to refine the radial distribution of points in the radial direction as to ensure a better resolution near the airfoil:

$$z = \ln(r + a)$$

with $a = \frac{R_{int}^2 - R_{max}r_0}{R_{max} + r_0 - 2R_{int}}$, where R_{max} is the radius of the computational domain and R_{int} an intermediary radius such that half of the points in the radial direction are between the airfoil and R_{int} . The effect of the choice of these radii is discussed in §4.1. This value of a ensures that the dimensional grid size close to the body is always 10 times smaller than the approximated thickness of the boundary layer computed by Stokes and Blasius formulae (Guglielmini, 2004). This is confirmed by the study of the flow fields in order to evaluate the number of grid nodes inside the boundary layer (cf. §4.1). The numerical resolution is done in the (z, θ) frame.

The derivative of equations B.1 and B.2 allow to find the relation between velocities in different references. We denote by (u, v) , (u_α, v_α) and (U, V) the components of velocity in the laboratory, aerodynamic and moving reference frames, respectively. Under these conditions:

$$\begin{cases} u_\alpha &= (U - \dot{\alpha}(t)Y) \cos(\alpha(t) - \alpha_0) - (V + \dot{\alpha}(t)X) \sin(\alpha(t) - \alpha_0) \\ v_\alpha &= (U - \dot{\alpha}(t)Y) \sin(\alpha(t) - \alpha_0) + (V + \dot{\alpha}(t)X) \cos(\alpha(t) - \alpha_0) + \dot{h}(t) \end{cases} \quad (\text{B.5})$$

Here again, (u, v) can be obtained by imposing $\alpha_0 = 0$.

Appendix C

Details of the flow and sensitivity equations

C.1 Flow equations

The dependence of the direct variables upon the control parameters can be written explicitly when expressing these variables in the airfoil-related reference frame (X, Y) . We write the direct variables as follows:

- Mean power:

$$\bar{P} = -\frac{1}{T} \int_0^T \left[F_X(t) \sin(\alpha(t)) \dot{h}(t) + F_Y(t) \cos(\alpha(t)) \dot{h}(t) + M_z(t) \dot{\alpha}(t) \right] dt,$$

- Mean horizontal force:

$$\bar{F} = \frac{1}{T} \int_0^T [F_X(t) \cos(\alpha(t) - \alpha_0) - F_Y(t) \sin(\alpha(t) - \alpha_0)] dt,$$

- Mean vertical force:

$$\bar{L} = \frac{1}{T} \int_0^T [F_X(t) \sin(\alpha(t) - \alpha_0) + F_Y(t) \cos(\alpha(t) - \alpha_0)] dt,$$

where T is the non-dimensional period of oscillation ($= 2\pi$), F_X , F_Y and M_z are respectively the horizontal and vertical forces in the airfoil related frame (X, Y) and the torque acting on the airfoil. These quantities depend on the pressure and velocity

gradients at the foil surface through the relations:

$$\left\{ \begin{array}{l} F_X = \int_0^{2\pi} \left(-p \frac{\partial Y}{\partial \theta} + \frac{2}{Re} \left[\frac{\partial Y}{\partial \theta} \frac{\partial U}{\partial X} - \frac{1}{2} \frac{\partial X}{\partial \theta} \left(\frac{\partial U}{\partial Y} + \frac{\partial V}{\partial X} \right) \right] \right) d\theta, \\ F_Y = \int_0^{2\pi} \left(p \frac{\partial X}{\partial \theta} + \frac{2}{Re} \left[\frac{1}{2} \frac{\partial Y}{\partial \theta} \left(\frac{\partial U}{\partial Y} + \frac{\partial V}{\partial X} \right) - \frac{\partial X}{\partial \theta} \frac{\partial V}{\partial Y} \right] \right) d\theta, \\ M_Z = \int_0^{2\pi} p \left(X \frac{\partial X}{\partial \theta} + Y \frac{\partial Y}{\partial \theta} \right) d\theta \\ \quad + \int_0^{2\pi} \frac{2}{Re} \left[-X \frac{\partial X}{\partial \theta} \frac{\partial V}{\partial Y} + \frac{1}{2} \left(X \frac{\partial Y}{\partial \theta} + Y \frac{\partial X}{\partial \theta} \right) \left(\frac{\partial U}{\partial Y} + \frac{\partial V}{\partial X} \right) - Y \frac{\partial Y}{\partial \theta} \frac{\partial U}{\partial X} \right] d\theta, \end{array} \right.$$

where U and V are the velocity components in the X and Y directions. The resolution of the flow equations (2.2) allows to determine the vorticity and stream function fields and consequently the velocity and pressure fields. The pressure is recovered from the equation:

$$p(\theta) = p_0 + \int_0^\theta \left(\frac{\partial p}{\partial X} \frac{\partial X}{\partial \theta} + \frac{\partial p}{\partial Y} \frac{\partial Y}{\partial \theta} \right) d\theta,$$

where p_0 is a reference pressure and

$$\left\{ \begin{array}{l} \frac{\partial p}{\partial X} = \left[\ddot{\alpha}(t)Y + \dot{\alpha}^2(t)X - \ddot{h}(t) \sin(\alpha(t)) \right] + \frac{1}{Re} \left[\frac{\partial^2 U}{\partial X^2} + \frac{\partial^2 U}{\partial Y^2} \right], \\ \frac{\partial p}{\partial Y} = \left[-\ddot{\alpha}(t)X + \dot{\alpha}^2(t)Y - \ddot{h}(t) \cos(\alpha(t)) \right] + \frac{1}{Re} \left[\frac{\partial^2 V}{\partial X^2} + \frac{\partial^2 V}{\partial Y^2} \right]. \end{array} \right.$$

Derivatives of the velocity components can be expressed in terms of the stream function as:

$$\left\{ \begin{array}{l} \frac{\partial U}{\partial X} = -\frac{\partial V}{\partial Y} = \frac{1}{J^2} \left[\cos 2\theta \frac{\partial X}{\partial \xi} \frac{\partial Y}{\partial \xi} + \frac{\sin 2\theta}{2} \left(\frac{\partial Y}{\partial \chi} \frac{\partial X}{\partial \xi} + \frac{\partial Y}{\partial \xi} \frac{\partial X}{\partial \chi} \right) \right] \frac{\partial^2 \psi}{\partial r^2}, \\ \frac{\partial U}{\partial Y} + \frac{\partial V}{\partial X} = \frac{1}{J^2} \left[\cos 2\theta \left(\left(\frac{\partial X}{\partial \chi} \right)^2 - \left(\frac{\partial X}{\partial \xi} \right)^2 \right) - 2 \sin 2\theta \frac{\partial X}{\partial \chi} \frac{\partial X}{\partial \xi} \right] \frac{\partial^2 \psi}{\partial r^2}, \end{array} \right.$$

whereas the Laplacian of U and V are written in terms of the vorticity as:

$$\left\{ \begin{array}{l} \Delta U = \frac{1}{J} \frac{\partial X}{\partial \chi} \left[\cos \theta \frac{\partial \omega}{\partial r} - \frac{\sin \theta}{r} \frac{\partial \omega}{\partial \theta} \right] - \frac{1}{J} \frac{\partial X}{\partial \xi} \left[\sin \theta \frac{\partial \omega}{\partial r} + \frac{\cos \theta}{r} \frac{\partial \omega}{\partial \theta} \right], \\ \Delta V = \frac{1}{J} \frac{\partial Y}{\partial \chi} \left[\cos \theta \frac{\partial \omega}{\partial r} - \frac{\sin \theta}{r} \frac{\partial \omega}{\partial \theta} \right] - \frac{1}{J} \frac{\partial Y}{\partial \xi} \left[\sin \theta \frac{\partial \omega}{\partial r} + \frac{\cos \theta}{r} \frac{\partial \omega}{\partial \theta} \right]. \end{array} \right.$$

C.2 Sensitivity equations

C.2.1 The gradient terms

The derivatives included in the gradient are computed through the following relations obtained by the derivation of the relations in §C.1 with respect to the generic control g :

$$\left\{ \begin{array}{l} \frac{\partial F_X}{\partial \omega} \frac{d\omega}{dg} = - \int_0^{2\pi} \left(\frac{\partial p}{\partial \omega} \frac{d\omega}{dg} \right) \frac{\partial Y}{\partial \theta} d\theta, \quad \frac{\partial F_X}{\partial g} = - \int_0^{2\pi} \left(\frac{\partial p}{\partial g} \right) \frac{\partial Y}{\partial \theta} d\theta, \\ \frac{\partial F_Y}{\partial \omega} \frac{d\omega}{dg} = \int_0^{2\pi} \left(\frac{\partial p}{\partial \omega} \frac{d\omega}{dg} \right) \frac{\partial X}{\partial \theta} d\theta, \quad \frac{\partial F_Y}{\partial g} = \int_0^{2\pi} \left(\frac{\partial p}{\partial g} \right) \frac{\partial X}{\partial \theta} d\theta, \\ \frac{\partial M_z}{\partial \omega} \frac{d\omega}{dg} = \int_0^{2\pi} \left(\frac{\partial p}{\partial \omega} \frac{d\omega}{dg} \right) \left(X \frac{\partial X}{\partial \theta} + Y \frac{\partial Y}{\partial \theta} \right) d\theta, \quad \frac{\partial M_z}{\partial g} = \int_0^{2\pi} \left(\frac{\partial p}{\partial g} \right) \left(X \frac{\partial X}{\partial \theta} + Y \frac{\partial Y}{\partial \theta} \right) d\theta, \end{array} \right.$$

$$\left\{ \begin{array}{l} \frac{\partial p}{\partial \omega} \frac{d\omega}{dg} = \int_0^{2\pi} - \frac{\partial X}{\partial \theta} \frac{1}{ReJ} \left(\left[- \frac{\partial X}{\partial \chi} \cos \theta + \frac{\partial X}{\partial \xi} \sin \theta \right] \frac{\partial \omega_{,g}}{\partial r} + \frac{1}{r} \left[\frac{\partial X}{\partial \chi} \sin \theta + \frac{\partial X}{\partial \xi} \cos \theta \right] \frac{\partial \omega_{,g}}{\partial \theta} \right) d\theta \\ \quad + \int_0^{2\pi} \frac{\partial Y}{\partial \theta} \frac{1}{ReJ} \left(\left[\frac{\partial Y}{\partial \chi} \cos \theta - \frac{\partial Y}{\partial \xi} \sin \theta \right] \frac{\partial \omega_{,g}}{\partial r} - \frac{1}{r} \left[\frac{\partial Y}{\partial \chi} \sin \theta + \frac{\partial Y}{\partial \xi} \cos \theta \right] \frac{\partial \omega_{,g}}{\partial \theta} \right) d\theta, \\ \frac{\partial p}{\partial g} = \int_0^{2\pi} \frac{\partial}{\partial g} \left(\ddot{\alpha}(t)Y + \dot{\alpha}^2(t)X - \ddot{h}(t) \sin(\alpha(t)) \right) \frac{\partial X}{\partial \theta} d\theta \\ \quad + \int_0^{2\pi} \frac{\partial}{\partial g} \left(-\ddot{\alpha}(t)X + \dot{\alpha}^2(t)Y - \ddot{h}(t) \cos(\alpha(t)) \right) \frac{\partial Y}{\partial \theta} d\theta, \end{array} \right.$$

$$\left\{ \begin{array}{l} \frac{\partial M_z}{\partial \psi} \frac{d\psi}{dg} = \\ \int_0^{2\pi} \left(\frac{2}{ReJ^2} \right) \left(X \frac{\partial X}{\partial \theta} - Y \frac{\partial Y}{\partial \theta} \right) \left[\cos 2\theta \frac{\partial X}{\partial \xi} \frac{\partial Y}{\partial \xi} + \frac{\sin 2\theta}{2} \left(\frac{\partial Y}{\partial \chi} \frac{\partial X}{\partial \xi} + \frac{\partial Y}{\partial \xi} \frac{\partial X}{\partial \chi} \right) \right] \frac{\partial^2 \psi_{,g}}{\partial r^2} d\theta \\ \quad + \int_0^{2\pi} \frac{1}{Re} \left(X \frac{\partial Y}{\partial \theta} + Y \frac{\partial X}{\partial \theta} \right) \frac{1}{J^2} \left[\cos 2\theta \left(\left(\frac{\partial X}{\partial \chi} \right)^2 - \left(\frac{\partial X}{\partial \xi} \right)^2 \right) - 2 \sin 2\theta \frac{\partial X}{\partial \chi} \frac{\partial X}{\partial \xi} \right] \frac{\partial^2 \psi_{,g}}{\partial r^2} d\theta, \end{array} \right.$$

and

$$\left\{ \begin{array}{l} \frac{\partial F_X}{\partial \psi} \frac{d\psi}{dg} = \frac{1}{Re} \int_0^{2\pi} \frac{2}{J^2} \frac{\partial Y}{\partial \theta} \left[\cos 2\theta \frac{\partial X}{\partial \xi} \frac{\partial Y}{\partial \xi} + \frac{\sin 2\theta}{2} \left(\frac{\partial Y}{\partial \chi} \frac{\partial X}{\partial \xi} + \frac{\partial Y}{\partial \xi} \frac{\partial X}{\partial \chi} \right) \right] \frac{\partial^2 \psi_{,g}}{\partial r^2} d\theta \\ \quad - \frac{1}{Re} \int_0^{2\pi} \frac{1}{J^2} \frac{\partial X}{\partial \theta} \left[\cos 2\theta \left(\left(\frac{\partial X}{\partial \chi} \right)^2 - \left(\frac{\partial X}{\partial \xi} \right)^2 \right) - 2 \sin 2\theta \frac{\partial X}{\partial \chi} \frac{\partial X}{\partial \xi} \right] \frac{\partial^2 \psi_{,g}}{\partial r^2} d\theta, \\ \\ \frac{\partial F_Y}{\partial \psi} \frac{d\psi}{dg} = \frac{1}{Re} \int_0^{2\pi} \frac{2}{J^2} \frac{\partial X}{\partial \theta} \left[\cos 2\theta \frac{\partial X}{\partial \xi} \frac{\partial Y}{\partial \xi} + \frac{\sin 2\theta}{2} \left(\frac{\partial Y}{\partial \chi} \frac{\partial X}{\partial \xi} + \frac{\partial Y}{\partial \xi} \frac{\partial X}{\partial \chi} \right) \right] \frac{\partial^2 \psi_{,g}}{\partial r^2} d\theta \\ \quad + \frac{1}{Re} \int_0^{2\pi} \frac{1}{J^2} \frac{\partial Y}{\partial \theta} \left[\cos 2\theta \left(\left(\frac{\partial X}{\partial \chi} \right)^2 - \left(\frac{\partial X}{\partial \xi} \right)^2 \right) - 2 \sin 2\theta \frac{\partial X}{\partial \chi} \frac{\partial X}{\partial \xi} \right] \frac{\partial^2 \psi_{,g}}{\partial r^2} d\theta. \end{array} \right.$$

C.2.2 The kinematics

Solving the sensitivity equations, computing the boundary conditions and evaluating the gradient requires to compute a number of derivatives which depend on the choice of the control parameter. In the previous section, we kept the generic parameter g for all computations. Here, the derivatives for different choices of g are given. All these derivatives can be deduced from 6 fundamental ones corresponding to the derivatives of $h(t)$, $\dot{h}(t)$, $\ddot{h}(t)$, $\alpha(t)$, $\dot{\alpha}(t)$ and $\ddot{\alpha}(t)$. We recall that:

$$\left\{ \begin{array}{ll} h(t) = \sum_{k=1}^N h_k \sin(\sigma_k t + \tau_k), & \alpha(t) = \sum_{k=1}^N \alpha_k \sin(\sigma_k t + \phi_k), \\ \dot{h}(t) = \sum_{k=1}^N h_k \sigma_k \cos(\sigma_k t + \tau_k), & \dot{\alpha}(t) = \sum_{k=1}^N \alpha_k \sigma_k \cos(\sigma_k t + \phi_k), \\ \ddot{h}(t) = -\sum_{k=1}^N h_k \sigma_k^2 \sin(\sigma_k t + \tau_k), & \ddot{\alpha}(t) = -\sum_{k=1}^N \alpha_k \sigma_k^2 \sin(\sigma_k t + \phi_k). \end{array} \right.$$

Case 1: $g = h_k$ or $g = \tau_k$

$$\left\{ \begin{array}{ll} \frac{\partial(h(t))}{\partial h_k} = \sin(\sigma_k t + \tau_k), & \frac{\partial(h(t))}{\partial \tau_k} = h_k \cos(\sigma_k t + \tau_k), \\ \frac{\partial(\dot{h}(t))}{\partial h_k} = \sigma_k \cos(\sigma_k t + \tau_k), & \frac{\partial(\dot{h}(t))}{\partial \tau_k} = -h_k \sigma_k \sin(\sigma_k t + \tau_k), \\ \frac{\partial(\ddot{h}(t))}{\partial h_k} = -\sigma_k^2 \sin(\sigma_k t + \tau_k), & \frac{\partial(\ddot{h}(t))}{\partial \tau_k} = -h_k \sigma_k^2 \cos(\sigma_k t + \tau_k). \end{array} \right.$$

In this case, the derivatives with respect to g of the terms involving $\alpha(t)$ or its temporal derivatives vanish.

Case 2: $g = \alpha_k$ or $g = \phi_k$

$$\left\{ \begin{array}{ll} \frac{\partial(\alpha(t))}{\partial\alpha_k} = \sin(\sigma_k t + \phi_k), & \frac{\partial(\alpha(t))}{\partial\phi_k} = \alpha_k \cos(\sigma_k t + \phi_k), \\ \frac{\partial(\dot{\alpha}(t))}{\partial\alpha_k} = \sigma_k \cos(\sigma_k t + \phi_k), & \frac{\partial(\dot{\alpha}(t))}{\partial\phi_k} = -\alpha_k \sigma_k \sin(\sigma_k t + \phi_k), \\ \frac{\partial(\ddot{\alpha}(t))}{\partial\alpha_k} = -\sigma_k^2 \sin(\sigma_k t + \phi_k), & \frac{\partial(\ddot{\alpha}(t))}{\partial\phi_k} = -\alpha_k \sigma_k^2 \cos(\sigma_k t + \phi_k). \end{array} \right.$$

Here, the derivatives with respect to g of the terms involving $h(t)$ or its temporal derivatives vanish.

Case 3: $g = \sigma_k$

$$\left\{ \begin{array}{l} \frac{\partial(h(t))}{\partial\sigma_k} = h_k t \cos(\sigma_k t + \tau_k), \\ \frac{\partial(\dot{h}(t))}{\partial\sigma_k} = h_k \cos(\sigma_k t + \tau_k) - h_k \sigma_k t \sin(\sigma_k t + \tau_k), \\ \frac{\partial(\ddot{h}(t))}{\partial\sigma_k} = -2h_k \sigma_k \sin(\sigma_k t + \tau_k) - h_k \sigma_k^2 t \cos(\sigma_k t + \tau_k), \end{array} \right.$$

and

$$\left\{ \begin{array}{l} \frac{\partial(\alpha(t))}{\partial\sigma_k} = \alpha_k t \cos(\sigma_k t + \phi_k), \\ \frac{\partial(\dot{\alpha}(t))}{\partial\sigma_k} = \alpha_k \cos(\sigma_k t + \phi_k) - \alpha_k \sigma_k t \sin(\sigma_k t + \phi_k), \\ \frac{\partial(\ddot{\alpha}(t))}{\partial\sigma_k} = -2\alpha_k \sigma_k \sin(\sigma_k t + \phi_k) - \alpha_k \sigma_k^2 t \cos(\sigma_k t + \phi_k). \end{array} \right.$$

C.3 CSDM equations

In the present section, we yield the relations allowing to compute the gradient once the complex system 3.6 is solved. The example of heaving amplitude control is considered. The case of another parameter is similar with more or less computations

due to the development into complex exponentials required for trigonometric functions, if we consider for example the case of τ_k or ϕ_k . However, the general case of a generic parameter g is hard to formulate due to the presence of filters indicating which parts are really complex. We write that:

$$\begin{aligned} \frac{d\ell}{dh_k} &= \frac{1}{\delta h_k} \text{Imag} \left[\tilde{\ell} \right] = \frac{1}{\delta h_k} \text{Imag} \left[\beta_P^2 \tilde{P} + \beta_F^2 \tilde{F} U_0 + \epsilon_\alpha^2 \overline{(\tilde{\alpha})^2} + \epsilon_h^2 \overline{(\tilde{h})^2} \right] \\ &= \frac{1}{\delta g} \text{imag} \left[\beta_P^2 \bar{P} (h_k + i\delta h_k) + \beta_F^2 \bar{F} (h_k + i\delta h_k) U_0 + \epsilon_h^2 \bar{h}^2 (h_k + i\delta h_k) \right]. \end{aligned} \quad (\text{C.1})$$

The last term in the latter equation is the simplest to evaluate, it reads as:

$$\begin{aligned} \epsilon_h^2 \frac{\partial \bar{h}^2(t)}{\partial h_k} &= \epsilon_h^2 \frac{1}{\delta h_k} \text{imag} \left[\sum_{m \neq k} h_m \sin(\sigma_m t + \tau_m) + (h_k + i\delta h_k) \sin(\sigma_k t + \tau_k) \right]^2 \\ &= \epsilon_h^2 \sum_{m=1}^N 2h_m \sin(\sigma_m t + \tau_m) \sin(\sigma_k t + \tau_k) \end{aligned}$$

On the other hand, using the relations for the flow equations (cf. Appendix C.1), we reach:

$$-2\pi \bar{P} (h_k + i\delta h_k) = \int_0^{2\pi} \left[F_X(\tilde{h}(t)) \sin(\alpha(t)) \dot{\tilde{h}}(t) + F_Y(\tilde{h}(t)) \cos(\alpha(t)) \dot{\tilde{h}}(t) + M_z(\tilde{h}(t)) \dot{\alpha}(t) \right] dt$$

$$2\pi \bar{F} (h_k + i\delta h_k) = \int_0^{2\pi} \left[F_X(\tilde{h}(t)) \cos(\alpha(t)) - F_Y(\tilde{h}(t)) \sin(\alpha(t)) \right] dt,$$

with,

$$\begin{aligned} \tilde{h}(t) &= \sum_{m \neq k} h_m \sin(mt + \tau_m) + (h_k + i\delta h_k) \sin(kt + \tau_k) \\ &= \sum_{m=1}^N (h_m + i\delta_{mk} \delta h_m) \sin(mt + \tau_m) \end{aligned}$$

where $\delta_{mk} \neq 0$ only when $m = k$.

Furthermore, we express the force components and the torque in terms of the velocity components and the pressure as:

$$F_X(\tilde{h}(t)) = \int_0^{2\pi} \left(-p(\tilde{h}(t)) \frac{\partial Y}{\partial \theta} + \frac{2}{Re} \left[\frac{\partial Y}{\partial \theta} \frac{\partial U}{\partial X} (\tilde{h}(t)) - \frac{1}{2} \frac{\partial X}{\partial \theta} \left(\frac{\partial U}{\partial Y} + \frac{\partial V}{\partial X} \right) (\tilde{h}(t)) \right] \right) d\theta,$$

$$F_Y(\tilde{h}(t)) = \int_0^{2\pi} \left(p(\tilde{h}(t)) \frac{\partial X}{\partial \theta} + \frac{2}{Re} \left[\frac{1}{2} \frac{\partial Y}{\partial \theta} \left(\frac{\partial U}{\partial Y} + \frac{\partial V}{\partial X} \right) (\tilde{h}(t)) - \frac{\partial X}{\partial \theta} \frac{\partial V}{\partial Y} (\tilde{h}(t)) \right] \right) d\theta,$$

$$M_Z(\tilde{h}(t)) = \int_0^{2\pi} p(\tilde{h}(t)) \left(X \frac{\partial X}{\partial \theta} + Y \frac{\partial Y}{\partial \theta} \right) d\theta \\ + \int_0^{2\pi} \frac{2}{Re} \left[-X \frac{\partial X}{\partial \theta} \frac{\partial V}{\partial Y} (\tilde{h}(t)) + \frac{1}{2} \left(X \frac{\partial Y}{\partial \theta} + Y \frac{\partial X}{\partial \theta} \right) \left(\frac{\partial U}{\partial Y} + \frac{\partial V}{\partial X} \right) (\tilde{h}(t)) - Y \frac{\partial Y}{\partial \theta} \frac{\partial U}{\partial X} (\tilde{h}(t)) \right] d\theta.$$

On the other hand, the pressure should be expressed as:

$$p[\theta, \tilde{h}(t)] = p_0 + \int_0^\theta \left(\frac{\partial p}{\partial X} (\tilde{h}(t)) \frac{\partial X}{\partial \theta} + \frac{\partial p}{\partial Y} (\tilde{h}(t)) \frac{\partial Y}{\partial \theta} \right) d\theta.$$

p_0 is a reference pressure and

$$\begin{cases} \frac{\partial p}{\partial X} (\tilde{h}(t)) = \left[\ddot{\alpha}(t)Y + \dot{\alpha}^2(t)X - \ddot{h}(t) \sin(\alpha(t)) \right] + \frac{1}{Re} \left[\frac{\partial^2 U}{\partial X^2} + \frac{\partial^2 U}{\partial Y^2} \right] (\tilde{h}(t)), \\ \frac{\partial p}{\partial Y} (\tilde{h}(t)) = \left[-\ddot{\alpha}(t)X + \dot{\alpha}^2(t)Y - \ddot{h}(t) \cos(\alpha(t)) \right] + \frac{1}{Re} \left[\frac{\partial^2 V}{\partial X^2} + \frac{\partial^2 V}{\partial Y^2} \right] (\tilde{h}(t)), \end{cases}$$

where,

$$\begin{cases} \Delta U(\tilde{h}(t)) = \frac{1}{J} \frac{\partial X}{\partial \chi} \left[\cos \theta \frac{\partial \omega}{\partial r} (\tilde{h}(t)) - \frac{\sin \theta}{r} \frac{\partial \omega}{\partial \theta} (\tilde{h}(t)) \right] - \frac{1}{J} \frac{\partial X}{\partial \xi} \left[\sin \theta \frac{\partial \omega}{\partial r} (\tilde{h}(t)) + \frac{\cos \theta}{r} \frac{\partial \omega}{\partial \theta} (\tilde{h}(t)) \right], \\ \Delta V(\tilde{h}(t)) = \frac{1}{J} \frac{\partial Y}{\partial \chi} \left[\cos \theta \frac{\partial \omega}{\partial r} (\tilde{h}(t)) - \frac{\sin \theta}{r} \frac{\partial \omega}{\partial \theta} (\tilde{h}(t)) \right] - \frac{1}{J} \frac{\partial Y}{\partial \xi} \left[\sin \theta \frac{\partial \omega}{\partial r} (\tilde{h}(t)) + \frac{\cos \theta}{r} \frac{\partial \omega}{\partial \theta} (\tilde{h}(t)) \right], \end{cases}$$

and

$$\begin{cases} \frac{\partial U}{\partial X} (\tilde{h}(t)) = -\frac{\partial V}{\partial Y} (\tilde{h}(t)) = \frac{1}{J^2} \left[\cos 2\theta \frac{\partial X}{\partial \xi} \frac{\partial Y}{\partial \xi} + \frac{\sin 2\theta}{2} \left(\frac{\partial Y}{\partial \chi} \frac{\partial X}{\partial \xi} + \frac{\partial Y}{\partial \xi} \frac{\partial X}{\partial \chi} \right) \right] \frac{\partial^2 \psi}{\partial r^2} (\tilde{h}(t)), \\ \left[\frac{\partial U}{\partial Y} + \frac{\partial V}{\partial X} \right] (\tilde{h}(t)) = \frac{1}{J^2} \left[\cos 2\theta \left(\left(\frac{\partial X}{\partial \chi} \right)^2 - \left(\frac{\partial X}{\partial \xi} \right)^2 \right) - 2 \sin 2\theta \frac{\partial X}{\partial \chi} \frac{\partial X}{\partial \xi} \right] \frac{\partial^2 \psi}{\partial r^2} (\tilde{h}(t)). \end{cases}$$

$\omega(\tilde{h}(t))$ and $\psi(\tilde{h}(t))$ are the solutions of the system 3.6.

Appendix D

Discretization

The flow and sensitivity equations are discretized before being numerically solved. The vorticity (respectively sensitivity of vorticity) equation is solved using an ADI (Alternating Direction Implicit) discretization method where a temporal step between n and $n + 1$ is subdivided into two sub-steps, the first implicit in θ between n and $n + \frac{1}{2}$ and the second implicit in z between $n + \frac{1}{2}$ and $n + 1$. Centred schemes are used to discretize the derivatives leading for each sub-step to a tridiagonal system more easily resolvable. The stream function equation (respectively the sensitivity of the stream function) is a Poisson-like equation and therefore its resolution is done using a Fourier transformation. This appendix gives the details about the discretization and the resolution of the equations. In the following, g denotes one generic control parameter, whereas, and for the sake of simplicity, Ω ($= \omega, g$) and Ψ ($= \psi, g$) denote the sensitivity of the vorticity and of the stream function, respectively.

The equations are written in the (t, z, θ) reference frame where z is defined by $z = \ln(r + a)$ allowing to introduce a logarithmic stretching of the grid for a better resolution of the high gradients near the wall. The parameter a depends on the distribution of points inside the computational domain, so it is constant for a given grid. Hence, we have:

$$\frac{\partial}{\partial r} = \frac{1}{e^z} \frac{\partial}{\partial z} \quad \text{and} \quad \frac{\partial^2}{\partial r^2} = \frac{1}{e^{2z}} \left(\frac{\partial^2}{\partial z^2} - \frac{\partial}{\partial z} \right).$$

D.1 The flow equations

D.1.1 The vorticity equation

The non-dimensional equation for vorticity reads:

$$\frac{\partial \omega}{\partial t} + \frac{1}{\sqrt{J}} \left[\frac{v_r}{e^z} \frac{\partial \omega}{\partial z} + \frac{v_\theta}{r} \frac{\partial \omega}{\partial \theta} \right] = \frac{1}{ReJ} \left[\frac{1}{e^{2z}} \frac{\partial^2 \omega}{\partial z^2} + \frac{a}{re^{2z}} \frac{\partial \omega}{\partial z} + \frac{1}{r^2} \frac{\partial^2 \omega}{\partial \theta^2} \right] \quad (\text{D.1})$$

Half step, implicit en θ

Starting from the initial condition of vanishing vorticity, we solve this equation progressing in time. This implies that when computing the instant $n + 1$, the solution at time step n is known. For the first half step implicit in θ , we write the θ derivatives at the instant $n + \frac{1}{2}$ and the z derivatives at the instant n . On the other hand, the terms involving v_r and v_θ depend on ψ , computed once the vorticity is known, which means that when computing the instant $n + \frac{1}{2}$, these velocities are known only until time n . Obviously, the multiplication of a term written at $t = n$ with another written at $t = n + \frac{1}{2}$ can be tolerated if the temporal step Δt is small enough.

$$\begin{aligned} \frac{\omega^{n+\frac{1}{2}} - \omega^n}{\frac{\Delta t}{2}} + \frac{1}{\sqrt{J}} \left[\left(\frac{v_r}{e^z} \right)^n \left(\frac{\partial \omega}{\partial z} \right)^n + \left(\frac{v_\theta}{r} \right)^n \left(\frac{\partial \omega}{\partial \theta} \right)^{n+\frac{1}{2}} \right] = \\ \frac{1}{ReJ} \left[\frac{1}{e^{2z}} \left(\frac{\partial^2 \omega}{\partial z^2} \right)^n + \frac{a}{re^{2z}} \left(\frac{\partial \omega}{\partial z} \right)^n + \frac{1}{r^2} \left(\frac{\partial^2 \omega}{\partial \theta^2} \right)^{n+\frac{1}{2}} \right] \end{aligned}$$

Using a classic centred scheme for the first and the second order derivatives, and isolating the unknown terms on the left hand side of the equation, we obtain for the node (i, j) where i is the index on θ and j on z :

$$\begin{aligned} \omega_{i+1,j}^{n+\frac{1}{2}} \left[\frac{rRe\sqrt{J}\Delta\theta v_\theta^n}{2} - 1 \right] + \omega_{i,j}^{n+\frac{1}{2}} \left[\frac{2r^2JRe(\Delta\theta)^2}{\Delta t} + 2 \right] + \omega_{i-1,j}^{n+\frac{1}{2}} \left[\frac{-rRe\sqrt{J}\Delta\theta v_\theta^n}{2} - 1 \right] \\ = \omega_{i,j+1}^n \left[\frac{-\sqrt{J}r^2Re(\Delta\theta)^2 v_r^n}{2e^z\Delta z} + \left(\frac{r\Delta\theta}{e^z\Delta z} \right)^2 + \frac{ar(\Delta\theta)^2}{2e^{2z}\Delta z} \right] \\ + \omega_{i,j}^n \left[\frac{2r^2JRe(\Delta\theta)^2}{\Delta t} - 2 \left(\frac{r\Delta\theta}{e^z\Delta z} \right)^2 \right] \\ + \omega_{i,j-1}^n \left[\frac{\sqrt{J}r^2Re(\Delta\theta)^2 v_r^n}{2e^z\Delta z} + \left(\frac{r\Delta\theta}{e^z\Delta z} \right)^2 - \frac{ar(\Delta\theta)^2}{2e^{2z}\Delta z} \right] \end{aligned} \tag{D.2}$$

This equation can be seen as a tridiagonal system of the form:

$$A(i)\omega(i+1) + B(i)\omega(i) + C(i)\omega(i-1) = D(i)$$

for $i = 1, N_\theta$, where $A(1) = C(N_\theta) = 0$ and N_θ is the number of discretization points in the azimuthal direction. The term $D(i)$ is known because it has been computed at the previous time step. This system is solved by a Thomas-like algorithm with the periodic boundary conditions which ensures that $\omega(t, \theta = 0, z) = \omega(t, \theta = 2\pi, z)$.

This kind of algorithm converges when the diagonal of the system is dominant, i.e. when $|B(k)| \geq |A(k)| + |C(k)|$ for $k = 2, N_\theta$ and $|B(1)| > |C(1)|$ and $|B(N_\theta)| > |A(N_\theta)|$. The principle of the algorithm is to perform two steps: a descent step, followed by an ascent one.

$$\begin{aligned} \underline{\text{Descent:}} \quad \beta_1 = B(1) \text{ and } \beta_k = B(k) - A(k) \frac{C(k-1)}{\beta_{k-1}}, \quad \text{for } k = 2, N_\theta \\ \gamma_1 = \frac{D(1)}{\beta_1} \text{ and } \gamma_k = \frac{-A(k)\gamma_{k-1} + D(k)}{\beta_k}, \quad \text{for } k = 2, N_\theta \end{aligned}$$

$$\underline{\text{Ascent:}} \quad \omega(N_\theta) = \gamma_{N_\theta}$$

$$\omega(k) = \gamma_k - \frac{C(k)}{\beta_k} \omega(k+1), \quad \text{for } k = N_\theta - 1, 1$$

When periodic conditions are imposed, the system dimension is increased by 2 to become $N_\theta + 2$ and the solution is a linear combination between the solution of the system of dimension N_θ and a part which accounts for the periodicity (Hirsch, 1988).

Half step, implicit en z

The previous half temporal step is completed by another half step between $t = n + \frac{1}{2}$ and $t = n + 1$ by alternating the implicit direction, i.e. this time, implicit scheme are used for the z derivatives. Hence, in the equation (D.1) the z -derivatives are written at the instant $t = n + 1$ whereas the θ -derivatives are written at $t = n + \frac{1}{2}$:

$$\begin{aligned} \frac{\omega^{n+1} - \omega^{n+\frac{1}{2}}}{\frac{\Delta t}{2}} + \frac{1}{\sqrt{J}} \left[\left(\frac{v_r}{e^z} \right)^n \left(\frac{\partial \omega}{\partial z} \right)^{n+1} + \left(\frac{v_\theta}{r} \right)^n \left(\frac{\partial \omega}{\partial \theta} \right)^{n+\frac{1}{2}} \right] = \\ \frac{1}{ReJ} \left[\frac{1}{e^{2z}} \left(\frac{\partial^2 \omega}{\partial z^2} \right)^{n+1} + \frac{a}{re^{2z}} \left(\frac{\partial \omega}{\partial z} \right)^{n+1} + \frac{1}{r^2} \left(\frac{\partial^2 \omega}{\partial \theta^2} \right)^{n+\frac{1}{2}} \right]. \end{aligned}$$

Using the centred schemes for the first and second order derivatives, we obtain:

$$\begin{aligned}
 & -\omega_{i,j+1}^{n+1} \left[-\frac{Re\sqrt{J}e^z\Delta z v_r^n}{2} + 1 + \frac{a\Delta z}{2r} \right] + \omega_{i,j}^{n+1} \left[\frac{2e^{2z}JRe(\Delta z)^2}{\Delta t} + 2 \right] - \\
 & \omega_{i,j-1}^{n+1} \left[\frac{Re\sqrt{J}\Delta z v_r^n}{2} + 1 - \frac{a\Delta z}{2r} \right] = -\omega_{i-1,j}^{n+\frac{1}{2}} \left(\frac{e^z\Delta z}{r\Delta\theta} \right)^2 \left[-\frac{\sqrt{J}rRe\Delta\theta v_\theta^n}{2} - 1 \right] \\
 & + \omega_{i,j}^{n+\frac{1}{2}} \left(\frac{e^z\Delta z}{r\Delta\theta} \right)^2 \left[\frac{2JRe r^2(\Delta\theta)^2}{\Delta t} - 2 \right] - \omega_{i+1,j}^{n+\frac{1}{2}} \left(\frac{e^z\Delta z}{r\Delta\theta} \right)^2 \left[\frac{\sqrt{J}rRe\Delta\theta v_\theta^n}{2} - 1 \right].
 \end{aligned} \tag{D.3}$$

Equation D.3 is a tridiagonal system under the form:

$$-A(j)\omega(j+1) + B(j)\omega(j) - C(j)\omega(j-1) = D(j) \tag{D.4}$$

for $j = 1, N_r$ where $A(1) = C(N_r) = 0$ and N_r the number of discretization points in the radial direction. Here, another Thomas algorithm (Hirsch, 1988) is used to take into account the different boundary conditions, since we impose a Dirichlet-like condition on the airfoil and a Neumann-like condition on the outflow boundary. The same condition of predominance of the main diagonal is also required here. The method postulates the existence of two vectors E and F such as the solutions of the system can be related to one another as:

$$\omega(k) = E_k\omega(k+1) + F_k \Rightarrow \omega(k-1) = E_{k-1}\omega(k) + F_{k-1}. \tag{D.5}$$

Substituting the relations D.5 inside the generic form of the tridiagonal system D.4 we reach:

$$\omega(k) = \frac{A(k)}{B(k) - C(k)E_{k-1}}\omega(k+1) + \frac{D(k) + C(k)F_{k-1}}{B(k) - C(k)E_{k-1}}. \tag{D.6}$$

Identifying the equations D.6 and D.5 leads to:

$$E_k = \frac{A(k)}{B(k) - C(k)E_{k-1}}, \quad F_k = \frac{D(k) + C(k)F_{k-1}}{B(k) - C(k)E_{k-1}}. \tag{D.7}$$

If we dispose of ω_0 , the value of vorticity on the airfoil boundary (Dirichlet condition), we can write that $\omega(1) = E_1\omega(2) + F_1 = \omega_0$. This implies that $E_1 = 0$ and $F_1 = \omega_0$. Thanks to the relations D.7, the values of E_k and F_k can be computed during this descent phase for $k = 2, N_r - 1$. The remaining question is how to compute the value of the vorticity on the airfoil ω_0 . This question will be addressed in Appendix E.1.

To initiate the ascent phase, we need to express the value of $\omega(N_r)$ in terms of E_{N_r-1} and F_{N_r-1} . This expression is computed through the condition on the outflow boundary. Suppose we have the Neumann condition $\frac{\partial\omega}{\partial z} = 0$. This means that to first order

$\omega(N_r-1) = \omega(N_r)$. At the same time, we have that $\omega(N_r-1) = E_{N_r-1}\omega(N_r) + F_{N_r+1}$, reaching finally $\omega(N_r) = \frac{F_{N_r-1}}{1 - E_{N_r-1}}$. The values of E_{N_r-1} and F_{N_r-1} are obtained with the descent phase and not by simple identification (which may lead to $E_{N_r-1} = 1$ and $F_{N_r-1} = 0$). Starting from the value of $\omega(N_r)$ and thanks to the relation D.5, all the values of ω can be computed.

D.1.2 The stream function equation

The Poisson-like equation for the stream function reads:

$$\frac{1}{e^{2z}} \frac{\partial^2 \psi}{\partial z^2} + \frac{a}{r e^{2z}} \frac{\partial \psi}{\partial z} + \frac{1}{r^2} \frac{\partial^2 \psi}{\partial \theta^2} = -J\omega. \quad (\text{D.8})$$

The solution for ψ at time step $n+1$ is computed once the value of ω at the same step is known, itself computed with the value of ψ at $t=n$. A Fourier transformation is well adapted for such a kind of equations. Hence, exploiting the periodicity the θ direction, we use a Fourier-series development for ψ and $J\omega$ in the azimuthal direction by writing:

$$\begin{cases} \psi(\theta, z) = \sum_{k=-N_\theta}^{N_\theta} \psi_k(z) e^{ik\theta} \\ J(\theta, z) \omega(\theta, z) = \sum_{k=-N_\theta}^{N_\theta} F_k(z) e^{ik\theta} \end{cases} \quad (\text{D.9})$$

F_k is the Fourier transform of $J\omega$ known, through an FFT, and k the wave number. Injecting the previous developments in equation D.8 and exploiting the orthogonality between the different modes we reach a set of $\frac{N_\theta}{2}$ ordinary differential equations:

$$\frac{1}{e^{2z}} \frac{d^2 \psi_k}{dz^2} + \frac{a}{(e^z - a)e^{2z}} \frac{d\psi_k}{dz} - \frac{k^2}{(e^z - a)^2} \psi_k = -F_k \quad (\text{D.10})$$

This reduction by two of the system dimension is the advantage of the fast Fourier transformation when N_θ is suitably chosen. Centred schemes are used to evaluate these derivatives yielding:

$$\psi_{k,j+1} \left[1 + \frac{a\Delta z}{2r} \right] - \psi_{k,j} \left[2 + \left(\frac{e^z \Delta z k}{r} \right)^2 \right] + \psi_{k,j-1} \left[1 - \frac{a\Delta z}{2r} \right] = -F_k e^{2z} (\Delta z)^2 \quad (\text{D.11})$$

Thus, we obtain a complex tridiagonal system under the form:

$$-A(j)\psi(j+1) + B(j)\psi(j) - C(j)\psi(j-1) = D(j) \text{ for } j = 1, N_\theta,$$

where $A(1) = C(N_\theta) = 0$. This tridiagonal system is solved with the same algorithm used for the implicit step in z . However, in this case, we impose two Neumann-like conditions (see Appendix E.1) corresponding to the values of $\frac{\partial\psi}{\partial\theta}$ on the airfoil and on the outflow boundary.

D.2 The sensitivity equations

As far as the sensitivity equations are concerned, the Poisson-like equation is exactly identical to the Poisson-like equation of the flow, whereas the sensitivity of the vorticity equation has a source term which can be included in the right hand side of the tridiagonal systems.

D.2.1 The vorticity sensitivity

If we denote by Ω and Ψ the sensitivity of vorticity and stream function respectively, we have:

$$\frac{\partial\Omega}{\partial t} + \frac{1}{\sqrt{J}} \left[\frac{v_r}{e^z} \frac{\partial\Omega}{\partial z} + \frac{v_\theta}{r} \frac{\partial\Omega}{\partial\theta} \right] + \underbrace{\frac{1}{\sqrt{J}} \left[\frac{1}{e^z} \frac{\partial v_r}{\partial g} \frac{\partial\omega}{\partial z} + \frac{1}{r} \frac{\partial v_\theta}{\partial g} \frac{\partial\omega}{\partial\theta} \right]}_{S_\Omega} = \tag{D.12}$$

$$\frac{1}{ReJ} \left[\frac{1}{e^{2z}} \frac{\partial^2\Omega}{\partial z^2} + \frac{a}{re^{2z}} \frac{\partial\Omega}{\partial z} + \frac{1}{r^2} \frac{\partial^2\Omega}{\partial\theta^2} \right]$$

The difference with respect to the flow equations is the underbraced source term S_Ω . It depends on the choice of the control parameter.

Half step, implicit in θ

The same method used for the flow equations is applied here. The term source can be evaluated at the time step n or at the subsequent step. However, the former possibility accelerates the computations since the solution for the sensitivity problem is done in the same time than the flow resolution: the left hand side coefficients of the tridiagonal system are identical for the flow and sensitivity equations. If we solve the sensitivity at the same time, we spare the memory needed to store these coefficients

or to recompute them. Therefore, we write:

$$\begin{aligned} & \frac{\Omega^{n+\frac{1}{2}} - \Omega^n}{\frac{\Delta t}{2}} + \frac{1}{\sqrt{J}} \left[\left(\frac{v_r}{e^z} \right)^n \left(\frac{\partial \Omega}{\partial z} \right)^n + \left(\frac{v_\theta}{r} \right)^n \left(\frac{\partial \Omega}{\partial \theta} \right)^{n+\frac{1}{2}} \right] \\ & + \frac{1}{\sqrt{J}} \left[\frac{1}{e^z} \left(\frac{\partial v_r}{\partial g} \right)^n \left(\frac{\partial \omega}{\partial z} \right)^n + \frac{1}{r} \left(\frac{\partial v_\theta}{\partial g} \right)^n \left(\frac{\partial \omega}{\partial \theta} \right)^n \right] = \\ & \frac{1}{ReJ} \left[\frac{1}{e^{2z}} \left(\frac{\partial^2 \Omega}{\partial z^2} \right)^n + \frac{a}{re^{2z}} \left(\frac{\partial \Omega}{\partial z} \right)^n + \frac{1}{r^2} \left(\frac{\partial^2 \Omega}{\partial \theta^2} \right)^{n+\frac{1}{2}} \right] \end{aligned}$$

Using the classical centred scheme for the first and the second order derivatives, and isolating the unknown terms at the left hand side of the equation, we obtain for the node (i, j) where i is the index on θ and j on z :

$$\begin{aligned} & \Omega_{i+1,j}^{n+\frac{1}{2}} \left[\frac{rRe\sqrt{J}\Delta\theta v_\theta^n}{2} - 1 \right] + \Omega_{i,j}^{n+\frac{1}{2}} \left[\frac{2r^2JRe(\Delta\theta)^2}{\Delta t} + 2 \right] + \Omega_{i-1,j}^{n+\frac{1}{2}} \left[\frac{-rRe\sqrt{J}\Delta\theta v_\theta^n}{2} - 1 \right] \\ & = \Omega_{i,j+1}^n \left[\frac{-\sqrt{J}r^2Re(\Delta\theta)^2 v_r^n}{2e^z\Delta z} + \left(\frac{r\Delta\theta}{e^z\Delta z} \right)^2 + \frac{ar(\Delta\theta)^2}{2e^{2z}\Delta z} \right] \\ & + \Omega_{i,j}^n \left[\frac{2r^2JRe(\Delta\theta)^2}{\Delta t} - 2 \left(\frac{r\Delta\theta}{e^z\Delta z} \right)^2 \right] \\ & + \Omega_{i,j-1}^n \left[\frac{\sqrt{J}r^2Re(\Delta\theta)^2 v_r^n}{2e^z\Delta z} + \left(\frac{r\Delta\theta}{e^z\Delta z} \right)^2 - \frac{ar(\Delta\theta)^2}{2e^{2z}\Delta z} \right] \\ & - \underbrace{\left(\sqrt{J}r^2Re(\Delta\theta)^2 \right) \left[\left(\frac{\partial v_r}{\partial g} \right)^n \left(\frac{\partial \omega}{\partial r} \right)^n + \frac{1}{r} \left(\frac{\partial v_\theta}{\partial g} \right)^n \left(\frac{\partial \omega}{\partial \theta} \right)^n \right]}_{S_\Omega^n} \end{aligned} \tag{D.13}$$

Here again, we have a tridiagonal system under the form:

$$A(i)\Omega(i+1) + B(i)\Omega(i) + C(i)\Omega(i-1) = D(i),$$

for $i = 1, N_\theta$ where $A(1) = C(N_\theta) = 0$ that we solve with the same algorithm used for tridiagonal system with periodic boundary conditions as for the flow equations. The source term S_Ω^n is discretized by writing:

$$\begin{aligned} & \left(\frac{\partial v_r}{\partial g} \right)^n \left(\frac{\partial \omega}{\partial r} \right)^n + \frac{1}{r} \left(\frac{\partial v_\theta}{\partial g} \right)^n \left(\frac{\partial \omega}{\partial \theta} \right)^n = \frac{1}{e^z} \left(\frac{\partial v_r}{\partial g} \right)^n \left(\frac{\partial \omega}{\partial z} \right)^n + \frac{1}{r} \left(\frac{\partial v_\theta}{\partial g} \right)^n \left(\frac{\partial \omega}{\partial \theta} \right)^n \\ & = \frac{1}{e^z} \left(\frac{\omega_{i,j+1}^n - \omega_{i,j-1}^n}{2\Delta z} \right) \left(\frac{\partial v_r}{\partial g} \right)^n + \frac{1}{r} \left(\frac{\omega_{i+1,j}^n - \omega_{i-1,j}^n}{2\Delta\theta} \right) \left(\frac{\partial v_\theta}{\partial g} \right)^n \end{aligned}$$

where

$$\begin{aligned} \left(\frac{\partial v_r}{\partial g}\right)^n &= -\frac{1}{\sqrt{J}} \left[\frac{\partial \left(\dot{h}(t) \sin \alpha(t) - \dot{\alpha}(t)Y \right)}{\partial g} \left(\frac{\partial X}{\partial \xi} \cos \theta + \frac{\partial X}{\partial \chi} \sin \theta \right) \right] \\ &\quad - \frac{1}{\sqrt{J}} \left[\frac{\partial \left(\dot{h}(t) \cos \alpha(t) + \dot{\alpha}(t)X \right)}{\partial g} \left(\frac{\partial Y}{\partial \xi} \cos \theta + \frac{\partial Y}{\partial \chi} \sin \theta \right) \right] \\ &\quad + \frac{1}{2r\sqrt{J}\Delta\theta} [\Psi_{i+1,j}^n - \Psi_{i-1,j}^n] \end{aligned}$$

and

$$\begin{aligned} \left(\frac{\partial v_\theta}{\partial g}\right)^n &= -\frac{1}{\sqrt{J}} \left[\frac{\partial \left(\dot{h}(t) \sin \alpha(t) - \dot{\alpha}(t)Y \right)}{\partial g} \left(\frac{\partial X}{\partial \chi} \cos \theta - \frac{\partial X}{\partial \xi} \sin \theta \right) \right] \\ &\quad - \frac{1}{\sqrt{J}} \left[\frac{\partial \left(\dot{h}(t) \cos \alpha(t) + \dot{\alpha}(t)X \right)}{\partial g} \left(\frac{\partial Y}{\partial \chi} \cos \theta - \frac{\partial Y}{\partial \xi} \sin \theta \right) \right] \\ &\quad - \frac{1}{2e^z\sqrt{J}\Delta z} [\Psi_{i,j+1}^n - \Psi_{i,j-1}^n] \end{aligned}$$

Half step, implicit in z

In this second half temporal step between time instants $n + \frac{1}{2}$ and $n + 1$, an implicit scheme is applied to the z derivatives:

$$\begin{aligned} &\frac{\Omega^{n+1} - \Omega^{n+\frac{1}{2}}}{\frac{\Delta t}{2}} + \frac{1}{\sqrt{J}} \left[\left(\frac{v_r}{e^z}\right)^n \left(\frac{\partial \Omega}{\partial z}\right)^{n+1} + \left(\frac{v_\theta}{r}\right)^n \left(\frac{\partial \Omega}{\partial \theta}\right)^{n+\frac{1}{2}} \right] \\ &+ \frac{1}{\sqrt{J}} \left[\frac{1}{e^z} \left(\frac{\partial v_r}{\partial g}\right)^n \left(\frac{\partial \omega}{\partial z}\right)^n + \frac{1}{r} \left(\frac{\partial v_\theta}{\partial g}\right)^n \left(\frac{\partial \omega}{\partial \theta}\right)^n \right] = \\ &\frac{1}{ReJ} \left[\frac{1}{e^{2z}} \left(\frac{\partial^2 \Omega}{\partial z^2}\right)^{n+1} + \frac{a}{re^{2z}} \left(\frac{\partial \Omega}{\partial z}\right)^{n+1} + \frac{1}{r^2} \left(\frac{\partial^2 \Omega}{\partial \theta^2}\right)^{n+\frac{1}{2}} \right]. \end{aligned}$$

Using the centered scheme for the first and second order derivatives we obtain:

$$\begin{aligned}
 & -\Omega_{i,j+1}^{n+1} \left[-\frac{Re\sqrt{J}e^z\Delta z v_r^n}{2} + 1 + \frac{a\Delta z}{2r} \right] + \Omega_{i,j}^{n+1} \left[\frac{2e^{2z}JRe(\Delta z)^2}{\Delta t} + 2 \right] \\
 & -\Omega_{i,j-1}^{n+1} \left[\frac{Re\sqrt{J}\Delta z v_r^n}{2} + 1 - \frac{a\Delta z}{2r} \right] = -\Omega_{i+1,j}^{n+\frac{1}{2}} \left(\frac{e^z\Delta z}{r\Delta\theta} \right)^2 \left[\frac{\sqrt{J}rRe\Delta\theta v_\theta^n}{2} - 1 \right] \\
 & + \Omega_{i,j}^{n+\frac{1}{2}} \left(\frac{e^z\Delta z}{r\Delta\theta} \right)^2 \left[\frac{2JRe r^2(\Delta\theta)^2}{\Delta t} - 2 \right] - \Omega_{i-1,j}^{n+\frac{1}{2}} \left(\frac{e^z\Delta z}{r\Delta\theta} \right)^2 \left[-\frac{\sqrt{J}rRe\Delta\theta v_\theta^n}{2} - 1 \right] \\
 & - \underbrace{(\omega_{i,j+1}^n - \omega_{i,j-1}^n) \left(\frac{\sqrt{J}Ree^z\Delta z}{2} \right) \left(\frac{\partial v_r}{\partial g} \right)^n - (\omega_{i+1,j}^n - \omega_{i-1,j}^n) \left(\frac{\sqrt{J}Ree^{2z}(\Delta z)^2}{2r\Delta\theta} \right) \left(\frac{\partial v_\theta}{\partial g} \right)^n}_{S_z^n}
 \end{aligned} \tag{D.14}$$

The last two terms are the source term S_z^n . This system is solved with the same algorithm than the flow equation by including the source term on the right hand side. Here, the Dirichlet-like boundary condition on the airfoil and the Neumann-like boundary condition on the outflow are computed by the derivation of the flow boundary conditions with respect to the control parameter (cf. Appendix E.2).

D.2.2 The stream function sensitivity

The sensitivity equation for the stream function is identical to the equation for the stream function. The same methodology as before is followed:

$$\frac{1}{e^{2z}} \frac{\partial^2 \Psi}{\partial z^2} + \frac{a}{re^{2z}} \frac{\partial \Psi}{\partial z} + \frac{1}{r^2} \frac{\partial^2 \Psi}{\partial \theta^2} = -J\Omega, \tag{D.15}$$

Ψ for the $n+1$ step is computed once the value of Ω is known at $n+1$, itself computed through the value of Ψ at $t = n$. A Fourier-series development for Ψ and $J\Omega$ in the θ direction is applied:

$$\begin{cases} \Psi(\theta, z) = \sum_{k=-N_\theta}^{N_\theta} \Psi_k(z) e^{ik\theta}, \\ J(\theta, z) \Omega(\theta, z) = \sum_{k=-N_\theta}^{N_\theta} F_k(z) e^{ik\theta}. \end{cases} \tag{D.16}$$

The set of ordinary differential equations with known right hand side, is in this case:

$$\frac{1}{e^{2z}} \frac{d^2 \Psi_k}{dz^2} + \frac{a}{(e^z - a)e^{2z}} \frac{d\Psi_k}{dz} - \frac{k^2}{(e^z - a)^2} \Psi_k = -F_k \tag{D.17}$$

We use centered scheme to evaluate this derivatives and we obtain the system:

$$\Psi_{k,j+1} \left[1 + \frac{a\Delta z}{2r} \right] - \Psi_{k,j} \left[2 + \left(\frac{e^z \Delta z k}{r} \right)^2 \right] + \Psi_{k,j-1} \left[1 - \frac{a\Delta z}{2r} \right] = -F_k e^{2z} (\Delta z)^2$$

Thus, we obtain a complex tridiagonal system of the form:

$$-A(j)\Psi(j+1) + B(j)\Psi(j) - C(j)\Psi(j-1) = D(j),$$

for $j = 1, N_\theta$, where $A(1) = C(N_\theta) = 0$. The system is solved with the same algorithm than the stream function equation. Two Neumann-like boundary conditions on $\frac{\partial \Psi}{\partial \theta}$ on the airfoil and on the outflow are used. They are obtained by derivation of the boundary conditions of the stream function equation with respect to the control parameter (cf Appendix E.2).

Appendix E

The boundary conditions

If we refer to Appendix D, the value of the vorticity (and its sensitivity) on the airfoil should be computed to initiate the descent phase of the Thomas algorithm in the z implicit half step. Furthermore, the derivatives with respect to θ of the stream function (and its sensitivity) should be evaluated on the airfoil and on the outflow boundary. Since the equations are solved in the moving frame, the airfoil is still and the velocity of the fluid on the airfoil should vanish in this referential. On the other hand, for a sufficiently large computational domain, the velocity is not disturbed and is equal to the free stream velocity. The expression of these boundary conditions for the flow equations and sensitivity equations represent the aim of the present appendix.

E.1 Flow boundary conditions

The radial and azimuthal velocities are related to the stream function by the relations E.1 valid for the whole computational domain:

$$\begin{aligned} v_r &= \frac{1}{\sqrt{J}} \left[\frac{1}{r} \frac{\partial \psi}{\partial \theta} - \left(\dot{h}(t) \sin(\alpha(t)) - \dot{\alpha}(t) Y \right) \left(\frac{\partial X}{\partial \xi} \cos \theta + \frac{\partial X}{\partial \chi} \sin \theta \right) \right. \\ &\quad \left. - \left(\dot{h}(t) \cos(\alpha(t)) + \dot{\alpha}(t) X \right) \left(\frac{\partial Y}{\partial \xi} \cos \theta + \frac{\partial Y}{\partial \chi} \sin \theta \right) \right], \\ v_\theta &= \frac{1}{\sqrt{J}} \left[-\frac{\partial \psi}{\partial r} - \left(\dot{h}(t) \sin(\alpha(t)) - \dot{\alpha}(t) Y \right) \left(\frac{\partial X}{\partial \chi} \cos \theta - \frac{\partial X}{\partial \xi} \sin \theta \right) \right. \\ &\quad \left. - \left(\dot{h}(t) \cos(\alpha(t)) + \dot{\alpha}(t) X \right) \left(\frac{\partial Y}{\partial \chi} \cos \theta - \frac{\partial Y}{\partial \xi} \sin \theta \right) \right]. \end{aligned} \tag{E.1}$$

E.1.1 The vorticity equation

The value of $\omega(\theta, z_0)$ is sought, where $z_0 = \ln(r_0 + a)$ and $r = r_0$ is the position of the airfoil (cf. Appendix B). We start by expressing ω in terms of ψ and its derivatives thanks to the Poisson-like equation:

$$\omega(\theta, z_0) = \frac{1}{J} \left[\frac{1}{e^{2z_0}} \left(\frac{\partial^2 \psi}{\partial z^2} \right)_{(\theta, z_0)} + \frac{a}{r_0 e^{2z_0}} \left(\frac{\partial \psi}{\partial z} \right)_{(\theta, z_0)} + \frac{1}{r_0^2} \left(\frac{\partial^2 \psi}{\partial \theta^2} \right)_{(\theta, z_0)} \right]. \quad (\text{E.2})$$

The second order derivative $\left(\frac{\partial^2 \psi}{\partial z^2} \right)$ is approximated with a first order finite differences scheme (Thom, 1928; Roache, 1972) as:

$$\left(\frac{\partial^2 \psi}{\partial z^2} \right)_{(\theta, z_0)} = \frac{2(\psi(\theta, z_0 + \Delta z) - \psi(\theta, z_0))}{\Delta z^2} - \frac{2}{\Delta z} \left(\frac{\partial \psi}{\partial z} \right)_{(\theta, z_0)} + O(\Delta z),$$

and the derivatives $\left(\frac{\partial \psi}{\partial z} \right)$ and $\left(\frac{\partial^2 \psi}{\partial \theta^2} \right)$ are evaluated from equation E.1. On the airfoil surface, the radial and tangential velocities vanish, i.e.:

$$\begin{aligned} \frac{1}{e^{z_0}} \left(\frac{\partial \psi}{\partial z} \right)_{\theta, z_0} &= - \left[\left(\dot{h}(t) \sin(\alpha(t)) - \dot{\alpha}(t) Y \right) \left(\frac{\partial X}{\partial \chi} \cos \theta - \frac{\partial X}{\partial \xi} \sin \theta \right) \right]_{(\theta, z_0)} \\ &\quad + \left[\left(\dot{h}(t) \cos(\alpha(t)) + \dot{\alpha}(t) X \right) \left(\frac{\partial Y}{\partial \chi} \cos \theta - \frac{\partial Y}{\partial \xi} \sin \theta \right) \right]_{(\theta, z_0)}, \end{aligned}$$

and

$$\begin{aligned} \frac{1}{r_0} \left(\frac{\partial^2 \psi}{\partial \theta^2} \right)_{(\theta, z_0)} &= - [(r \dot{\alpha}(t) J)]_{(\theta, z_0)} \\ &\quad - \left[\left(\dot{h}(t) \sin(\alpha(t)) - \dot{\alpha}(t) Y \right) \left(\frac{\partial X}{\partial \xi} \sin \theta - \frac{\partial^2 X}{\partial \xi \partial \theta} \cos \theta - \frac{\partial X}{\partial \chi} \cos \theta - \frac{\partial^2 X}{\partial \chi \partial \theta} \sin \theta \right) \right]_{(\theta, z_0)} \\ &\quad - \left[\left(\dot{h}(t) \cos(\alpha(t)) + \dot{\alpha}(t) X \right) \left(\frac{\partial Y}{\partial \xi} \sin \theta - \frac{\partial^2 Y}{\partial \xi \partial \theta} \cos \theta - \frac{\partial Y}{\partial \chi} \cos \theta - \frac{\partial^2 Y}{\partial \chi \partial \theta} \cos \theta \right) \right]_{(\theta, z_0)}. \end{aligned}$$

Injecting the last three relations in equation E.2, we finally obtain:

$$\begin{aligned}
 \omega(\theta, z_0) = & \dot{\alpha}(t) - \frac{2[\psi(\theta, z_0 + \Delta z) - \psi(\theta, z_0)]}{(\Delta z)^2 e^{2z_0} J(\theta, z_0)} \\
 & + \frac{1}{J(\theta, z_0) e^{z_0}} \left(-\frac{2}{\Delta z} + \frac{a}{r_0} \right) \left[\left(\dot{h}(t) \sin(\alpha(t)) - \dot{\alpha}(t) Y \right) \left(\frac{\partial X}{\partial \chi} \cos \theta - \frac{\partial X}{\partial \xi} \sin \theta \right) \right]_{(\theta, z_0)} \\
 & + \frac{1}{J(\theta, z_0) e^{z_0}} \left(-\frac{2}{\Delta z} + \frac{a}{r_0} \right) \left[\left(\dot{h}(t) \cos(\alpha(t)) + \dot{\alpha}(t) X \right) \left(\frac{\partial Y}{\partial \chi} \cos \theta - \frac{\partial Y}{\partial \xi} \sin \theta \right) \right]_{(\theta, z_0)} \\
 & + \frac{1}{r_0 J(\theta, z_0)} \left[\left(\dot{h}(t) \sin(\alpha(t)) - \dot{\alpha}(t) Y \right) \left(\frac{\partial X}{\partial \xi} \sin \theta - \frac{\partial^2 X}{\partial \xi \partial \theta} \cos \theta - \frac{\partial X}{\partial \chi} \cos \theta - \frac{\partial^2 X}{\partial \chi \partial \theta} \sin \theta \right) \right]_{(\theta, z_0)} \\
 & + \frac{1}{r_0 J(\theta, z_0)} \left[\left(\dot{h}(t) \cos(\alpha(t)) + \dot{\alpha}(t) X \right) \left(\frac{\partial Y}{\partial \xi} \sin \theta - \frac{\partial^2 Y}{\partial \xi \partial \theta} \cos \theta - \frac{\partial Y}{\partial \chi} \cos \theta - \frac{\partial^2 Y}{\partial \chi \partial \theta} \sin \theta \right) \right]_{(\theta, z_0)}.
 \end{aligned} \tag{E.3}$$

E.1.2 The stream function equation

Since ψ is developed into a Fourier-series in θ , it is practical to write the conditions on $\frac{\partial \psi}{\partial \theta}$ at $z = z_0$ and $z = z_{max}$, with $z_0 = \ln(r_0 + a)$ and $z_{max} = \ln(R_{max} + a)$ (cf. Appendix B). Therefore, we write $\frac{\partial \psi}{\partial \theta} = f(t)g(\theta)$ and we compute the Fourier-transformation of the right hand side:

$$f(t)g(\theta) = \sum_{k=-N_\theta}^{N_\theta} G_k(t) e^{ik\theta}.$$

On the other hand,

$$\frac{\partial \psi}{\partial \theta} = \sum_{k=-N_\theta}^{N_\theta} ik \psi_k(z, t) e^{ik\theta},$$

leading to

$$\psi_k(z, t) = \frac{G_k(t)}{ik}.$$

Hence, we need to express the function $f(t)g(\theta)$ at z_0 and z_{max} and compute its Fourier transformation.

Wall boundary condition

The radial velocity v_r must vanish on the airfoil, at $z = z_0$ (cf. equation E.1):

$$\begin{aligned} \frac{1}{r_0} \left(\frac{\partial \psi}{\partial \theta} \right)_{z_0} &= \left(\dot{h}(t) \sin(\alpha) - \dot{\alpha}(t) Y \right) \left(\frac{\partial X}{\partial \xi} \cos \theta + \frac{\partial X}{\partial \chi} \sin \theta \right)_{z_0} \\ &+ \left(\dot{h}(t) \cos(\alpha) + \dot{\alpha}(t) X \right) \left(\frac{\partial Y}{\partial \xi} \cos \theta + \frac{\partial Y}{\partial \chi} \sin \theta \right)_{z_0}. \end{aligned}$$

Hence, at the wall,

$$\begin{aligned} \left(\frac{\partial \psi}{\partial \theta} \right)_{(\theta, z_0)} &= r_0 \left[\left(\dot{h}(t) \sin(\alpha) - \dot{\alpha}(t) Y \right) \left(\frac{\partial X}{\partial \xi} \cos \theta + \frac{\partial X}{\partial \chi} \sin \theta \right) \right]_{(\theta, z_0)} \\ &+ r_0 \left[\left(\dot{h}(t) \cos(\alpha) + \dot{\alpha}(t) X \right) \left(\frac{\partial Y}{\partial \xi} \cos \theta + \frac{\partial Y}{\partial \chi} \sin \theta \right) \right]_{(\theta, z_0)} = f(t)g(\theta). \end{aligned} \quad (\text{E.4})$$

Outflow boundary condition

At the outer limit of the computational domain, we want to impose a velocity which is not perturbed by the presence of the airfoil, equal to the free stream velocity. For an airfoil having an angle of attack equal to α_0 and a pitching angle $\alpha(t)$, the velocities in the moving frame are:

$$\begin{cases} U = u_\alpha \cos(\alpha(t) - \alpha_0) + (v_\alpha - \dot{h}(t)) \sin(\alpha(t) - \alpha_0) + Y \dot{\alpha}(t), \\ V = -u_\alpha \sin(\alpha(t) - \alpha_0) + (v_\alpha - \dot{h}(t)) \cos(\alpha(t) - \alpha_0) - X \dot{\alpha}(t). \end{cases} \quad (\text{E.5})$$

On the other hand, we have:

$$\begin{cases} U = \frac{\partial \psi}{\partial Y} - \dot{h}(t) \sin(\alpha(t) - \alpha_0) + Y \dot{\alpha}(t), \\ V = -\frac{\partial \psi}{\partial X} - \dot{h}(t) \cos(\alpha(t) - \alpha_0) - X \dot{\alpha}(t), \end{cases} \quad (\text{E.6})$$

which implies:

$$\begin{cases} \frac{\partial \psi}{\partial X} = u_\alpha \sin(\alpha(t) - \alpha_0) - v_\alpha \cos(\alpha(t) - \alpha_0), \\ \frac{\partial \psi}{\partial Y} = u_\alpha \cos(\alpha(t) - \alpha_0) + v_\alpha \sin(\alpha(t) - \alpha_0). \end{cases} \quad (\text{E.7})$$

In the particular case in which $u_\alpha = U_0$ and $v_\alpha = 0$ and applying the relation between the derivatives in the moving frame (X, Y) and the Joukowski one (χ, ξ) , and then between (χ, ξ) and the polar frame (r, θ) we reach:

$$\frac{\partial \psi}{\partial \theta} = rU_0 \cos(\alpha - \alpha_0) \left[\frac{\partial X}{\partial \xi} \cos \theta + \frac{\partial X}{\partial \chi} \sin \theta \right] - rU_0 \sin(\alpha - \alpha_0) \left[\frac{\partial Y}{\partial \xi} \cos \theta + \frac{\partial Y}{\partial \chi} \sin \theta \right].$$

Hence, at $z = z_{max}$:

$$\begin{aligned} \left(\frac{\partial \psi}{\partial \theta} \right)_{(\theta, z_{max})} &= R_{max} U_0 [\cos(\alpha - \alpha_0)] \left[\frac{\partial X}{\partial \xi} \cos \theta + \frac{\partial X}{\partial \chi} \sin \theta \right]_{(\theta, z_{max})}, \\ &- R_{max} U_0 [\sin(\alpha - \alpha_0)] \left[\frac{\partial Y}{\partial \xi} \cos \theta + \frac{\partial Y}{\partial \chi} \sin \theta \right]_{(\theta, z_{max})} = f(t)g(\theta). \end{aligned} \quad (\text{E.8})$$

E.2 Sensitivity boundary conditions

E.2.1 The sensitivity of the vorticity

The same method applied in Appendix E.1.1 to the vorticity boundary condition can be employed here for the boundary conditions of the Ω -equation. This includes a use of a Taylor development and the relations between the derivatives of the velocity with respect to the control parameter g and Ψ (cf. Appendix D.2). Since the radial and azimuthal velocities vanish on the airfoil, their derivatives with respect to g vanish also, leading to the value of $\Omega(t, \theta, z_0)$. However, this value can be obtained easily, if we apply directly the derivation, with respect to g , to the vorticity boundary conditions:

$$\begin{aligned} \Omega(\theta, z_0) &= \frac{\partial}{\partial g} (\dot{\alpha}(t)) - \frac{2 [\Psi(\theta, z_0 + \Delta z) - \Psi(\theta, z_0)]}{(\Delta z)^2 e^{2z_0} J(\theta, z_0)} \\ &+ \frac{1}{J(\theta, z_0) e^{z_0}} \left(-\frac{2}{\Delta z} + \frac{a}{r_0} \right) \left[\frac{\partial}{\partial g} (\dot{h}(t) \sin(\alpha(t)) - \dot{\alpha}(t)Y) \left(\frac{\partial X}{\partial \chi} \cos \theta - \frac{\partial X}{\partial \xi} \sin \theta \right) \right]_{(\theta, z_0)} \\ &+ \frac{1}{J(\theta, z_0) e^{z_0}} \left(-\frac{2}{\Delta z} + \frac{a}{r_0} \right) \left[\frac{\partial}{\partial g} (\dot{h}(t) \cos(\alpha(t)) + \dot{\alpha}(t)X) \left(\frac{\partial Y}{\partial \chi} \cos \theta - \frac{\partial Y}{\partial \xi} \sin \theta \right) \right]_{(\theta, z_0)} \\ &+ \left[\frac{1}{r_0 J} \frac{\partial}{\partial g} (\dot{h}(t) \sin(\alpha(t)) - \dot{\alpha}(t)Y) \left(\frac{\partial X}{\partial \xi} \sin \theta - \frac{\partial^2 X}{\partial \xi \partial \theta} \cos \theta - \frac{\partial X}{\partial \chi} \cos \theta - \frac{\partial^2 X}{\partial \chi \partial \theta} \sin \theta \right) \right]_{(\theta, z_0)} \\ &+ \left[\frac{1}{r_0 J} \frac{\partial}{\partial g} (\dot{h}(t) \cos(\alpha(t)) + \dot{\alpha}(t)X) \left(\frac{\partial Y}{\partial \xi} \sin \theta - \frac{\partial^2 Y}{\partial \xi \partial \theta} \cos \theta - \frac{\partial Y}{\partial \chi} \cos \theta - \frac{\partial^2 Y}{\partial \chi \partial \theta} \sin \theta \right) \right]_{(\theta, z_0)} \end{aligned} \quad (\text{E.9})$$

E.2.2 The sensitivity of the stream function

The boundary conditions for Ψ may be computed with the same principle used for ψ boundary conditions or they can be directly deduced by a derivation with respect to the control parameter g .

Wall boundary condition

$$\begin{aligned} \left(\frac{\partial \Psi}{\partial \theta} \right)_{(\theta, z_0)} &= r_0 \left[\frac{\partial}{\partial g} \left(\dot{h}(t) \sin(\alpha) - \dot{\alpha}(t) Y \right) \left(\frac{\partial X}{\partial \xi} \cos \theta + \frac{\partial X}{\partial \chi} \sin \theta \right) \right]_{(\theta, z_0)} \\ &+ r_0 \left[\frac{\partial}{\partial g} \left(\dot{h}(t) \cos(\alpha) + \dot{\alpha}(t) X \right) \left(\frac{\partial Y}{\partial \xi} \cos \theta + \frac{\partial Y}{\partial \chi} \sin \theta \right) \right]_{(\theta, z_0)} = f(t)g(\theta). \end{aligned} \quad (\text{E.10})$$

Outflow boundary condition

$$\begin{aligned} \left(\frac{\partial \Psi}{\partial \theta} \right)_{(\theta, z_{max})} &= R_{max} U_0 \frac{\partial}{\partial g} [\cos(\alpha - \alpha_0)] \left[\frac{\partial X}{\partial \xi} \cos \theta + \frac{\partial X}{\partial \chi} \sin \theta \right]_{(\theta, z_{max})} \\ &- R_{max} U_0 \frac{\partial}{\partial g} [\sin(\alpha - \alpha_0)] \left[\frac{\partial Y}{\partial \xi} \cos \theta + \frac{\partial Y}{\partial \chi} \sin \theta \right]_{(\theta, z_{max})} = f(t)g(\theta). \end{aligned} \quad (\text{E.11})$$

Bibliography

- A.R. Ahmadi and S.E. Windall. Unsteady lifting-line theory as a singular-perturbation problem. *Journal of Fluid Mechanics*, 153, pp. 59–81, 1985.
- C. Airiau, A. Bottaro, and S. Walther. A methodology for optimal laminar flow control: application to the damping of tollmien-schlichting waves in a boundary layer. *Physics of Fluids*, 15, pp. 1131–1143, 2003.
- M.R. Alam, W. Liu, and G. Haller. Closed-loop separation control: An analytical approach. *Physics of Fluids*, 18(043601), 2006.
- R. Albertani, B. Stanford, J.P. Hubner, and P.G. Ifju. Aerodynamic coefficients and deformation measurements on flexible micro air vehicle wings. *Journal of Experimental Mechanics*, 47(5), pp. 625–635, 2007.
- R. Ames, O. Wong, and N. Komerath. On the flowfield and forces generated by a flapping rectangular wing at low reynolds number. *American Institute of Aeronautics and Astronautics, (Mueller, 2001)*, 195, pp. 287–305, 2001.
- O. Amoignon, J.O. Pralits, A. Hanifi, M. Berggren, and D.S. Henningson. Shape optimization for delay of laminar-turbulent transition. *AIAA Journal*, 44(5), pp. 1009–1024, 2006.
- J.M. Anderson. *Vortex control for efficient propulsion*. PhD thesis, Joint Program MIT/Woods Hole Oceanographic Institute, Cambridge, MA, 1996.
- J.M. Anderson, K. Streitlien, D.S. Barret, and M.S. Triantafyllou. Oscillating foils of high propulsive efficiency. *Journal of Fluid Mechanics*, 360, pp. 41–72, 1998.
- P.R. Bandyopadhyay, J.M. Castano, J.Q. Rice, R.B. Philips, W.H. Nedderman, and W.K. Macy. Low-speed maneuvering hydrodynamics of fish and small underwater vehicles. *Journal of Fluids Engineering - Transactions of the American Society of Mechanical Engineers*, 119, pp. 136–144, 1997.

- R. Bannasch. From soaring and flapping bird flight to innovative wing and propeller constructions. *American Institute of Aeronautics and Astronautics*, (Mueller, 2001), 195, pp. 453–471, 2001.
- G.E. Bartlett and R. J. Vidal. Experiment investigation of influence of edge sharp on the aerodynamics characteristics of low aspect ratio wings at low speeds. *Journal of the Aeronautical Sciences*, 22(8), pp. 517–533, 1955.
- A. Barut, M. Das, and E. Madenci. Non-linear deformations of flapping wings on a micro air vehicle. *AIAA Paper*, (2006-1662), 2006.
- A. Bejan and J.H. Marden. Unifying structural theory for scale effects in running, swimming and flying. *Journal of Experimental Biology*, 209, pp. 238–248, 2006.
- G.J. Berman and Z.J. Wang. Energy-minimizing kinematics in hovering insect flight. *Journal of Fluid Mechanics*, 582, pp. 153–168, 2007.
- D.J. Betteridge and R.D. Archer. A study of the mechanics of flapping flight. *Aero Q.*, 25, pp. 129–142, 1974.
- A. Betz. Ein beitrage zur erklarung des segelfluges. *Zeitschrift für Flutechnik und Motorluftschiffahrt*, 3, pp. 269–272, 1912.
- W. Birnbaum. Das ebene problem des schlagenden flüels. *Zeitschrift für Angewandte Mathematik und Mechanik*, 4(4), pp. 277–292, 1924.
- R. Blake. *Fish Locomotion*. Cambridge University Press, Cambridge, UK, 1983.
- P. Blondeaux, F. Fornarelli, L. Guglielmini, M.S. Triantafyllou, and R. Verzicco. Numerical experiments on flapping foils mimicking fishlike locomotion. *Physics of Fluids*, 17(113601), 2005.
- W. Bollay. A non-linear wing theory and its application to rectangular wings of small aspect ratio. *Zeitschrift für Angewandte Mathematik und Mechanik*, 19, pp. 21–35, 1939.
- A. Borthwick. Comparison between two finite-difference schemes for computing the flow around a cylinder. *International Journal of Numerical Methods in Fluids*, 6, pp. 275–290, 1986.
- A. Bottaro. Note on open boundary conditions for elliptic flow. *Numerical Heat Transfer. Part B: Fundamentals*, 18, pp. 243–256, 1990.
- A. Bottaro, H. Soueid, and B. Galletti. Secondary vortices in turbulent square duct. *AIAA Journal*, 44(4), pp. 803–811, 2006.

- M. Bozkurttas, H. Dong, Mittal. R, P. Madden, and G.V. Lauder. Hydrodynamic performance of deformable fish fins and flapping foils. *AIAA Paper*, (2006-1392), 2006.
- M. Bozkurttas, H. Dong, V. Seshadri, Mittal. R, and Najjar. F. Towards numerical simulation of flapping foils on fixed cartesian grids. *AIAA Paper*, (2005-79), 2005.
- M. Braza. *Simulation numérique du décollement instationnaire externe par une formulation vitesse pression. Application à l'écoulement autour d'un cylindre*. PhD thesis, Institut national polytechnique de Toulouse, France, 1981.
- M. Braza, P. Chassaing, and H. Ha Minh. Numerical study and physical analysis of the pressure and velocity fields in the near wake of a circular cylinder. *Journal of Fluid Mechanics*, 165, pp. 79–130, 1986.
- J.Y. Cheng, L.X. Zhuang, and B.G. Tong. Analysis of swimming three-dimensional plates. *Journal of Fluid Mechanics*, 232, pp. 341–355, 1991.
- D.H. Choi and L. Landweber. Inviscid analysis of two-dimensional airfoils in unsteady motion using conformal mapping. *AIAA Journal*, 28(12), pp. 2025–2033, 1990.
- M.G. Chopra. Hydromechanics of a lunate-tail swimming propulsion. *Journal of Fluid Mechanics*, 64, pp. 375–391, 1974.
- M.G. Chopra. Large amplitude lunate tail theory of fish locomotion. *Journal of Fluid Mechanics*, 74, pp. 161–182, 1976.
- J.D. DeLaurier. The development of an efficient ornithopter wing. *Aeronautical Journal*, 965, pp. 153–162, 1993.
- M.O. Dickinson, F.O. Lehmann, and S.P. Sane. Wing rotation and the aerodynamic basis of insect flight. *Science*, 284, pp. 1954–1960, 1999.
- C.P. Ellington. The aerodynamics of hovering insect flight - IV. Aerodynamic mechanism. *Philosophical Transactions of the Royal Society of London. B*, 305, pp. 79–113, 1984.
- C.P. Ellington and J.R. Usherwood. Lift and drag characteristics of rotary and flapping wings. *American Institute of Aeronautics and Astronautics*, (Mueller, 2001), 195, pp. 231–248, 2001.
- C.P. Ellington, C. Van der Berg, A.P. Willmott, and A.L.R. Thomas. Leading-edge vortices in insect flight. *Nature*, 384, pp. 626–630, 1996.

- K.D. Fampton, M. Goldfarb, D. Monopoli, and D. Cveticanin. Passive aeroelastic tailoring for optimal flapping wings. *American Institute of Aeronautics and Astronautics*, (Mueller, 2001), 195, pp. 473–482, 2001.
- F.E. Fish. The myth and reality of gray’s paradox: implication of dolphin drag reduction for technology. *Bioinspiration and Biomimetics*, 1(17-25), 2006.
- P. Freymuth. Propulsive vortical signature of plunging and pitching airfoils. *AIAA Journal*, 26(7), pp. 881–884, 1988.
- L.E. Garrick. Propulsion of a flapping and oscillating airfoil. *NACA TR*, 567, 1936.
- C.H. Gibbs-Smith. *The first half of the nineteenth century. A history of flying*. Batsford, London, Chapter 4 , pp. 108–112, 1953.
- R. Gopalkrishnan, M.S. Triantafyllou, G.S. Triantafyllou, and D.S. Barrett. Active vorticity control in a shear flow using a flapping foil. *Journal of Fluid Mechanics*, 274, pp. 1–21, 1994.
- J. Gray. Studies in animal locomotion. VI. The propulsive powers of the dolphin. *Journal of Experimental Biology*, 13, pp. 135–154, 1936.
- J.L. Guermond and L. Quartapelle. Uncoupled $\omega - \psi$ formulation for plane flows in multiply connected domains. *Mathematical Models and Methods in Applied Sciences*, 7(6), pp. 731–767, 1997.
- L. Guglielmini. *Modeling of thrust generating foils*. PhD thesis, Environmental Engineering Department, University of Genoa, Genoa, Italy, 2004.
- L. Guglielmini and P. Blondeaux. Propulsive efficiency of oscillating foils. *European Journal of Mechanics B/Fluids*, 23(2), pp. 255–278, 2004.
- M.D. Gunzburger. Inverse design and optimization methods: introduction into mathematical aspects of flow control and optimization. *von Karman Institute for Fluid Dynamics Lecture Series.*, (1997-05), 1997.
- D. Gyllhem, K. Mohseni, D. Lawrence, and P. Geuzaine. Numerical simulation of the flow around the colorado micro aerial vehicle. *AIAA Paper*, (2005-4757), 2005.
- K.C. Hall and S.R. Hall. Minimum induced power requirements for flapping flight. *Journal of Fluid Mechanics*, 323, pp. 285–315, 1996.
- K.C. Hall, S.A. Pigott, and S.R. Hall. Power requirements for large-amplitude flapping flight. *Journal of Aircraft*, 35, pp. 352–361, 1998.

- H. Hertel. *Structure, Form, Movement*. Rheinhold, New York, 1966.
- C. Hirsch. *Numerical Computation of Internal and External Flows*. John Wiley & Sons, 1988.
- S.F. Hoerner. *Fluid dynamic drag*. Hoerner Fluid Dynamics, Brick Town, NJ. , pp. 7.16–7.21, 1965.
- S.F. Hoerner and H.V. Brost. *Fluid dynamic lift*. Hoerner Fluid Dynamics, Brick Town, NJ. , pp. 17.1–17.15, 1975.
- F.S. Hover, Ø. Haugsdal, and M.S. Triantafyllou. Effect of angle of attack profiles in flapping foil propulsion. *Journal of Fluids and Structures*, 19, pp. 37–47, 2004.
- A. Iollo and L. Zannetti. Optimal control of vortex trapped by an airfoil with a cavity. *Flow, Turbulence and Combustion*, 65(34), pp. 417–430, 2000.
- K. Isogai, Y. Shinmoto, and Y. Watanabe. Effects of dynamic stall on propulsive efficiency and thrust of flapping foil. *AIAA Journal*, 37(10), pp. 1145–1151, 1999.
- K.D. Jones, C.M. Dohring, and M.F. Platzer. Experimental and computational investigation of the Knoller-Betz effect. *AIAA Journal*, 36(7), pp. 1240–1246, 1998.
- K.D. Jones, T.C. Lund, and M.F. Platzer. Experimental and computational investigation of flapping wing propulsion for micro air vehicles. *American Institute of Aeronautics and Astronautics, (Mueller, 2001)*, 195, pp. 307–339, 2001.
- K.D. Jones and M.F. Platzer. Numerical computation of flapping wing propulsion and power extraction. *AIAA Paper*, (97-0826), 1997.
- J. Katz and D. Weihs. Behavior of vortex wakes from oscillating airfoils. *Journal of Aircraft*, 15(1), pp. 861–863, 1978.
- R. Knoller. Die gesetze des lufrowiderstandes. *Flug und Motortechnik*, 3(21), pp. 1–7, 1909.
- M. Koochesfahani. Vortical patterns in the wake of an oscillating foil. *AIAA Journal*, 27, pp. 1200–1205, 1989.
- I. Kroo and P. Kunz. Mesoscale flight and miniature rotorcraft development. *American Institute of Aeronautics and Astronautics, (Mueller, 2001)*, 195, pp. 503–517, 2001.
- D. Kuchemann and J. Weber. *Aerodynamic propulsion in nature*. Aerodynamics of Propulsion. McGraw-Hill, New York, pp. 248–260, 1953.

- A. Kvist, A. Lindstrom, M. Green, T. Piersma, and G.H. Visser. Carrying large fuel loads during sustained bird flight is cheaper than expected. *Nature*, 413, pp. 730–732, 2001.
- J.C.S. Lai and M.F. Platzer. Jet characteristics of a plunging airfoil. *AIAA Journal*, 37, pp. 1529–1537, 1999.
- G.C. Lewin and H. Haj-Hariri. Modelling thrust generation of a two-dimensional heaving airfoil in a viscous flow. *Journal of Fluid Mechanics*, 492, pp. 339–362, 2003.
- M.J. Lighthill. Note on the swimming of slender fish. *Journal of Fluid Mechanics*, 9, pp. 305–317, 1960.
- M.J. Lighthill. Hydromechanics of aquatic animal propulsion. *Annual Review of Fluid Mechanics*, 1, pp. 413–446, 1969.
- M.J. Lighthill. Aquatic animal propulsion of high hydromechanical efficiency. *Journal of Fluid Mechanics*, 44, pp. 265–301, 1970.
- P.F. Linden and J.S. Turner. The formation of 'optimal' vortex rings and the efficiency of propulsion devices. *Journal of Fluid Mechanics*, 427, pp. 61–72, 2001.
- H. Liu, C.P. Ellington, K. Kawachi, C. van der Berg, and A.P. Willmott. A computational fluid dynamic study of hawkmoth hovering. *Journal of Experimental Biology*, 201, pp. 461–477, 1998.
- H. Liu and K. Kawachi. A numerical study of insect flight. *Journal of Computational Physics*, 146(1), pp. 124–156, 1998.
- P. Liu and N. Bose. Propulsive performance from oscillating propulsors with spanwise flexibility. *Proceedings of the Royal Society of London*, 453, pp. 1763–1770, 1997.
- J.N. Lyness and C.B. Moler. Numerical differentiation of analytic functions. *SIAM*, 4, pp. 202–210, 1967.
- J.R.R.A. Martins, P. Strudza, and J.J. Alonso. The complex-step derivative approximation. *ACM Transaction on Mathematical Software.*, 29(3), pp. 245–262, 2003.
- T. Maxworthy. The fluid dynamics of insect flight. *Annual Review of Fluid Mechanics*, 13, pp. 329–350, 1981.
- W.J. Maybury. *The aerodynamics of birds bodies*. PhD thesis, School of Biological Sciences, University of Bristol, UK, 2000.

- W.J. Maybury and J.M.V. Rayner. The avian tail reduces body parasite drag by controlling flow separation and vortex shedding. *Proceedings of the Royal Society of London B*, 268, pp. 1405–1410, 2001.
- K. W. McAlister, L.W. Carr, and W.J. McCroskey. Dynamic stall experiments on the naca0012 airfoil. *Technical Paper, NASA*, 1100, 1978.
- W.J. McCroskey and S.L. Pucci. Viscous-inviscid interaction on oscillating airfoils. *AIAA Paper*, (81-0051), pp. 1–16, 1981.
- W. McKinney and J. DeLaurier. The wingmill: an oscillating wing windmill. *Journal of energy*, 5(2), pp. 109–115, 1981.
- J.H. McMasters and M.L. Henderson. Low speed single element airfoil synthesis. *Technical Soaring*, 2(2), pp. 1–21, 1980.
- R. Mittal, Najjar. F., and H. Dong. Immersed boundary methods. *Annual Review of Fluids Mechanics*, 37, pp. 239–261, 2005.
- B. Mohammadi and O. Pironneau. Shape optimization in fluid mechanics. *Annual Review of Fluid Mechanics*, 36, pp. 255–279, 2004.
- T.J. Mueller. *Fixed and flapping wing aerodynamics for micro air vehicle applications*. Progress in Astronautics and Aeronautics, 2001.
- H. Ohashi and N. Ishikawa. Visualization study of flow near the trailing edge of an oscillating airfoil. *Bulletin of JSME*, 15(85), pp. 840–847, 1972.
- K. Ohmi, M. Coutanceau, T.P. Loc, and A. Dulieu. Vortex formation around an oscillating and translating airfoil at large incidences. *Journal of Fluid Mechanics*, 311, pp. 37–60, 1990.
- Y. Oshima and K. Oshima. Vortical flow behind an oscillating foil. In *Proceedings 15th IUTAM International Congress*, pages 357–368, North Holland, 1980.
- T.J. Pedley and S.J. Hill. Large amplitude undulatory fish swimming: fluid mechanics coupled to internal mechanics. *Journal of Experimental Biology*, 202, pp. 3431–3438, 1999.
- G.H. Pedro, A. Suleman, and Djilali N. A numerical study of the propulsive efficiency of a flapping hydrofoil. *International Journal for Numerical Methods in Fluids*, 42 (5), pp. 493–526, 2003.
- P.J. Phlips, R.A. East, and N.H. Pratt. An unsteady lifting line theory of flapping wings with application to the forward flight of birds. *Journal of Fluid Mechanics*, 112, pp. 97–125, 1981.

- E.C. Polhamus. Predictions of vortex-lift characteristics by a leading-edge suction analogy. *Journal of Aircraft*, 3(4), pp. 193–199, 1971.
- J.R. Praga, M.F. Reeder, and T. Leveron. An experimental study of micro air vehicle with rotatable tail. *AIAA Paper*, (2005-4756), 2005.
- J.O. Pralits and A. Hanifi. Optimization of steady suction for disturbance control on infinite swept wings. *Physics of Fluids*, 15(9), pp. 2756–2772, 2003.
- R. Radespiel, J. Windte, and U. Scholz. Numerical and experimental flow analysis of moving airfoils with laminar separation bubbles. *AIAA Journal*, 45(6), pp. 1346–1356, 2007.
- R. Ramamurti and W. Sandberg. Computational study of 3-D flapping foil flows. *AIAA Paper*, (2001-0605), 2001.
- R. Ramamurti and W. Sandberg. A three-dimensional computational study of the aerodynamic mechanisms of insect flight. *Journal of Experimental Biology*, 205, pp. 1507–1518, 2002.
- R. Ramamurti, W. Sandberg, and R. Löhner. Simulation of the dynamics of micro air vehicles. *AIAA Paper*, (2002-0896), 2000.
- J.M.V. Rayner. Form and function in avian flight. *Current Ornithology*, 5, pp. 1–77, 1988.
- J.M.V. Rayner. Biomechanical constraints on size in flying vertebrates. In P.J. Miller, editor, *Miniature vertebrates*, Symposia of the Zoological Society of London, pages 83–109, Oxford, 1996. Oxford University Press.
- J.M.V. Rayner. Thrust and drag in flying birds: application to birdlike micro air vehicle. *American Institute of Aeronautics and Astronautics*, (Mueller, 2001), 195, pp. 217–230, 2001.
- D.A. Read, F.S. Hover, and M.S. Triantafyllou. Forces on oscillating foils for propulsion and maneuvering. *Journal of Fluids and Structures*, 17, pp. 163–183, 2003.
- P.J. Roache. *Computational Fluid Dynamics*. Hermosa Publishers, 1972.
- W. Shyy and H. Liu. Flapping wing and aerodynamic lift: the role of leading-edge vortices. *AIAA Journal*, 45(12), pp. 2817–2819, 2007.
- J. Siekmann. Theoretical studies of sea animal locomotion, part i. *Ingenieur Archiv*, 31, pp. 214–228, 1962.

- D. Silin, B. Malladi, and S. Shkarayev. The university of arizona micro ornithopters. *The 2nd US-European Competition and Workshop on Micro Air Vehicles, Sandestin, FL, October 30- November 2, 2006*, 2006.
- M.J.C. Smith. Simulating moth wing aerodynamics: towards the development of flapping-wing technology. *AIAA Journal*, 34(7), pp. 1348–1355, 1996.
- R.W. Smith and J.A. Wright. Simulation of the propulsion characteristics of a flapping auv. *AIAA Paper*, (2005-4758), 2005.
- G.R. Spedding. The aerodynamics of flight. In R. McN Alexander, editor, *Advances in comparative and environmental physiology - Vol.II. Mechanics of animal locomotion*. Springer-Verlag, 1992.
- W. Squire and G. Trapp. Using complex variables to estimate derivatives of real functions. *SIAM Review*, 40(1), pp. 110–112, 1998.
- K. Streitlien and G.S. Triantafyllou. On thrust estimates for flapping foils. *Journal of Fluid and Structures*, 12, pp. 47–55, 1998.
- K. Streitlien, G.S. Triantafyllou, and M.S. Triantafyllou. Efficient foil propulsion through vortex control. *AIAA Journal*, 34(11), pp. 2315–2319, 1996.
- K. Streitlien and M.S. Triantafyllou. Force and moment on a Joukowski profile in the presence of point vortices. *AIAA Journal*, 33(4), pp. 603–610, 1995.
- M. Sun and J. Tang. Unsteady aerodynamic force generation by a model fruit fly wing in flapping motion. *Journal of Experimental Biology*, 205, pp. 55–70, 2002.
- G.K. Taylor, R.L. Nudds, and L.R.T. Adrian. Flying and swimming animals cruise at a strouhal number tuned for high power efficiency. *Nature*, 425, pp. 707–711, 2003.
- T.E. Tezduyar and J. Liou. On the downstream boundary conditions for vorticity-stream function formulation of two-dimensional incompressible flows. *Computer Methods in Applied Mechanics and Engineering*, 85, pp. 207–217, 1991.
- T. Theodorsen. General theory of aerodynamic instability and the mechanism of flutter. *NACA TR*, 496, 1935.
- A. Thom. An investigation of fluid flow in two dimensions. Technical Report 1194, Aerospace Research Center R. and M., United Kingdom, 1928.
- G.S. Triantafyllou, M.S. Triantafyllou, and M.A. Grosenbaugh. Optimal thrust development in oscillating foils with application to fish propulsion. *Journal of Fluids and Structures*, 7, pp. 205–224, 1993.

- M.S. Triantafyllou, G.S. Triantafyllou, and R. Gopalkrishnan. Wake mechanics for thrust generation in oscillating foils. *Physics of Fluids A*, 3(12), pp. 2835–2837, 1991.
- I.H. Tuncer and m. Kaya. Optimization of flapping airfoils for maximum thrust and propulsive efficiency. *AIAA Journal*, 43(11), pp. 2329–2336, 2005.
- I.H. Tuncer and M.F. Platzer. Computational study of flapping airfoil aerodynamics. *Journal of Aircraft*, 37(3), pp. 514–520, 2000.
- V.N. Vatsa. Computation of sensitivity derivatives of navier-stokes equations using complex variables. *Advances in Engineering Software*, 31, pp. 655–659, 2000.
- E. von Holst and D. Kuchermann. Biological and aerodynamical problems of animal flight. *Journal of the Royal Aeronautical Society*, 46, pp. 39–56, 1942.
- T. von Karman and J.M. Burgers. *General Aerodynamic Theory: perfect fluid*. Aerodynamic theory, Volume II. Springer Verlag, Leipzig, 1934.
- K.L. Wadlin, J.A. Ramsen, and V.L. Jr. Vaughan. The hydrodynamics characteristics of modified rectangular flat plates having aspect ratio of 1, 0.25 and 0.125 and operating near a free water surface. *NACA TR*, 1246, 1955.
- S. Walther, C. Airiau, and A. Bottaro. Optimal control of tollmien-schlichting waves in a developing boundary layer. *Physics of Fluids*, 13(7), pp. 2087–2096, 2001.
- Z.J. Wang. Vortex shedding and frequency selection in flapping flight. *Journal of Fluid Mechanics*, 410, pp. 323–341, 2000.
- Z.J. Wang, J.M. Birch, and M.H. Dickinson. Unsteady forces and flows in low Reynolds number hovering flight: two-dimensional computations vs robotic wing experiments. *Journal of Experimental Biology*, 207, pp. 449–460, 2004.
- H. Weimerskirch, J. Martin, Y. Clerquin, P. Alexandre, and S. Jiraskova. Energy saving in flight formation. *Nature*, 413, pp. 697–698, 2001.
- F. Weinig. Lift and drag of wings with small span. *NACA TM*, 1151, 1947.
- A.P Willmott and C.P. Ellington. The mechanics of flight in the hawkmoth *manduca sexta*. ii. aerodynamic consequences of kinematic and morphological variation. *Journal of Experimental Biology*, 200, pp. 2723–2745, 1997.
- P. Willmott. Unsteady lifting-line theory by the method of matched asymptotic expansions. *Journal of Fluid Mechanics*, 186, pp. 303–320, 1988.

- M. Wolfgang, Anderson J.M., M.A. Grosenbaugh, D.K.P. Yue, and M.S. Triantafyllou. Near-body flow dynamics in swimming fish. *Journal of Experimental Biology*, 202, pp. 2303–2327, 1999a.
- T. Wu. Swimming of waving plate. *Journal of Fluid Mechanics*, 10, pp. 321–344, 1961.
- T.Y.T. Wu. Hydromechanics of swimming propulsion. part 1. swimming of a two-dimensional flexible plate at variable forward speeds in an inviscid fluid. *Journal of Fluid Mechanics*, 46, pp. 337–355, 1971.
- J. Young and J.C.S. Lai. Mechanisms influencing the efficiency of oscillating airfoil propulsion. *AIAA Journal*, 45(7), pp. 1695–1702, 2007.
- C.H. Zimmerman. Characteristics of clark y airfoils of small aspect ratio. *NACA TR*, 431, 1932.
- D. Zuo, S. Peng, W. Chen, and Z. Weiping. Numerical simulation of flapping-wing insect hovering flight at unsteady flow. *International Journal of Numerical Methods in Fluids*, 53(12), pp. 1801–1817, 2006.